



# University of HUDDERSFIELD

## University of Huddersfield Repository

Tang, Dawei

Investigation of Line-Scan Dispersive Interferometry for In-Line Surface Metrology

### Original Citation

Tang, Dawei (2016) Investigation of Line-Scan Dispersive Interferometry for In-Line Surface Metrology. Doctoral thesis, University of Huddersfield.

This version is available at <http://eprints.hud.ac.uk/id/eprint/29153/>

The University Repository is a digital collection of the research output of the University, available on Open Access. Copyright and Moral Rights for the items on this site are retained by the individual author and/or other copyright owners. Users may access full items free of charge; copies of full text items generally can be reproduced, displayed or performed and given to third parties in any format or medium for personal research or study, educational or not-for-profit purposes without prior permission or charge, provided:

- The authors, title and full bibliographic details is credited in any copy;
- A hyperlink and/or URL is included for the original metadata page; and
- The content is not changed in any way.

For more information, including our policy and submission procedure, please contact the Repository Team at: [E.mailbox@hud.ac.uk](mailto:E.mailbox@hud.ac.uk).

<http://eprints.hud.ac.uk/>

**INVESTIGATION OF LINE-SCAN DISPERSIVE  
INTERFEROMETRY FOR IN-LINE  
SURFACE METROLOGY**

**DAWEI TANG**

A thesis submitted to the University of Huddersfield in partial fulfilment of the requirements  
for the degree of Doctor of Philosophy

The University of Huddersfield

March 2016

## **Copyright statement**

- i. The author of this thesis (including any appendices and/or schedules to this thesis) owns any copyright in it (the “Copyright”) and s/he has given The University of Huddersfield the right to use such copyright for any administrative, promotional, educational and/or teaching purposes.
- ii. Copies of this thesis, either in full or in extracts, may be made only in accordance with the regulations of the University Library. Details of these regulations may be obtained from the Librarian. This page must form part of any such copies made.
- iii. The ownership of any patents, designs, trademarks and any and all other intellectual property rights except for the Copyright (the “Intellectual Property Rights”) and any reproductions of copyright works, for example graphs and tables (“Reproductions”), which may be described in this thesis, may not be owned by the author and may be owned by third parties. Such Intellectual Property Rights and Reproductions cannot and must not be made available for use without the prior written permission of the owner(s) of the relevant Intellectual Property Rights and/or Reproductions.

## Abstract

Advanced manufacturing techniques enable ultra-precision surfaces to be fabricated with various complicated and large-area structures. For instance, the cost-effectiveness of Roll-to-Roll (R2R) manufacturing technology has been widely demonstrated in industries making high volume as well as large-area foil products and flexible electronics. Evaluation of these fine surfaces by an expensive trial-and-error approach is unadvisable due to the high scrap rate. Therefore quality control using in-line metrology of the functional surface plays an important role in the success of employing R2R technology by enabling a high product yield whilst guaranteeing high performance and a long lifespan of these multi-layer products.

This thesis presents an environmentally robust line-scan dispersive interferometry (LSDI) technique that is suitable for applications in in-line surface inspection. Obtaining a surface profile in a single shot allows this interferometer to minimise the effect of external perturbations and environmental noise. Additionally, it eliminates the mechanical scanning and has an extended axial measurement range without the  $2\pi$  phase ambiguity problem by dispersing the output of the spectrometer onto the camera. Benefiting from high-speed camera, general-purpose graphics processing unit and multi-core processor computing technology, the LSDI can achieve high dynamic measurement with a high signal-to-noise ratio and is effective for use on the shop floor.

Two proof-of-concept prototypes aimed at different applications are implemented. The cylindrical lens based prototype has a large lateral range up to 6 mm and can be used for characterisation of additively manufactured surface texture, surface form and surface blemish. The second prototype using a 4X microscope objective with a diffraction limited lateral resolution ( $\sim 4 \mu\text{m}$ ) is aiming at characterisation of surface roughness, micro-scale defects, and other imperfections of the ultra-precision surfaces. System design, implementation, fringe analysis algorithms and system calibrations are presented in detail in this thesis. Their performances are evaluated experimentally by measuring several standard step heights as well as  $\text{Al}_2\text{O}_3$  coated polyethylene naphthalate (PEN) films. The measurement results acquired using both prototypes and a commercial available instrument (Talysurf CCI 3000) align with each other acceptably. This shows that the developed metrology sensors may potentially be applied to production lines such as R2R surface inspection where only defects present on the surface are

concerned in terms of quality assurance. Implementation of these prototypes offers an attractive solution to improve manufacturing processing and reliability for the products in ultra-high-precision engineering.

## Acknowledgements

After four years of the Ph.D. journey, I finally put my name on the front cover of this thesis. What I acquired from this long journey is not only the thesis itself, but also the valuable research experience, the kind supports from my supervisors, friends and colleagues and the endless love from my family. I want to thank all the people who have helped me in this research.

First and foremost, I would like to express my sincere gratitude to my supervisor Professor Xiangqian Jiang for her support, guidance, motivation and encouragement during my Ph.d. course. I was so grateful for the confidence that she bestowed on me when first writing to her. I am forever indebted to her for offering me the opportunity to pursue my doctoral degree and have been a great honour to be her student. Her advice on both research as well as career have been priceless and helped me to be able to perform independent research. Additionally, I really appreciate all her contributions in providing the necessary facilities and funding to undertake this research and supporting my attendances at various conferences outside and inside the UK.

A special thanks to Dr. Feng Gao for his valuable advice and technical assistance in the experiments. He has always offered me tremendous supports whenever I met technical or practical problems during my Ph.D. course. It was so excited to successfully develop the proof-of-concept prototypes for my research work under his guidance. Also I really appreciate the time and effort he spent on reviewing my writings including annual reports, conference/journal papers and this thesis.

Thanks to all members in the EPSRC Centre for Innovative Manufacturing in Advanced Metrology including Professor Liam Blunt, Dr. Haydn Martin, Dr. Hussam Muhamedsalih and Dr. Prashant Kumar. You have all made for a wonderful and enjoyable place to work.

Last, but certainly not least, I would like to thank my family especially my parents for raising me as well as all the strong supports and profound love. Thanks to my beloved wife for her understanding, patience and encouragement in all my pursuits. I cannot image how to go through these days when I worked to midnight without her company. I also want to express my gratitude to my younger brother for taking care of our parents allowing me to fully concentrate on my research.

*This thesis is dedicated to my beloved mother (Rongyu Jiang), my father (Jineng Tang), my wife (Shuo Zhang) and my younger brother (Daqing Tang).*

# Table of Contents

<b>Copyright statement</b> .....	<b>2</b>
<b>Abstract</b> .....	<b>3</b>
<b>Acknowledgements</b> .....	<b>5</b>
<b>Table of Contents</b> .....	<b>6</b>
<b>List of Tables</b> .....	<b>9</b>
<b>List of Figures</b> .....	<b>10</b>
<b>List of abbreviations</b> .....	<b>16</b>
<b>1 Introduction</b> .....	<b>18</b>
1.1 Application background .....	18
1.2 Metrological techniques overview .....	19
1.3 Aim .....	22
1.4 Objectives .....	22
1.5 Contribution.....	23
1.6 Thesis organization.....	23
1.7 Publications .....	24
<b>2 Surface Metrology</b> .....	<b>25</b>
2.1 Introduction .....	25
2.2 Surface metrology .....	25
2.3 Surface characterisation.....	26
2.4 Measurement process types .....	28
2.5 Instrumentation for surface metrology .....	29
2.5.1 Contact profilometers.....	29
2.5.2 Non-contact profilometers .....	31
2.6 The requirements for in-line sensors .....	39
2.7 Summary.....	39
<b>3 Interferometry</b> .....	<b>41</b>
3.1 Introduction .....	41
3.2 Interference principle.....	41
3.3 Phase shifting interferometry .....	43
3.3.1 Single wavelength interferometry .....	43
3.3.2 Two and multiple wavelength interferometry.....	45
3.4 Vertical scanning interferometry .....	46
3.5 Wavelength scanning interferometry .....	49
3.6 Dispersive interferometry .....	52
3.7 Summary.....	56
<b>4 LSDI system development</b> .....	<b>58</b>

4.1	Introduction .....	58
4.2	System scheme .....	58
4.2.1	Light source .....	59
4.2.2	Interferometric objective.....	61
4.2.3	Spectrometer .....	64
4.2.4	Console .....	70
4.3	Alignment of interferometric objective .....	70
4.3.1	Simulation of cylindrical lens-based LSDI.....	71
4.3.2	Alignment strategy.....	74
4.4	Calibration of chromaticity axis of camera .....	75
4.4.1	Light source for calibration.....	75
4.4.2	Calibration equation.....	77
4.5	Summary.....	79
<b>5</b>	<b>Data processing.....</b>	<b>81</b>
5.1	Introduction .....	81
5.2	Fringe pattern.....	81
5.3	Fringe Analysis.....	83
5.3.1	Background removing.....	83
5.3.2	Wavelength calibration .....	86
5.3.3	Coordinate transformation .....	86
5.3.4	Phase calculation.....	88
5.3.5	Height map of a one-dimensional profile .....	95
5.4	Resolution of the algorithm .....	95
5.5	Investigation of data parallelism using GPU .....	97
5.5.1	GPU and CUDA overview.....	97
5.5.2	Data parallelism implementation for LSDI.....	100
5.6	Summary.....	101
<b>6</b>	<b>Optical apparatus 1: Cylindrical lens based LSDI .....</b>	<b>103</b>
6.1	Introduction .....	103
6.2	Methodology of long profile measurement .....	104
6.3	Measurement procedure .....	105
6.4	Validation of the experimental setup.....	106
6.4.1	Experimental conditions .....	106
6.4.2	Measurement of step heights samples.....	107
6.4.3	Inspection of the flat surface.....	112
6.5	Prototype implementation .....	114
6.5.1	Key points of design .....	114
6.5.2	Initial prototype.....	117
6.6	System performance .....	120
6.6.1	Lateral range and resolution.....	120
6.6.2	Axial measurement range .....	122
6.6.3	Angular measurement range .....	124
6.6.4	Measurement noise .....	128
6.7	Measurement results.....	130
6.7.1	Case 1: Standard step sample (4.707 $\mu\text{m}$ ).....	130

6.7.2	Case 2: Diamond-turned step sample (100 nm).....	131
6.8	Summary.....	133
<b>7</b>	<b>Optical apparatus 2: Microscope based LSDI.....</b>	<b>135</b>
7.1	Introduction .....	135
7.2	Surface profile measurement with high lateral resolution.....	136
7.3	Prototype design .....	136
7.3.1	Microscope objective .....	137
7.3.2	Tube lens .....	138
7.3.3	FOV of the interferometric objective.....	139
7.3.4	Initial prototype.....	140
7.4	System features.....	142
7.4.1	Lateral range and resolution.....	142
7.4.2	Axial measurement range .....	143
7.4.3	Angular measurement range .....	144
7.4.4	Measurement noise .....	144
7.5	Application 1: Evaluation of step height samples .....	145
7.6	Application 2: In-line defect detection for PEN film surface.....	147
7.7	Investigation of the effect from environmental disturbances .....	154
7.8	Summary.....	157
<b>8</b>	<b>Conclusion and Future Work.....</b>	<b>158</b>
8.1	Discussion.....	158
8.2	Conclusion.....	159
8.3	Future work .....	161
	<b>References .....</b>	<b>165</b>
	<b>Appendix A (Experimental data).....</b>	<b>176</b>
A.1	Simulation of cylindrical-LSDI system.....	176
A.2	Investigation of spot sizes in both x and y direction .....	178
A.3	Wavelength calibration data for cylindrical-LSDI.....	179
A.4	Wavelength calibration data for microscope-LSDI .....	180
	<b>Appendix B (MATLAB scripts).....</b>	<b>181</b>
B.1	FFT based algorithm .....	181
B.2	Carré algorithm.....	183
	<b>Appendix C (Measurement results).....</b>	<b>185</b>
C.1	Measurement results of the standard flat artefact.....	185
C.2	Measurement results of the 4.707 $\mu\text{m}$ standard step heights .....	186
C.3	Measurement results of the 100 nm diamond-turned step sample .....	187
C.4	Measurement results of the 100 nm standard step height.....	188
C.5	Measurement results of the 500 nm reference step sample.....	189

## **List of Tables**

Table 5.1 Processing time for different frame size using different types of algorithms	97
Table 5.2 Parallel programming performance (based on FFT algorithm)	101
Table 6.1 Details of the off-the-shelf components used in experimental setup	107
Table 6.2 Measurement results of two step heights samples	111
Table 6.3 Relative errors of measurement	111
Table 6.4 Off-the-shelf components used for prototype design (cylindrical – LSDI)	119
Table 6.5 Measurement noise estimation of cylindrical- LSDI	130
Table 7.1 Off-the-shelf components used for prototype design (microscope- LSDI)	136
Table 7.2 Measurement noise evaluation of microscope-LSDI	145
Table 7.3 Measured average heights of 500 nm step height	146
Table 7.4 Defects specifications (size, location)	153
Table 7.5 Measurement noises under different environmental conditions	156

## List of Figures

Figure 2.1 Surface characterisation: (a) extracted (raw) surface, (b) primary surface, (c) S-F surface, (d) S-L surface. ....	27
Figure 2.2 Procedure of surface assessment.....	28
Figure 2.3 Schematic representation of stylus profilometer [Adapted from Lee & Cho, 2012]....	30
Figure 2.4 SPM: (a) AFM, (b) STM [Adapted from Geisse, 2009 and Chen et al., 2014, respectively]. ....	30
Figure 2.5 Relationship between the true contact point P and the vertex of the stylus V.....	31
Figure 2.6 Machine vision system [Adapted from ISRA Vision, 2015].....	33
Figure 2.7 Principle of optical scatterometry .....	35
Figure 2.8 Schema of a focus variation instrument [Adapted from Leach, 2014].....	36
Figure 2.9 Schema of confocal microscopy: (a) Monochromatic type, (b) Chromatic type (CCM). .....	38
Figure 2.10 Measurement ranges for different instruments [Adapted from Jiang et al., 2007]....	40
Figure 3.1 Schematic of vertical scanning interferometry .....	47
Figure 3.2 Localisation of coherence peak using VSI technique .....	47
Figure 3.3 Signals of the step object with WSI technique .....	51
Figure 3.4 An enhanced WSI with an active servo system to eliminate the environmental noise [Adapted from Muhamedsalih, 2013] .....	51
Figure 3.5 Optical setup of dispersive interferometry [Adapted from Schwider and Zhou, 1994] .....	53
Figure 3.6 Hyperspectral interferometer for single-shot 3D shape measurement [Adapted from Huntley et al., 2010].....	54
Figure 3.7 Optical configuration of SDSCI system [Adapted from Hassan et al., 2014] .....	55
Figure 3.8 Optical setup of SDOCT [Adapted from Yasuno et al., 2006].....	56
Figure 4.1 Schematic representation of employing the LSDI metrology system on a production line.....	58
Figure 4.2 Block diagram of the LSDI system.....	59
Figure 4.3 Typical electromagnetic spectrum with visible light highlighted.....	60
Figure 4.4 Light source device .....	61

Figure 4.5 Spectral distribution of the developed light source device .....	61
Figure 4.6 Schemas of interferometric objectives: (a) Linnik, (b) Michelson, (c) Mirau and (d) Fizeau. ....	62
Figure 4.7 Diffraction of light using a grating .....	65
Figure 4.8 Investigation of the optimal incident angle: (a) Surface mesh result, (b) D-W curve at the incident angle of $\theta_i=10^\circ$ , (c) Standard deviation of linearity errors with respect to incident angle. ....	66
Figure 4.9 Typical optical bench configurations for a spectrometer: (a) crossed Czerny-Turner, (b) unfolded Czerny-Turner, (c) concave-holographic configuration, (d) lens-based configuration [(a) & (b) adapted from B&W Tek Inc. and Photonics, respectively]. ....	68
Figure 4.10 3D layout of LSDI model in ZEMAX. 1, white light source; 2 & 11, collimator; 3, iris diaphragm; 4 & 6, beamsplitter; 5, cylindrical lens; 7, reference mirror; 8, tested surface; 9, tube lens; 10, slit; 12, grating; 13, imaging lens; 14, camera. ....	71
Figure 4.11 Comparison of the spot diagrams between system with and without aberrations (CYL: cylindrical lens, SPL: spherical lens).....	72
Figure 4.12 Misalignments: (a) tilt of the cylindrical lens, (b) tilt of the beamsplitter. CL, cylindrical lens; BS, beamsplitter; RM, reference mirror; TS, tested surface. ....	72
Figure 4.13 Simulations regarding the tilts of optical components: (a) spot diagram results by tilting the cylindrical lens, (b) interferogram results through tilting the beamsplitter. ....	73
Figure 4.14 Alignment of the reference mirror in an interferometric objective .....	75
Figure 4.15 Calibration of chromaticity axis of camera: (a) spectrum of cadmium lamp on the camera, (b) calculated wavelength for each pixel. ....	76
Figure 4.16 Schematic diagram of the developed light source device for wavelength calibration .....	77
Figure 4.17 Wavelength calibration using commercial spectrometer: (a) wavelength validation using CCS100, Thorlabs Inc., (b) the corresponding spectral line on the camera. ....	78
Figure 4.18 Calibration of chromaticity axis of camera: (a) calibrated curves using equation (4.3) and (4.5), (b) calibrated results with an appropriate amount of offset. ....	79
Figure 5.1 Fringe pattern for a step object using LSDI.....	81
Figure 5.2 Flowchart of the developed algorithms .....	82

Figure 5.3 Interference signal with background intensity variation: (a) original signal, (b) corresponding Fourier transform spectrum with an undesired peak. ....	84
Figure 5.4 Background signal extracted from the spectral interferogram and its filtered curve...	84
Figure 5.5 Interference signal after removing the background (a) corrected signal, (b) Fourier transform spectrum of the corrected signal. ....	85
Figure 5.6 Coordinate transformation: (a) original signal – wavelength related curve, (b) signal after coordinate transformation and resampling– wavenumber related curve with equal k spacing. ....	87
Figure 5.7 Fourier transform spectrum .....	89
Figure 5.8 Fourier transform spectrum after filtrated out the DC and the phase conjugate term .	90
Figure 5.9 Wrapped phase distribution with discontinuities (FFT algorithm).....	91
Figure 5.10 The offset phase distribution for correcting the discontinuities .....	91
Figure 5.11 Unwrapped phase distribution and its LS fitted curve (FFT algorithm).....	92
Figure 5.12 Spectral signal with shifted phases .....	93
Figure 5.13 Wrapped phase distribution with discontinuities (Carré algorithm).....	94
Figure 5.14 Unwrapped phase distribution and its LS fitted curve (Carré algorithm).....	94
Figure 5.15 Floating point operation per second for the CPU and GPU [adapted from NVIDIA, 2015].....	98
Figure 5.16 General execution of a CUDA program [adapted from Kirk & Wen-me, 2012] .....	99
Figure 5.17 Thread hierarchy and Memory hierarchy [adapted from Muhamedsalih, 2013].....	99
Figure 5.18 The CUDA program structure of FFT algorithm.....	100
Figure 6.1 Schematic diagram of cylindrical lens based LSDI.....	103
Figure 6.2 Perspectives of the optical setup: (a) y-z plane (horizontal), (b) x-z plane (vertical). C1, collimator 1; BS, beamsplitter; CL, cylindrical lens; TL, tube lens; C2, collimator 2; G, grating; IL, imaging lens. ....	104
Figure 6.3 Spectral interferogram of the 9.759 $\mu\text{m}$ step sample .....	107
Figure 6.4 Cross-sectional profile results of 9.759 $\mu\text{m}$ step sample: (a) the LSDI result, (b) the CCI result. ....	108
Figure 6.5 Measured surface maps of the 9.759 $\mu\text{m}$ step sample: (a) the LSDI result, (b) the CCI result. ....	108
Figure 6.6 Step heights sample from Rubert & Co. Ltd. ....	109

Figure 6.7 Spectral interferogram of the 30 $\mu\text{m}$ step sample .....	109
Figure 6.8 Cross-sectional profile results of 30 $\mu\text{m}$ step sample: (a) the LSDI result, (b) the CCI result. ....	110
Figure 6.9 Measured surface map of the 30 $\mu\text{m}$ step sample: (a) the LSDI result, (b) the CCI result. ....	110
Figure 6.10 Surface profile measurement of the mirror surface .....	112
Figure 6.11 A detective mirror and the corresponding fringe pattern.....	112
Figure 6.12 Surface inspection results of the defective mirror with a scratch: (a) cross-sectional profile, (b) measured surface map.....	113
Figure 6.13 Study of spot shape using ZEMAX simulation .....	115
Figure 6.14 Different spot sizes in x and y axis .....	115
Figure 6.15 Effect resulting from the misalignment of the collimator.....	116
Figure 6.16 Distorted spectral lines observed in experiment due to the misalignment of collimator 2 .....	117
Figure 6.17 Effect resulting from the misalignment of the camera: (a) low fringe visibility, (b) overlapping of the spectral lines, (c) well-separated spectral lines.....	117
Figure 6.18 Initial prototype of cylindrical-LSDI.....	118
Figure 6.19 Calibration of chromaticity axis of camera for cylindrical-LSDI prototype .....	119
Figure 6.20 USAF target: (a) the image of the USAF test target, (b) size chart of group 0. ....	121
Figure 6.21 Determination of the CCD pixelation: (a) image of the USAF target captured by camera, (b) corresponding intensity modulation.....	122
Figure 6.22 Measurement result of a reference sample with 200 $\mu\text{m}$ step height: (a) spectral interferogram, (b) surface profile result. ....	123
Figure 6.23 Schema of the maximum measurable slope.....	124
Figure 6.24 Profile results of the concave mirrors using cylindrical-LSDI.....	126
Figure 6.25 Surface map results of the concave mirrors: (a) RC=76.2 mm, (b) RC=100 mm, (c) RC=300 mm, (d) RC=610 mm.....	126
Figure 6.26 Beam deviations by rotating two optical wedges with different angles .....	127
Figure 6.27 Introducing two pairs of dual-optical wedges into interferometric objective. $\varphi$ : Relative rotation angle between two optical wedges. ....	128

Figure 6.28 Subtraction technique for estimating the measurement noise of cylindrical-LSDI: (a) five profiles with surface roughness, (b) four new profiles after removing the intrinsic roughness. ....	129
Figure 6.29 Measurement results for 4.707 $\mu\text{m}$ standard step height sample: (a) surface profiles using FFT algorithm and Carré algorithm, respectively, (b) constructed surface map through scanning.....	131
Figure 6.30 Measurement results for 100 nm step height sample: (a) surface profile using FFT algorithm, (b) constructed surface map through scanning. ....	132
Figure 7.1 Schematic diagram of microscope based LSDI.....	135
Figure 7.2 Typical microscope optical systems: (a) using finite microscope objective, (b) using infinity-corrected microscope objective. ....	137
Figure 7.3 Dimension specifications of an infinity microscope system .....	139
Figure 7.4 Perspective of the optical setup. S1-S4, spot image; C1, collimator 1; BS, beamsplitter; MS, microscope TL, tube lens; C2, collimator 2; G, grating; IL, imaging lens....	139
Figure 7.5 Initial prototype of microscope-LSDI.....	141
Figure 7.6 Calibration of chromaticity axis of camera for microscope-LSDI prototype.....	141
Figure 7.7 Microscope slide R1L3S1P under magnification [adapted from Thorlabs, Inc.].....	142
Figure 7.8 Determination of the CCD pixelation: (a) image of the stage micrometre using 4X objective, (b) relationship between divisions and pixelation. ....	142
Figure 7.9 Results for micro fluid chip-100 $\mu\text{m}$ step height: (a) measured surface, (b) cross-sectional profile. ....	143
Figure 7.10 Subtraction technique for estimating the measurement noise of microscope-LSDI: (a) five profiles with surface roughness, (b) four new profiles after removing the intrinsic roughness.....	144
Figure 7.11 Measurement results for 100 nm standard step height sample: (a) surface profile using FFT algorithm, (b) constructed surface map through scanning.....	146
Figure 7.12 Measurement results for 500 nm reference step height sample: (a) surface profile using FFT algorithm, (b) constructed surface map through scanning.....	147
Figure 7.13 Schematic of the flexible PV Module [adapted from Flisom, Switzerland].....	148
Figure 7.14 Main defects present on the PEN film substrate by AFM [Adapted from Elrawemi, 2015].....	149

Figure 7.15 Structure of the PEN film by Environmental Scanning Electron Microscopy (ESEM) [Adapted from Elrawemi, 2015] .....	150
Figure 7.16 Images of defects observed by camera 1 in microscope-LSDI prototype .....	151
Figure 7.17 Surface map of defects on the area 1 of the barrier film surface (raw results without data post-processing): (a) CCI result, (b) LSDI result. ....	152
Figure 7.18 Surface map of defects on the area 2 of the barrier film surface (raw results without data post-processing): (a) CCI result, (b) LSDI result. ....	152
Figure 7.19 2D view of defects on the Al <sub>2</sub> O <sub>3</sub> ALD barrier film surface (performed data processes such as form removing and levelling): (a) CCI result, (b) LSDI result. ....	153
Figure 7.20 Interference signals affected by the environmental disturbances .....	154
Figure 7.21 Measurement noise curves under different environmental conditions. Red line, almost no environmental noise; Black line, air turbulence applied; Green line, vibration applied; Blue line, vibration & air turbulence applied. ....	155
Figure 7.22 Surface maps constructed by 20 surface profiles: (a) almost no environmental noise, (b) vibration applied, (c) air turbulence applied, (d) vibration & air turbulence applied.....	156

## List of abbreviations

AM	Additive manufacturing
R2R	Roll-to-Roll
PV	Photovoltaic
CIGS	$\text{CuIn}_x\text{Ga}_{(1-x)}\text{Se}_2$
CFS	Coherent Fourier Scatterometry
OLED	Organic Light Emitting Display
OPV	Organic Photovoltaic
AFM	Atomic force microscopy
SEM	Scanning electron microscopy
CCM	Chromatic confocal microscopy
FV	Focus variation
POCT	Parallel optical coherence tomography
WSI	Wavelength scanning interferometer
SD-OCT	Spectral-domain optical coherence tomography
LSDI	Line-scan dispersive interferometry
GUGPU	General purpose graphic processing unit
SPMs	Scanning Probe Microscopes
STM	Scanning Tunneling Microscope
WLI	White light interferometry
FOV	Field of view
ROI	Region of interest
SNR	Signal-to-noise ratio
NA	Numerical aperture
ND	Neutral density
PSI	Phase shifting interferometry
PZT	Piezoelectric transducers
OPD	Optical path difference
DOF	Depth of field

VSI	Vertical scanning interferometry
WLSI	White light scanning interferometry
CCI	Coherence correction interferometry
AOTF	Acousto-optic tunable filter
FFT	Fast Fourier transform
SRWLI	Spectrally resolved white light interferometry
WLCSI	White light channelled spectrum interferometry
SDOCT	Spectral domain optical coherence tomography
LSLO	Line-scanning laser ophthalmoscopy
HSI	Hyperspectral interferometry
SDSCI	Spatially dispersed short-coherence interferometry
CUDA	Compute Unified Device Architecture
PPM	Photodiode power meter
FWHM	Full width at half maximum
IFFT	Inverse fast Fourier transform
LS	Least square
PV	Peak-valley
RMS	Root-Mean-Square
PEN	Polyethylene naphthalate
NPL	National Physical Laboratory
ALD	Atomic layer deposition
WVTR	Water vapour transmission rate
CPI	Centre for Process Innovation
RC	Radius of curvature

# 1 Introduction

## 1.1 Application background

Surfaces act as interfaces which have a direct influence on the functional behaviour of a product (De Chiffre et al., 2003). It has been shown that 90% of all engineering component failures in practice are surface initiated, through mechanisms such as adhesive wear, fretting wear, and erosion (Blunt & Jiang, 2003). Therefore, surface metrology plays an important role in manufacturing as well as optimising the performance of a workpiece for quality assurance.

Advanced manufacturing techniques such as additive manufacturing (AM) and Roll-to-Roll (R2R) manufacturing technologies, enable ultra-precision surfaces to be fabricated with increasingly large areas, complicated curvatures and customised nanostructures (Leach et al., 2015). Instead of milling a work piece from solid block, AM refers to ‘a process of joining materials to make objects from 3D model data, usually layer upon layer, as opposed to subtractive manufacturing methodologies’ (Standard, 2012). It makes components built up highly complex with reduced part count and shorter design cycle and is an ideal technology for making high-value parts. AM is increasingly being applied to make components in the aerospace, automotive and medical sectors (Platform, 2014). R2R, always involving the deposition and patterning of multi-layer thin films on large area substrates, is also one of the most cost-effective manufacturing processes applied in numerous fields such as flexible and large-area organic electronics devices (Søndergaard et al., 2013; Willmann et al., 2014), solar panels (Krebs et al., 2010; Schulz-Ruhtenberg et al., 2014), flexible displays (Gregg et al., 2005), thin-film batteries (Keranen et al., 2012) and chemical separation membranes (Morse, 2012). It has been reported that the flexible Photovoltaic (PV) films based on  $\text{CuIn}_x\text{Ga}_{(1-x)}\text{Se}_2$  (CIGS) could conserve the light energy with an efficiency up to 19% (Jackson et al., 2011). The extreme miniaturisation of critical feature sizes to the nano-scale makes the R2R technology of considerable interest to modern industry (Morse, 2012).

However, surface quality is one of the main constraints concerning AM (Grimm et al., 2015) and R2R technology (Lee et al., 2010). One of the biggest challenges faced by industry is characterisation of surface texture, defects, and other imperfections as surface effects are responsible for 10% of the failure rate for manufactured parts (Leach, 2011). Meanwhile, it has been reported that traditionally high quality fabrication relies mainly on experience or trial-and-

error, which makes the manufactured items suffer from a scrap rate as high as 50-70% (Heeren & El-Fataty, 2008; Jiang et al., 2010). It is suggested that in-process measurement is the ideal way to monitor the manufacturing process but with a great challenge, which subsequently stimulates the development of modern metrological instrumentation. Take R2R manufactured components as an example, the film products must be uniform and largely perfect across most of the area of the foil. Defects are undesirable for printed electronics since they cause open and short circuits, thus preventing correct function. Likewise, the defects present on an Al<sub>2</sub>O<sub>3</sub> barrier layer of flexible PV cells make the active elements suffer from environmental degradation due to the penetration of water and oxygen vapour (Carcia et al., 2006; Rossi & Nulman, 1993) and thus are detrimental to the performance of the PV module (Blunt et al., 2014; Elrawemi et al., 2013). Therefore, concerning the success of employing R2R technology, an in-line surface inspection system needs to be implemented to optimise the manufacturing process for coated polymer films in terms of quality control. After the effective inspection, further processes like local repair techniques can be applied according to the provided feedback to remove the defects and correct the fabrication anomalies, which consequently achieves a reduction in product costs and throughput time as well as guarantees a high performance and long lifespan of these multi-layer products.

## **1.2 Metrological techniques overview**

Advances in modern manufacturing have led to the progress and development of wide range of metrology devices and instrumentation. Faster measurement speed with sophisticated computational capabilities has been made possible with the use of modern computers and efficient algorithms. This section details various examples of developed metrology instruments so far, which mainly based on two classifications, namely contact and non-contact types (Conroy & Armstrong, 2005; Malacara, 2007; Whitehouse, 1997).

Contact profilometers such as stylus based instruments can cover a large measurement range up to several millimetres in height with nanometre axial resolution. Yet they are not capable of performing in-line measurement due to slow measuring speed and non-immunity to manufacturing environment (Bhushan, 2000; Young et al., 1980). While optical techniques, based on either non-interferometric or interferometric principle, can provide damage-free measurements for ultra-precision surface with fine axial and lateral resolution and have the potential to be used in in-line surface metrology. There are several critical factors that determine

the performance of in-line surface inspection such as outstanding dynamic range, excellent signal-to-noise ratio, high measurement speed and flexible and easy integration into a production environment (Martin, 2010). Currently the instruments, whether commercially available or not, developed potentially for on-line/in-line surface inspection in terms of quality assurance mainly adopt techniques such as machine vision (Chin & Harlow, 1982), scatterometry (Stover, 1995), confocal microscopy (Petroll et al., 1993), focus variation (Bremen et al., 2012), and optical interferometry (Yatagai, 1994).

Machine vision system is one of the most common optical methods for surface inspection (Leach & Sherlock, 2014; Shankar & Zhong, 2005). ISRA Vision reported a high-speed camera-based inspection system for substrate surface. A well-aligned line-scan camera bank covers the complete product width with certain defined overlaps and the switchable LED illuminations at different positions make it capable of performing defects detection for different applications (ISRA-Vision, 2015). Nonetheless, it is not suitable for the metrological field where defects or fine structures are smaller than the diffraction limit of the instrument used. In this case, surface inspection using scatterometry can be a preferred solution due to its super-resolution breaking the diffraction limit (Ke et al., 2010; Leach & Sherlock, 2014). An enhanced Coherent Fourier Scatterometry (CFS) with signal-to-noise ratio is proposed for contamination detection in R2R production of Organic Light Emitting Display (OLED) and Organic Photovoltaic (OPV) devices (Pereira, 2015). The overall nanometre accuracy performance of CFS can be comparable to that of AFM and SEM measurements on the same sample (Kumar et al., 2014). Yet both of the two methods mentioned above are either only 2D image which is impossible to reconstruct for 3D information of defects, or just detection with no images of tested surface at all (Thonya et al., 2003).

Some companies such as Precitec, Nanofocus and Polytec offer chromatic confocal microscopy (CCM) solutions for real-time quality control of various engineering surfaces. A series of optical sensors developed by Precitec has been applied for contact-free measurement in industries such as Photovoltaics, glass, semiconductor and medicine. These sensors can be directly integrated into the in-line production process because of their high speed and the possibility to handle up to three encoder signals with a high measurement rate. The spot diameter of the optical probe is only few micrometres which enables the detection of small surface defects. Nanofocus also has been working at the CCM sensors which can be flexibly and easily

integrated into manufacturing machines. With more than one million measurements per second, the measurement sensors such as  $\mu$ sprint products offer a good solution for a broad range of applications from 3D form, topography and defect detection. The CCMs eliminate the scanning in height; however their vertical measurement ranges are restricted by the capability of its optical system to separate the broadband wavelength along the optical axis.

Alicona offers a range of optical metrology products based on focus variation (FV) method (Triantaphyllou et al., 2015) enabling the measurement of functional parameters such as surface texture and roughness. Compared to most optical measurement techniques restricted by an angle of slope of  $60^\circ$ , FV technique is capable of measuring the angle of slopes bigger than  $80^\circ$ . Therefore, FV instruments are of great interest in the metrology of AM surfaces, where there is a requirement to perform the measurements on complex geometries with steep slopes as well as large vertical range. Regarding interferometry techniques, Heliotis developed a series of products (HeliInspect H3, H4, etc.) utilising the parallel optical coherence tomography principle (POCT) (Ducros et al., 2002) to be engineered for industrial applications requiring high throughput in harsh environment. Fast vertical scan speed (up to 50 mm/s), high-speed camera combing with in-pixel signal processing and special physical design make these systems meet the requirements of the most demanding 3D in-line inspection tasks such as measuring roughness, step height and defects. Additionally, an enhanced wavelength scanning interferometer (WSI) for detecting defects on PV films was proposed as well (Jiang et al., 2010; Muhamedsalih et al., 2014). Compared to conventional WSI it combines four new techniques, namely compensation of environmental noise by a built-in stabilisation system, wide wavelength scanning technique using acousto-optic tunable filter (AOTF), analysing the interferograms in a parallel manner using GPU technology (Muhamedsalih et al., 2013), and auto-focus function through a multiplexed reference interferometer along with a translation stage (Muhamedsalih et al., 2015). Yet for the moment FV, POCT and WSI system are still limited to some extent in that they require the sample surface to keep stationary when performing measurements.

Compared to the above-mentioned interferometers, single shot interferometry stands out because it eliminates the mechanical scanning along the optical axis and enables measurement of the surface in motion. “FlexCam”, one of such kind of systems developed by 4D Technology (George, 2014; Kimbrough, 2015), is implemented to detect defects for PV barrier films manufactured by R2R technology due to its anti-environmental disturbance and fast

measurement with 3D surface topography. It provides sub-nanometre vertical resolution and micrometre-scale lateral resolution for in-process roughness and defect quantification and enables real-time monitoring and control of roughness to less than 0.5 nm rms. However, the vertical measurement range of this system is limited to sub-microns (George, 2014), which is problematic when attempting to identify and classify features or defects with large vertical range (a few micrometres to a few tens micrometres). Line-scan dispersive interferometry is another promising technique for monitoring the manufacturing process. It has an extended axial measurement range without the  $2\pi$  phase ambiguity problem by spatially separating the broadband beam along the detector pixels of the spectrometer. Fast surface profiling by analysis of a single interferogram allows this system to minimise the effect of external environmental disturbances. In the last decades it has been widely used in applications such as surface profile and thin-film thickness measurements (Debnath & Kothiyal, 2005; Malacara, 2007).

### **1.3 Aim**

The aim of this research work is to investigate the potential for applying the line-scan dispersive interferometry (LSDI) in in-line metrology of functional surfaces or R2R surface inspection where only defects on film surfaces are concerned in terms of quality assurance. By combining the single shot interferometry technique with high speed CCD/CMOS camera and graphic processing unit (GPU) technology, the developed metrology devices shall be environmentally robust and realise high dynamic measurement ratio with a high signal-to-noise ratio to overcome the technology barriers of the current white light interferometry, and thus be potentially applied to monitor the samples in production lines. By using different types of interferometric objectives, the line-scan dispersive interferometer shall have the measurement capabilities for characterisation of surface profiles in large range (up to 6 mm) or defects with microscale sizes.

### **1.4 Objectives**

- To investigate approaches for designing a single shot interferometry system for surface inspection to achieve vertical resolution in the nanometre range while maximising lateral range and resolution.
- To develop and optimise efficient absolute phase measurement algorithms to improve the measuring accuracy and speed.

- To build compact prototypes equipped with different types of interferometric objectives able to measure surface profile instantly in the manufacturing environment.
- To evaluate the performances of developed sensor systems to prove their feasibilities and reliabilities as metrology tools for in-line micro/nano scale surface profile measurement.
- To calibrate the developed prototypes in terms of accuracy, resolution, measurable range and repeatability.

## 1.5 Contribution

This research project contained in this thesis has made the following contributions:

- Development and demonstration of a single shot dispersive interferometry technique with extended lateral range by using cylindrical lens to observe the tested surface with line focus. It can achieve real-time surface inspection with a long profile up to 5.885 mm and may potentially be used for characterisation of additively manufactured surface texture, surface form and surface blemish present on the functional surface.
- Development and demonstration of an instantaneous line-scan dispersive interferometry using a 4X microscope objective to measure the smaller structure dimensions and features on engineering surface and detect defects present on the PV barrier films manufactured by R2R technology.
- Demonstration of the efficiency and accuracy of the developed algorithms and further acceleration of computing process through data parallelism using GPU technology (based on FFT technique).

## 1.6 Thesis organization

This research work presents the development of the line-scan dispersive interferometry for in-line surface inspection with the aim of producing an environmentally robust, instantaneous metrology instrument capable of performing nanoscale measurements. The thesis is organised into eight chapters to present the overall aim of the research project.

- Chapter 2 first presents a brief introduction about surface metrology and some of related terminologies used in the field. It also gives a description of various metrology techniques proposed for surface characterisation with emphasis on the

optical metrology techniques, which may be potentially applied in in-line surface measurement.

- Chapter 3 shifts the emphasis to introduction of interferometry for precision surface metrology, including the interference principle and methodologies of various interferometry based instruments. Due to the particular interest in dispersive interferometry, its principles and advantages over other interferometers are discussed in some detail.
- Chapter 4 presents the development strategy of the line scan dispersive interferometry in detail by dividing it into four parts, namely light source, interferometric objective, spectrometer and the console. Additionally, the alignment of interferometric objective and wavelength calibration are described due to the crucial influence on the system performance.
- Chapter 5 describes the fringe analysis of the spectral interferogram in five steps. Two algorithms are presented to analyse the measurement data recorded by the developed metrology sensor. Subsequently the resolution of the algorithm and a parallel programming model for accelerating the computing process using GPU technology are discussed.
- Chapter 6 reports a cylindrical lens-based interferometer prototype which aims at long profile measurement mainly in terms of surface form evaluation. The performance was evaluated by measuring the reference step samples with heights ranging from 100 nm to 200  $\mu\text{m}$ .
- Chapter 7 presents an appraisal of the other prototype using a 4X microscope objective in the optical probe head. It has potential to be used for R2R surface inspection where only defects on the film surface are concerned. Both step height samples and flexible PV films were measured to assess the system's performance.
- Chapter 8 gives the overall discussion of the developed LSDI systems and provides the conclusions and proposal for further investigation and improvement.

## **1.7 Publications**

The work in this thesis has produced one peer reviewed journal paper, and six conference papers. A full publication list can be found in the 'Publications and Awards' section at the end of this thesis.

## **2 Surface Metrology**

### **2.1 Introduction**

Surface metrology is of great importance in manufacturing and optimising the performance of a workpiece. Roughness, waviness and form are three basic geometrical features used to evaluate an engineered surface. Among all various measurement processes, in-process techniques stand out because it offers not only assessment but also effective feedback. This chapter briefly introduces surface metrology and then presents a detailed overview of the recent trends in surface metrology with special emphasis on non-contact optical metrology techniques, which may potentially be used for the in-line retrieval of surface topographic information. Finally, a description of the requirements for in-line metrological sensors is made.

### **2.2 Surface metrology**

Surface metrology refers to the measurement that describes the surface deviation between a structured surface and its ideal shape (Whitehouse, 2004). It also defined by Jiang et al. (2007) as, ‘the science of measuring small-scale geometrical features on surfaces: the topography of the surface.’ It specifically covers measurements such as surface texture, surface roughness, surface shape, surface finish, etc.

Manufactured surfaces are allowed to be specially designed with a particular function and can be classified into two main categories, namely engineered surface and non-engineered surface (Stout & Blunt, 2001). The engineered surfaces are generally manufactured to provide functional properties such as bearing and sealing, or to have high fluid retention capabilities. The assessment of these surfaces is critical because a significant proportion of engineered component failures in practice are surface initiated due to surface defects resulting from the friction, corrosion and wear. In the past numerous metrological work had been conducted on the surfaces manufactured by processes such as turning, milling, grinding and polishing, which generate surface roughness ranging from several micrometres to sub-micrometres. With the evolution of manufacturing technology, surface metrology has shown its significant importance not only in traditional mechanical production, but also extension into semiconductor industry, optoelectronics industries and biomedical field where feature characterisation at nanometre scale is required (Lonardo et al., 2002). The significant challenges of surface topography consequently stimulate the development of modern metrological instrumentation.

Various metrological techniques for quality assurance of surfaces have been developed according to different applications and described in detail in scientific literatures by several authors (Grous, 2013; Mainsah & Chetwynd, 2013; Vorburger et al., 2007; Whitehouse, 1997). As mentioned in chapter 1, measurement techniques based on off-line approaches make the manufactured items suffer from a high scrap rate. This is especially true for the production of high value components where a high level of innovation is normally involved. Therefore, in-process metrology for ensuring great accuracy and functionality of a component will significantly contribute to the manufacture of these products in a cost-effective and environmentally sustainable manner (Leach, 2014), because it not only allows the assessment of manufactured components but also offers valuable feedback to the control system for optimised manufacturing or post-process repairs.

### 2.3 Surface characterisation

A number of different frequency components related to the manufacturing process or the production technique are superimposed to form the structures on the surfaces (Mainsah & Chetwynd, 2013; Thomas, 1998). These different frequency components affect the performance of a workpiece in both functional and aesthetic aspects. Surface features are generally characterised along the vertical direction by height parameters and along the horizontal direction by spatial (wavelength) parameters (Sherrington & Smith, 1988). According to the spatial frequency, the frequency components for a surface profile are generally divided into three types of surface features, namely form, waviness and roughness (Blunt & Jiang, 2003; ISO, 1997; Raja et al., 2002; Texture, 1995). For areal surface characterisation, the concept of scale-limited surface is introduced. The scale-limited surface contains S-F surface and S-L surface (as shown in Figure 2.1), which are created by combination of S-filter, L-filter and F-operator (ISO, 2012).

- **S-filter**, which defined as a filter that removes small scale lateral components from the surface resulting in the primary surface.
- **L-filter**, which is used to remove large-scale lateral components from the primary surface or S-F surface.
- **F-operator**, which removes the form from the primary surface.

An S-F surface results from the use of an S-filter and an F-operator in combination on a surface, and an S-L surface by the use of an L-filter on an S-F surface.

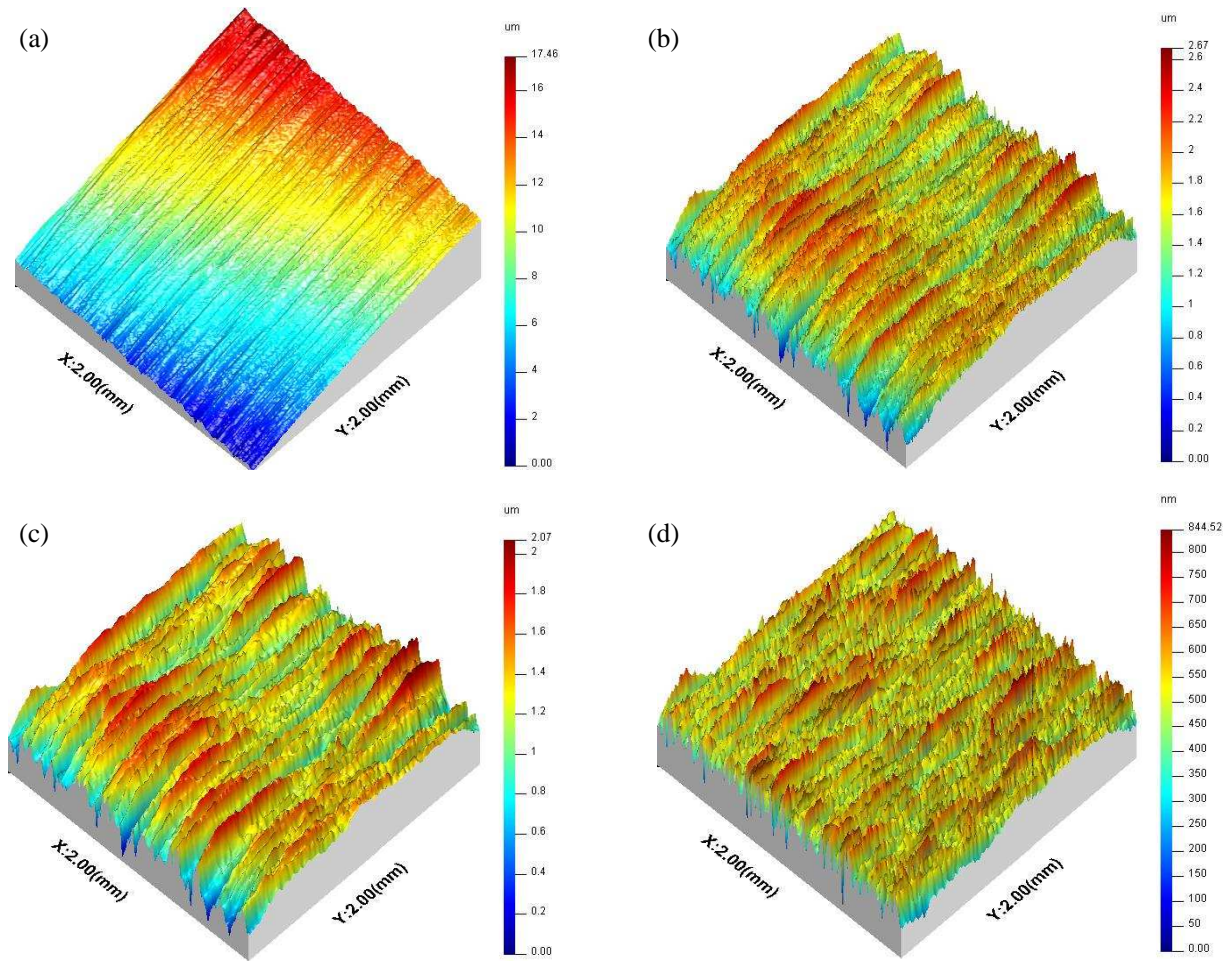


**Figure 2.1 Surface characterisation: (a) extracted (raw) surface, (b) primary surface, (c) S-F surface, (d) S-L surface.**

The separation and characterisation of the surface texture allow a direct assessment of the manufacturing process and prediction of the functional performance of the work piece (Davim, 2010; Jiang & Whitehouse, 2012). Additionally, with the guiding information the manufacturing process can be modified to obtain the acceptable surface features. Figure 2.2 is a schematic representation of the procedure of surface assessment.

- Select an instrument for measurement to acquire information of the surface topography.
- Decompose the information into primary features (scale-limited surface) by filtration.
- Characterise the surface by parameterisation.
- Assess the function of the component based on the measurement and predict possible functional capabilities.
- Use the gained information to modify the manufacturing process.

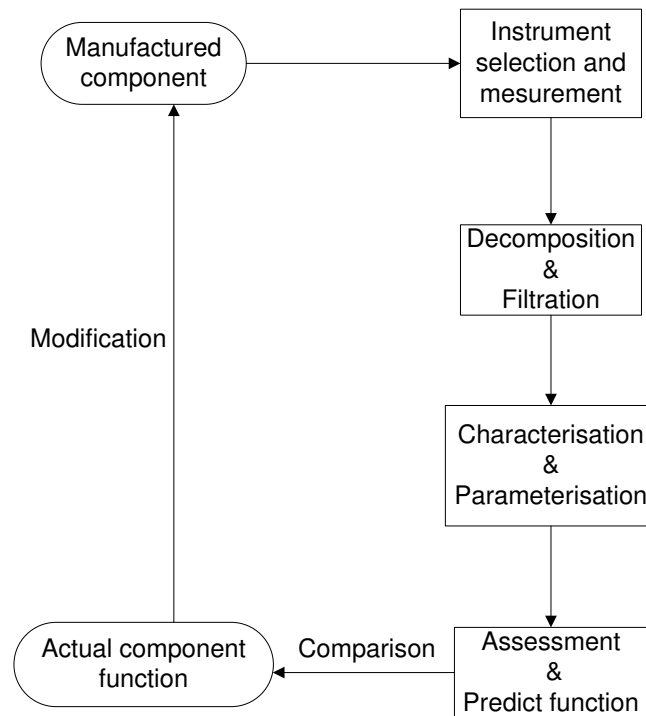


**Figure 2.2 Procedure of surface assessment**

## 2.4 Measurement process types

Surface characterisation can be performed at different conditions according to the requirements of applications. Vacharanukul and Mekid (2005) provided a classification for the act of measurement during the manufacturing process in three groups, namely in-process, in-situ and post-process.

### **In-process**

In-process measurement refers to the act of measuring performed while the workpiece is being manufactured. It can be developed with the control system to provide real-time feedback information for compensation of manufacturing errors and is therefore the most challenging measurement process in that harsh factory environment, such as machining forces, heat loads, added difficulties of vibration and presence of lubricants or debris, needs to be dealt with.

### **In-situ**

In-situ measurement is that which can be conducted without removing the machined workpiece from the machine tool. It is also known as on-machine or on-line measurement. The manufacturing is actually halted during the measurement process. Compared to in-process measurement, it not only significantly relaxes the challenges for implementation due to a mild

assessment surroundings, but also still takes the advantages of not having to remove/refit the workpiece in terms of further modification.

### **Post-process**

Post-process measurement is an off-line metrology mode in high precision manufacturing. Measurement is performed after the manufacturing is completed and the workpiece is removed from the machine. Its advantages are reflected in the ultra-precision applications where the workpiece is required to be measured at a specific temperature, humidity, pressure as well as anti-vibration environment. The drawbacks of post-process measurement are its time-consuming nature and the unavoidable need to realign the workpiece on the machine tool for further alteration.

## **2.5 Instrumentation for surface metrology**

Before the turn of the nineteenth century, assessment of the surface quality primarily relied on skilled and experienced workers using their senses of sight and touch. With the development of high-precision sensors and increasing ability to process large volumes of data using modern computers, instruments for surface metrology have been making great progress. As mentioned in previous section, modern metrology devices can be classified into contact and non-contact types depending on the nature of probes.

### **2.5.1 Contact profilometers**

Stylus profilometry (Figure 2.3) and Scanning Probe Microscopes (SPMs, Figure 2.4) are generally grouped as contact profilometers due to the use of a tactile probe. The stylus-based instrument is the earliest form of profilometer developed for measuring surface topography. It traces a contacting stylus through a transducer (acting as a gauge) and measures the vertical variation of the stylus as it traverses across the surface of interest (Gauler, 1982). Stylus instruments have the benefit of a large measurement range up to several millimetres in height as well as a vertical resolution in nanoscale. The lateral resolution is determined by the radius of curvature of stylus tip and the slopes of the surface irregularities (Bennett & Dancy, 1981). Many commercially available products have been developed such as Talysurf PGI and Talyrond series (applied to surface form and roundness measurement, respectively) from Taylor Hobson Limited. SPMs came about with the invention of the Scanning Tunneling Microscope (STM) in 1982 (Binnig & Rohrer, 1983), which has the Atomic Force Microscope (AFM) (Binnig et al.,

1986) as a further extension for measuring the electrically non-conductive materials. In principle, the SPM has much in common with stylus instrument in that it has a similar lever with a fine tip to scan the measured surface. The main difference is that the parameters directly measured by STM/AFM is the charge density or atomic forces (Alvarez & Siqueiros, 2010), not the height data. A number of authors have described the principle and applications of the STM and AFM in detail in scientific literature (Braga & Ricci, 2004; G untherodt & Wiesendanger, 1994; Schneir et al., 1989; Serry & Schmit, 2006).

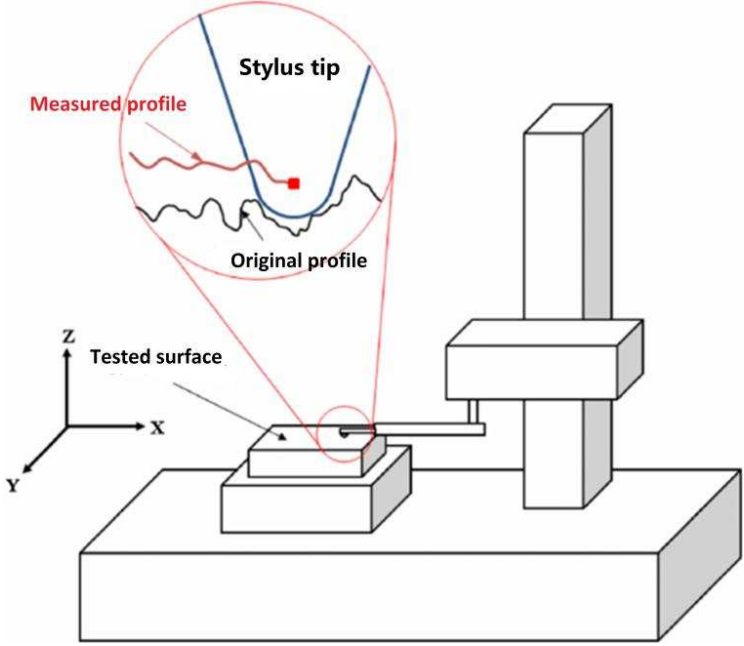


Figure 2.3 Schematic representation of stylus profilometer [Adapted from Lee & Cho, 2012]

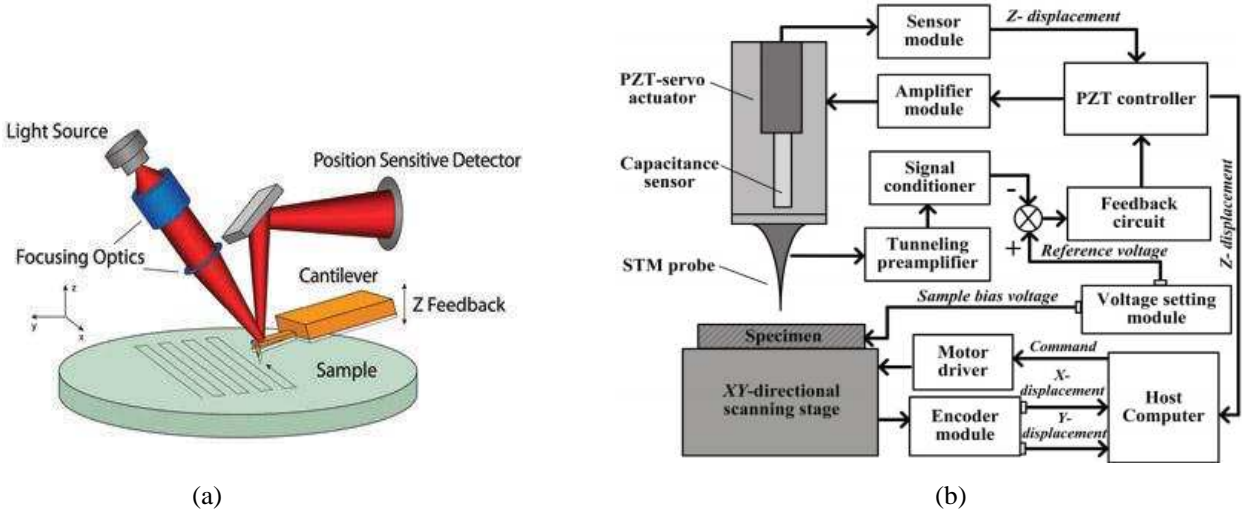
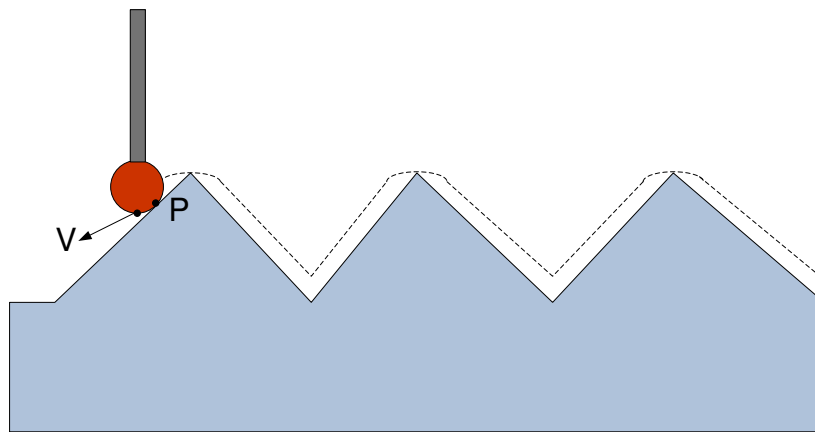


Figure 2.4 SPM: (a) AFM, (b) STM [Adapted from Geisse, 2009 and Chen et al., 2014, respectively].

Although having the advantages of high lateral/vertical resolution and large measurable range, stylus-based instruments have numerous drawbacks. Not only do the stylus tips have the chance to be damaged in harsh measurement environment, but also the tested sample, especially the soft and delicate surface, may get scratched or even functionally damaged when it is traversed across by the stylus. Furthermore, the finite size of stylus tip makes it impossible to penetrate into all valleys of the true surface and introduces a non-linear distortion into the measured envelope as well (Lonardo, et al., 2002). As shown in Figure 2.5, the trajectory of the true contact point P is different from the nominal point V on the vertex of the stylus.



**Figure 2.5 Relationship between the true contact point P and the vertex of the stylus V**

SPMs are also not applicable to the metrology in manufacturing environment. Moreover, the STM further narrows its applications due to the requirement for a conductive tested surface and the image resolution is highly dependent on the tip geometry (Van Loenen et al., 1990).

Meanwhile, measurements of surface topography based on contact profilometer are time-consuming because such instrument performs point by point scanning to acquire 2D mapping of the tested surface. In conclusion, all factors such as slow speed, destructive nature, finite size of stylus and sensitivity to environment restrict the contact profilometry to be applied to on/in-line surface metrology in manufacturing (Bhushan, 2000; Young, et al., 1980).

### **2.5.2 Non-contact profilometers**

To overcome the above-mentioned limitations of contact profilometry, the metrological techniques based on optical phenomena are developed. By replacing the stylus with the light beam probe, optical metrology takes advantage of being non-contact and fast measurement speed with fine vertical and lateral resolution. Many reviews have been written regarding various

optical methods (Hocken et al., 2005; Whitehouse, 1997), offering a detailed list of categories such as polarization interferometry, speckle interferometry, heterodyne interferometry, white light interferometry, moiré and structured light methods, holographic methods, confocal microscopy, optical scattering, focus variation, etc. All these categories can be divided into two types, namely non-interferometric and interferometric techniques. The following sections give an overview of some main optical techniques for surface tomography.

### **2.5.2.1 Optical interferometry**

In recent times, significant development in electronics, software and high performance computing has made optical interferometry a popular technique for metrological applications. Interferometry makes use of the interference principle of two beams originating from the same source but travel on different paths in the interferometric objective and provides nanoscale vertical resolution for precise surface metrology by analysing the captured interferogram.

According to the light source used in the interferometer, interferometric techniques can be divided into two main groups, namely monochromatic interferometry (including single wavelength and multi-wavelength interferometry) and white light interferometry. Monochromatic interferometry, well developed in phase shifting interferometer, can achieve surface measurements with low noise and a high resolution of the level of angstrom. Nevertheless, it is limited to the measurement of relatively smooth surfaces due to the well-known  $2\pi$  phase ambiguity problem.

White light interferometry (WLI), using broadband illumination such as super-luminescent diodes and halogen lamps, has been used for determining the absolute distance between the testing surface and the reference surface without the  $2\pi$  phase ambiguity problem (Bowe & Toal, 1998; Tang et al., 2014; Zhu & Wang, 2012). Additionally, dependent on the different scanning methods used when performing measurement, subdivision of WLI can be made with three categories, namely vertical scanning interferometry (Scott et al., 2005), wavelength scanning interferometry (Gao et al., 2012) and dispersive interferometry (Malacara, 2007) such as LSDI in this thesis.

Though optical interferometry takes advantage of accurate and non-contact measurement, it has a drawback of extreme sensitivity to environmental noise such as mechanical vibration, air turbulence and temperature drift (Adhikari, 2004). To solve this issue, the measurement data need to be taken instantly by using a high speed camera and fast scanning method. Additionally,

compensation of the environmental disturbances is also an effective method to stabilise the metrology device and then provide the nanometre measurement accuracy (Jiang, et al., 2010).

Chapter 3 will go on to describe the basic principles of interferometry and various interferometric techniques developed for efficient surface characterisation, which provides a basis for investigation of the proposed metrology system.

### 2.5.2.2 Machine vision

Machine vision is one of the most common optical metrological techniques for surface inspection in terms of quality assurance in industry. The basic working principle of such imaging-based system is shown in Figure 2.6. It is comprised of four main parts, namely illumination system, imaging optical system, detector and computer system for real-time image view and data analysis. The tested surface is first illuminated by a light source and then the highlighted features within the field of view (FOV) are imaged by a group of optics, normally a microscope system (Harding, 2013). A high speed camera is then employed to receive the image of the region of interest (Logofătu et al., 2004). Finally the recorded grayscale images are binarized and might be smoothed through data processes such as averaging and filtering to characterise the surface features of interest.

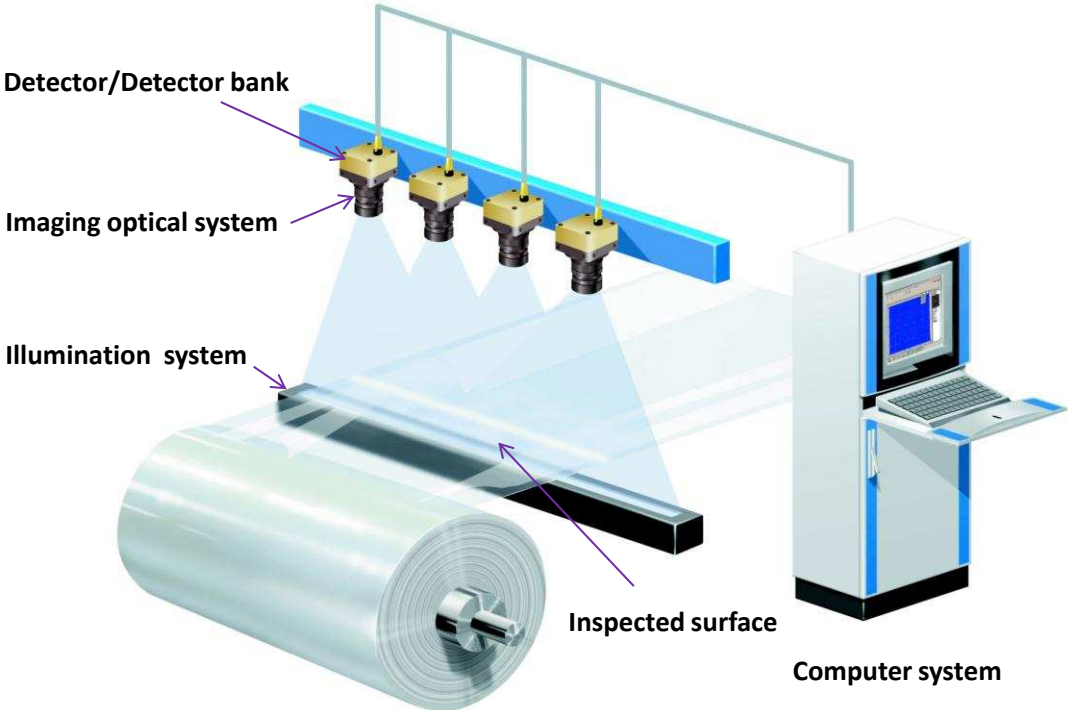


Figure 2.6 Machine vision system [Adapted from ISRA Vision, 2015]

Appropriate illumination is crucial for surface inspection. Depending on the applications, various illumination schemes can be adopted in machine vision system, such as bright field transmission illumination for transparent or nearly transparent material, dark field preferred for glossy surfaces, diffuse illumination for low contrast surface irregularities and directional lighting for emphasising the topographical structures of the surface like scratches (Harding, 2013). The optical system determines the resolution and FOV of ROI inspected for each measurement. A high speed camera is required and should be selected considering factors such as web speed and the minimum feature size on the tested surface. The commercial sprint series of CMOS-cameras from Basler offer line rates up to 140 KHz with 4K pixels and 10  $\mu$ m pixel size. The data processing unit of the machine vision system is based on techniques such as reconfigurable hardware (FPGA) and is used to store and analyse the high throughput data.

Currently the machine vision technique has been widely used in industry for applications such as die attach bond inspection, ball grid array inspection, solar & PV device inspection, metal surface inspection and print inspection. Kurada and Bradley (1997) gave a review of machine vision sensors for tool wear assessment. Luo et al. (1999) presented a colour machine vision system for identification of various types of damaged kernels in wheat. Various morphological and colour features were extracted from the captured images using a developed software and all average identification accuracies for various damaged kernels were up to 90%. Additionally, Blasco et al. (2003) utilised the machine vision technique for on-line estimation of the quality grade of fruit in terms of size, colour, stem location and external blemishes. The results showed that it had a good performance with repeatability in blemish detection and size estimation of 86% and 93% respectively. ISRA Vision (2015) has also developed vision-based system for efficient detecting surface and web defects on various R2R processes.

However, the limitation of this technique reflects in only offering 2D captured images, which is impossible to reconstruct into a 3D surface topography and cannot obtain the depth information of the sample surface. Additionally, it is limited to be applied in the metrological field where the defects or fine structures are smaller than the diffraction limit of the instrument.

### **2.5.2.3 Optical scatterometry**

Optical scatterometry is a non-destructive technique usually applied for characterisation of periodic features (Logofătu, et al., 2004) and surface roughness (Jean Bennett & Mattsson, 1989; Vorburger et al., 1993) by measuring and analysing the variations in the intensity of light

reflected from the tested surface. It is a simple apparatus which is composed of a laser or white light illumination device and a detection part, as shown in Figure 2.7. Depending on the surface types, the scattered light can be both specular (satisfying the law of reflection in geometric optics) and diffuse (the angle of reflection is not equal to the angle of incidence, including diffraction lights). Scatterometry does not measure the absolute value of surface parameter, while it is commonly employed to investigate the process change (Leach, 2014).

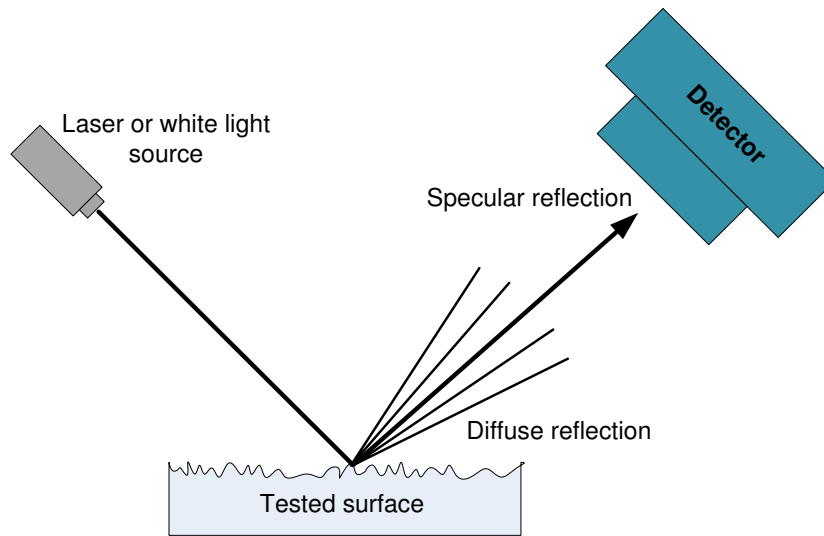


**Figure 2.7 Principle of optical scatterometry**

Having many advantages such as being fast and relatively immune to environmental turbulence, contamination free, no Rayleigh limit and cost-effectiveness enables this technique to be widely used for in-process measurements such as defect detection and tool condition monitoring. Persson (1998) reported a scatterometry instrument with laser illumination used for evaluating the surface roughness in a grinding process. The measurement results of surface roughness (within the ranges of  $0.09 \mu\text{m} \leq \text{Ra} \leq 0.16 \mu\text{m}$  and  $3.0 \mu\text{m} \leq \text{Ra} \leq 3.4 \mu\text{m}$ ) were of the same order as when a stylus instrument was used. EI Gawhary et al. (2011) carried out a theoretical analysis on a spatially coherent optical scatterometry, which was demonstrated to have an increase in the accuracy of the grating's profile reconstruction compared to incoherence case. Moreover, an enhanced coherent Fourier scatterometry with signal-to-noise ratio (SNR) was presented for contamination detection in R2R production of OLED and organic-PV device (Pereira, 2015). Roy et al., (2014) showed that the SNR could be enhanced through partial blocking of the aperture and have discussed how this technique can be applied to detect the isolated particles down to size of diameter 100 nm on a wafer surface.

Though the optical scatterometry overcomes the limitation of low SNR and diffraction limit, it cannot offer real-time images of the inspected surface.

#### 2.5.2.4 Focus variation

Focus variation is a method that tracks the focus variation of the objective to reconstruct the surface topography with full FOV by computing the sharpness at each position within the scanning measurement range (Helml, 2011). The schema of a focus variation instrument is shown in Figure 2.8. The collimated beam is first brought to an objective and is focused onto the ROI of tested surface. All reflected rays then go back to the objective and are gathered by a camera through an imaging lens. The numerical aperture (NA) of objective determines the FOV or measurement ranges in the two orthogonal directions of the camera. The axial measurable range is dependent on the scanning range along the optical axis, which is affected by the working distance of the objective. Compared to other optical techniques, co-axial illumination is not the only choice for focus variation instrument but various illumination schemes can be used (Hirsemenzel et al., 2012). For example, a ring light illumination can greatly enhance the measurable slopes of the system up to  $80^\circ$  (Danzl et al., 2009). Additionally, the polariser and analyser showed in the schema can be used as filters to polarise the light, which is of great help for measurement of metallic surfaces with steep and flat surface elements (Leach, 2014).

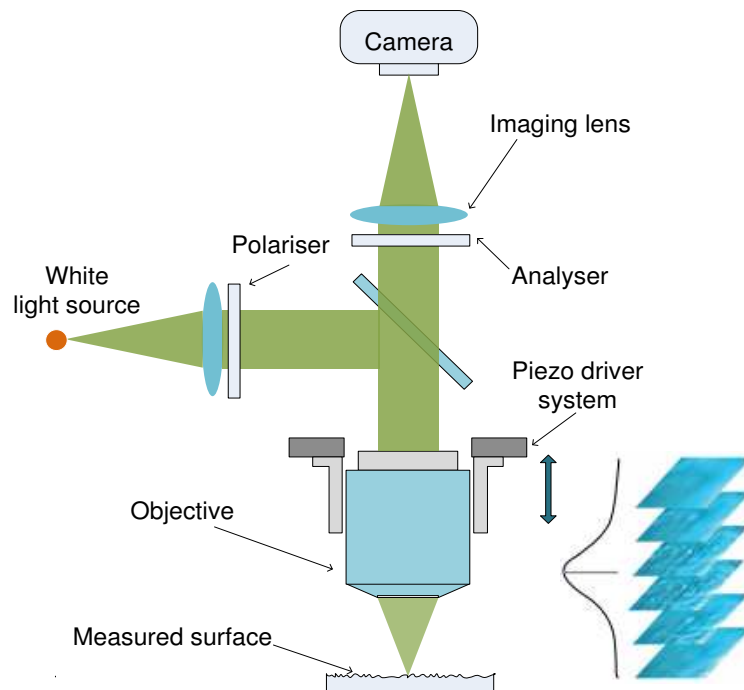


Figure 2.8 Schema of a focus variation instrument [Adapted from Leach, 2014]

This technique can achieve measurement with vertical resolution as low as 10 nm and a high dynamic range, which is applicable to surfaces with complex structures and large discontinuities. Danazi et al. (2011) have demonstrated that the focus variation is a robust technique for 3D surface metrology with high resolution by evaluation of surface roughness, form measurement and engineering tools. The roughness results of focus variation instruments and tactile devices (offering reference) are comparable to each other with differences of a few nanometres, and then measurement repeatability is less than 100 nm when measuring standard hemi-spherical calottes. The assessments of steep surface flanks and welding spots using focus variation method further validated its ability of measuring slope of up to 80°. Focus variation instrument from Alicona was also applied as one of the characterisation methods to investigate the additive manufacturing process such as selective laser melting and electron beam melting (Triantaphyllou, et al., 2015).

However, the focus variation technique is limited by the requirement of the mechanical scanning in height and thus cannot be employed for in-line metrology. Additionally, it is not applicable to transparent samples.

#### **2.5.2.5 Confocal microscopy**

Unlike the conventional microscope, confocal microscopy has two pinhole apertures as spatial filters. Figure 2.9 shows the principle of confocal microscopy. Monochromatic or white light source travels through a pinhole and converges on the sample surface. The reflected rays then return to a detector or a spectrometer. The other pinhole prior to the detector only allows the focused rays to transmit and to be received by the detector. Vertical scanning is required for monochromatic confocal microscopy to retrieve the height information of a point (Conchello et al., 1994) and scanning in two more directions (x,y) is required for reconstruction of the surface topography. While the chromatic type (CCM) achieves parallelisation of the depth scan without any mechanical scanning in that a series of focus points can be acquired along the optical axis by focusing the supercontinuum white light generated from a broadband light-source device (Shi et al., 2004). Each wavelength of the illumination corresponds to a focal plane along the optical axis. A spectrometer is then used to detect the wavelength (value) with respect to the pixel number. The depth measurement range of CCM is dependent on the capability of the optical system to separate the broadband wavelength along the vertical height direction.

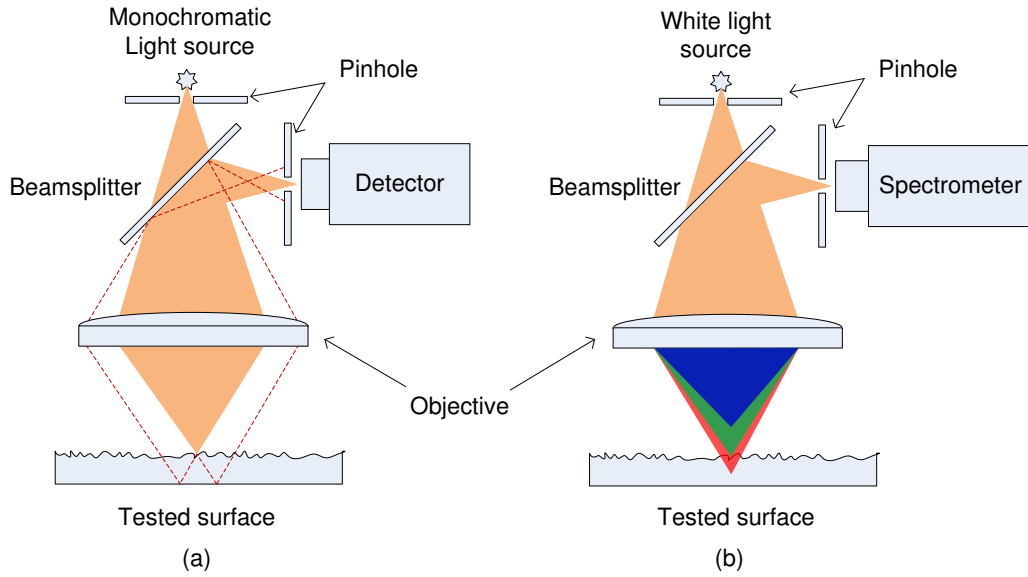


**Figure 2.9 Schema of confocal microscopy: (a) Monochromatic type, (b) Chromatic type (CCM).**

Due to the compact arrangement of system, simple analysis of captured image and fast measurement speed (especially for CCM), confocal microscopy has great potential to be applied in in-process metrology. Tiziani and Uhde (1994) presented a chromatic confocal microscopy which has potential to be applied in measurements of moving objects. The colour impression was used for depth discrimination and three images were required for areal topography which significantly reduced the measurement throughput. Many CCM point sensors are already commercially available from company such as Precitec, Nanofocus and Micro-Epsilon. However, most of these metrology sensors require XY direction scanning to measure the surface topography. Ruprecht et al. (2004) presented a CCM sensor which eliminates one direction of scanning using a line focus, achieving the measurement with a height range of 0.7 mm along a line of 2.4 mm. Moreover, they also investigated the maximum parallelisation of the CCM through measuring an area in one shot using a colour camera.

The confocal microscopy suffers from the same problems as other microscopy instruments such as vertical measurement range depending on the working distance of objective or the optical capability of wavelength separation in depth, lateral ranges determined by the magnification of objective and lateral resolution restricted by the diffraction limit of objective used if not camera-limited (Leach, 2014).

## **2.6 The requirements for in-line sensors**

As mentioned in section 2.4, in-situ or in-process metrology can avoid the errors caused by moving and re-positioning the workpiece during measurement process. Meanwhile, the ongoing evolution in modern manufacturing technologies such as R2R and AM technologies enable surfaces with increasingly large-area as well as complicated structures to be fabricated, which also pushes forward the in-line metrology technique in order to monitor the manufacturing process for ensuring great accuracy and functionality of a component. By using in-line optical sensors, the measurement efficiency and throughput time can be significantly improved. Therefore, the work in this thesis aims at devising of an approach with measurement resolution in nanometre scale, which is suitable for applications on production lines. The drawback of damaging the delicate features on the tested surface precludes stylus based instruments for this task without controversy.

The requirement for an in-line probe is that first it should have reasonable measurement speed to match the production line. Secondly, the probing system must be environmentally robust to vibration and other turbulences to be effective for use in manufacturing surroundings. Additionally, it is supposed to be compact enough for integration into a machine. Optical probes based on techniques such as interferometry, confocal microscope, machine vision and scatterometry are preferred for in-line metrology because the non-contact nature can provide much faster measurement.

In this thesis a single shot dispersive interferometry is investigated, which can measure a surface profile with nanometre resolution and repeatability without any mechanical scanning. Unlike single shot interferometry proposed by 4D Technology (George, 2014), it has a much larger axial measurement range to assess large vertical features or defects by spatially dispersing the interference beam along the camera pixels. Additionally, by utilising a cylindrical lens to observe the tested surface, a large lateral measurement range can be acquired; while using a microscope objective in the probe head, micro-scale lateral resolution is achieved for measuring the finer structure dimensions and features on the specimen.

## **2.7 Summary**

This chapter has given the brief coverage to the historical development of surface metrology as well as the characterisation and measurement process. The current popular metrological techniques and instrumentation for carrying out surface metrology are presented in detail. The

contact methods are by far the most widely used for surface characterisation, which gather data by physical contact with the tested surface. Due to its point by point contact scanning nature, the measurement speed and chance to damage the precision surface contact methods are restricted in their applications to in-process metrology. The results from the stylus profilometry tend to be more used as a reference for evaluating other techniques in future.

Optical methods are the most popular alternatives to contact techniques. By using an optical probe, they assess the tested surface in a non-contact manner without generating any damage. The principles of optical interferometry and non-interferometric techniques such as machine vision, scatterometry, focus variation and confocal microscopy are presented. Though optical instruments have many advantages over contact instruments, it should be noted that their performance will be affected by aberrations generated by imperfection of the optical components or misalignments of the optical system. The finite parameters of the microscope used also set limitations such as lateral resolution, measurable slope and maximum measurement range.

An appropriate measurement technique for the surface metrology should be determined according to the function of the surface and the applications. Figure 2.10 shows the measurement ranges of different instruments as a reference. It can be seen that stylus profilometry has the largest vertical measurement range while the optical profilometry and AFM perform better in both vertical and lateral resolution. With respect to a method of in-line measurement, a single shot interferometry technique will be investigated in this thesis and its principle and implementation will be discussed in the next chapters.

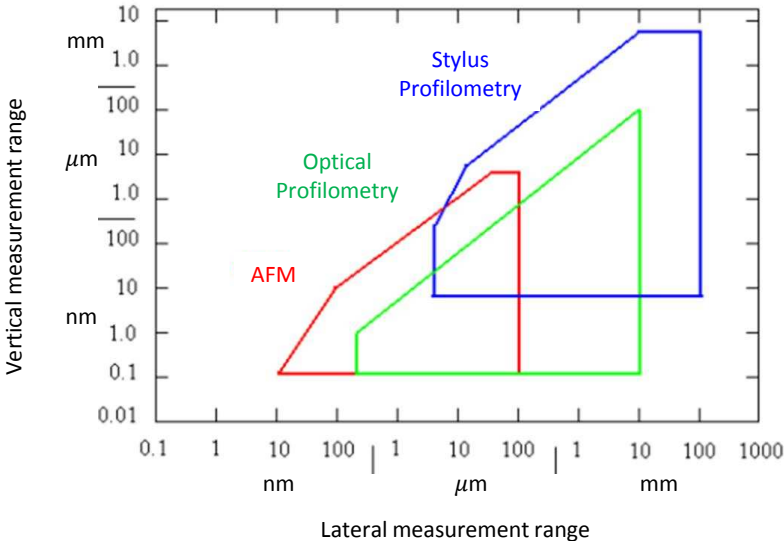


Figure 2.10 Measurement ranges for different instruments [Adapted from Jiang et al., 2007]

## 3 Interferometry

### 3.1 Introduction

As discussed in Chapter 2, optical interferometry benefits from fast and non-contact measurement and has great potential to be applied to in-line metrology. By utilising an optical probe the pressure on the tested surface is released and the measurement with nanoscale vertical resolution can be achieved by interpreting the interferogram. In this chapter, basic concepts of interference are presented and some main interferometry techniques for surface characterisation are discussed in detail. Dispersive interferometry is of particular interest due to its advantages over the alternative techniques.

### 3.2 Interference principle

Interference fringes were discovered in 1802 by Thomas Young through the famous double-slit experiment. Subsequently, the first interferometry instrument was implemented by Albert A. Michelson in 1882. Some basic concepts concerning interference are presented in this section.

The phenomenon of optical interference refers to the superposition of two or more electromagnetic waves originating from the same source, which generates the modulation in the distribution of light irradiance in the spatial domain. The bands of varying intensity are known as fringes, which can be classified into many categories such as Newton, Brewster and Fizeau. Accordingly, the fringe pattern may be presented as various shapes such as circles, parallel lines or anything in between, depending on the instrument or method by which they are created. Moreover, for the interferometers using the white light illumination, colourful fringes will be generated within the measurement FOV. Equation (3.1) mathematically describes the interference produced by the coherent superposition of two waves, which forms the basis for the field of interferometry and derives many and widely varying applications.

$$I(x, y) = I_1(x, y) + I_2(x, y) + 2\sqrt{I_1(x, y)I_2(x, y)} \cos \Delta\varphi \quad (3.1)$$

where  $I(x, y)$  is the intensity of the interference fringes and  $(x, y)$  denotes the spatial coordinates of the interferogram.  $I_1(x, y)$  and  $I_2(x, y)$  are the intensities of the two beams with the same frequency and  $\Delta\varphi$  is the phase difference between them. Therefore, it can be deduced from equation (3.1) that the intensity within a fringe pattern varies between two limits  $I_{\max}$  and

$I_{\min}$ . In the case of complete coherence, the maximum and minimum intensities are simply expressed as

$$\begin{pmatrix} I_{\max} \\ I_{\min} \end{pmatrix} = \begin{pmatrix} I_1(x, y) + I_2(x, y) + 2\sqrt{I_1(x, y)I_2(x, y)} \\ I_1(x, y) + I_2(x, y) - 2\sqrt{I_1(x, y)I_2(x, y)} \end{pmatrix} \quad (3.2)$$

The interference visibility ( $v$ ), an important concept for interferometry, is defined as the contrast of the fringe pattern. It can be theoretically calculated by

$$v = \frac{I_{\max} - I_{\min}}{I_{\max} + I_{\min}} = \frac{2\sqrt{I_1 I_2}}{I_1 + I_2} \quad (3.3)$$

The maximum fringe visibility will occur when the two interfering beams are of equal intensity ( $I_1 = I_2$ ). However, it is a difficult task for the interferometer to achieve the maximum visibility because the specimen and the reference mirror have different reflectivities. In general, the value of  $v$  is between 0 and 1. In order to obtain good fringe visibility, the irradiance of the two reflected beams should be balanced in practice. For a sample surface with low reflectivity, the visibility is more likely to be low. In this case, properly using the neutral density (ND) filters in the optical arrangement offers the most simple and effective solution to match the intensities of the two interference beams.

Additionally, there are two types of coherence, namely spatial coherence and temporal coherence. Spatial coherence refers to a measure of the phase correlation between two points on the same wavefront (Shulman, 1970). It is associated with the size of the source. The overlapping of numbers of patterns of interference fringes produced by a broadband source will lead to a uniform illumination without fringes. Temporal coherence is a measure of phase correlation between two points at the same point but at different times (Hariharan, 2010). It is related to the spectral bandwidth. All interferometry techniques discussed in this thesis belong to the category of temporal coherence.

The coherence length ( $l_c$ ), another vital property in interferometry, can be used for qualifying the degree of temporal coherence. It is related inversely to the spectral bandwidth of the light and is defined as

$$l_c = \frac{\lambda^2}{\Delta\lambda} \quad (3.4)$$

where  $\lambda$  represents the central wavelength and  $\Delta\lambda$  is the bandwidth of the light.

Equation (3.4) shows that a narrower spectral bandwidth corresponds to a longer coherence length. For this reason the Fizeau interferometer employs the single-wavelength light illumination to produce fringes between the two unequal-path arms for measurement. Additionally, the spectral profile of the illumination system has influence on the coherence length and therefore a correction formula is expressed as

$$l_c^* = \eta\lambda^2 / \Delta\lambda \quad (3.5)$$

where  $l_c^*$  is the corrected coherence length and  $\eta$  is correction factor depending on the spectral profile. For the spectrum with Gaussian distribution,  $\eta=2 \ln 2/\pi = 0.44$  (Ohta et al., 2008).

On the whole, interferometry is a technique which produces the interference fringes (or interferograms) and subsequently performs fringe analysis to determine a variation in a measurand using all the information such as fringe spacing, shape, deviation, rate of translation and colour depending on the specific application (Martin, 2010). The following sections will discuss some main interferometry techniques more specifically.

### 3.3 Phase shifting interferometry

#### 3.3.1 Single wavelength interferometry

Phase shifting interferometry (PSI) using monochromatic light source has been the most popular and preferred techniques for high precision surface metrology in controlled environments since the 1960s (Deck, 2001). It was proved that PSI has a high measurement resolution up to  $\lambda/1000$  ( $\lambda$  being the wavelength of light) peak-valley in optimum conditions (Cheng & Wyant, 1984; Kafri, 1989). The earliest reference to this technique can be traced back to Carré (1966). With the advancement in powerful computers, solid-state detector arrays and high precision piezoelectric transducers (PZT), the single wavelength technique has occupied an important position in modern optical metrology. It has many advantages such as high phase measurement accuracy, fast measurement speed, results independent of intensity variations across the pupil, phase obtained at fixed grid of points and good results with low contrast fringes (Cheng & Wyant, 1984).

The basic idea of PSI is to measure height variations by means of precisely determining phase angles in an interferogram (De Groot, 1995). In general, PSI electronically stores a sequence of interferograms with a precisely controlled phase change between them (Sykora & de Groot, 2011). There are many methods that can be used for phase shifting such as moving the reference mirror with a PZT, moving a diffraction grating, using a Bragg Cell, tilting a glass plate, rotating a half-wave plate and using an acousto-optic or electro-optic modulator. For each recorded interferogram, the modulated intensity represented in equation (3.1) can be rewritten as

$$I = I_0 (1 + v \cos \phi(x, y)) \quad (3.6)$$

where  $I_0$  is the background intensity of the two beams,  $v$  refers to the fringe visibility and  $\phi(x, y)$  is the phase. In the case of a  $n$ -step phase shifting, the following mathematical equation can be deduced

$$\begin{bmatrix} I_1 \\ I_2 \\ I_3 \\ \cdot \\ \cdot \\ I_n \end{bmatrix} = \begin{bmatrix} I_0 (1 + v \cos (\phi(x, y) + \delta_1)) \\ I_0 (1 + v \cos (\phi(x, y) + \delta_2)) \\ I_0 (1 + v \cos (\phi(x, y) + \delta_3)) \\ \cdot \\ \cdot \\ I_0 (1 + v \cos (\phi(x, y) + \delta_n)) \end{bmatrix} \quad (3.7)$$

After phase shifting, the original wavefront phase is recovered by analysis of the variations of irradiance as a function of reference phase shift (Schreiber & Bruning, 2006). The number of frames required depends on the phase extraction algorithm employed, the performance of the computer and the range of PZT actuators (if used). To determine the three unknowns in equation (3.6) at least three temporally phase shifted intensity patterns are required. Various popular phase extraction algorithms such as three-step algorithm, four-step algorithm, five-step algorithm and Carré algorithm, have been studied since the PSI technique came out (Carré, 1966; Hariharan et al., 1987; Schwider et al., 1983; Wyant et al., 1984).

Sensitivity to external vibrations is probably the most serious impediment to wider use of PSI, which was proved through analysis by de Groot (1995). Environmental vibrations lead to incorrect phase shifts between data frames. The ways to avoid or mitigate the errors due to vibrations include retrieving frames effectively and fast (Deck, 1996), controlling the

environment, using common-path interferometers, measuring vibration and introducing vibration 180 degrees out of phase to cancel vibration, and so on.

In terms of the phase ambiguity problem due to the noise or  $2\pi$  wrapping limitation of trigonometric functions, various phase unwrapping algorithms have been developed for PSI to solve this issue and achieve phase continuity (Charette & Hunter, 1996; Huntley, 1989). Yet the single wavelength PSI is still confined by the phase ambiguity problem when the optical path difference (OPD) jump between any adjacent pixels is greater than  $\lambda/2$ , where  $\lambda$  is the wavelength of the light used, and restricted to application for characterisation of the smooth surface with discontinuities not higher than  $\lambda/4$ . Use of multiple-wavelength interferometry (as discussed in next section) can mitigate this problem. Additionally, the utilisation of monochromatic wavelength restricts its applicability to ranges where only continuous fringes can be acquired (Ali, 2012).

### 3.3.2 Two and multiple wavelength interferometry

As discussed above, conventional single wavelength interferometry can offer excellent vertical resolution. However, it has difficulty in achieving accurate measurement for surfaces with high discontinuities. To overcome this issue, the two- or multiple- wavelength interferometry technique has been developed, which provides a way to extend the vertical measurement range by creating fringes at a longer synthesized wavelength. This method has the benefit of keeping the resolution constant, as it is in the single wavelength technique, while increasing the dynamic range of the measurement. The term two-wavelength interferometry was first mentioned by Polhemus (1973). A widely used definition of the effective wavelength (or synthetic wavelength)  $\lambda_{\text{eff}}$  for two-wavelength technique is expressed as

$$\lambda_{\text{eff}} = \lambda_1 \lambda_2 / |\lambda_1 - \lambda_2| \quad (3.8)$$

where  $\lambda_1$  and  $\lambda_2$  are the two wavelengths used.

Multiple-wavelength technique is an extension of two-wavelength, and have been developed to solve the problems of single wavelength interferometry as well (Decker et al., 2003). Multiple wavelengths include three, four or sometimes many wavelengths to produce a series of effective wavelengths enabling ultra-precision metrology over a wider range of surface. Much research into two- or multiple-wavelength interferometry for surface measurement has been carried out.

Cheng and Wyant (1984) proposed a two-wavelength phase shifting interferometry which achieved measurement repeatability better than 25 Å (angstrom) RMS for measuring a steep optical surface. It could possibly be applied to measurement of the steep aspheric or large deformation surfaces. Deck and Demarest (1993) developed a stable two-colour light-emitting-diode source with a synthetic wavelength of 10.77 μm for their multi-wavelength interferometry, and achieved an unambiguous vertical measurable range greater than 2.5 μm with sub-angstrom measurement repeatability. Kumar et al. (2008) exploited a three-wavelength interferometry and used an 8-step algorithm to compensate phase shifting errors due to phase-step miscalibration.

Study showed that the measurement dynamic range may not be limited by the effective wavelength calculated using equation (3.8). Instead, this wavelength can be increased several times through analytical methods if the fractional phases at the single and effective wavelengths are known. However, this technique suffers from longer calculation time and measurement noise (De Groot, 1995; Malacara, 2007). Since the two- or multiple-wavelength interferometry just extends the measurement range, this technique still suffers from  $2\pi$  phase ambiguity when the OPD between two adjacent pixels exceeds half of the synthetic wavelength  $\lambda_{\text{eff}}$ . It is also important to mention here that the depth of field (DOF) of the interferometric objective for PSI may set a limit to the vertical measurable range as well. With respect to the measurement time, two- or multiple-wavelength interferometry takes twice as much as single wavelength PSI when performing a measurement. There are two ways to reduce the required time for measurement. One is to capture the two- or multiple-wavelength superimposed interferograms in one frame and analyse it using the Fourier transform method (Onodera & Ishii, 1997). Another method is to utilise a colour CCD camera to record the interferogram (Pfortner & Schwider, 2001).

### **3.4 Vertical scanning interferometry**

Broadband light source is widely used to further extend the measurement dynamic range. Vertical scanning interferometry (VSI), also known as white light scanning interferometry (WLSI) or coherence correlation interferometry (CCI), is not a new technique but has become extremely powerful with development of modern science. It differs from single wavelength PSI technique by using low-coherence white light, which consequently creates a new pattern of fringes due to the superposition of fringes for each individual wavelength (Malacara, 2007). Figure 3.1 shows the schematic diagram of VSI. Like other interferometers, the white light beam is split into two parts to travel along the two arms of the interferometer and are then brought

together to generate interference fringes within the range of coherence length. The camera captures a series of sequential frames during the vertical scanning of interferometric probe.

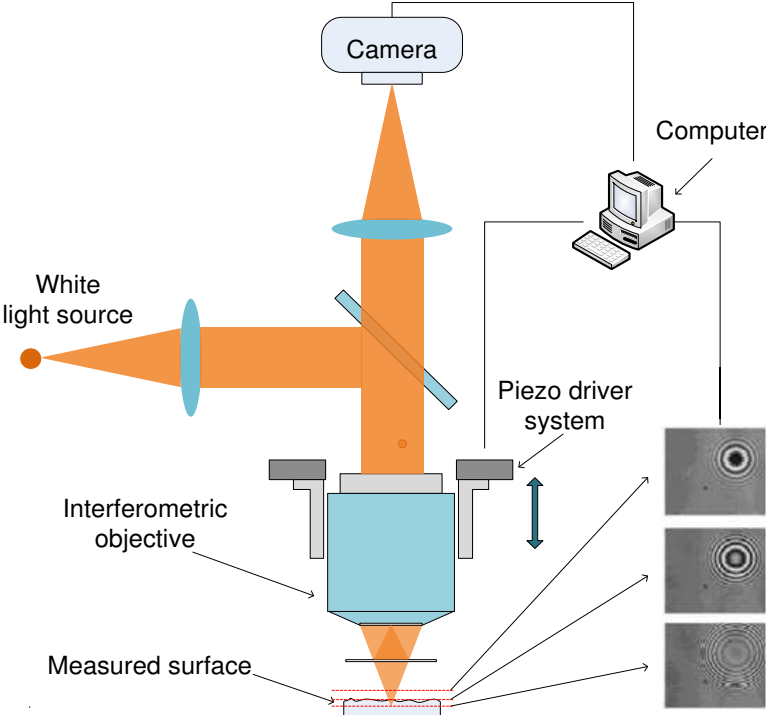


**Figure 3.1 Schematic of vertical scanning interferometry**

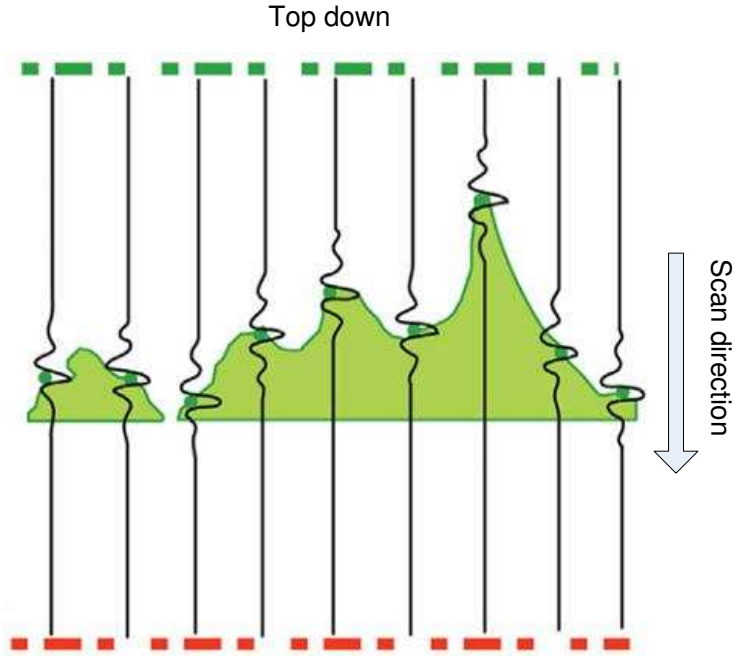


**Figure 3.2 Localisation of coherence peak using VSI technique**

The basic principle of VSI for retrieving the absolute distance of tested surface with respect to reference plane is to determine the locations of coherence peaks from the captured interferograms. As shown in Figure 3.2, the maximum fringe visibility occurs when the OPD between the reference arm and the measurement arm equals zero, whereas it falls quickly when the OPD increases. Surface topography can be acquired after tracking all coherence peaks within the field of view of the interferometric objective.

VSI overcomes the limitation existing in PSI techniques and extends its metrological application to rough surfaces and structured surfaces with large discontinuities. Its axial measurable range is dependent on the working distance of the objective and the scanning range of the translation system. Since it was first proposed by Balasubramanian (1982), many studies have discussed various applications of this technique. Davidson employed the VSI technique to measure the profile of integrated circuits (Davidson et al., 1987) and Adi et al. (2008) used it to assess the surface roughness of micro-sized particles for dry powder inhalation. Santo Padula II (2009) demonstrated that the VSI technique is a robust, repeatable and precise approach to assess the defects present on the orbiter window. Many commercial products using VSI technique have been developed, such as Talysurf CCI 6000 from the Taylor Hobson Ltd. with a vertical resolution of 0.1 angstrom and NewView 7300 from the ZYGO Corporation with a vertical resolution smaller than 0.1 nm (Taylor-Hobson, 2005; ZYGO-Corporation, 2014). The vertical scanning range of these VSI instruments varies between a few micrometres to a few centimetres.

The drawback of VSI technique is that a large amount of interferograms must be recorded and processed before the height distribution of the surface can be calculated. On one hand, the mechanical scanning required in height means that the VSI technique is limited to in-situ/off-line measurement, not applicable to the in-line metrological applications. On the other hand, the scanning range sets a limitation in measurement range and speed. Furthermore, the non-linearity errors due to the PZT hysteresis have an influence on the measurement accuracy as well (Kang et al., 1999), which makes an extra calibration and compensation process necessary for the instrument before use. Some other issues such as spiky errors and bat wings occurring at the edge of surface features, may need to be considered as well when using VSI (Gao et al., 2008; Harasaki & Wyant, 2000). Additionally, the adoption of the white light source and the finite size of the beamsplitter lead to dispersion problem and incorrect profiles, especially for Linnik and Michelson interferometric objectives (Pförtner & Schwider, 2001).

### 3.5 Wavelength scanning interferometry

Wavelength scanning interferometry (WSI), proposed for the first time by Takeda and Yamamoto (1994), is an alternative to VSI and multi-wavelength interferometry. It takes advantage of shifting the phase by tuning wavelengths of the broadband light source without any mechanical scanning and obtaining good contrast of fringes even for dispersive media when compared to VSI (Malacara, 2007). Not only can WSI easily characterise the rough and smooth surfaces without  $2\pi$  phase ambiguity, but it can also be extended to metrological applications such as film thickness measurement through separation of interference signals from the top and the bottom of film surface in frequency-domain (Gao, et al., 2012; Ghim & Kim, 2009).

A wavelength tunable light source, an interferometric objective and a high speed camera in conjunction with the sophisticated computer are three critical parts of the WSI system. The NA of the objective used determines the lateral resolution of WSI and measurement FOV, and the camera speed along with the computing capability of data processing unit determines measurement time. Additionally, the wavelength tuning range and minimum tuning step have effect on the measurement accuracy and the maximum measurable range of the system, respectively. The vertical resolution or the minimum measurable height difference ( $\delta_h$ ) of WSI is expressed as (Malacara, 2007)

$$\delta_h = \frac{\pi}{\Delta k} = \frac{\lambda_{\min} \lambda_{\max}}{2(\lambda_{\max} - \lambda_{\min})} \quad (3.9)$$

where  $\lambda_{\max}$  and  $\lambda_{\min}$  denote the maximum wavelength and minimum wavelength corresponding to the scanning range. The maximum measurable range ( $h_{\max}$ ) is given by (Malacara, 2007)

$$h_{\max} = \pi / \delta_k \quad (3.10)$$

where  $\delta_k$  is the minimum tuning step. According to equation (3.9), wider scanning range offers a high measurement resolution. However, it needs to be noted that chromatic aberrations produced by the optical system may increase as well due to the broader bandwidth used. The axial measurement capability is first restricted by the minimum tuning step, which is consequently dependent on the performance of wavelength-tuning device such as AOTF. Additionally, DOF of the probing objective also sets a limitation to the maximum measurable range, as expressed by

$$\text{DOF} = \lambda \sqrt{1 - \text{NA}^2} / \text{NA}^2 \quad (3.11)$$

where NA represents the numerical aperture of the objective and  $\lambda$  is the wavelength used. When the measurement is performed, the sample should be placed within the DOF of the objective to resolve the details of the tested surface. Fringes still can be observed as the OPD between the tested surface and reference surface exceeds the DOF, the visibility of the fringes and the signal-to-noise of the interference output, however, is greatly decreased and eventually no interference exists when the OPD is greater than the coherence length. Overall, the maximum measurement range is related to  $h_{\text{max}}$  and DOF calculated by equation (3.10) and (3.11), respectively; and is determined by the smaller of the two values.

As a matter of fact, the evolution of the WSI was directly related to the development of the tunable light source. In the early stage of WSI development, the narrow scanning range and the mode hopping problem existing in laser diodes limited the measurement accuracy to sub-millimetre (Thiel et al., 1995). Yamamoto et al. (2001) proposed a high resolution WSI using titanium: sapphire laser with a scanning range up to 100 nm to enhance the measurement accuracy. Jiang et al. (2010) also presented a WSI system using an AOTF to scan the wavelength emitted from a halogen lamp, which achieved a wide scanning range up to 150 nm and a tuning step of 0.48 nm.

As mentioned above, WSI produces phase shifting though altering the wavelength of a broadband light source, therefore the equation (3.6) can also be expressed as

$$I = I_0 [1 + v \cos (2h (k + \delta k))] \quad (3.12)$$

where  $h$  is the OPD between the two arms of the interferometer,  $k$  is wave number and  $\delta k$  is its variation due to wavelength scanning. To obtain a height map of the sample surface with full FOV, a series of frames are captured by a two-dimensional camera during wavelength scanning. Figure 3.3 shows the signals of a step object using the WSI technique. To analyse the fringes and retrieve the phase information, various algorithms have been developed such as techniques based on the zero crossing technique (Kuwamura & Yamaguchi, 1997), fast Fourier transform (FFT) (Takeda & Yamamoto, 1994), convolution (Muhamedsalih et al., 2012) and Carré algorithm (Carré, 1966).



The WSI technique has the same shortcoming as the VSI, which is that a large number of frames need to be captured for each areal measurement which may take a few seconds to record and process. Due to the sensitive nature of the method to the environmental noises such as mechanical vibration and air turbulence, implementation of a stabilisation system in WSI system is considered as an effective solution to minimise the environmental effects and achieve the high measurement accuracy. Jiang et al. (2010) proposed an enhanced WSI which introduced an active servo control system to monitor and compensate the environment noise, as shown in Figure 3.4. The additional interferometer, called as reference interferometer, uses a Super Luminescent Light Emitting Diode (SLED) light source with working wavelength of 830 nm. This reference interferometer is utilised as a feedback source for a close loop control system to stabilise the entire interferometry. Its output is detected by Silicon PIN detector and is fed into a PI controller which controls a piezo transducer's movement to compensate for the vertical mechanical vibration (Muhamedsalih et al., 2013). Furthermore, by combining the technologies such as GPU and auto-focus kinematic stage, this improved WSI has been demonstrated for potentially used in on-line defect assessment on a R2R process (Muhamedsalih, et al., 2015). However, for the moment the WSI system still cannot perform in-process metrology because it requires the tested sample to keep still during the measurement process.

### **3.6 Dispersive interferometry**

Dispersive interferometry, normally named spectrally resolved white light interferometry (SRWLI) or white light channelled spectrum interferometry (WLCSI) in other literatures (Malacara, 2007), is another interferometry technique that achieves phase shifting through wavelength variations without mechanical scanning. It has an advantage of fast measurement speed over the VSI and the WSI because of obtaining a surface profile in a single shot. All information of the measured profile with respect to the spectral bandwidth is registered in a single two-dimensional frame (spectral interferogram) by using a spectrometer. More specifically, unlike VSI and WSI techniques, the interference beam produced by the interferometric objective is spatially dispersed using a diffraction grating or prism before being focused onto the camera, in which way the channelled spectrum is obtained and the phase information is encoded as a function of wavenumber along the chromaticity axis of the camera. Normally the diffraction grating is preferred to be used because the prism struggles to achieve a

big diffraction angle and makes the whole system bulky as well. The details of spectrometer system will be further discussed in next chapter.

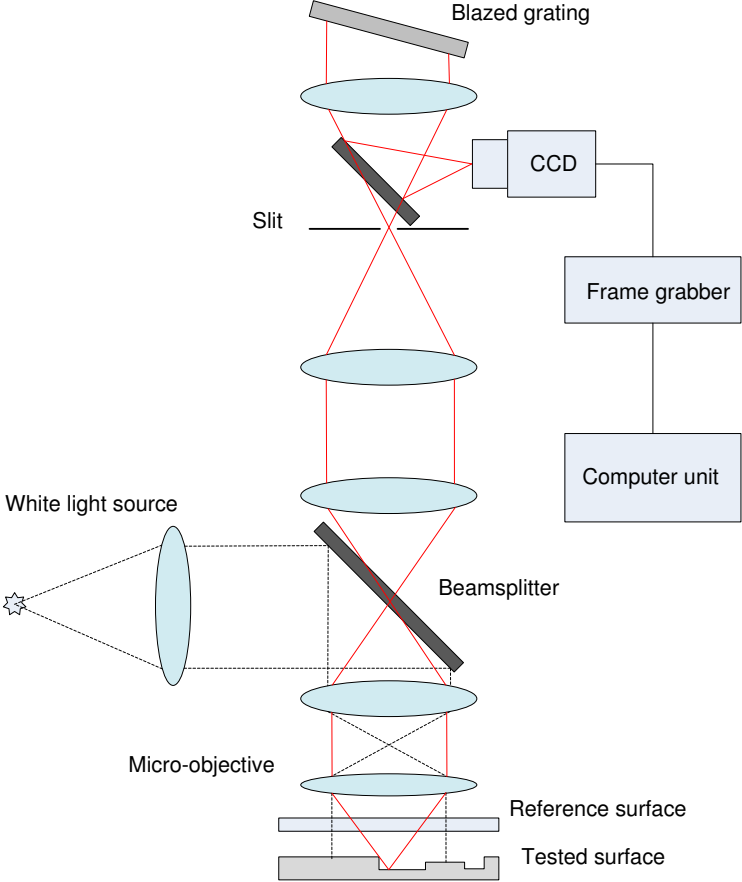


**Figure 3.5 Optical setup of dispersive interferometry [Adapted from Schwider and Zhou, 1994]**

Dispersive interferometry for use in surface metrology was first described by Schwider and Zhou (1994), which was based on a Fizeau system as shown in Figure 3.5. Since then, the technique has been reported by many researchers in the fields of surface profile measurement (Calatroni et al., 1996), absolute distance measurement (Hlubina, 2002; Joo & Kim, 2006) and thin-film thickness measurement (Debnath et al., 2006; Ghim & Kim, 2009) over the last two decades. Schnell and Dändliker (1996) extended the application of dispersive interferometry for absolute distance measurement to efficiently measure in-situ the effects of the dielectric thin-film coated on a sample. The experiment results showed the thickness of these layers can be accurately measured at a level of 10 nm provided that the refractive indices are known, and finally the correct mechanical distance to the top surface of the target can be obtained. In the case of film thickness measurement, it can be achieved using dispersive interferometry by

separating the signals from different layers in frequency domain (Zuluaga & Richards-Kortum, 1999). However, this metrology application may suffer from the ghost frequency peaks from multiple reflections of many interfaces (Malacara, 2007). Therefore, Wojtkowski et al. (2002) suggested that dispersive interferometry in conjunction with PSI could be an effective approach to measure the film thickness without ambiguity. Debnath et al. (2006) presented a dispersive phase shifting interferometry with a windowed 8-step algorithm to rapidly and accurately measure the thickness of thin film ranging from 150 nm to a few micrometres.

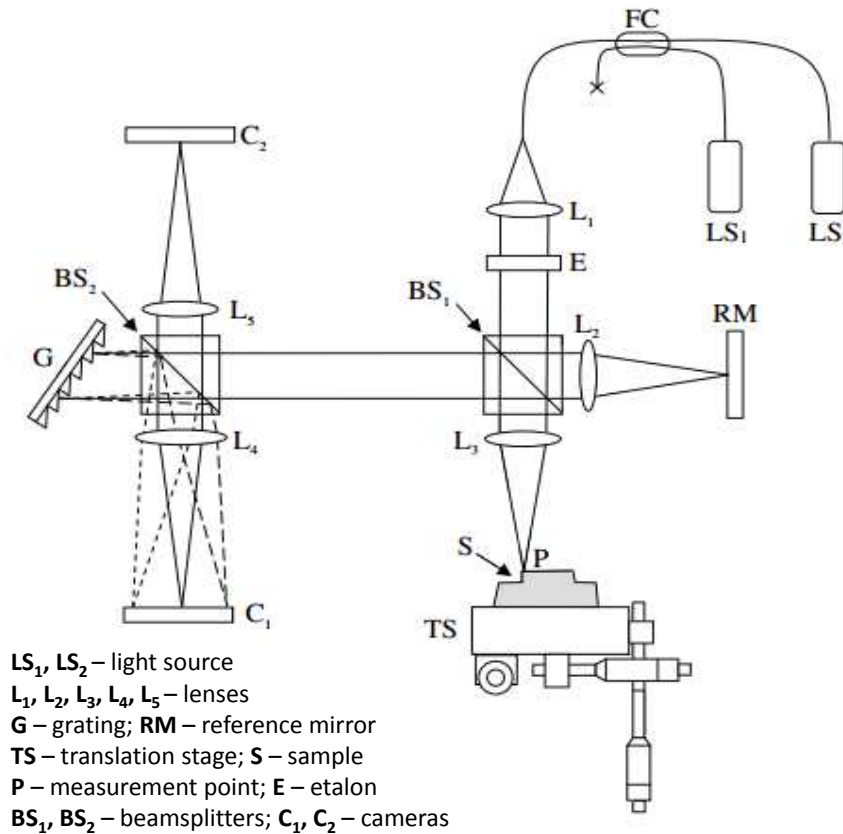


**Figure 3.6 Hyperspectral interferometer for single-shot 3D shape measurement [Adapted from Huntley et al., 2010]**

In order to construct a surface topography of the sample surface, additional lateral scanning is commonly needed for a dispersive interferometer. To overcome the issue of just one line profile measurement, Huntley et al. (2010) presented a hyperspectral interferometry (HSI) to achieve single-shot 3D shape measurement with great immunity from the environmental disturbances, as shown in Figure 3.6. By using a hyperspectral imager the white light interferogram was split into a series of sub-interferograms with a narrow spectral band within the

broad spectral illumination envelope. Therefore, the measurement of two-dimensional optical path distributions can be obtained by analysing the hyperspectral images (Widjanarko et al., 2012). The measurements of a planar sample and a step sample demonstrated the applicability of the HSI system to single-shot areal measurement ( $11 \times 19$  pixels) with an unambiguous depth measurable range of  $350 \mu\text{m}$  and a depth measurement precision of  $80 \text{ nm}$ . However, this proposed system has a problem to be integrated into machines in the production line due to the large overall size. Moreover, further improvement needs to be made to achieve images across the full detector.

Additionally, a spatially dispersed short-coherence interferometry (SDSCI) has been proposed and investigated for on-line surface profile measurement (Hassan et al., 2014), as shown in Figure 3.7. Unlike the SRWLI discussed above, it has a dispersive probe in the measurement arm, which is composed of a grating and a collimator. The tested surface is therefore observed by a spatially dispersed line beam and finally the produced spectral interferogram is analysed by a spectrometer. This novel technique can achieve profile measurement over large ranges; however, it suffers from the same  $2\pi$  phase ambiguity problem as the PSI does and is generally used for characterisation of ultra-precision surfaces.

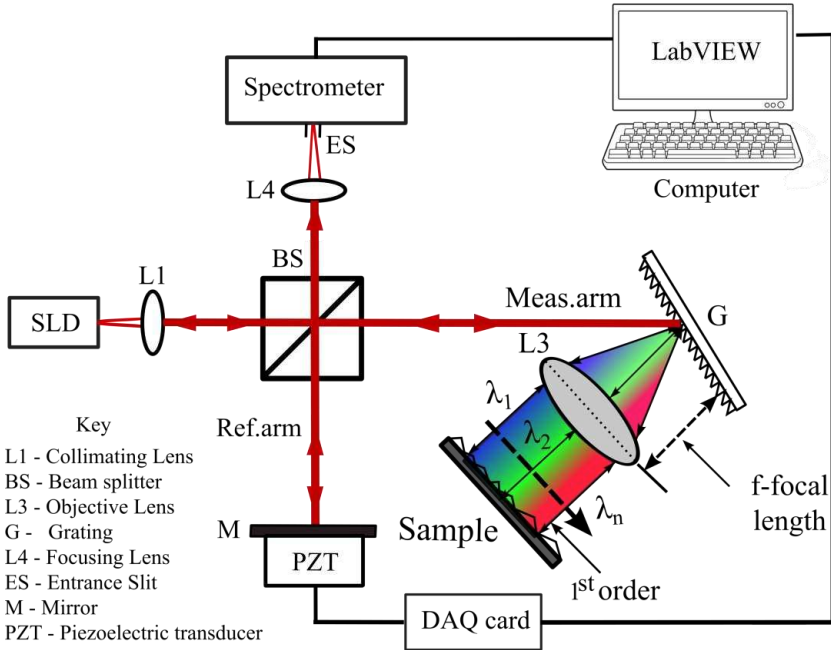


**Figure 3.7 Optical configuration of SDSCI system [Adapted from Hassan et al., 2014]**

As one of the variations of spectrally resolved interferometry, spectral domain optical coherence tomography (SDOCT) is widely employed in the biological field. It offers a fast

measurement technique for ophthalmic diagnosis and other biological tissues in vivo (Brezinski, 2006; Nakamura et al., 2007; Yaqoob et al., 2009). For example, Grajciar et al. (2005) presented a parallel SDOCT with a long slit illumination on the sample which allows in vivo real time imaging of human eye structures. Yasuno et al. (2006) demonstrated a 3D SDOCT for in vivo dermatological investigation. It only required one-dimensional lateral scanning along the direction perpendicular to the measured profile through a Galvano mirror, as shown in Figure 3.8. Iftimia et al. (2006) also developed a compact instrument by integration of SDOCT and line-scanning laser ophthalmoscopy (LSLO). The SDOCT/LSLO hybrid instrument provides both bigger picture on global ocular health and high resolution detail of retinal cellular in the region of interest. The axial resolution of SDOCT, dependent on the bandwidth of the light source used, is generally in micrometre or sub-micrometre scale. Therefore, the SDOCT has limitation in metrology of ultra-precision surfaces in manufacturing process.

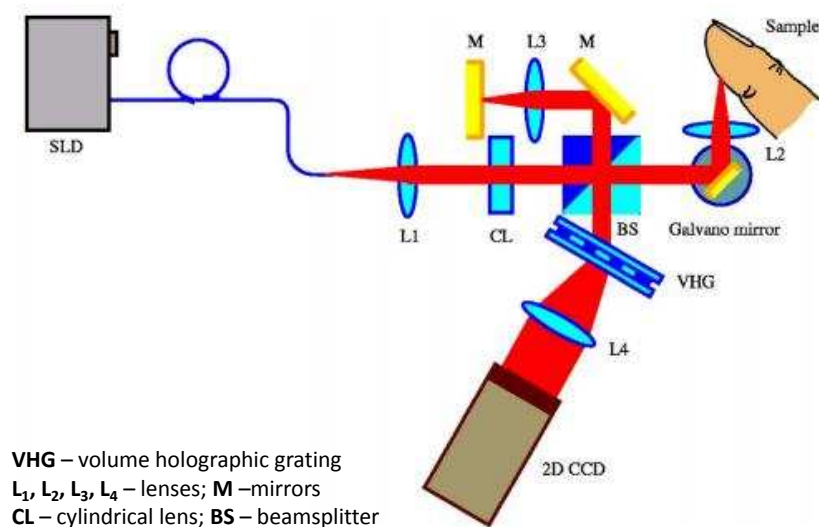


Figure 3.8 Optical setup of SDOCT [Adapted from Yasuno et al., 2006]

### 3.7 Summary

Optical interferometry is based on the analysis of the fringes generated by two beams with the same frequency. It can be classified into different groups depending on the coherence length of the light source used, such as single wavelength PSI and WLI. Generally the PSI in conjunction with a (single wavelength) light source with long coherence length offers outstanding axial resolution. Nevertheless, it is restricted to metrology of smooth surfaces or step

heights less than a quarter of a wavelength. The WLI techniques such as VSI, WSI and dispersive interferometry all belong to low-coherence interferometry. They benefit from the use of a broadband light source which removes the  $2\pi$  phase ambiguity problem and have been widely used in applications such as inspection of the surfaces with large discontinuities and characterisation of internal surface and optical material with the development of the new light source, detectors and processing techniques.

The interference signal of VSI and WSI is temporally localised which requires a large number of interferograms to be captured and thus introduces lots of environmental noises to the measurement. In addition, the tested sample needs to be kept still during each measurement process. Both of the above-mentioned drawbacks make it an issue when they are applied on a production line. Dispersive interferometry stands out because the single shot nature of the approach makes it immune to the environmental disturbances when the measurement is carried out on the shop floor, and therefore it has the potential to perform in-line surface inspection. Based on the overview of various interferometers, the environmental robust single shot dispersive interferometry is of particular interest and is practically investigated in this thesis.

The next chapter details the development of the proposed line-scan dispersive interferometry part by part.

## 4 LSDI system development

### 4.1 Introduction

This chapter presents the development of the snapshot line-scan dispersive interferometer for in-line surface measurement. For those interferometric techniques requiring scanning to fulfil each measurement, whether mechanical scanning or wavelength scanning, they are restricted to in-situ or off-line applications where the sample surface keeps still. LSDI has the benefit of utilising single-shot measurement and has potential to perform in-line metrology of the surface in motion. One of the promising applications for this technique is to inspect flexible PV film products manufactured by R2R technology, as shown in Figure 4.1. This chapter details the system scheme of LSDI, alignment issues and wavelength calibration.

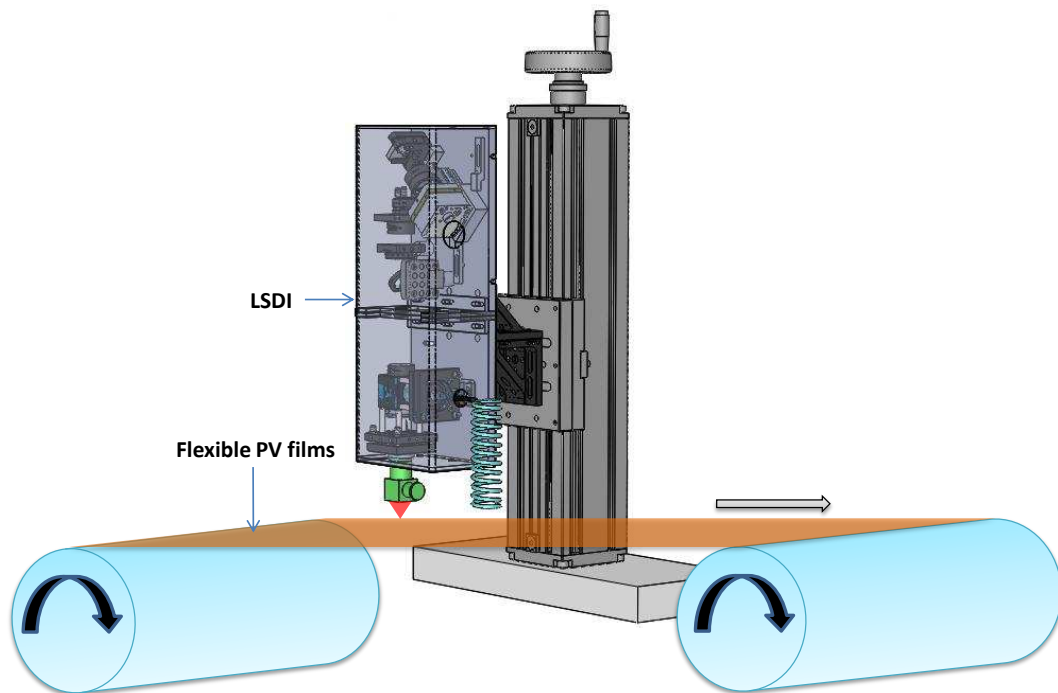


Figure 4.1 Schematic representation of employing the LSDI metrology system on a production line

### 4.2 System scheme

The basic configuration of the proposed LSDI is shown in Figure 4.2. It is comprised of four main parts, namely the light source, optical probe, spectrometer and console. The light source with broadband spectrum provides the white light illumination for the metrology device. An interferometric objective serves as the optical probe and observes the tested surface without

physical contact. Optical probe is the determinant of the resolving ability for the metrology sensor. When the OPD between the two arms of interferometric objective is within the scope of coherence length, numbers of fringes occur. The spectrometer is then used to spatially disperse the interference beam along the rows (or columns) of the CCD pixels, generating a two-dimensional spectral interferogram. Finally the recorded channelled spectrum is interpreted by the computing unit of the console and the evaluation result of a surface profile can be acquired.

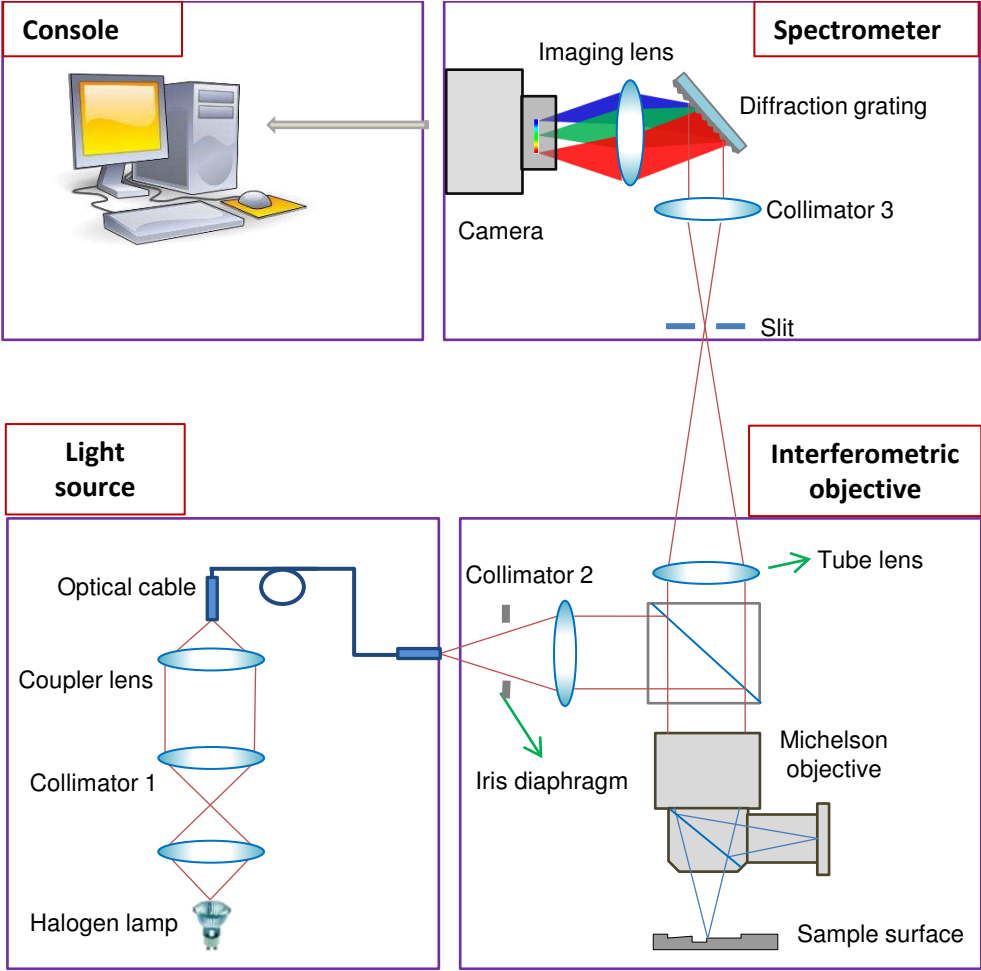


Figure 4.2 Block diagram of the LSDI system

**4.2.1 Light source**

The illumination scheme is dependent on the type of the tested surface. In general monochromatic illumination is used for smooth optical surfaces, while broadband chromatic illumination is applicable to objects with larger discontinuities, roughness and heights (Malacara,

2007). For the proposed LSDI, a continuum broadband illumination scheme is required due to the dispersion measurement principle. Selecting an appropriate light source for metrology device various factors should be considered such as centre wavelength, bandwidth, spectral shape, power and stability (Drexler & Fujimoto, 2008). For the dispersive interferometry, the axial measurement resolution is related to the optical bandwidth of the light source used, as given in equation (3.9). High power light source is desired to acquire enough exposure on the sensor especially when a high speed camera is used. For a diffraction-limited optical instrument, relative shorter centre wavelength can offer better lateral resolution. Nevertheless, there is a trade-off especially for systems such as SDOCT applied in the field of biology. This is because shorter wavelengths are more highly scattered in biological tissue, which then results in less imaging penetration (Boppart, 2003).

We selected a light source working in visible wavelength region (normally from 400 to 700 nm), which is highlighted in electromagnetic spectrum in Figure 4.3.

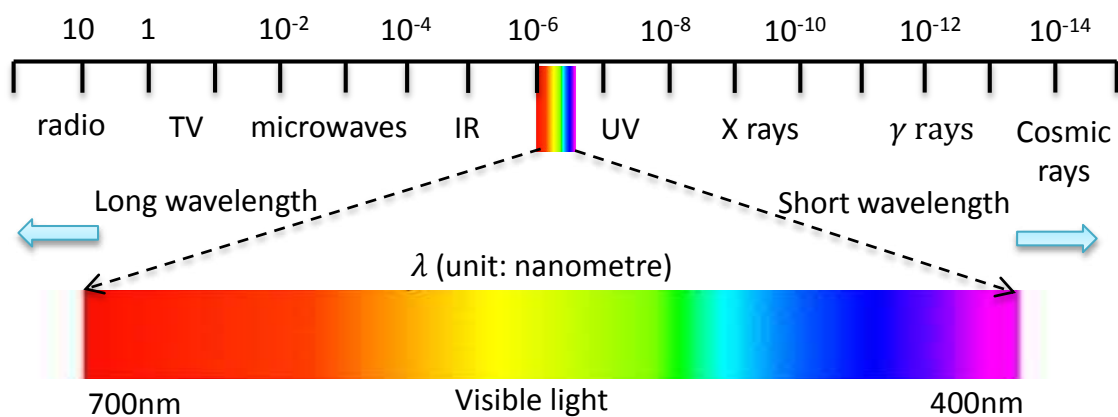


**Figure 4.3 Typical electromagnetic spectrum with visible light highlighted**

More specifically, a halogen lamp from Philips is utilised to generate white light illumination for LSDI and the designed light source device is shown in Figure 4.4. This device is a standalone system and connects with the interferometer using a flexible multi-mode fibre. The relatively low-cost halogen lamp has enough power with an output of 150 Watts and can be easily replaced. A plano-convex spherical lens collimates the emitted white light and then a fibre coupling lens (F810SMA-635, Thorlabs) focuses the light into the multi-mode fibre (both ends using SMA-connector). The intensity of the light source can be adjusted using a lighting transformer. A cooling fan is also installed in the circuit to prevent the device from overheating.

By using a spectrometer from Thorlabs Inc. (CCS100), the spectral distribution of the light source can be obtained and shown as Figure 4.5.

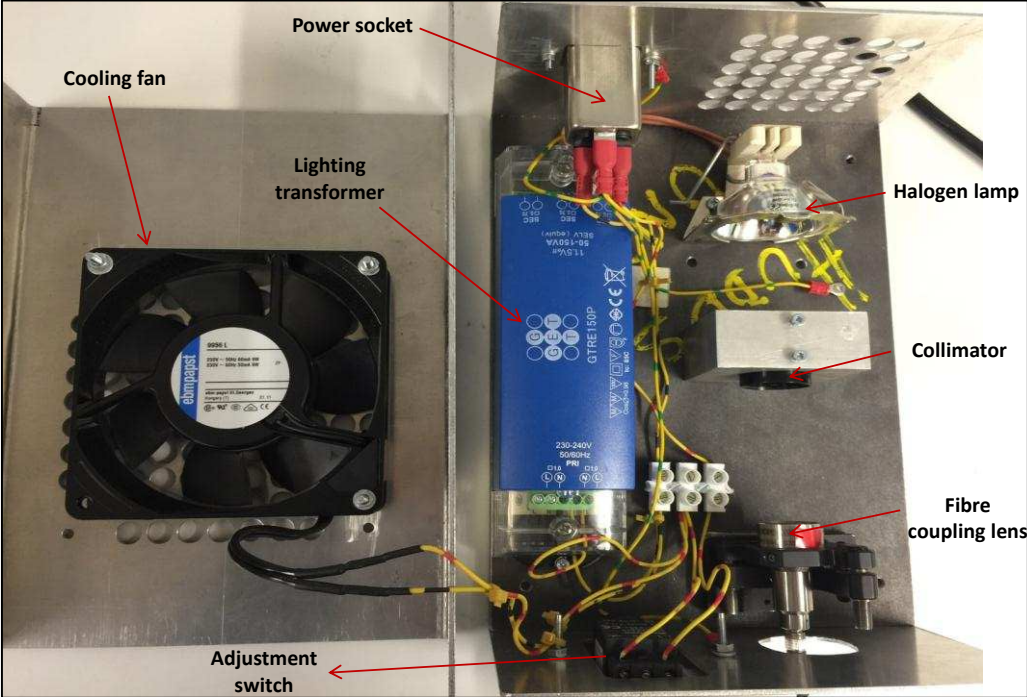


Figure 4.4 Light source device

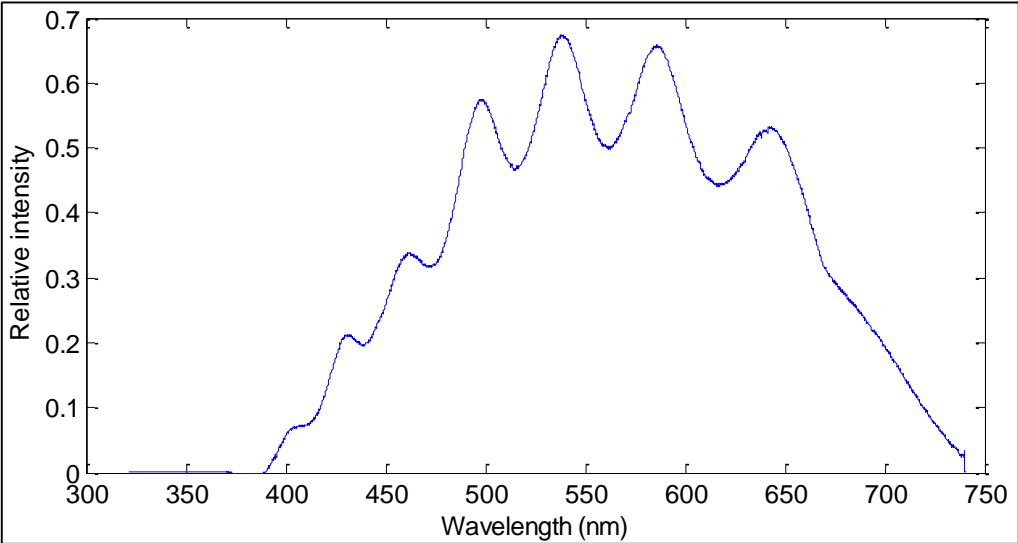
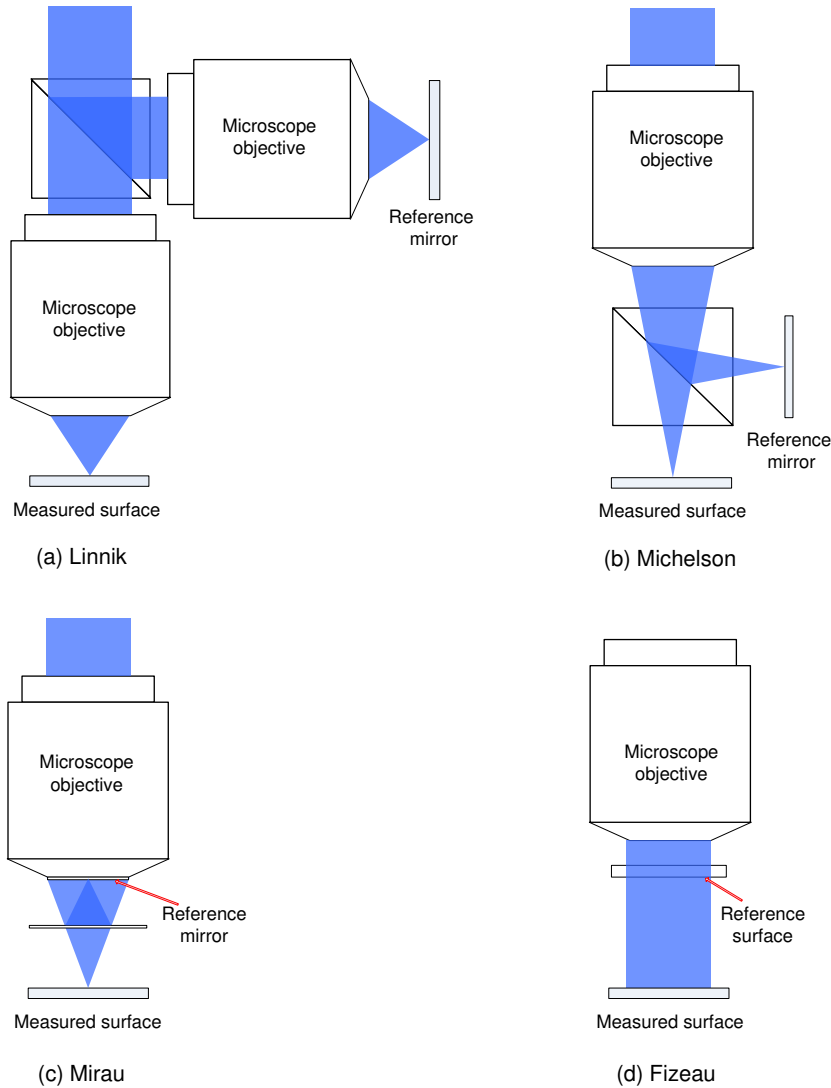


Figure 4.5 Spectral distribution of the developed light source device

### 4.2.2 Interferometric objective

Interferometric measurement requires an optical objective, in which two or more beams originating from the same source but traveling along different paths, are brought to interfere

(Hariharan, 2010). This interferometric objective serving as the optical probe can be generally classified into four types for different applications, namely Linnik, Michelson, Mirau, and Fizeau. The way in which the beam is split into reference and measurement beams distinguishes these objectives. Schemas of these four interferometric objectives are shown in Figure 4.6.



**Figure 4.6 Schemas of interferometric objectives: (a) Linnik, (b) Michelson, (c) Mirau and (d) Fizeau.**

Within all of the interferometers except Fizeau, there is a cone of light incident upon the tested surface and the corresponding reference mirror is placed at the best focus of the objective. Interference fringes with best contrast can be acquired when the tested surface coincides with the focal plane, where the OPD between the reference arm and the measurement arm is nearly zero.

The Michelson interferometer is historically important for its use by Michelson and Morley (1887) to provide experimental evidence against the theory of the luminiferous aether. For this

configuration the beamsplitter is set between the objective lens and the tested surface. On the one hand, it takes advantage of keeping balance of optical aberrations introduced by imperfect optics, which it is difficult to achieve for the Linnik interferometer. On the other hand, this configuration limits its application in objectives having low-magnification and long working distance. In case of the further optimization of the Michelson configuration, Kühnhold et al. (2013) proposed a correction system with three additional single lenses set at both entrance and exit of the beamsplitter to solve the dispersion problem caused by beamsplitter. In general the commercially available interferometric objectives with a magnification lower than 5X are based on Michelson configuration, such as the products from Nikon and Polytec.

Regarding the Mirau interferometric objective, it is a common path system with compact size. To achieve the interference across the full field of view of the objective, the reference reflective spot must be larger or equal to the objective's FOV. The reference spot (or reflective mirror) is inserted between the objective and beamsplitter, which consequently leads to the central obscuration in the system. Mirau objective is commercially available at a mid-magnification between 10X and 50X. For magnifications higher than 50X, the short working distance may not allow enough space for inserting a beamsplitter plate. The Linnik system solves this problem of working distance and is normally used with a high-magnification objective. Unfortunately, Linnik configuration is sensitive to mechanical influences and difficult to align. The two objective lenses of Linnik need to be well matched with a beamsplitter to assure that a wavefront with minimum aberration and maximum fringe contrast is provided (Malacara, 2007). Any tilt of the objectives or beamsplitter with respect to the optical axis need to be avoided.

Compared to the three objectives mentioned above, Fizeau interferometer is an unequal path system. It therefore requires a light source with a long coherence length and is normally used in single wavelength interferometry. It is a common path interferometer just as Mirau configuration but its reference surface can be spherical or flat according to different applications such as testing of flat surface, concave (convex) surface, optical lens and system. Commercial Fizeau interferometers have been available for many years and are still under development and optimisation to meet the high demands from the modern precision optical manufacturing. For instance, Kimbrough et al. (2008) used a pixelated polarisation mask spatial carrier phase shifting technique in conjunction with a high coherence source to significantly reduce the vibration sensitivity of Fizeau interferometer. Sykora and de Groot (2011) reported on a Fizeau-

type interferometer optimised for light-efficient, single-frame carrier fringe acquisition for instantaneous metrology at high lateral resolution.

Several systemic factors, including level of magnification, optical resolution, measurable slope and measurable height range, need to be considered to determine a proper objective for particular measurement. The best selection of objective will allow the smallest lateral features, the maximum height range and maximum slopes to be measured (Malacara, 2007). A high numerical aperture provides finer optical resolution and bigger measurable slope. The objective lens should have sufficient working distance for not coming into contact with the tested sample to prevent damages of the functional surfaces (Niehues et al., 2012).

As mentioned by Deck and Evans (2005), Fizeau interferometer is in general used in the spatial frequency range from 0.5 to 10 mm<sup>-1</sup> and the other three objectives can be applied to measure finer scale deviations from 1 to 1000 mm<sup>-1</sup>. Considering the aim of our project, Michelson interferometric objective is preferentially utilised due to relatively easy alignment and good performance in balancing optical aberrations.

### 4.2.3 Spectrometer

The spectrometer plays an important role in LSDI system. The basic components of a spectrometer are a slit, a collimator, a grating, an imaging focal lens and a detector. Different from WSI using an acoustic-optic tunable filter for wavelength scanning, LSDI employs a grating or dispersive prism to separate a series of constituent monochromatic interferograms which encode the phase as a function of wavenumber along the chromaticity axis of the camera (Debnath & Kothiyal, 2006; Tang, et al., 2014). For a diffraction grating with spacing  $d$ , if a plane wave is incident with an angle of  $\theta_i$ , the diffraction angle is  $\theta_m$  at the order  $m$ , then the fundamental grating equation giving the relationship between the angles  $\theta_i$  and  $\theta_m$  for a incident beam (wavelength  $\lambda$ ) can be expressed as

$$m\lambda = d (\sin \theta_i + \sin \theta_m) \quad (4.1)$$

Due to the relatively higher diffraction efficiency, defined as the ratio between the energy flow in the corresponding order and the energy flow in the incident order (Popov, 2012), the diffracted light in first order is selected to be gathered by the camera for spectral analysis.

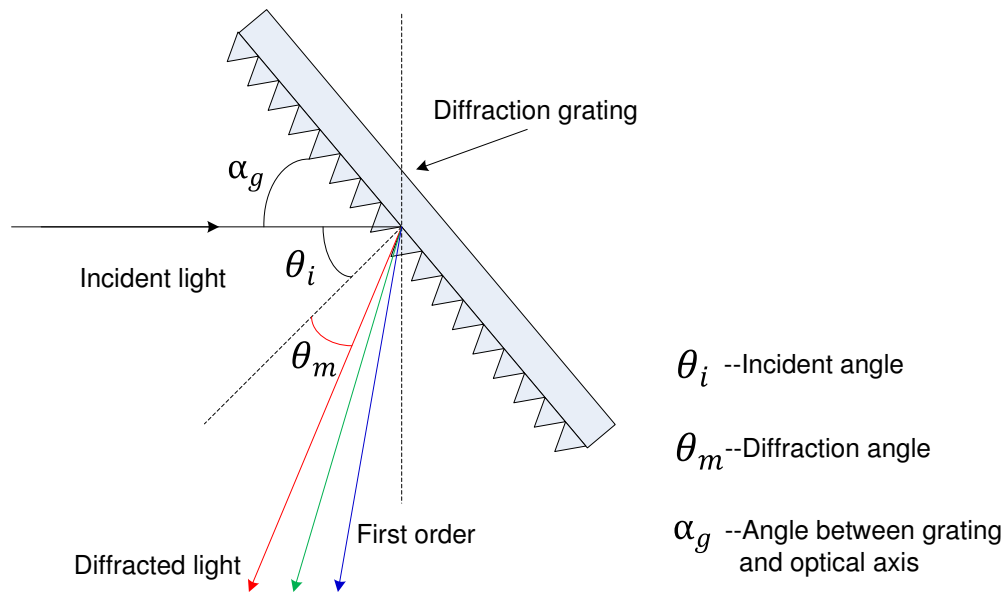


**Figure 4.7 Diffraction of light using a grating**

The optimal incident angle  $\theta_i$  is determined by investigating the linearity of the diffraction angle for the bandwidth being diffracted, as shown in Figure 4.7. Suppose the bandwidth received by the CCD camera has a wavelength range from 550 nm to 680 nm and the grating used has a groove density of 1200 groove/mm, then the diffraction angles with respect to the incident angles from  $0^\circ$  to  $90^\circ$  can be calculated using equation (4.1). Figure 4.8(a) shows the surface mesh result which represents the relationship between the incident angle and diffraction angle at the given bandwidth. Figure 4.8(b) specifically shows the linearity analysis of the diffraction angle with respect to the broadband wavelength at an incident angle of  $10^\circ$  (referred to as D-W curve). By fitting the D-W curves at different incident angles (from  $0^\circ$  to  $90^\circ$ ), it was found that the minimal standard deviation of the linearity errors could be obtained when the incident angle is equal to  $49^\circ$  (see Figure 4.8(c)). It means that the optimal angle between the optical axis and the diffraction grating is  $41^\circ$ , where the spectrum received by the camera almost linearly spreads along the chromaticity axis of the pixels.

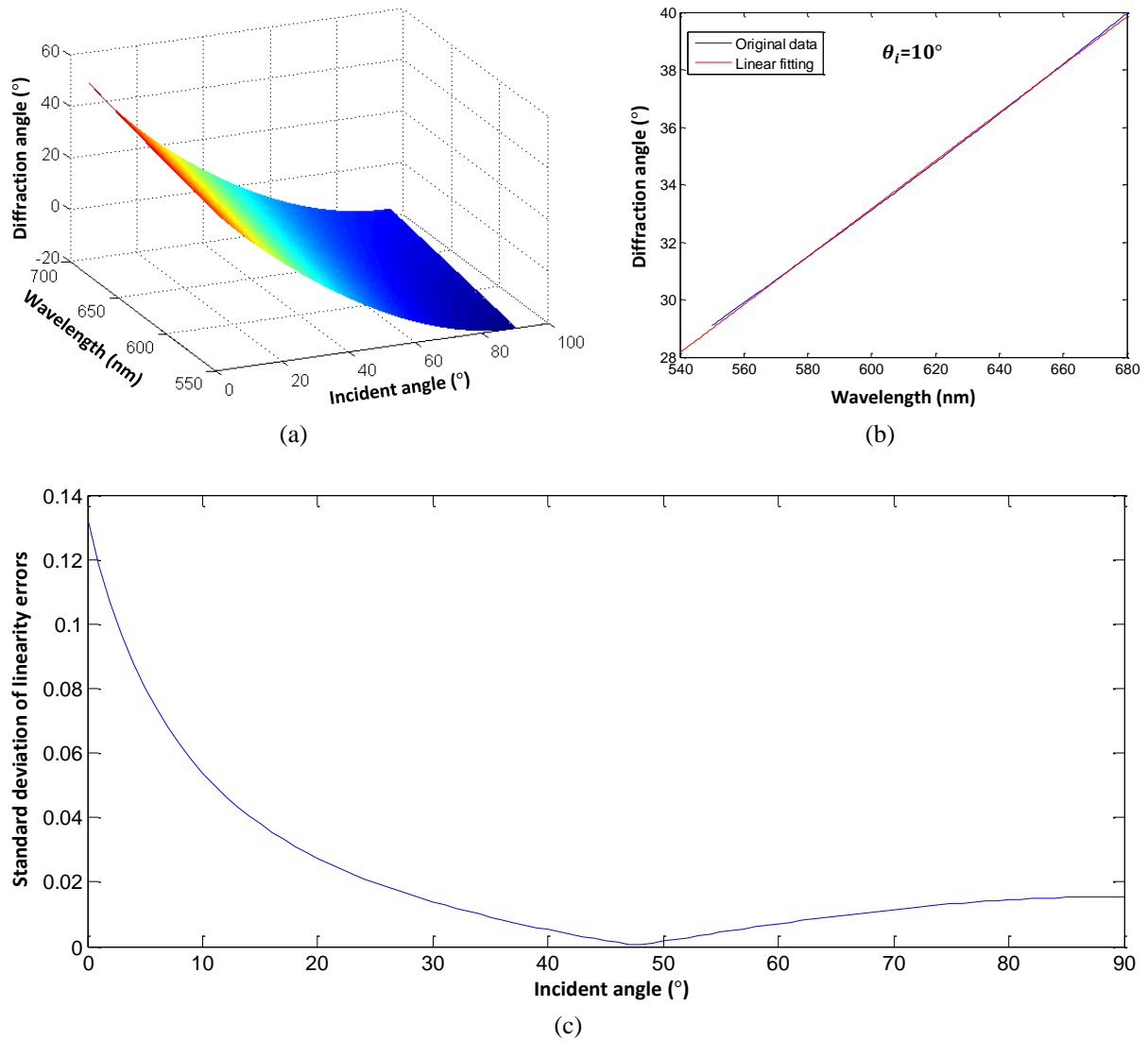


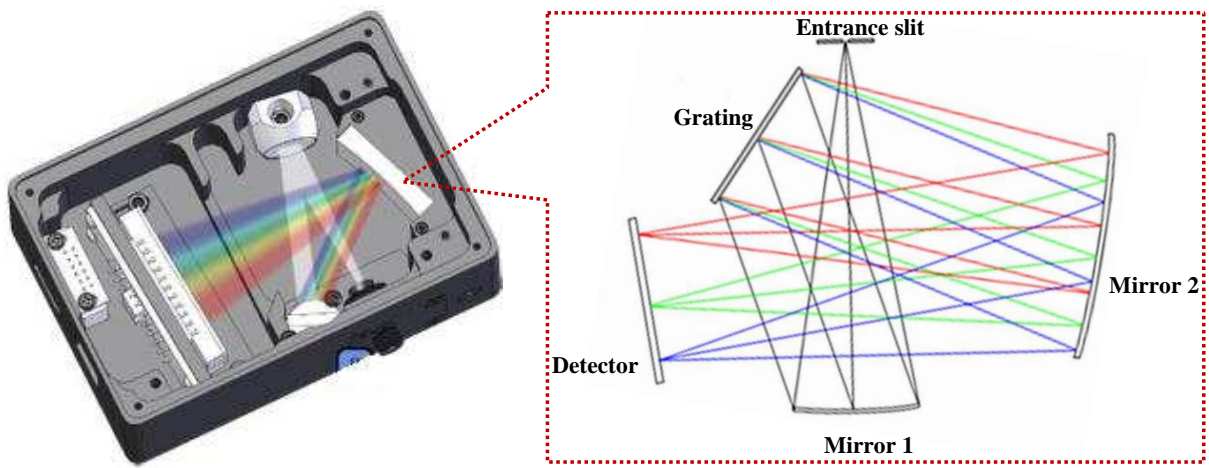
**Figure 4.8 Investigation of the optimal incident angle: (a) Surface mesh result, (b) D-W curve at the incident angle of  $\theta_i = 10^\circ$ , (c) Standard deviation of linearity errors with respect to incident angle.**

Therefore, by selecting suitable optical parameters (e.g., the grating spacing and focal length of imaging lens) as well as properly setting the relative position between the components (such as the camera location and the grating orientation), the camera is able to observe the desired spectral bandwidth with good linearity of the diffraction angles and relatively high intensity or good fringes when performing measurements.

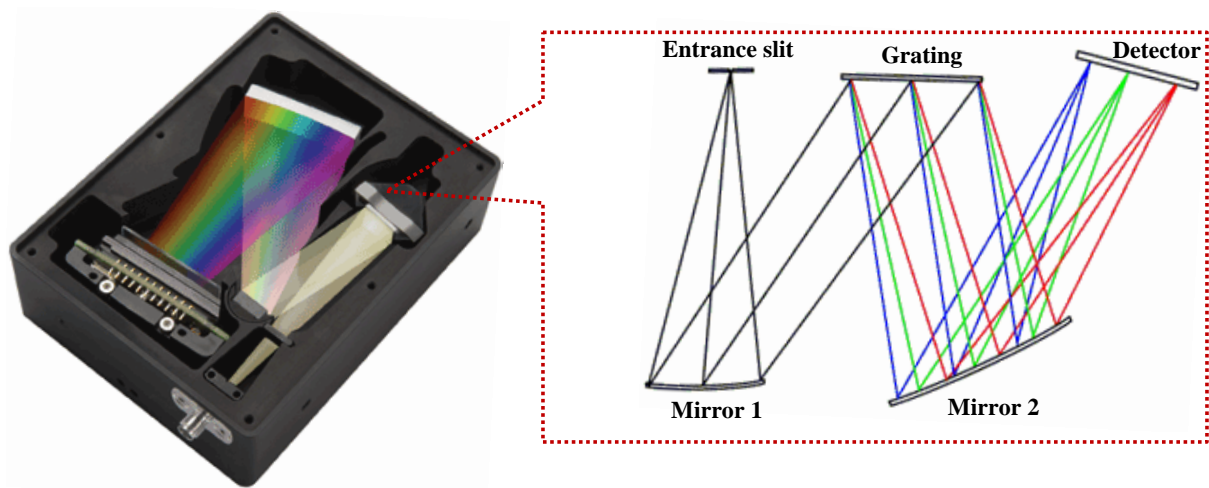
Additionally, some other crucial issues need to be carefully considered to build an applicable spectrometer, which are discussed in the following subsections.

### 4.2.3.1 Optical bench

Though there are various optical bench configurations, they are classified into four typical categories in this thesis, namely crossed Czerny-Turner, unfolded Czerny-Turner, concave-holographic configuration and lens-based configuration (see Figure 4.9). The former three configurations utilise mirrors to collimate and focus the beam and are widely adopted in commercial products, while the transmissive lens-based one is mostly used by many researchers in surface metrology field (Pavlíček & Häusler, 2005; Schwider & Zhou, 1994; Zhu & Wang, 2012).



(a)



(b)

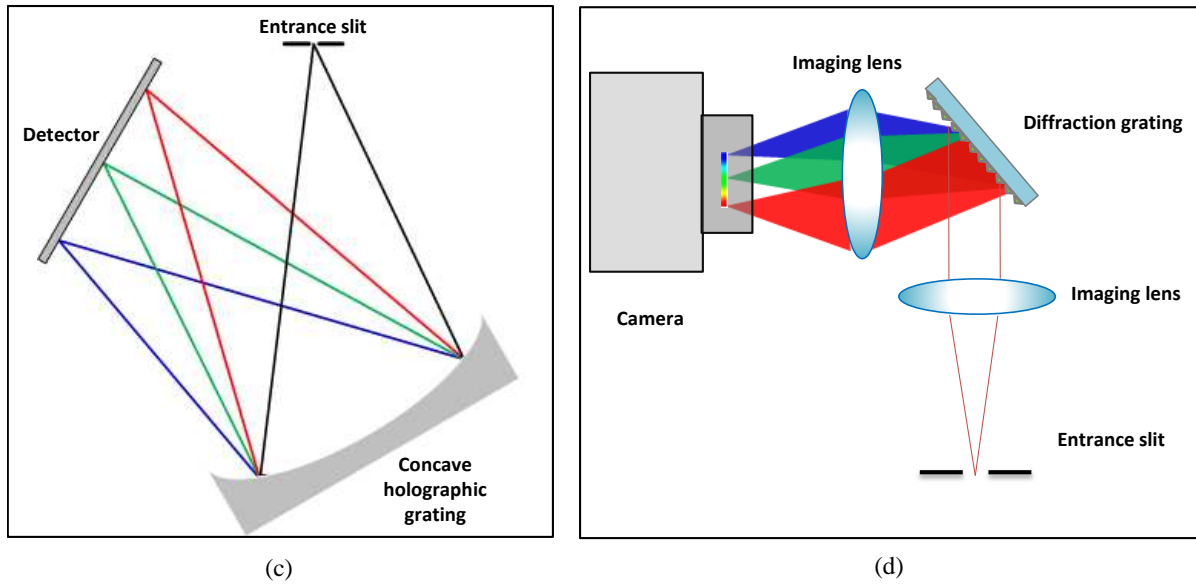


**Figure 4.9 Typical optical bench configurations for a spectrometer: (a) crossed Czerny-Turner, (b) unfolded Czerny-Turner, (c) concave-holographic configuration, (d) lens-based configuration [(a) & (b) adapted from B&W Tek Inc. and Photonics, respectively].**

Each of these optical benches has advantages and drawbacks and a perfect decision should be made by consideration of the applications. The crossed Czerny-Turner configuration offers a compact spectrometer design and a flattened spectral field may be produced by optimising the geometry of the configuration (Mohammadi & Eslami, 2010). The unfolded Czerny-Turner optical bench then cost-effectively mitigates the issue of high level of stray light. However, the off-axis configuration brings significant optical aberrations, especially the notable astigmatism which is its proportional to the square of the off-axis angle (Lerner & Thevenon, 1988; Lerner, 2006). Therefore, the aspheric mirrors are required in the modern Czerny-Turner spectrometer. The concave-holographic configuration makes the spectrometer even more compact because the grating and imaging elements are the same component. Yet all these reflective configurations suffer more from the thermal/mechanical instability compared to transmissive spectrometer (Lewis & Edwards, 2001).

In the case of LSDI system, we built an on-axis lens-based spectrometer to minimize the off-axis aberrations and obtain good quality of spectral lines at the focal plane.

#### 4.2.3.2 The grating

The diffraction grating is one of the most important optical elements directly determining the performance of the spectrometer and is generally grouped into two main types, namely

reflective gratings and transmission gratings. Reflective gratings are of a particular interest to make a compact LSDI system. The surface relief grating pattern of the reflective type can be either mechanically ruled on a plane substrate using a ruling machine (ruled grating), or holographically formed on different substrates such as plane, spherical and toroidal by interfering two ultraviolet beams (holographic grating) (Cotel et al., 2014; Lewis & Edwards, 2001).

Ruled gratings can be manufactured at low cost and normally have higher diffraction efficiency than holographic ones at each diffraction order. The disadvantage of ruled gratings is the stray light and ghost problem due to periodic errors, spacing errors and surface irregularities resulting from the fabrication, which is proportional to the square of order and groove density (Lerner, 2006). Holographic gratings presents up to over a 10 times reduction in stray light compared to ruled gratings. Therefore, holographic grating is preferentially selected for our system especially with high groove densities of up to 1200 groove/mm.

#### **4.2.3.3 The detector**

To begin with, the spectrometer is not an independent system outside the whole LSDI system. Any design of the spectrometer should match and serve the target theme of performing in-line metrology. An area-array CCD/CMOS camera with high speed is required for the developed LSDI to achieve surface profile measurement on a production line. The current camera technology provides micro-scale pixel size which is always smaller than the image size of the entrance slit and consequently the spectral resolution will be not limited by the pixel size. The trade-off between the lateral resolution and the amount of time to read out the data is considered more to determine the pixel size (or pixel density) of the detector for the metrology device.

#### **4.2.3.4 Spectral resolution**

The spectral resolution is defined as the ability of the instrument to separate two close spectral lines. There are a number of factors that determine the spectral resolution such as slit width, image quality of the optics, pixel size of the detector and resolving power of the grating (Lewis & Edwards, 2001). One practical equation given by B&W Tek, Inc. to calculate the spectral resolution  $\delta_\lambda$  is expressed as

$$\delta_\lambda = \frac{\Delta\lambda W_s RF}{NW_p} \quad (4.2)$$

where  $\Delta\lambda$  is the spectral range of the spectrometer,  $W_s$  represents the slit width, RF is the resolution factor, N is the pixel number in the chromaticity axis and  $W_p$  denotes the pixel size. The finite spectral resolution affects the vertical measurable range of the LSDI system, which is discussed in detail in chapter 6.

#### 4.2.4 Console

The console is designed to control the LSDI system in terms of data processing and capturing sequence of the CCD. For the in-line surface inspection, the camera is triggered in a continuous mode with the frame rate meeting the requirements of lateral sampling interval and web moving speed. The measurement data produced by the LSDI is recorded by the high-speed camera and then transferred to the console to analyse the fringe pattern and evaluate the sample surface. Moreover, analysis of all pixels in one frame can be accelerated using GPUs with CUDA (Compute Unified Device Architecture) programming model. By generating thousands to millions of threads (in our case equal the pixel number in the lateral profile direction), data parallelism can improve measurement speed and increase the potential to present real-time surface profiles.

### 4.3 Alignment of interferometric objective

The alignment of the interferometric objective is crucially important for the overall performance of LSDI. To obtain the high quality image or best visibility of fringes on the camera, the entrance surface of the beamsplitter should be perpendicular to the optical axis and the position of the reference mirror needs to be set at the best focus of the objective. As mentioned in the introduction section, two prototypes using different objective lenses (cylindrical lens and microscope objective, respectively) were investigated in this project. In this section, take cylindrical lens-based LSDI as an example, first simulation has been carried out using optical software ZEMAX to better understand the effect of alignment errors as well as offer the instructions for conducting assembly of the interferometer. Then a practical alignment strategy of the interferometric objective is briefly presented.

### 4.3.1 Simulation of cylindrical lens-based LSDI

ZEMAX is a multi-function software which can model, analyse, and assist in the design of optical systems. For accurate simulation purposes, the cylindrical lens-based LSDI system is modelled in sequential mode of ZEMAX using real data of optical components provided by the manufacturers (see Appendix A.1). With the aid of multi-configuration function in the software, the 3D layout of the cylindrical lens-based LSDI is shown in Figure 4.10.

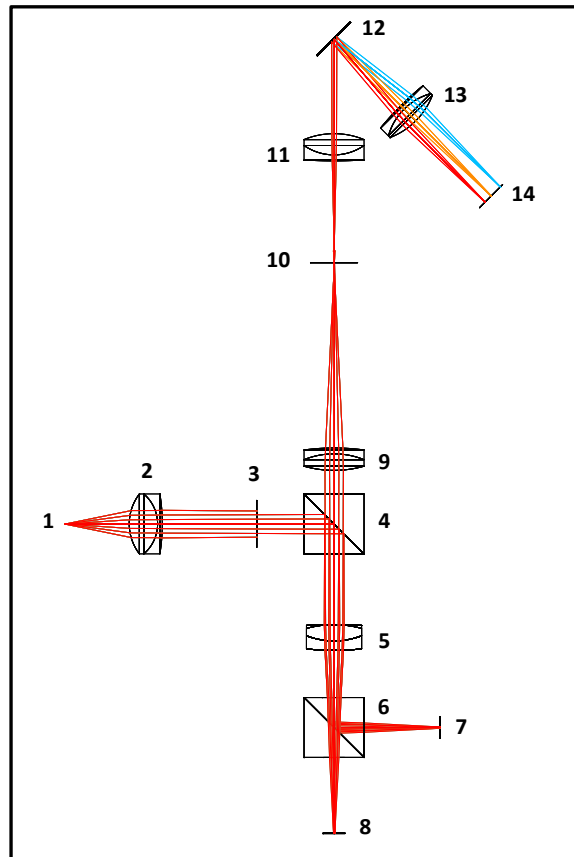


**Figure 4.10 3D layout of LSDI model in ZEMAX. 1, white light source; 2 & 11, collimator; 3, iris diaphragm; 4 & 6, beamsplitter; 5, cylindrical lens; 7, reference mirror; 8, tested surface; 9, tube lens; 10, slit; 12, grating; 13, imaging lens; 14, camera.**

For an ideal optical system without any aberrations and misalignments from optical components, the beams from the two arms of the interferometer are expected to travel back along the same paths and finally the interference beam is perfectly reconstructed with symmetric spherical wavefront. However, even if all lenses had already been optimised individually there are still some popular residual aberrations, such as spherical aberration, coma and astigmatism

which may be even magnified when being integrated together in the optical system. Figure 4.11 shows comparison of the spot diagrams between the systems with and without aberrations.

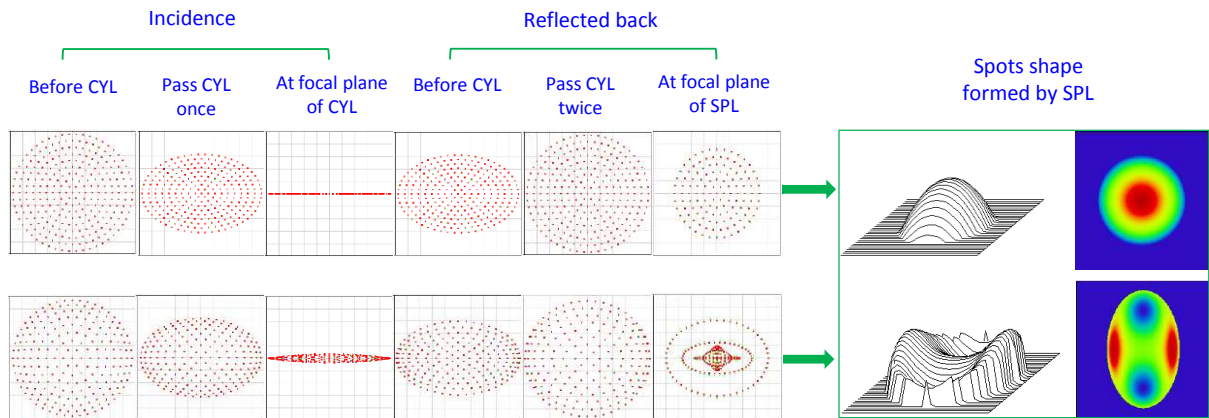


**Figure 4.11 Comparison of the spot diagrams between system with and without aberrations (CYL: cylindrical lens, SPL: spherical lens)**

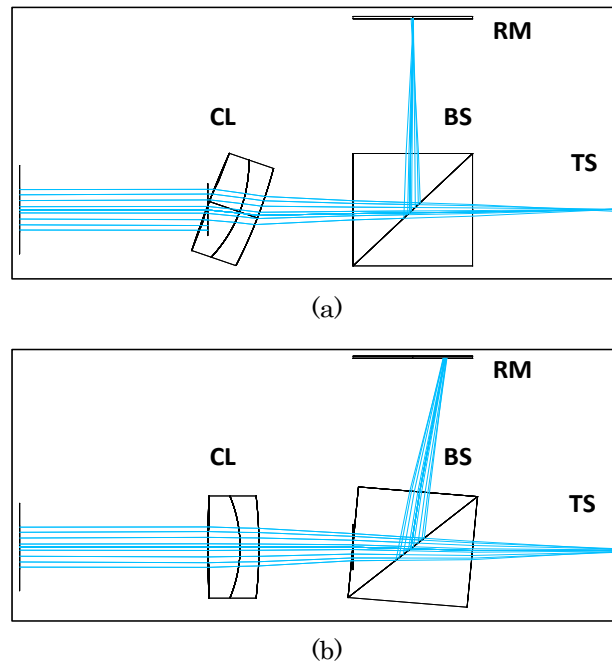


**Figure 4.12 Misalignments: (a) tilt of the cylindrical lens, (b) tilt of the beamsplitter. CL, cylindrical lens; BS, beamsplitter; RM, reference mirror; TS, tested surface.**

As illustrated above, the LSDI system is built with the off-the-shelf components and thus there are few freedoms for optimisation of the whole system. In this section, the aberrations resulting from the optical lenses are classified into system errors for particularly investigating the alignment errors. Compared to the optical aberrations which can normally be balanced between

the two arms of the interferometer, alignment errors are relatively significant for introducing additional OPDs and do have an influence on the accuracy of measurement results. There are mainly two kinds of misalignments, namely tilts and offsets of the optical components. Tilt errors are of particular interest in our simulation, as shown in Figure 4.12.

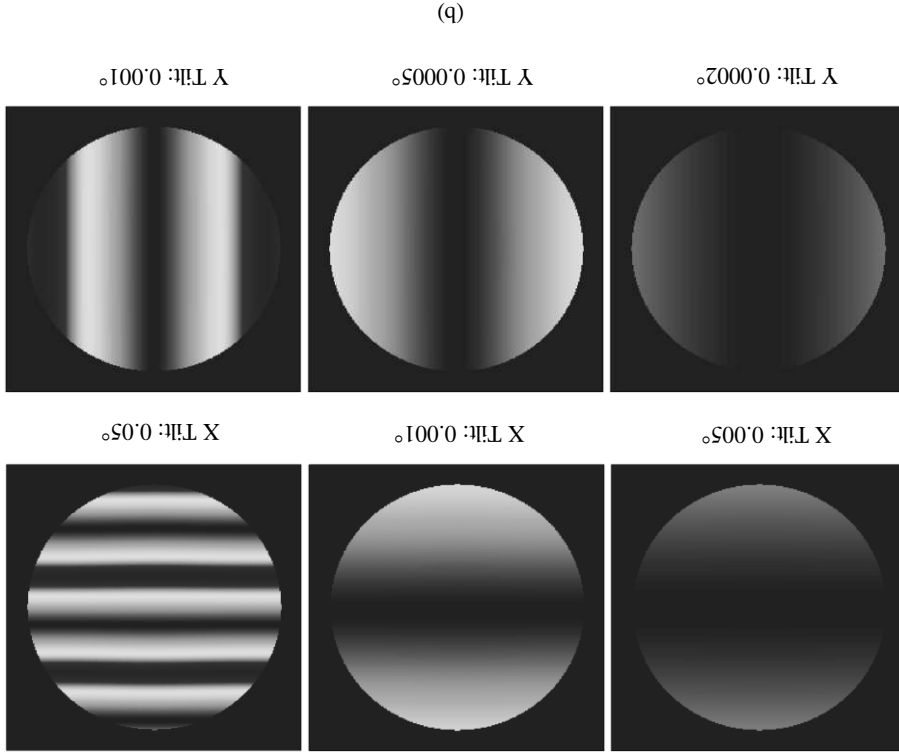
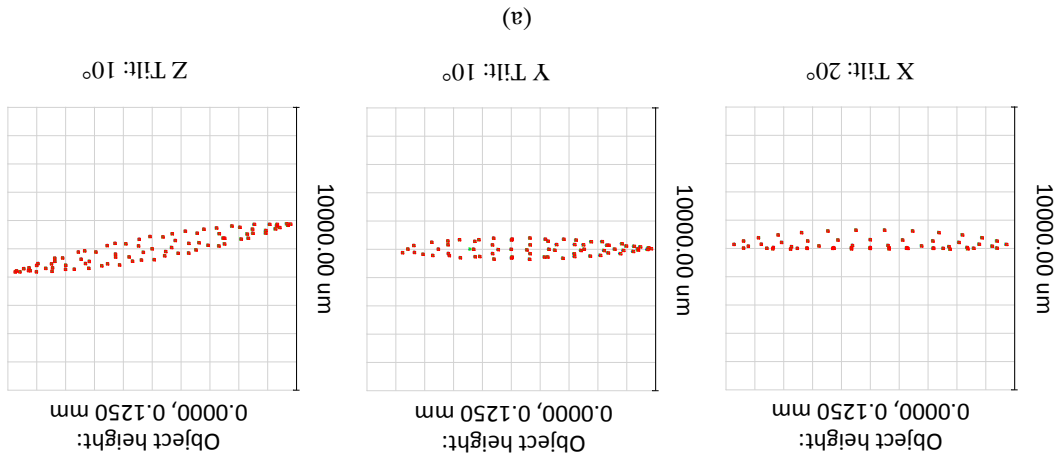


Figure 4.13 Simulations regarding the tilts of optical components: (a) spot diagram results by tilting the cylindrical lens, (b) interferogram results through tilting the beamsplitter.

Figure 4.13 (a) indicates that tilts of the cylindrical lens lead to the deformation of the line focusing beam on the tested surface. More specifically, tilts about X axis and Y axis make the

focusing beams asymmetrical and tilt along the Z axis only rotates the direction of measuring beam. In this case, no extra fringes generate because the OPD between the two arms of the interferometer remains the same. However, tilts of the beamsplitter or reference mirror will lead to a tilt of the optical axis and thus the light beam will no longer travel along the same path, in which case straight fringes with equal intervals are generated on the image plane (Figure 4.13 (b)). The simulated interferograms show that the OPD is sensitive to the tilts of the beamsplitter, therefore attention should be paid to beamsplitter cube when carrying out alignments. Likewise, tilts of the reference mirror will generate the similar effect on the interferograms as the beamsplitter does.

#### **4.3.2 Alignment strategy**

The simulation shows that the OPD is sensitive to the tilts due to the optical axis deviation. For the developed interferometric objective of LSDI, the beamsplitter and the reference mirror are both fixed on the kinematic mounts which offer tip/tilt angle adjustments. A collimated laser beam with small aperture was used to evaluate the tilt errors of the beamsplitter through measuring the heights of two split beams at a distance. Adjusting the tip/tilt buttons of the mount until these two heights are equal, this will ensure the beamsplitter is well aligned and its entrance surface shall be perpendicular to the primary optical axis.

After the objective and the beamsplitter are aligned, the position of the reference mirror needs to be accurately set at the best focus as well. There are four steps to achieve this and the methodology is shown in Figure 4.14. First, the reference mirror is moved to a few or tens of microns away from the focal plane of the objective, where almost the smallest image spot impinges on the mirror surface. Second, a photodiode power meter (PPM, available at Thorlabs, Inc.) was placed at the focus of the tube lens. The maximum output of energy can be received by the PPM sensor through properly adjusting the tip/tilt of the reference mirror, where the optical axis is supposed to be perpendicular to the mirror surface. Third, a standard sample with nano-scale step heights is placed underneath the objective in the measurement arm, and the PPM is replaced with a CCD camera. Blocking the reference arm and adjusting the sample in terms of tip/tilt and position along the optical axis until a sharp image of these small step features are observed on the camera. Last, the reference mirror is brought to focus and zero fringes occur when the OPD between the two arms of the interferometer becomes zero. Once at this position the adjustment buttons are locked and the reference mirror is supposed to be well aligned.

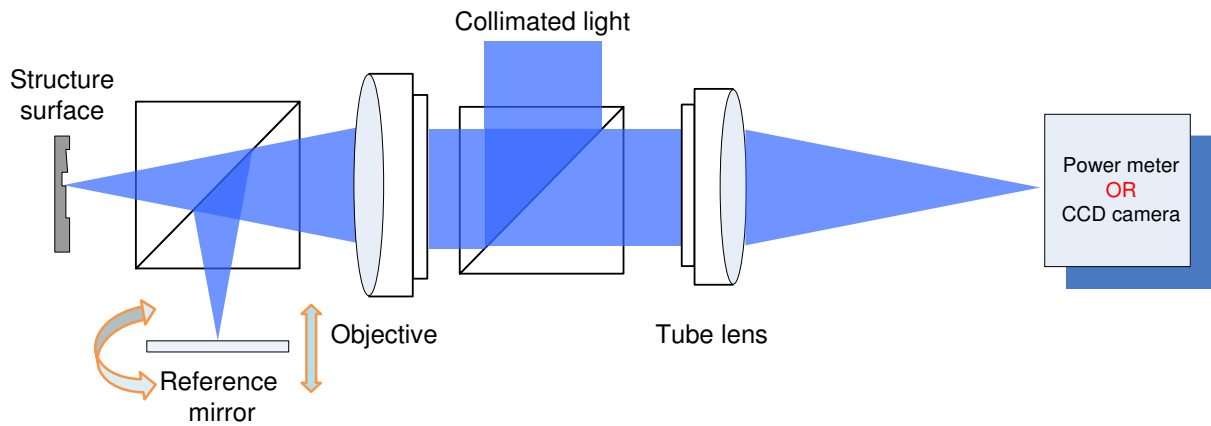


Figure 4.14 Alignment of the reference mirror in an interferometric objective

#### 4.4 Calibration of chromaticity axis of camera

##### 4.4.1 Light source for calibration

The interference beam generated by the LSDI probe is spatially decomposed along the rows (or columns) of the CCD pixels. The grating equation (4.1) shows that the relationship between the dispersed wavelength and pixel number is not linear. In order to validate the spectrum obtained by the camera, it is necessary to perform wavelength calibration. It means experimentally calibrating the exact relationship between the pixel number and the specific wavelength. In general the chromaticity axis of the camera is calibrated with a cadmium spectral lamp (Debnath & Kothiyal, 2005), which emits four spectral lines and are assigned to corresponding pixels on the camera, as shown in Figure 4.15(a). The wavelengths of the rest of the pixels (see Figure 4.15(b)) are then given by Hartmann's formula defined as (Malacara, 2007)

$$\lambda = \lambda_0 + C / (d_0 - d) \quad (4.3)$$

where  $\lambda_0$ ,  $C$ , and  $d_0$  are constants. Through using three pairs of  $(\lambda, d)$  from a reference light source, the values of three unknown constants can be determined. Therefore the relationship between wavelength  $\lambda$  and pixel number  $d$  along the chromaticity can be acquired by substituting the calculated constants in equation (4.3).

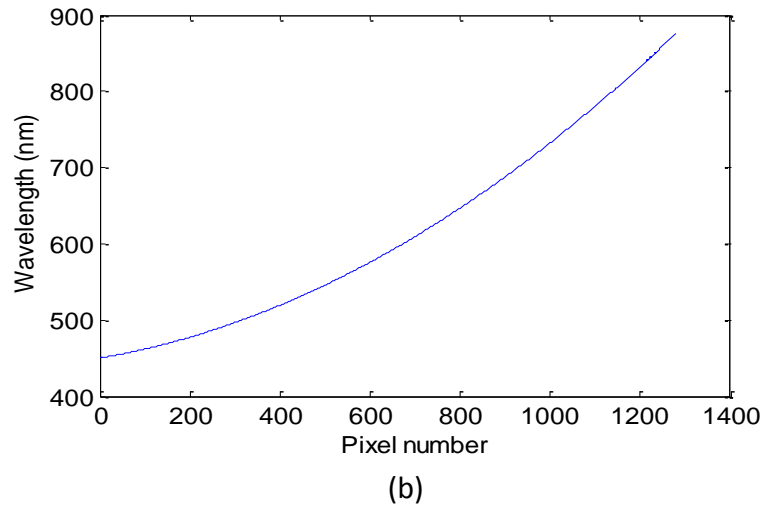
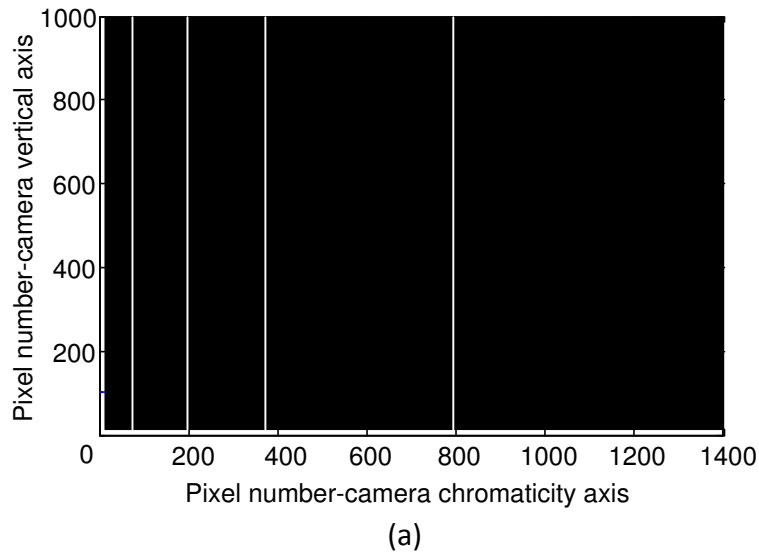


**Figure 4.15 Calibration of chromaticity axis of camera: (a) spectrum of cadmium lamp on the camera, (b) calculated wavelength for each pixel.**

With regard to a CCD array spectrometer, the collection of many partial spectra from the light source is required to perform the task of wavelength calibration over an extended wavelength range (Gaigalas et al., 2009). However, there are only four spectral lines available within the range from 470 nm to 645 nm for a cadmium lamp. This means a certain angle of grating and position of camera are required to receive at least three of those four reference spectral lines, which consequently restricts the system's performance. Therefore, a reference irradiance source with continuum spectrum is designed for calibration of the proposed LSDI, as shown in Figure 4.16.

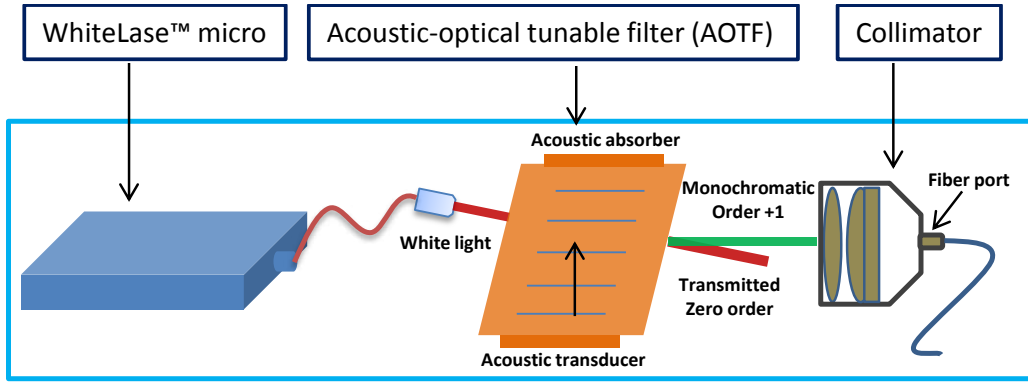


**Figure 4.16 Schematic diagram of the developed light source device for wavelength calibration**

This illumination system is comprised of a white light laser source (WhiteLase™ micro), an AOTF and a Fiberport collimator (PAF-X-15-B). WhiteLase™ micro is an ultra-compact super continuum source based on a mode-locked fibre laser, which possesses an output power of more than 200 mW and covers a broad bandwidth at least 450 nm to 2000 nm. The AOTF works at the wavelength range from 420 nm to 700 nm and has a resolution (Full width at half maximum-FWHM) higher than 0.3 nm (@ 560 nm). The selected collimator has an effective focal length of 15.4 mm and NA of 0.16. After the broadband incident light passes through the AOTF, a specific wavelength with high accuracy is then selected by controlling the propagation velocity and frequency of the acoustic wave. The selected wavelength is determined by

$$\lambda = \Delta n \alpha v_a (f_a)^{-1} \quad (4.4)$$

where  $\Delta n$  is the birefringence of the crystal used as the diffractive material,  $\alpha$  is a parameter depending on the design of the AOTF, and  $v_a$ ,  $f_a$  are the propagation velocity and frequency of the acoustic wave, respectively.

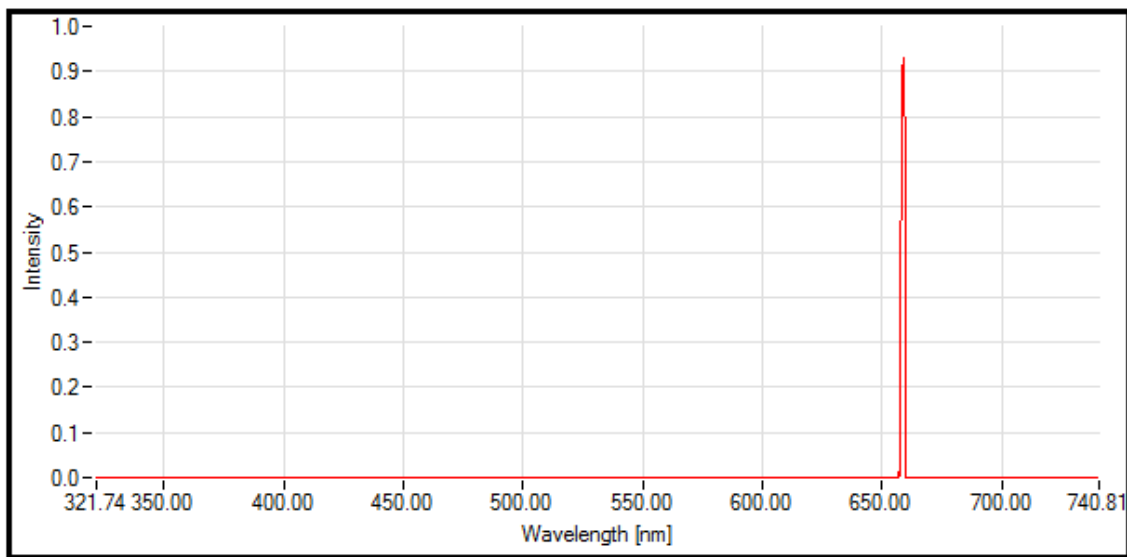
#### 4.4.2 Calibration equation

Taking advantage of the continuum spectrum of the developed calibration light source, a series of experimental data points (wavelength, pixel number) can be acquired by exposing the reference spectrum onto the camera and therefore more accurate calibration can be achieved. In the experiment, every selected wavelength  $\lambda$  is first measured using a commercial spectrometer (traced by a laser diode with wavelength of 650 nm) and then brought to illuminate the LSDI system to record the spectral line on the camera, as shown in Figure 4.17. Finally a data matrix  $M(\lambda, p)$  registering the information of wavelength with respect to pixel number can be obtained.

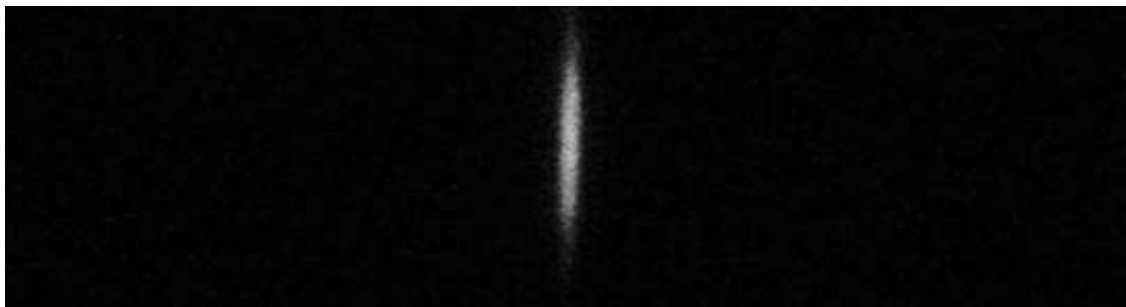
Instead of using equation (4.3), a second-order polynomial presented by Ocean Optics is used to represent the relationship between pixel number and wavelength, as shown in equation (4.5).

$$\lambda_p = Ap^2 + Bp + C \quad (4.5)$$

where  $\lambda_p$  is the wavelength of pixel  $p$ ,  $C$  is the wavelength of pixel 0,  $B$  is the 1st order coefficient (nm/pixel) and  $A$  is the 2nd order coefficient (nm/pixel<sup>2</sup>). The values for  $A$ ,  $B$  and  $C$  are calculated through a least squares equation using all the collected experimental data.



(a)

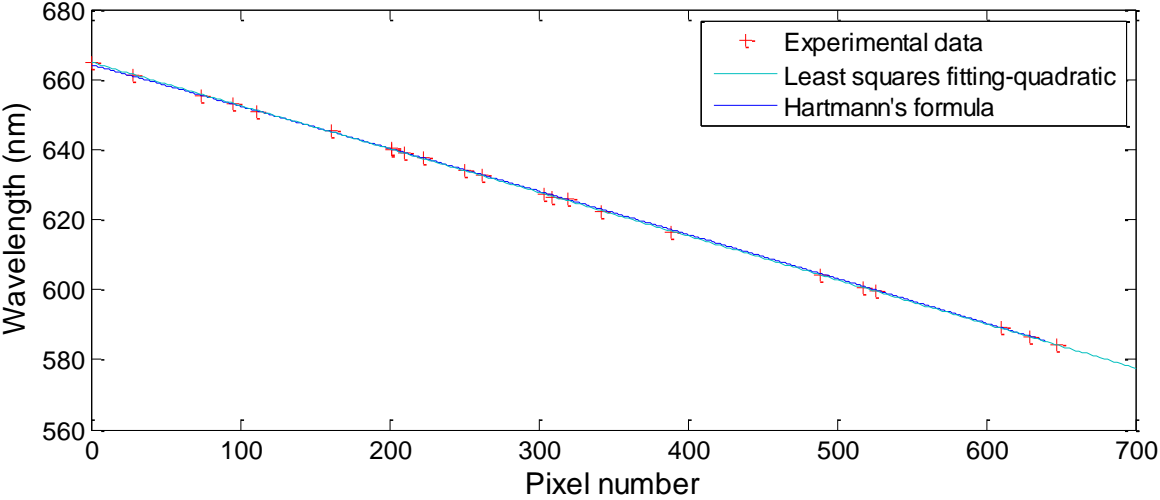


(b)

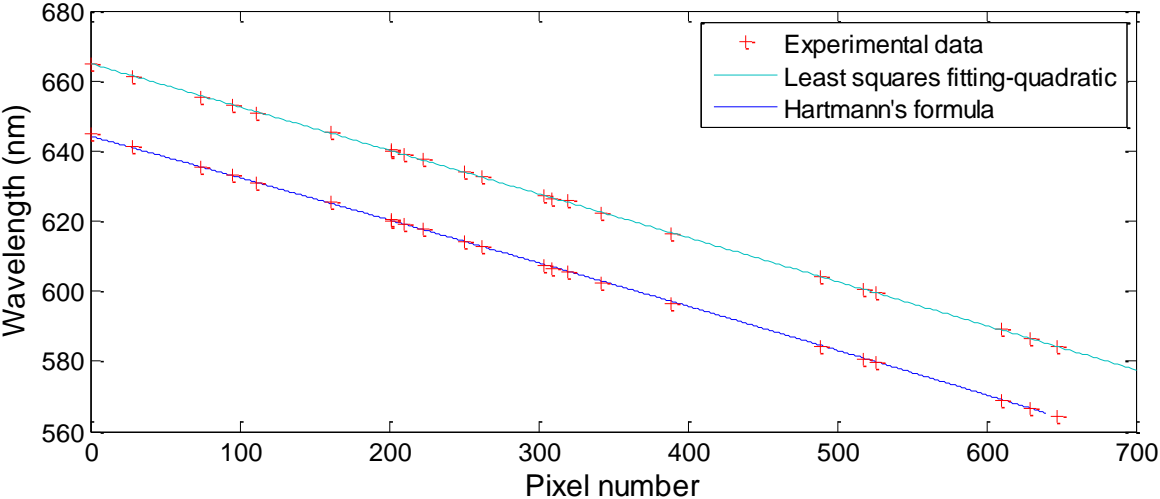
**Figure 4.17 Wavelength calibration using commercial spectrometer: (a) wavelength validation using CCS100, Thorlabs Inc., (b) the corresponding spectral line on the camera.**

Figure 4.18 depicts wavelength calibration using equation (4.3) and (4.5), respectively. To make a better visualisation, an appropriate amount of offset is added to separate the plots (Figure 4.18(b)). It turned out that the two calibration results are in agreement with each other, however,

the latter method is more accurate due to the close alignment with all spectral lines obtained in the experiment.



(a)



(b)

**Figure 4.18 Calibration of chromaticity axis of camera: (a) calibrated curves using equation (4.3) and (4.5), (b) calibrated results with an appropriate amount of offset.**

**4.5 Summary**

Four main parts of the LSDI are functionally combined together to enable the instantaneous measurement in a single shot. The illumination system was designed using a halogen bulb along with collimators and a multi-mode fibre was employed to transfer the broadband white light to the interferometer. Due to the large NA (0.39) and core diameter (400 μm) of the selected fibre,

enough output of luminous intensity and a larger FOV on the observed surface can be obtained. By making trade-offs between the various factors according to the requirements of our practical applications, the Michelson interferometric objective and the lens-based spectrometer configuration are determined for the proposed LSDI.

Regarding the alignment of the interferometric objective, tilts of the beamsplitter and reference mirror with respect to the optical axis make the beams impinging on the two arms of the interferometer travel along different paths and consequently introduce additional unpredictable OPD into the system. Simulations using ZEMAX demonstrated that the effects from tilts are more significant than the errors caused by the apochromatic objective itself. Therefore, good alignment of these two optical elements is essential for obtaining the reliable and accurate measurement.

The white-light interferogram corresponding to a surface profile is captured by the camera with the phase information encoded as a function of wavenumber along the chromaticity axis. Calibrating the chromaticity axis of the camera is therefore an indispensable procedure before the LSDI is used for surface measurement. The next chapter focuses on the techniques for interpretation of the spectral interferogram.

# 5 Data processing

## 5.1 Introduction

Data processing of the captured spectral interferogram is performed to evaluate the surface profile. Through analysing the interference fringes with high resolution algorithms, the height information of the surface profile can be accurately retrieved. This chapter provides a brief introduction to the fringe pattern obtained using the LSDI probe and gives the detailed processes of fringe analysis. The algorithms based on FFT and Carré techniques are both developed to calculate the phase variation. The mathematical description of the developed algorithms and the resolution capability are presented. Finally the data parallelism is concisely introduced for investigating the potential to accelerate the measurement speed to the level required for the in-line surface metrology.

## 5.2 Fringe pattern

The fringes observed by the detector are basically channelled spectrum. This spectral interferogram comprises of a series of constituent monochromatic interferograms which are spectrally decomposed by a spectrometer and encode the phase as a function of wavenumber along the chromaticity axis. It is a two-dimensional image recorded by an area-array camera, with one axis (horizontal) being used to provide the phase information, and the other (vertical) giving the length information of the measured surface profile (Hart et al., 1998). The depth information can be extracted after all the pixels in the spectral interferogram are analysed.

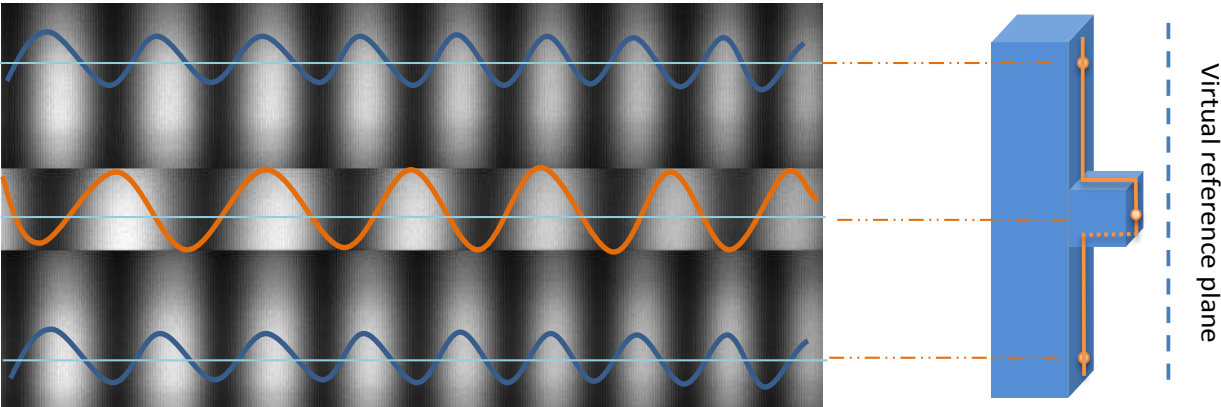


Figure 5.1 Fringe pattern for a step object using LSDI

Figure 5.1 shows the fringe pattern of a step sample using LSDI. The OPDs between the tested surface and the reference plane produce different numbers of fringes along the profile direction. Each row signal along the chromaticity axis represents the height information of a point, and the absolute distance between each tested point and the corresponding reference point can be determined by calculating either the phase slope due to wavelength shifting or the fringe frequency. Therefore, by analysing a series of row signals the height map of a one-dimensional profile can be acquired. Since the proposed technique performs absolute distance measurement with respect to the reference point, the height direction can be positive or negative depending on whether the tested surface is above or below the virtual reference plane during the measurement. Combining temporal phase shifting technique could give more accurate results, which at the same time can determine the sign of the measured height to overcome the height ambiguity problem. Yet the phase shifting method is limited when measuring a surface in motion.

Figure 5.2 shows the flowchart of the developed algorithms for interpreting the spectral interferogram. The initial data required for analysis include a spectral interferogram (measurement information), a reference interferogram (background information) and the calibrated wavelength matrix across the chromaticity axis (dispersion information). All this information is processed with five main steps, namely background removing, wavelength calibration, coordinate transformation, phase calculation and acquisition of height map of a one-dimensional profile. The following section will go on to present the details of each step.

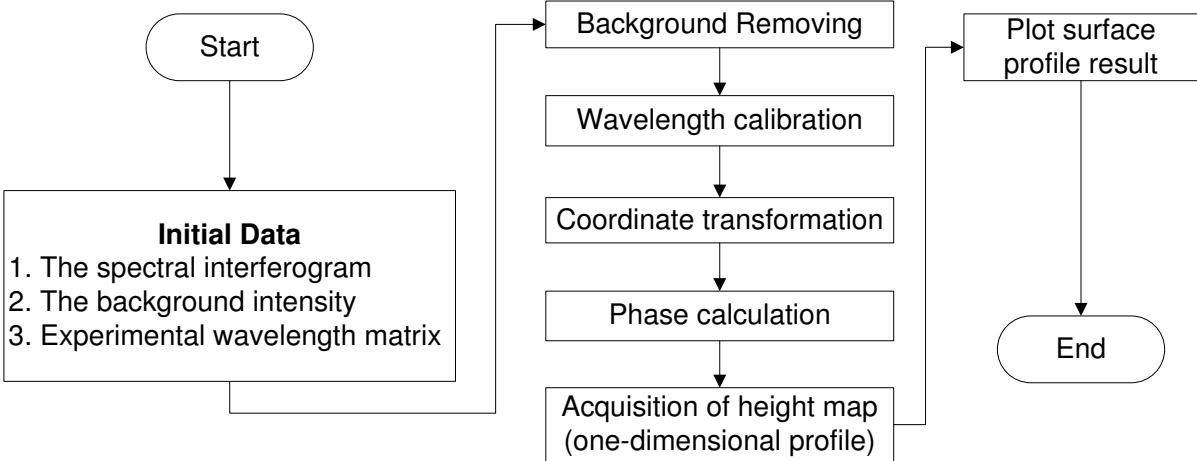


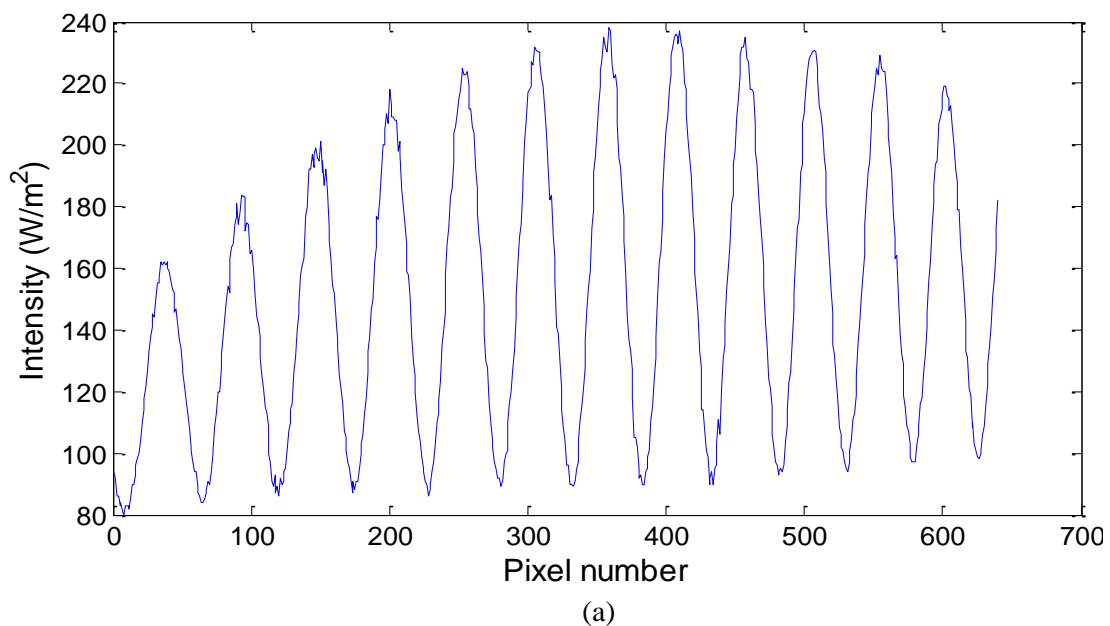
Figure 5.2 Flowchart of the developed algorithms

## 5.3 Fringe Analysis

### 5.3.1 Background removing

The recorded interferogram contains a background intensity variation which results from the spectral distribution of the light source and the spectral response of the camera. The low frequency components due to the background intensity are systematically existing in the interferogram and may lead to wrong analysis results in the frequency domain such as incorrect localisation of the peak position. Therefore, it is necessary to remove the background signals before calculating the phase variation.

An interference signal was selected from the channelled spectrum to give a further illustration, as shown in Figure 5.3. Figure 5.3(a) shows the original signal containing the background intensity variation, which is apparently modulated by a low frequency signal. After performing FFT, the Fourier transform spectrum of the selected signal is shown in Figure 5.3 (b). It shows that there is an undesired peak close to the desired peak, which may be an issue for accurately localising the peak for phase calculation.



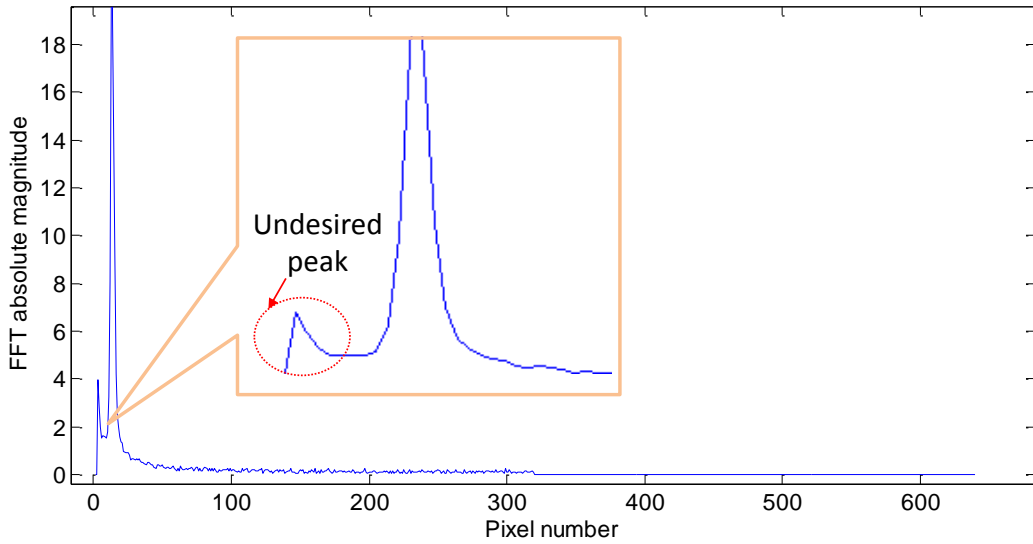


**Figure 5.3 Interference signal with background intensity variation: (a) original signal, (b) corresponding Fourier transform spectrum with an undesired peak.**

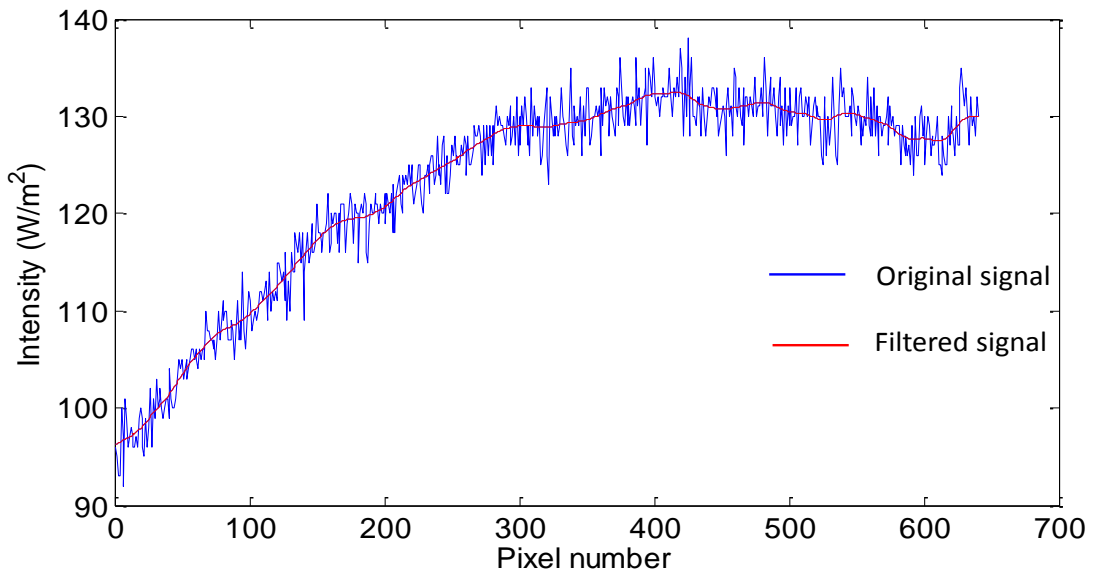


**Figure 5.4 Background signal extracted from the spectral interferogram and its filtered curve**

To remove the background, the measurement arm of the interferometer is blocked and then a reference frame without the interference effect can be captured. The corresponding background signal for the interference signal in Figure 5.3(a) is shown in Figure 5.4. It is filtered by a Gaussian filter with a cut-off of 0.25 mm and then divided by the interference signal (Reolon et al., 2006). Finally the corrected signal without background intensity can be obtained, as shown in Figure 5.5(a). The corresponding Fourier transform spectrum is depicted in Figure 5.5(b), which shows the undesired peak was removed compared with Figure 5.3(b). All row signals obtained

from the interferogram need to perform background removing using the corresponding (same row) background signals.

The spectral intensity recorded at the output of the interferometer can then be rewritten as

$$\bar{I}(x, y; \lambda) = I_{\text{Interf}}(x, y; \lambda) / I_{\text{Backg}}(x, y; \lambda) \quad (5.1)$$

where  $\bar{I}(x, y; \lambda)$  is the intensity without background intensity variation,  $I_{\text{Interf}}(x, y; \lambda)$  and  $I_{\text{Backg}}(x, y; \lambda)$  represent the interference signal and background signal, respectively.

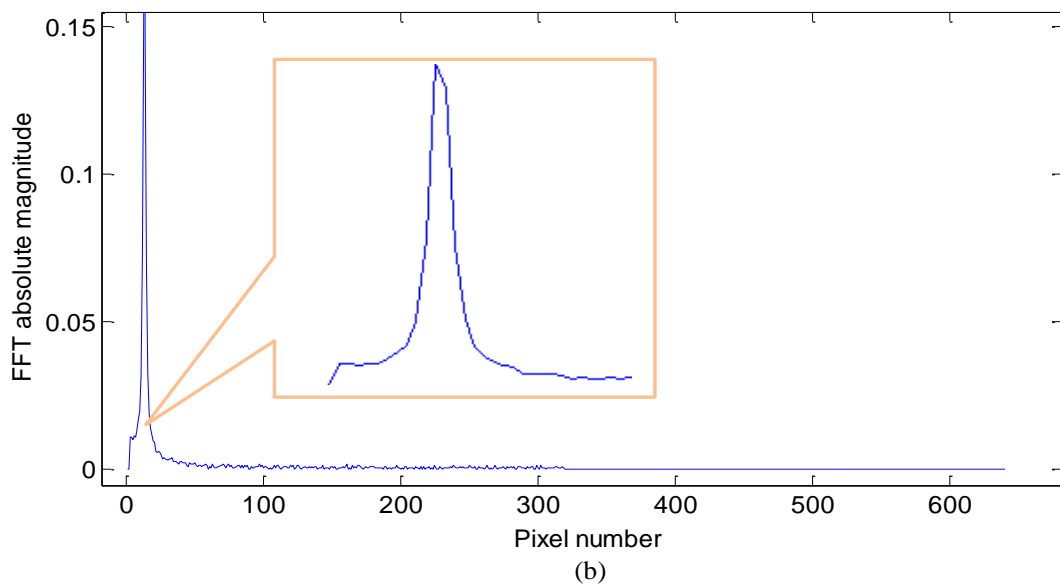
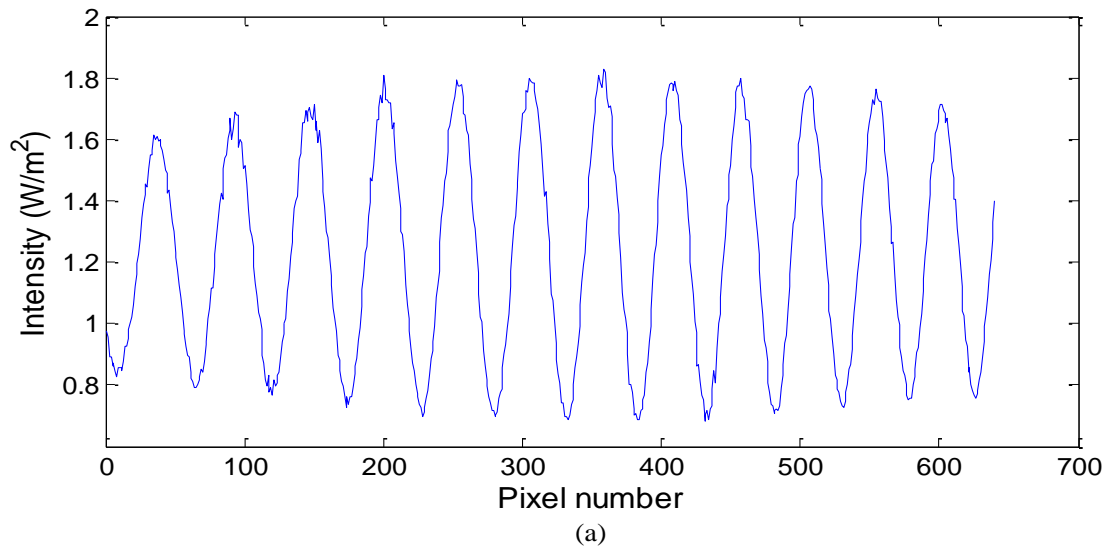


**Figure 5.5 Interference signal after removing the background (a) corrected signal, (b) Fourier transform spectrum of the corrected signal.**

### 5.3.2 Wavelength calibration

The interference beam obtained by the LSDI probe is dispersed by a spectrometer with the horizontal direction of the 2D detector as the chromaticity axis. The interferogram delivers spectral fringes in chromatic-spatial coordinates (Malacara, 2007). The dispersed wavelength along the chromaticity axis is actually not linearly related to the pixel number and consequently the procedure of wavelength calibration is a necessity. For calibrating the chromaticity axis, each pixel is accurately assigned a specific wavelength through using the known spectral lines on the camera and other polynomial fitted values. Section 4.4 illustrated the calibration method for the developed LSDI. During this procedure, more than 30 groups of experiment data (spectral lines) were recorded to calculate the values for A, B and C in equation (4.5) using least squares equation. The calibration results, varying with the optical configurations of the spectrometers, will be given in chapter 6 and chapter 7. For an assembled LSDI system, wavelength calibration is only required when it is used for the first time.

### 5.3.3 Coordinate transformation

The original signal obtained is a curve of irradiance with respect to wavelength  $\lambda$  (or pixel number). However, the phase variation extracted from the channelled spectrum is linearly related to the wavenumber  $k$  ( $k = 1/\lambda$ ). Therefore the coordinate transformation needs to be conducted to convert the original sinusoidal signals along each row to wavenumber related curves. After the initial transformation, the same number of data points as the previous signal is generated with uneven spacing across the wavenumber axis. Resampling is then performed to obtain data points in equal intervals through an elaborate interpolation scheme such as cubic spline interpolation, which was also utilised by other researchers (Choma et al., 2003; Dorrer et al., 2000; Kumar et al., 2010). Figure 5.6 shows the implementation of coordinate transformation using Matlab.

After coordinate transformation, each interference signal in the spectral interferogram is reconstructed with even  $k$  spacing as expressed in equation (5.2), which is prepared for the Fourier transform process.

$$\bar{I}(x, y; k) = a(x, y; k) + b(x, y; k) \cos [\varphi(x, y; k)] \quad (5.2)$$

where  $\bar{I}(x, y; k)$  is the interference signal with respect to wavenumber  $k$  without background,  $a(x, y; k)$  and  $b(x, y; k)$  represents the DC background intensity and fringe visibility, respectively;

and the phase  $\varphi(x, y; k)$  is defined by the following formula

$$\varphi(x, y; k) = 4\pi\lambda^{-1} \times h(x, y) + \varphi_0 = 4\pi k \times h(x, y) + \varphi_0 \quad (5.3)$$

where the  $h(x, y)$  represents the surface elevation,  $\varphi_0$  is the initial phase.

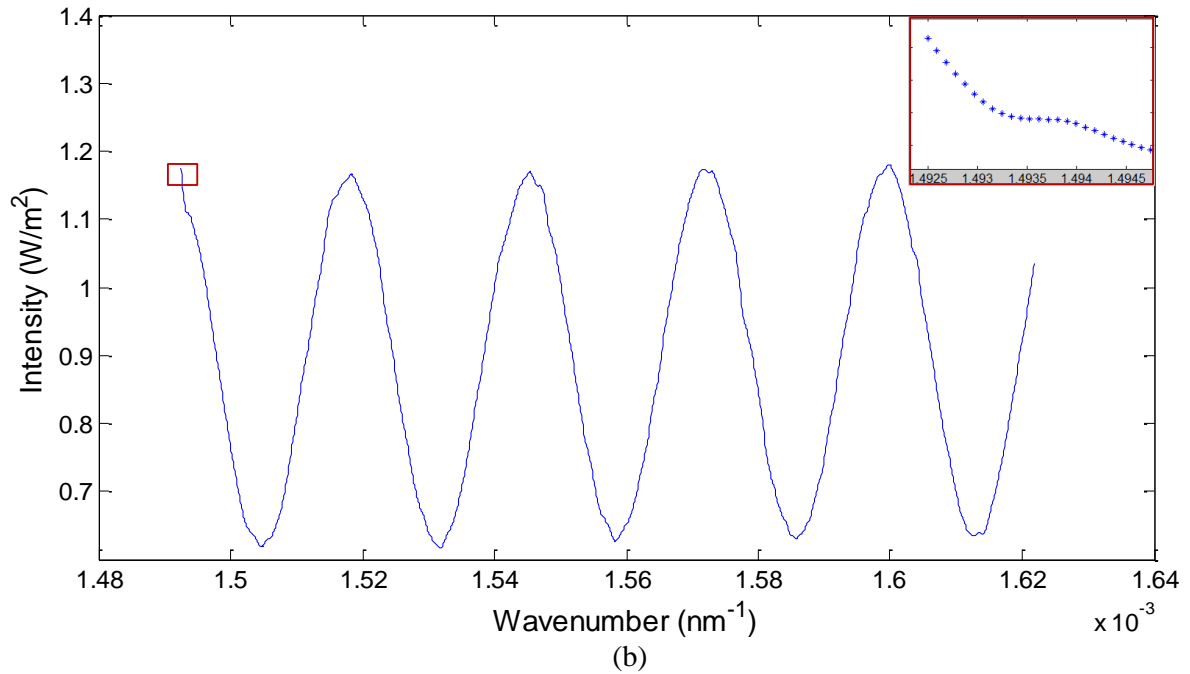
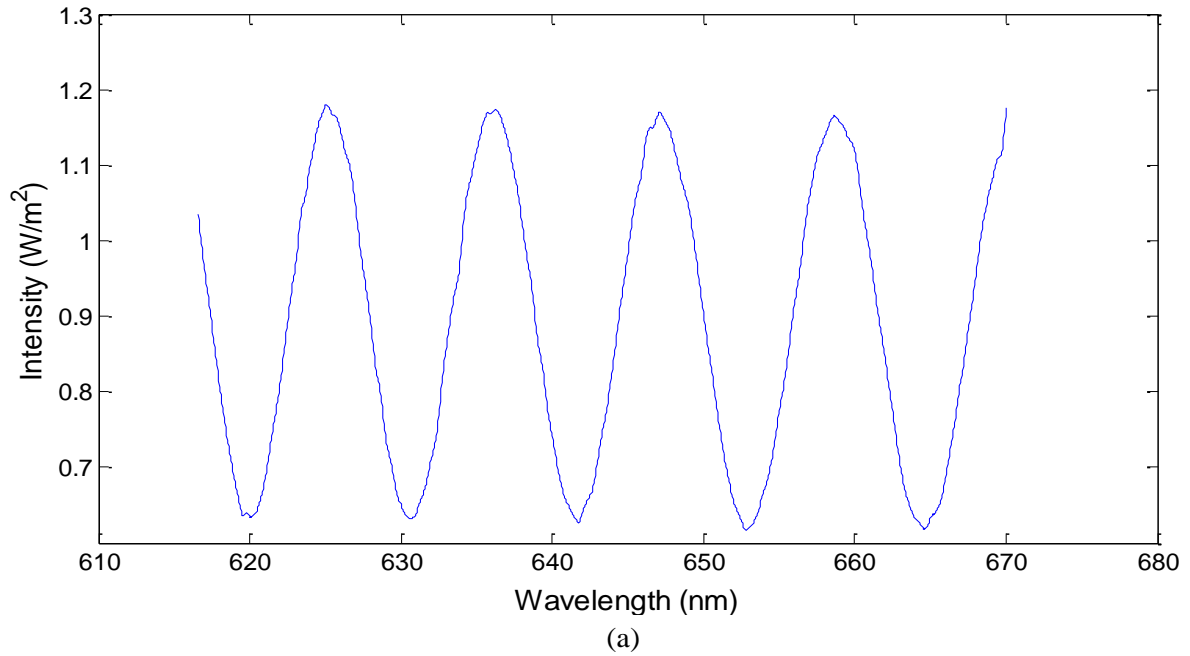


**Figure 5.6 Coordinate transformation: (a) original signal – wavelength related curve, (b) signal after coordinate transformation and resampling– wavenumber related curve with equal  $k$  spacing.**

### 5.3.4 Phase calculation

The resolution of measurement depends on the algorithm used for calculating the phase variation from the interference fringes. The more accurate determination of the phase variation the higher resolution is achieved. Many algorithms have been developed to extract the phase, including techniques based on FFT (Takeda et al., 1982), Carré phase shifting (Malacara & Servin, 2005), convolution (Sainz et al., 1990) and Hilbert transform (Debnath & Kothiyal, 2006), etc.

This section presents two developed algorithms for the proposed system to calculate the phase slope. The first algorithm is an FFT based algorithm, which is widely used because it is effective, accurate and insensitive to intensity noise (Jiang, et al., 2010; Muhamedsalih, et al., 2012). The sinusoidal interference signal is processed through FFT and inverse FFT, in which way the desired phase information can be separated from the DC component and the unwanted conjugate term. The second one uses Carré phase shifting to calculate the phase slope in a single interferogram without any extra multi-frames (Muhamedsalih et al., 2012). It has the benefit of high precision and independence of the amount of phase shift.

#### 5.3.4.1 FFT based algorithm

This method was first proposed by Takeda et al. (1982) to analyse the fringe pattern for computer-based topography and interferometry and was verified by experiments in terms of accuracy and sensitivity. As illustrated above, the height information of a point is registered in a sinusoidal signal and can be retrieved by determining the phase variation over the dispersed wavelength range. As an illustration, the corrected interference signal after the background removing and coordinate transformation (see Figure 5.6(b)) is analysed using FFT based algorithm.

First the mathematical expression of spectral intensity  $\bar{I}(x, y; k)$  can be written in another form as

$$\bar{I}(x, y; k) = a(x, y; k) + \frac{1}{2}b(x, y; k)e^{i\varphi(x, y; k)} - \frac{1}{2}b(x, y; k)e^{-i\varphi(x, y; k)} \quad (5.4)$$

let

$$c(x, y; k) = \frac{1}{2}b(x, y; k) \exp[i \varphi(x, y; k)] \quad (5.5)$$

then

$$\tilde{I}(x, y; k) = a(x, y; k) + c(x, y; k) + c^*(x, y; k) \quad (5.6)$$

where \* denotes a complex conjugate.

The Fourier transform is applied to equation (5.6) to acquire the spectrum ( $\tilde{I}(x, y; f)$ ) in frequency domain, which is expressed in equation (5.7) and shown in Figure 5.7.

$$\tilde{I}(x, y; f) = A(x, y; f) + C(x, y; f - f_0) + C^*(x, y; f + f_0) \quad (5.7)$$

where the capital letters denote the Fourier spectra,  $f$  and  $f_0$  are the spatial frequency and spatial-carrier frequency related to the initial phase, respectively.

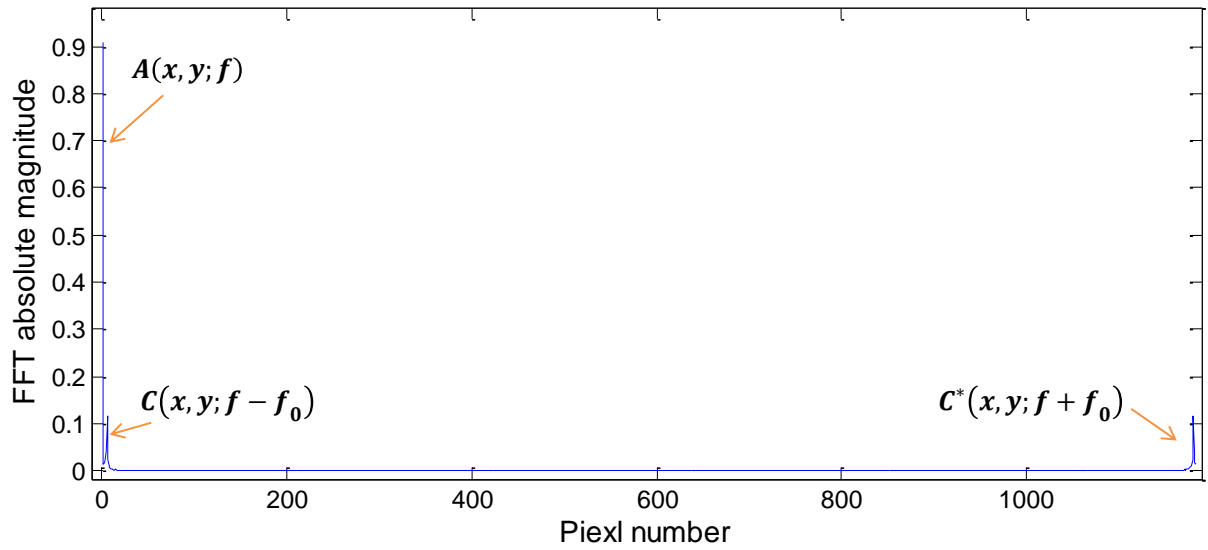


**Figure 5.7 Fourier transform spectrum**

There are three terms in the Fourier domain, namely DC term related to the light intensity in each spectral signal and two other components related to the phase shift linearly related to the wavenumber across the chromaticity axis. To extract the phase information, the unwanted DC ( $A(x, y; f)$ ) and one of the phase conjugate terms ( $C^*(x, y; f + f_0)$ ) are filtered out by selecting a suitable filtration window and replacing their values with zeros. Finally only  $C(x, y; f - f_0)$  is kept for the further processes, as shown in Figure 5.8.

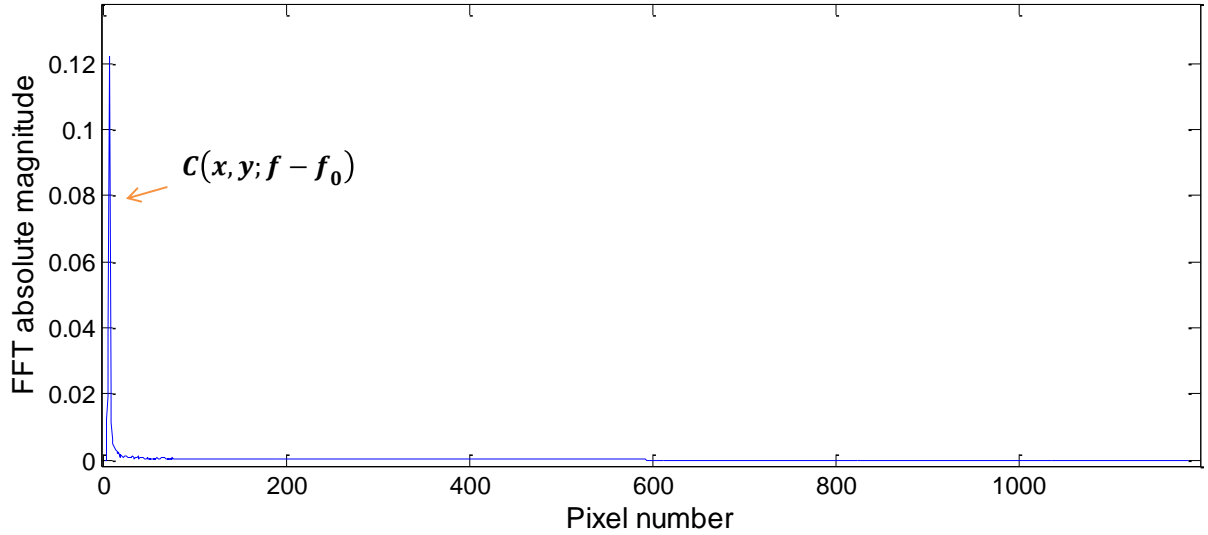


**Figure 5.8** Fourier transform spectrum after filtrated out the DC and the phase conjugate term

Then the inverse fast Fourier transform (IFFT) is performed on the desired term  $C(x, y; f - f_0)$  to reconstruct the  $c(x, y; k)$ . Taking the natural logarithm of the IFFT result, the phase  $\varphi(x, y; k)$  of each sample point is extracted as the imaginary part of equation (5.8).

$$\ln\left\{\frac{1}{2}b(x, y; k)\exp[i\varphi(x, y; k)]\right\} = \ln\left[\frac{1}{2}b(x, y; k)\right] + i\varphi(x, y; k) \quad (5.8)$$

However, the phase obtained from the exponential term of equation (5.8) is wrapped into the range  $[-\pi, \pi]$ , as shown in Figure 5.9. To correct this discontinuities phase distribution, the absolute phase difference between two adjacent points needs to be compared using an appropriate criterion to determine the phase offsets (Takeda, et al., 1982). More specifically, if the phase jump between two adjacent points  $(\varphi_i, \varphi_{i+1})$  is larger than  $0.9 \times 2\pi$ , then addition or subtraction of a  $2\pi$  phase jump should be performed every time according to the direction of the phase difference. The phase offset  $\text{offset}_{-\varphi_{i+1}}$  is expressed as

$$\text{offset}_{-\varphi_{i+1}} = \left\langle \begin{array}{l} 0 \\ \text{offset}_{-\varphi_i} + 2\pi \\ \text{offset}_{-\varphi_i} - 2\pi \\ \text{offset}_{-\varphi_i} \end{array} \middle| \begin{array}{l} \text{if } i = 0 \\ \text{if } \varphi_{i+1} - \varphi_i < -0.9 \times 2\pi \\ \text{if } \varphi_{i+1} - \varphi_i > 0.9 \times 2\pi \\ \text{if } \varphi_{i+1} - \varphi_i < 0.9 \times 2\pi \end{array} \right\rangle \quad (5.9)$$

After detecting all the offset  $\varphi_i$  (see Figure 5.10), the continuous phase unwrapping  $\varphi_{i+1}$  is then obtained by equation (5.10) and shown in Figure 5.11 (blue line).

$$\text{unwrapping } \varphi_{i+1} = \varphi_{i+1} + \text{offset } \varphi_{i+1} \quad (5.10)$$

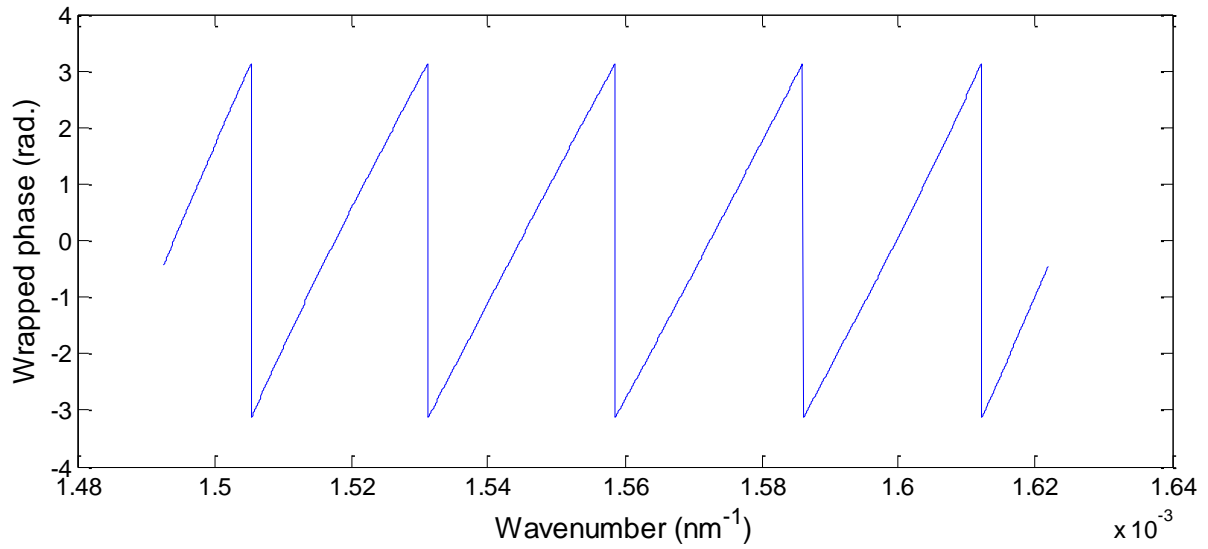


**Figure 5.9** Wrapped phase distribution with discontinuities (FFT algorithm)

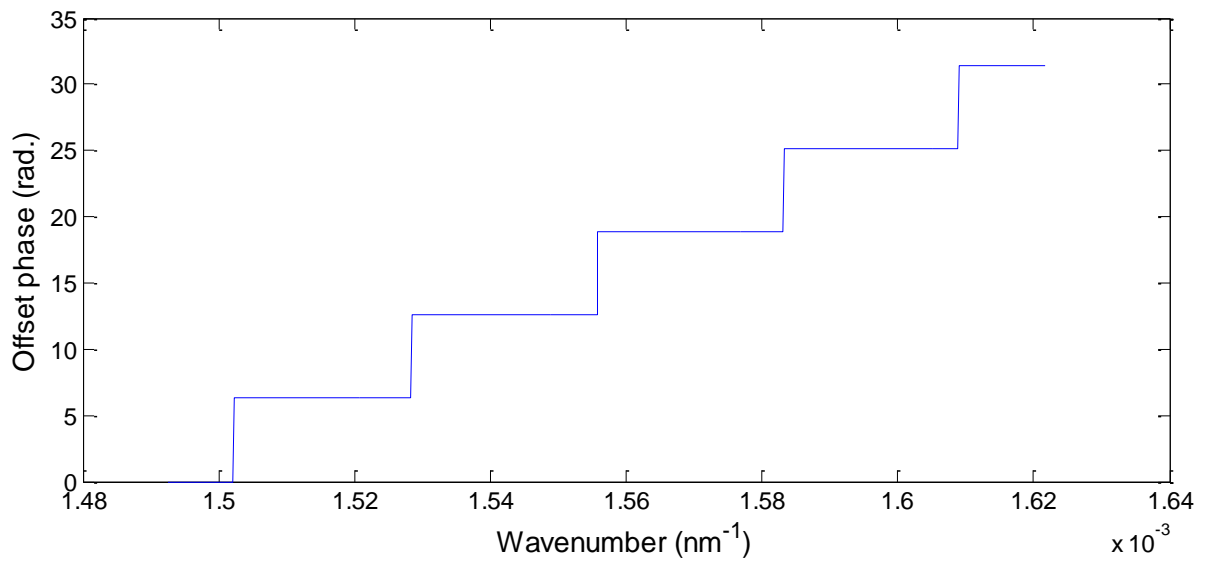


**Figure 5.10** The offset phase distribution for correcting the discontinuities

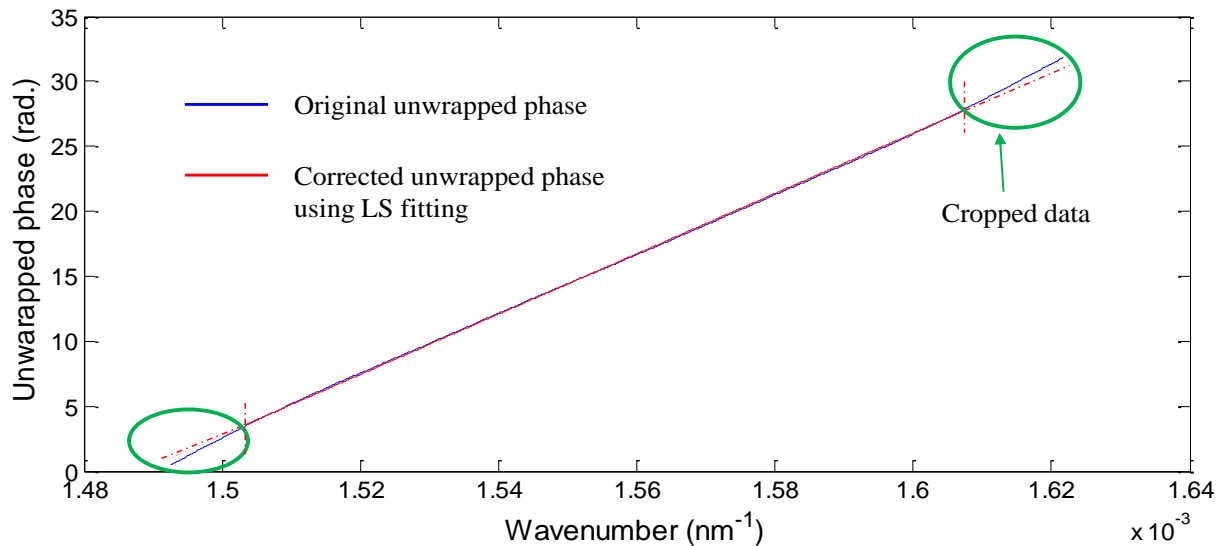


**Figure 5.11 Unwrapped phase distribution and its LS fitted curve (FFT algorithm)**

The unwrapped phase should be continuous without discontinuities and linearly related to the wavenumber. However, both ends of this obtained phase distribution suffer from the nonlinear deviations due to the effect from the selected window for filtration- spectral leakage (Harris, 1978). It will generate errors over the measurement surface profile and therefore limit the measurement resolution. Two steps can be adopted to overcome this issue and accurately retrieve the phase information. The first step is cropping the distorted data at both ends and keeping the middle part for phase calculation. It is a simple way to reduce the measurement error. The second step is fitting the selected part of the phase curve. In the developed algorithm, least squares (LS) approach is utilised to fit the unwrapped phase with eliminating the noise appearing in the distribution and accurately calculating the phase slope (see the red curve in Figure 5.11).

#### **5.3.4.2 Carré algorithm**

The phase shifting algorithms are widely used for phase retrieval with high measurement resolution and accuracy. Carré algorithm is one of the phase shifting techniques using unknown and constant phase step. The principle of Carré algorithm has been described in many scientific papers (Carré, 1966; Malacara & Servin, 2005; Qian, 2001). Moreover, much work were also carried out to optimise Carré algorithm in terms of the accuracy and optimal phase step (Kemao et al., 2000; Van Wingerden et al., 1991). With the Carré technique the phase  $\varphi$  can be extracted

by modulating and registering the fringe intensity at four equally shifted positions  $(-3\alpha, -\alpha, \alpha, 3\alpha)$ , which can be expressed as

$$\tan \varphi = \frac{\sqrt{[3(I_2 - I_3) - (I_1 - I_4)][(I_2 + I_3) - (I_1 + I_4)]}}{(I_2 + I_3) - (I_1 + I_4)} \quad (5.11)$$

where  $I_1, I_2, I_3$  and  $I_4$  are the intensity values at four equally shifted positions,  $2\alpha$  is the phase amount for each shifting step.

There are four main steps to compute the phase using Carré algorithm. The signal in Figure 5.6(b) is again used as an illustration. First FFT is applied to the selected signal and the peak position of  $C(x, y; f - f_0)$  is localised in the Fourier domain, in which way the integer number of the interference cycles can be estimated. Secondly, assuming that the phase shifting step is determined as

$$2\alpha = N/6D \quad (5.12)$$

where  $N$  represents the total data points contained in the selected signal and  $D$  is the integer number of the interference cycles. Thirdly, unlike the FFT algorithm using IFFT to reconstruct the term related to the phase shifting, Carré equation (5.11) is adopted to calculate the phase value. Figure 5.12 shows the four data points designated to solve an ‘initial’ phase value. This process is repeated by shifting the calculation to the next adjacent pixel each time and finally a wrapped phase similar to Figure 5.9 is obtained, as shown in Figure 5.13.

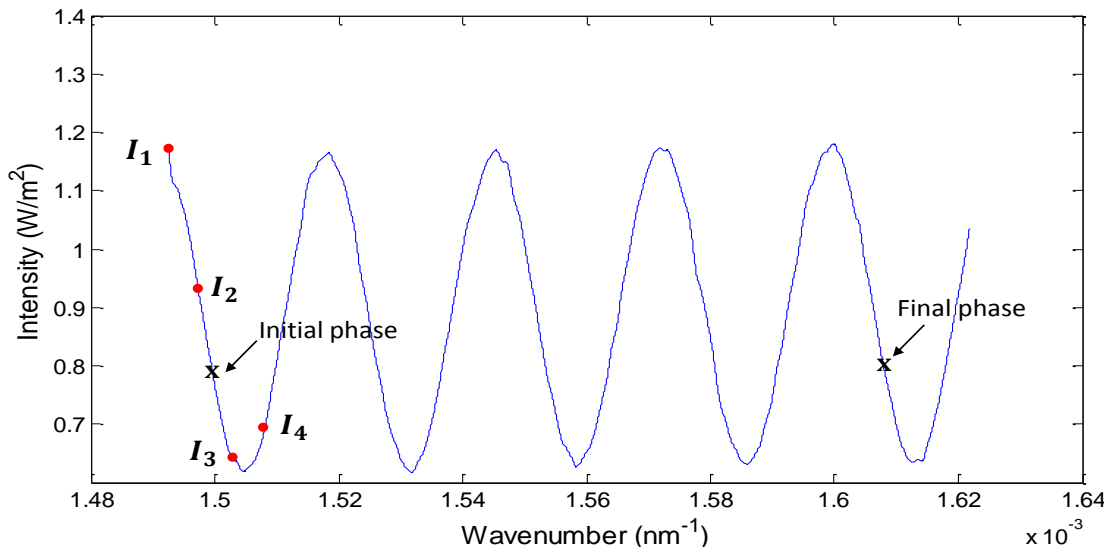
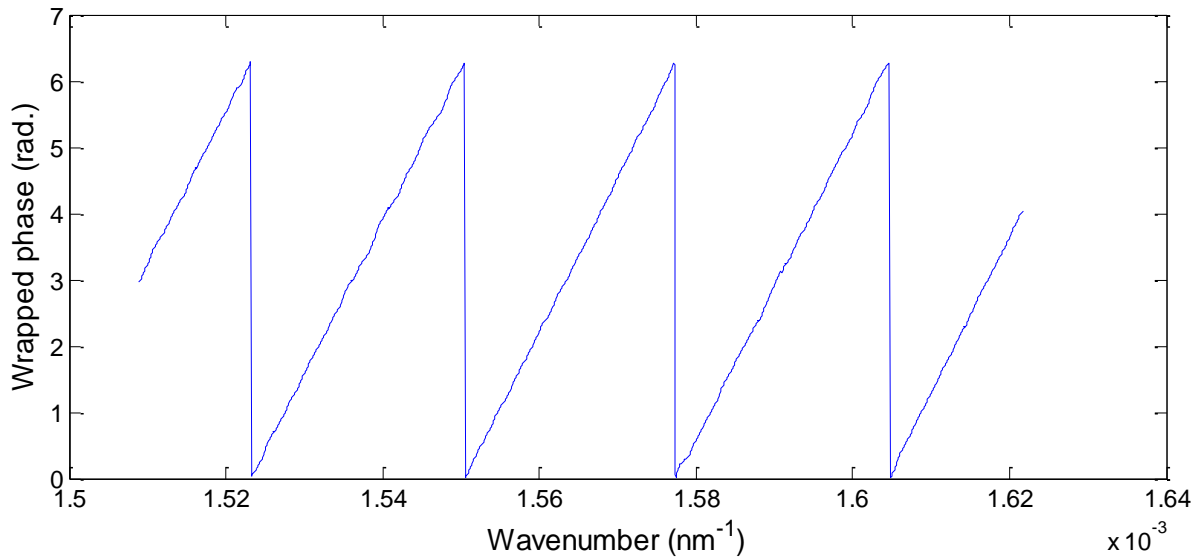
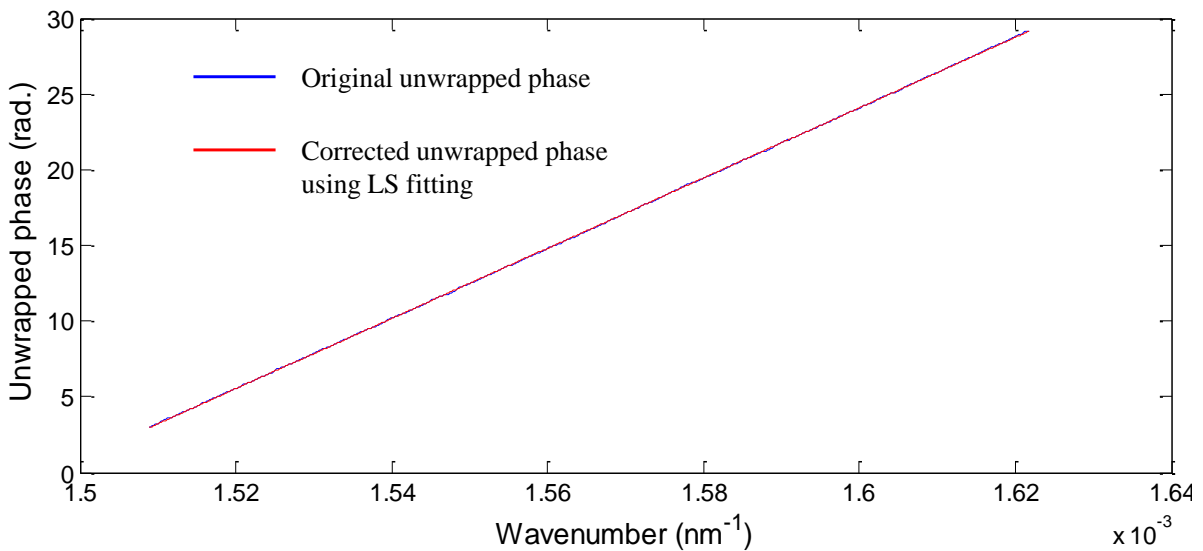


Figure 5.12 Spectral signal with shifted phases



**Figure 5.13** Wrapped phase distribution with discontinuities (Carré algorithm)



**Figure 5.14** Unwrapped phase distribution and its LS fitted curve (Carré algorithm)

The fourth step is performing phase unwrapping to achieve continuous phase distribution by detecting the phase offsets as illustrated above. The unwrapped phase distribution is depicted in Figure 5.14. Compared to the FFT based algorithm, there is no distortion at both ends of the phase distribution. Likewise, by combining the LS fitting approach, the developed algorithm can be robust against the error sources.

### 5.3.5 Height map of a one-dimensional profile

After the phase calculation, phase slope  $S$  of the unwrapped phase curve can be easily determined using the equation below

$$S = \frac{\Delta\varphi}{\Delta k} = (\varphi_e - \varphi_s) / (k_e - k_s) \quad (5.13)$$

where  $\Delta\varphi$  represents the phase difference corresponding to wavenumber shift  $\Delta k$ ,  $\varphi_e$  and  $\varphi_s$  are the phases corresponding to the wavenumber of  $k_e$  and  $k_s$ , respectively. The phase slope is related to the absolute OPD between the tested surface and reference plane. By using the phase slope obtained from equation (5.13), the height value ( $h$ ) can be calculated as

$$h = \frac{S}{4\pi} = \Delta\varphi [4\pi\Delta k]^{-1} = (\varphi_e - \varphi_s) [4\pi(k_e - k_s)]^{-1} \quad (5.14)$$

For the developed metrology devices in this research work, vertical axis of the spectral interferogram represents one-dimension of lateral resolution and each row signal registers the height information of one point. After processing all row signals in one single frame, the height map of a surface profile can be acquired.

The Matlab scripts for surface profile measurement (both FFT and Carré algorithm) are given in Appendix B.

### 5.4 Resolution of the algorithm

For a metrology system, the measurement precision can be affected by such factors as aberrations of the optical system, quantisation of the detector signal, nonlinear phase shifter, environmental disturbances and algorithms' computing resolution (Creath, 1988). The overall performance of measurement resolution is determined by the combined effect from all error sources. Resolution of the algorithm is investigated in this section. Both algorithms illustrated above can achieve highly accurate measurement, e.g., the measurement precision using Carré algorithm is less than  $\lambda/100$  for a well-calibrated interferometry instrument (Creath, 1988).

Detailed analysis about resolutions of the algorithms will not be discussed in this thesis in every aspect. The following mathematical description based on the equation for height value calculation is used to evaluate the measurement precision. As expressed in equation (5.14), the measurement resolution of the algorithm is determined by the phase variation and the corresponding wavenumber shift. The absolute error transfer function can be express as

$$\delta h = \left| \frac{\partial h}{\partial (\Delta \varphi)} \right| \delta \varphi + \left| \frac{\partial h}{\partial (\Delta k)} \right| \delta k \quad (5.15)$$

with

$$\delta \varphi = \frac{2\pi(F_n + \varepsilon)}{P_n} \quad (5.16)$$

and

$$\delta k = \frac{(k_e - k_s)}{P_n} \quad (5.17)$$

where the  $\delta h$  represents the height resolution and  $\partial$  denotes the partial differential operation;  $\delta \varphi$  and  $\delta k$  are the phase resolution and spectral resolution, respectively;  $F_n$  is the integer number of fringe cycles for the interference signal,  $\varepsilon$  is the remaining fraction of fringe cycles and  $P_n$  refers to the pixel number covered by the whole signal. Finally, equation (5.15) can be written as

$$\delta h = \frac{(F_n + \varepsilon)}{2P_n(k_e - k_s)} + \frac{(F_n + \varepsilon)}{2P_n^2(k_e - k_s)} \quad (5.18)$$

Compared to the number of fringe cycles,  $P_n^2$  is normally a much bigger number and thus the second term of equation (5.18) can be ignored. The height resolution is therefore given by

$$\delta h = \frac{(F_n + \varepsilon)}{2P_n(k_e - k_s)} \quad (5.19)$$

Suppose the fringes number of interference signal is 3.5 and the wavenumber spreads along the CCD pixels ( $P_n = 640$ ) with a range of  $0.3 \mu\text{m}^{-1}$ , then the height resolution can be calculated as 9 nm. The obtained resolution varies with the fringes number ( $F_n + \varepsilon$ ), which means that each row signal of the interferogram (or each point in surface profile) has a different resolution.

By accurately determining the phase slope, both the developed algorithms are effective for metrological applications with high accuracy. The FFT algorithm has better performance than the Carré algorithm in terms of insensitivity to intensity noise and processing speed, while Carré technique takes advantage of eliminating the spectral leakage problem. It was found that the measurement difference between the two algorithms is only 18 nm on average by measuring a standard step sample with height of  $4.707 \mu\text{m}$ , which is shown in detail in section 6.7.

## 5.5 Investigation of data parallelism using GPU

In-line surface metrology requires a matching measurement speed with the moving samples. The measurement time for a single frame contains times for image capturing and data processing. The processing time is particularly crucial for the overall performance of LSDI in terms of measurement speed. Based on the Matlab implementation of two algorithms, the sequential execution is performed using a quad-core AMD Phenom™ II processor with a clock rate of 2.5 GHz. Table 5.1 shows the processing times for two types of frames with different resolutions (pixels) using different algorithms (FFT & Carré, Matlab codes). It shows that the minimum time to interpret a spectral interferogram in sequential mode is 475 milliseconds (ms) in the case of 480 x 640 resolution. Considering that the camera used in this project has a capturing speed of 4.8 ms per frame, the processing time requires a further enhancement. Data parallelism using GPUs is investigated for this purpose.

**Table 5.1 Processing time for different frame size using different types of algorithms**

Frame size	Processing time for a single frame - Matlab codes (Unit: ms)	
	FFT algorithm	Carré algorithm
Pixels: 480 x 640	475.5	1384.1
Pixels: 960 x 1280	1610.2	6592.1

### 5.5.1 GPU and CUDA overview

With the challenging requirements for high-quality real time graphics, the programmable GPU has been developed into a powerful processor with tremendous computational power as well as high memory bandwidth (NVIDIA, 2015). The floating-point operation per second for CPU and GPU is depicted in Figure 5.15. It shows that Geforce 780 Ti has a theoretical computing power up to 5350 GFLOP/s, which is almost 7 times faster than the Intel CPU (Ivy Bridge). The GPUs has a dominant advantage over CPUs in the powerful computing capability because many-core trajectories in the GPUs are used to process the data in a parallel manner. The performance of data parallelism will be enhanced by increasing the number of processor cores. In conclusion, GPUs provide an attractive solution for data parallelism.

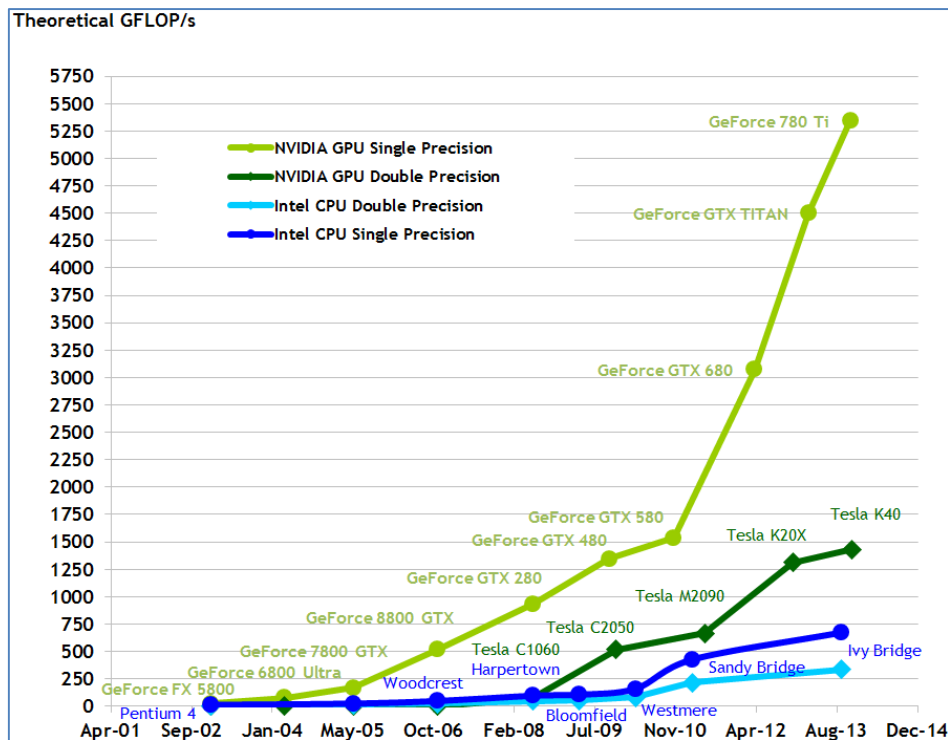


**Figure 5.15 Floating point operation per second for the CPU and GPU [adapted from NVIDIA, 2015]**

A parallel programming model called CUDA was created by NVIDIA in 2006 to provide a platform for scaling the data parallelism to many-core GPUs in various computation applications (NVIDIA, 2015). A CUDA program contains both host code and device code that are sequentially executed on the CPU and the GPU. The device code is composed with standard ANSI C extended with the keywords to designate data-parallel functions (kernels) and their associated structures (Kirk & Wen-mei, 2012; Ryoo et al., 2008). The general execution of a CUDA program is illustrated in Figure 5.16. It starts from the host execution and the kernel function will be launched with the execution of numerous threads on a device. More specifically, the construction inside a kernel is depicted as the thread hierarchy in Figure 5.17. The threads are grouped into blocks, which are logically aggregated into a grid (De Donno et al., 2010). Figure 5.17 illustrates the memory allocation as well. For every thread, it has a private local memory as well as a shared memory accessed by all threads within a block. Additionally, all threads launched by a kernel have access to the global memory and two read-only memories: the constant and texture memory spaces (NVIDIA, 2015). The global memory is off-chip and requires a certain latency time, therefore an optimal design of kernels should minimise the number of global memory reads (De Donno, et al., 2010).

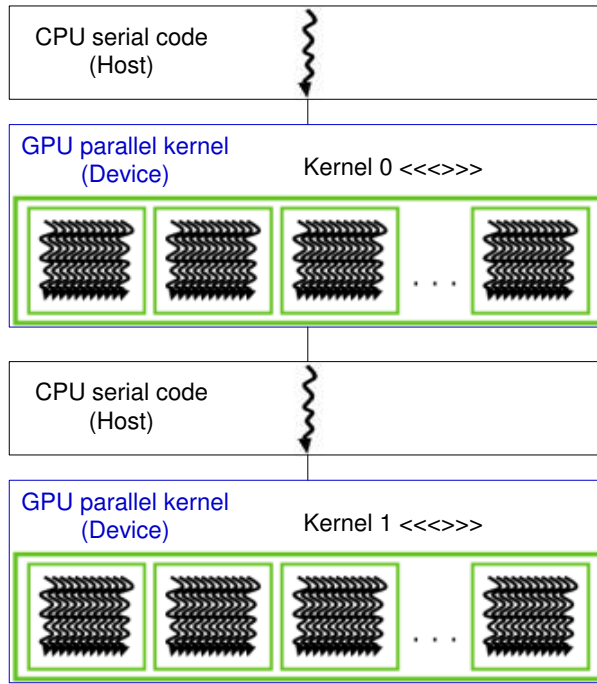


Figure 5.16 General execution of a CUDA program [adapted from Kirk & Wen-me, 2012]

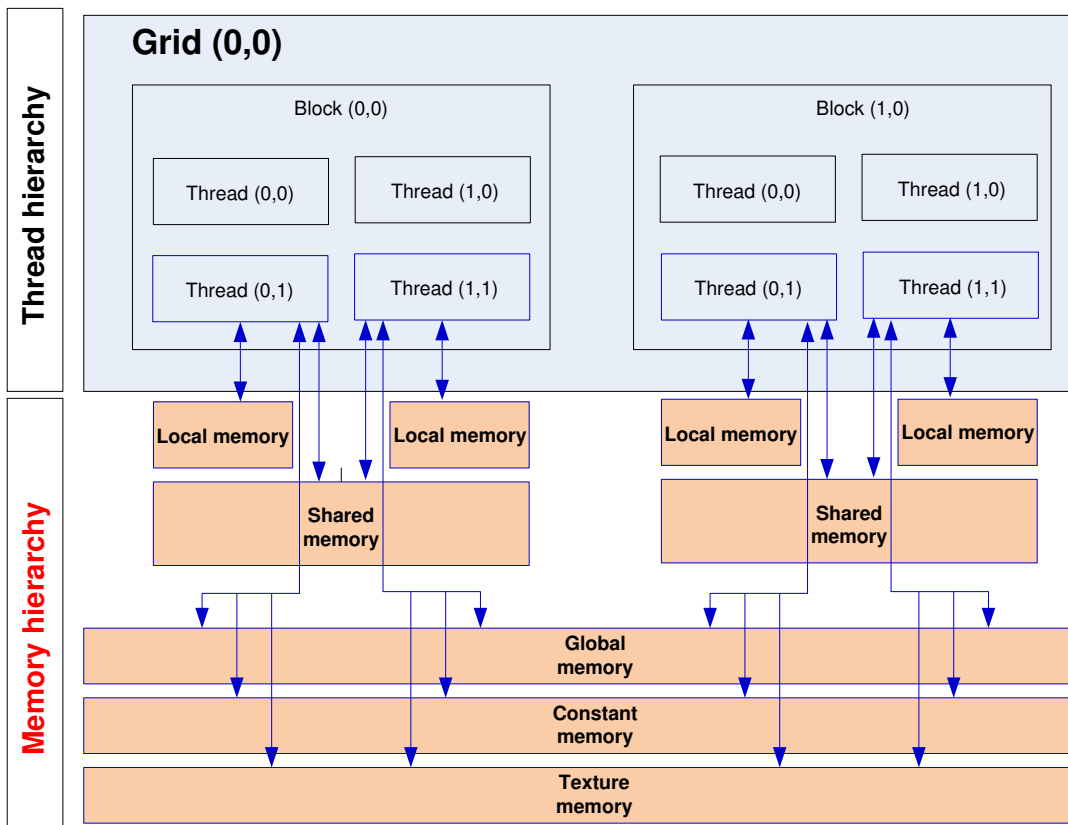


Figure 5.17 Thread hierarchy and Memory hierarchy [adapted from Muhamedsalih, 2013]

### 5.5.2 Data parallelism implementation for LSDI

To achieve real-time measurement on a production line, not only the capturing speed but also the computing speed is critical for this application. The frame rate of camera is limited by the current technologies in the field such as semiconductor, while the computing speed is influenced by the complexity of the algorithm. In order to obtain the surface profile from the obtained fringe pattern, the fringe analysis presented in section 5.3 should be applied to each row signal. Assuming the record spectral interferogram has a resolution of 480 x 640 (Height x Width) and the direction of tested profile is along the frame height, then the data processing needs to be executed 480 times in a sequential manner. The processing time could not be improved significantly even by compiling the algorithms with the C++ programming language (more than 300 ms).

Therefore, analysis of all pixels in one frame using GPU with CUDA C programming model was investigated. By generating thousands to millions of threads, data parallelism has great potential to accelerate the process time for the developed LSDI.

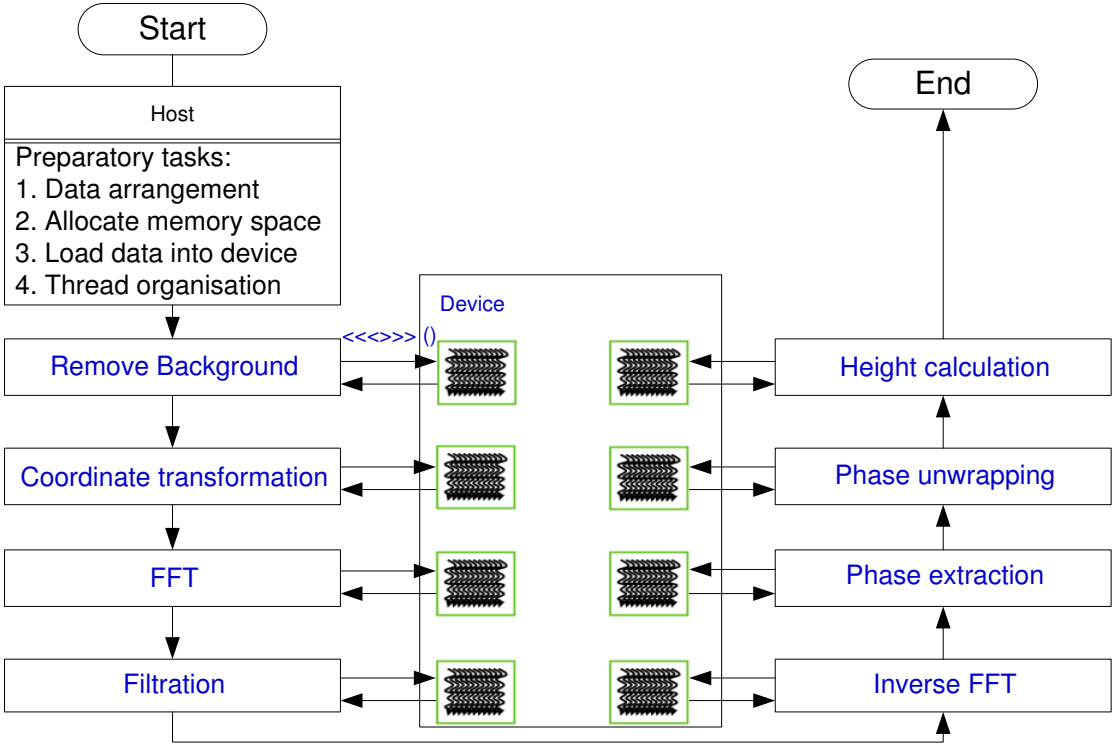


Figure 5.18 The CUDA program structure of FFT algorithm

The FFT algorithm was selected for parallel programming and the CUDA structure is illustrated in Figure 5.18. By equipping an GPU (GeForce GTX 285) available in our laboratory to the same computer using for execution of Matlab program, the developed CUDA program was tested to investigate the acceleration of the computing process. The processing time took the average value of 100 execution cycles for the same program, which then gives the results of 125 ms for a single frame with resolution of 480 x 640 and 453 ms for 960 x 1280, as shown in Table 5.2. It shows that an acceleration factor approximately 4 is achieved when processing a single frame using GPU. Enhanced algorithms, optimal organisation of threads and updated hardware (GPUs and CPUs) will further enhance the acceleration factor. Though data parallelism using GPUs can improve the processing time for each interferogram, its advantage compared to the sequential analysis will be reflected better when an image with higher resolution (large data points) is processed or many frames are analysed at the same time.

**Table 5.2 Parallel programming performance (based on FFT algorithm)**

<b>Frame size</b>	<b>Pixels: 480 x 640</b>	<b>Pixels: 960 x 1280</b>
<b>Matlab processing time (ms)</b>	475.5	1610.2
<b>CUDA C processing time (ms)</b>	125	453
<b>Acceleration factor</b>	3.8	3.6

## 5.6 Summary

This chapter introduces the fringe pattern obtained by the LSDI probe, which registers the height information into a 2D spectral interferogram. The algorithm used to interpret the captured interferogram is divided into five steps, namely background removing, wavelength calibration, coordinate transformation, phase extraction and height calculation. The first two steps are only performed when the metrology sensor is used for the first time, unless a new light source with a different spectral distribution is used for system illumination.

Both of the two algorithms using FFT method and Carré method, distinguishing from each other in phase extraction, can provide accurate measurement result. FFT algorithm is shown to be insensitive to intensity noise and can perform precise measurement even when the visibility of fringes is low. Carré algorithm can overcome the spectral leakage problem existing in the FFT method. The computing speed is influenced by the complexity of the algorithms. Carré algorithm

is relatively slower than FFT algorithm because many loops in terms of phase shifting needs to be performed to extract the phase variation from each row signal. The measurement times for a single frame using Matlab codes are 475.5 ms and 1384.1 ms corresponding to the FFT method and the Carré method in the case of 480 x 640 resolution.

The computing speed can be further improved by replacing the sequential analysis mode with data parallelism mode. Utilisation of GPU can be an effective way to accelerate the execution time of arithmetic calculation with floating point operation. The test results show that the execution time for a single interferogram can be accelerated with a factor of approximately 4. The enhanced data processing consequently shows the great potential for the LSDI to be qualified for in-line surface inspection.

Considering the overall performance of the algorithms and the high measurement speed required by in-line metrology, the measurement results in the next two chapters will be given using FFT algorithm.

# 6 Optical apparatus 1: Cylindrical lens based LSDI

## 6.1 Introduction

Based on the fundamental principle of LSDI illustrated in chapter 4, two optical systems utilising different objectives have been developed. This chapter reports a cylindrical lens based LSDI (hereinafter referred to as cylindrical-LSDI), which observes the tested surface through a line focus. The optical schematic diagram is shown in Figure 6.1. The measurable length of the surface profile (or lateral measurement range), determined by several factors such as the NA of the illumination system and the size of sensor for receiving the image, is up to 5.885 mm. The basic methodology is briefly reviewed and the measurement operations are introduced. Then the initial prototype is described along with several key issues. Finally the performance of the metrology device is evaluated using a flat artefact and step samples. This cylindrical-LSDI device aims at long surface profile measurement in production lines and may potentially be used for characterisation of additively manufactured surface textures, surface form and blemishes present on the functional surface.

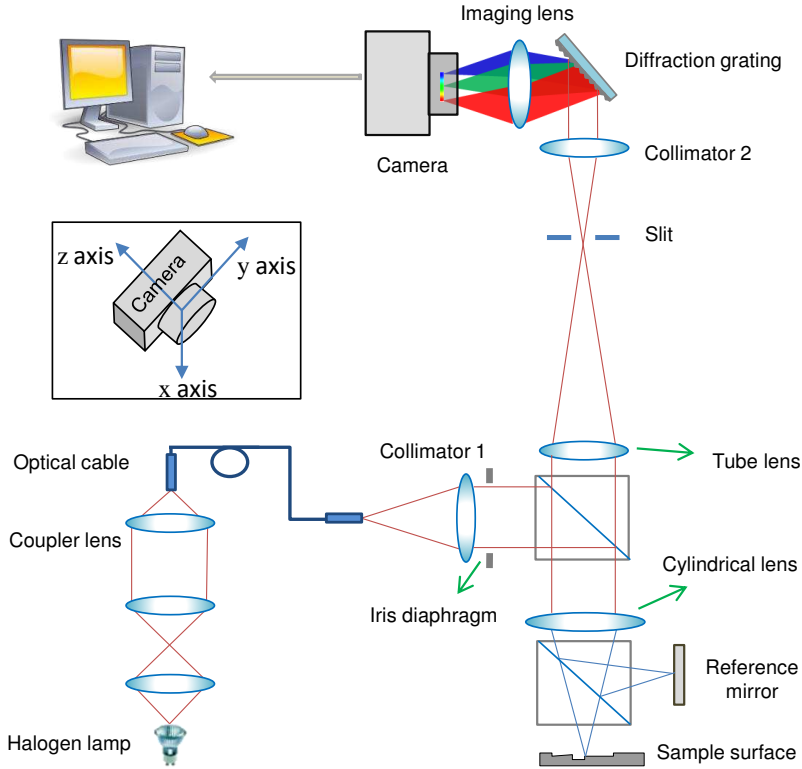
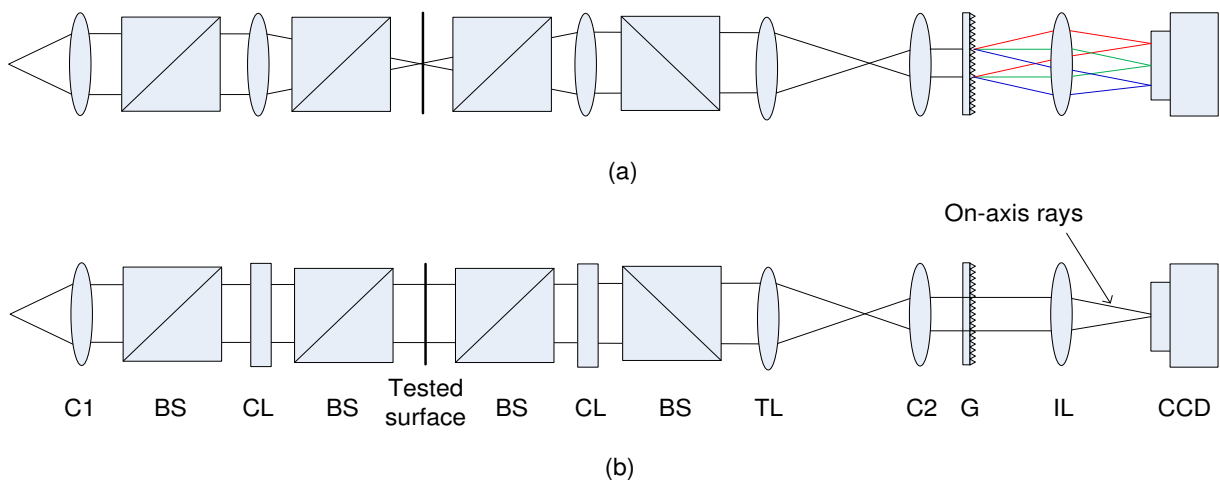


Figure 6.1 Schematic diagram of cylindrical lens based LSDI

## 6.2 Methodology of long profile measurement

The white light beam generated by the light source device is coupled into a multi-mode optical fibre and then collimated by a collimator. An achromatic cylindrical lens is employed to construct the Michelson interferometric probe. Therefore, a line-shape probing beam is generated on the tested object enabling a long surface profile to be sampled in each measurement. A local coordinate system is defined with x axis parallel to the line illumination along the measured profile (vertical), y axis perpendicular to the line focus (horizontal), and z axis representing the propagation direction of light (optical axis). The beams on both reference plane and tested surface are thus focused on the y-z plane without any effect on the x-z plane. Figure 6.2 shows the perspectives of the proposed system on y-z plane and x-z plane.

Interference occurs when two light beams reflected from the reference arm and the measurement arm are brought together and the interference beam is focused by a spherical tube lens. Instead of being directly received by a camera, the interference signal is introduced to the spectrometer and dispersed by a holographic grating. The direction of the slit is set to be parallel to the columns of CCD pixels (x axis), so that the dispersion axis is along the rows (y axis). The spectral interferogram recorded by the detector therefore registers the height information in two-dimension, namely lateral information in x direction and chromaticity information in y direction. The 2D surface profile, mathematically represented as height information with lateral displacement along x direction, can be acquired by processing a single frame without any mechanical scanning.



**Figure 6.2 Perspectives of the optical setup: (a) y-z plane (horizontal), (b) x-z plane (vertical). C1, collimator 1; BS, beamsplitter; CL, cylindrical lens; TL, tube lens; C2, collimator 2; G, grating; IL, imaging lens.**

When a scanning is applied in  $y$  direction, translating the tested sample with a linear motorized stage, in-line surface inspection can be simulated and the metrology can be extended to the areal surface topography. The sampling interval along the direction perpendicular to the measured surface profile is determined by the capturing time of a single frame and the scanning speed. Additionally, it should be noted that in this experimental study the acquired surface topography is constructed by numbers of independent surface profiles. Due to the non-linearity errors of the stage, it is generally not accurate to parameterise the constructed surface area and make a comparison with the results by an areal measurement technique.

### **6.3 Measurement procedure**

The measurement procedure of LSDI is simple. If the optical metrology system is first used, preparations are required in terms of background issue, wavelength calibration and calibration of lateral measurement ranges for different objectives. For a well aligned LSDI system, wavelength calibration as presented in chapter 4 only needs to be carried out once. Likewise, only one frame without interference effect is required to remove the background for an encapsulated setup. The data matrix extracted from the background frame is saved and directly called by the algorithms for each measurement. Lateral measurable ranges of the equipped objectives can be calibrated using the standard artefact, which will be presented in detail in the section 6.6.

When performing measurements, the tested sample is placed underneath the objective. By manually translating the linear stage, the sample can closely be brought to the focal plane. Adjusting the tip/tilt of the sample mount, zero fringes can be viewed on the camera when the tested surface plane coincides with the virtual reference plane. However, it was demonstrated by reduplicative experiments that better results were achieved when up to three fringes exist across the full measurement field. Therefore, a certain OPD is introduced between the two arms of the interferometer to generate several fringes in the spectral interferogram. At this position the frames are captured and then analysed by an appropriate algorithm. Actually, the shape of the fringe pattern generally provides information about the structures on the tested surface, e.g., the fringe numbers are apparently different for the two surfaces of a step height (see Figure 5.1). When the lateral scanning in  $y$  direction is available and the working mode of the camera is set to continuous capturing, fast inspection of the sample surface in motion can be achieved.

## 6.4 Validation of the experimental setup

### 6.4.1 Experimental conditions

An experimental setup was first built to verify the measurement methodology before the prototype design. The commercially available optical components, as shown in Table 6.1, were used to establish the optical setup. The CCD camera used has a maximum resolution of 480 x 640 pixels and can record the interferogram with a frame rate of 208 fps in normal working conditions. It means that only 4.8 milliseconds are required to capture one frame corresponding to the height information of a surface profile. Two types of sample surfaces, namely step height surface and flat surface, had been measured using this optical setup. Apart from the surface profile measurement, in-line surface inspection was simulated as well by translating the tested samples. Suppose the measured sample on a production line moves at a constant speed  $v$  in the direction perpendicular to the measured profiles and the frame rate of the CCD camera is  $f$  fps, then the real-time surface inspection has a sampling interval  $\Delta y$  as follows

$$\Delta y = v / f \quad (6.1)$$

For the established instantaneous measurement system, a surface profile with length up to 5.45 mm was finally imaged on the camera with 220 rows, which means the lateral sampling resolution is 24.8  $\mu\text{m}$  in the profile direction. The scanning speed of the tested sample was set as 1.5 mm/s to achieve characterisation of surface features with a size of around 7.2  $\mu\text{m}$  in  $y$  direction. The wavenumber  $k$  spreads along the chromaticity axis in a range of 1.57  $\mu\text{m}^{-1}$  to 1.82  $\mu\text{m}^{-1}$ . The FFT algorithm was used to process the spectral interferogram in this validation procedure. A total of 694 frames (corresponding to 694 profiles) have been captured to construct the surface topography of the tested surface, which represents a scanning length of 4.99 mm. The constructed surface maps by LSDI are provided in the following experiments as the simulation results of the in-line surface inspection.

Moreover, the corresponding results of the same measurement area using the commercial instrument Talysurf CCI 3000 (a Coherence Correlation interferometer from Taylor Hobson) were also provided for reference. The 5X and 20X interferometric objective of CCI offer measurement areas of 3.6mm x 3.6 mm and 0.9 mm x 0.9 mm, respectively.

**Table 6.1 Details of the off-the-shelf components used in experimental setup**

Components	Model	Suppliers	Main parameters
Collimator 1	ACY254-030-A-ML	Thorlas, Inc.	f = 30 mm, Ø1" Achromatic doublet
Cylindrical lens	ACY254-075-A-ML		f = 75 mm, Ø1" Achromatic doublet
Tube lens	RMS4X	Olympus	f=45 mm, NA=0.1, Achromat Objectives
Collimator 2	AC254-050-A-ML	Thorlas, Inc.	f=50 mm, Ø1" Achromatic Doublet
Diffraction grating	GH25-12V		Visible Reflective Holographic Grating, 1200/mm, 25 mm x 25 mm x 6 mm
Imaging lens	AC254-045-A-ML		f=45 mm, Ø1" Achromatic Doublet
Optical fibre	M28L02		Core diameter Ø400 µm, 0.39 NA
Camera	ICL-B0620	Imperx	Resolution 480 x 640, 7.4 µm pixel size, 208 fps.

#### 6.4.2 Measurement of step heights samples

Two reference step height samples were measured to assess the performance of the established system, and both profile and constructed surface map results were provided for surface evaluation. The first standard sample from Wyko has a single step calibrated with a height of 9.759 µm. Figure 6.3 shows the recorded fringe pattern of the tested surface. Figure 6.4 and Figure 6.5 depict the measurement results acquired by the LSDI setup and Talysurf CCI, respectively.

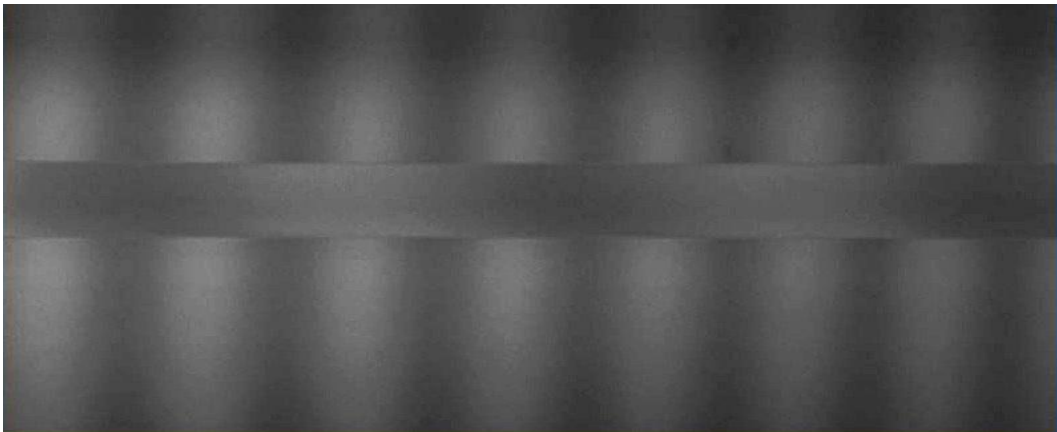


**Figure 6.3 Spectral interferogram of the 9.759 µm step sample**

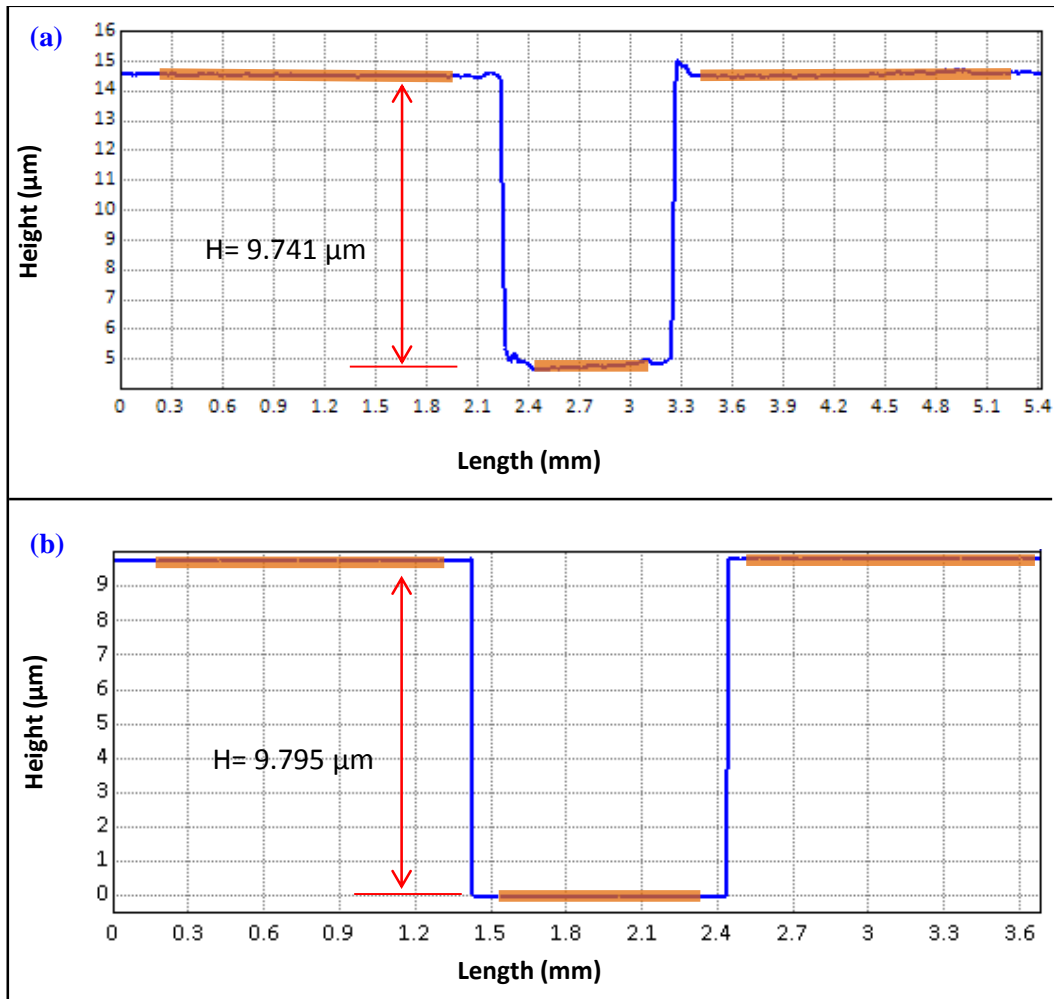


Figure 6.4 Cross-sectional profile results of 9.759  $\mu\text{m}$  step sample: (a) the LSDI result, (b) the CCI result.

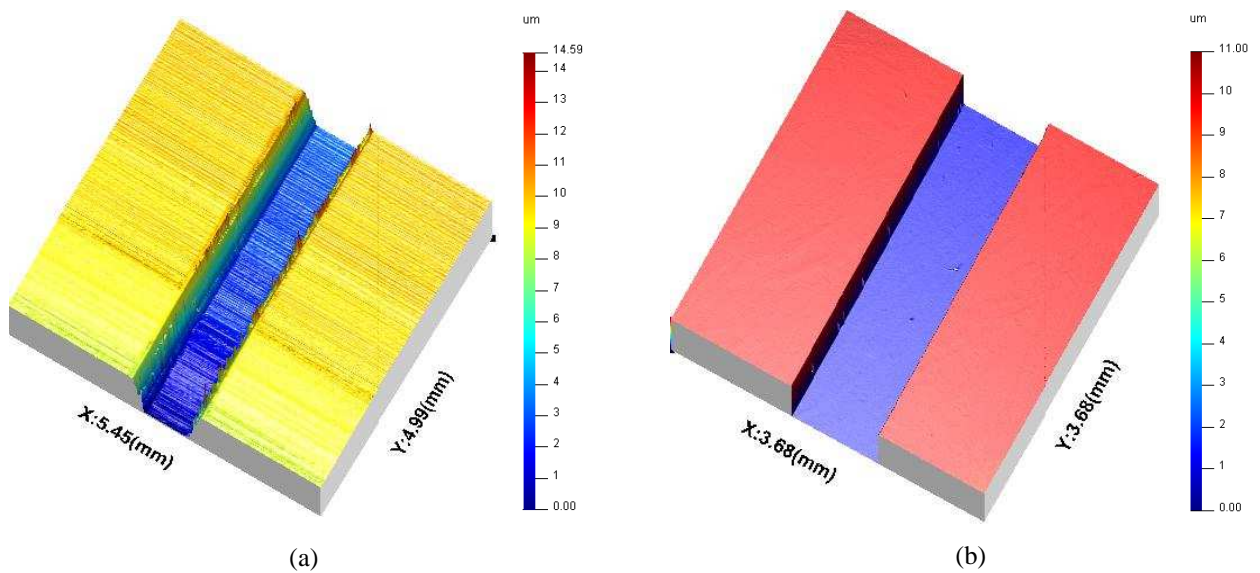


Figure 6.5 Measured surface maps of the 9.759  $\mu\text{m}$  step sample: (a) the LSDI result, (b) the CCI result.

As discussed in previous sections, LSDI produces surface profile results in each measurement, as shown in Figure 6.4 (a). By mechanically translating the sample, a surface map in Figure 6.5(a) was constructed. The surface irregularities along the y axis result from the scanning errors and have no effect on the evaluation of the surface profile. For the CCI instrument, it offers areal measurement for each measurement (see Figure 6.5(b)). Figure 6.4(b) shows one of the cross-sectional profiles of the surface map.

The second reference sample (see Figure 6.6) was manufactured by Rubert & Co. Ltd., which has four grooves with different heights and widths. The fringe pattern of the 30  $\mu\text{m}$  step height is shown in Figure 6.7. The distorted fringes also provide information about the surface finish of the sample, which is obviously not good as the first standard sample. The iris diaphragm in the built setup was adjusted to crop the low-visibility fringes at both edges of the spectral interferogram to avoid measurement errors. Therefore, the sampling length on the tested surface was reduced to 4.44 mm (corresponding to 180 pixels). The measurement results of the 30  $\mu\text{m}$  step height using both the LSDI and CCI are depicted in Figure 6.8 and Figure 6.9.

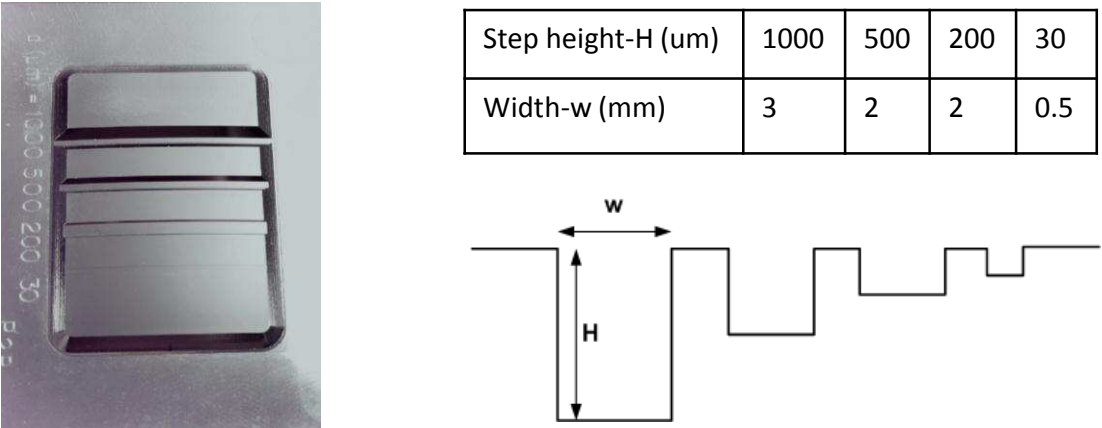


Figure 6.6 Step heights sample from Rubert & Co. Ltd.

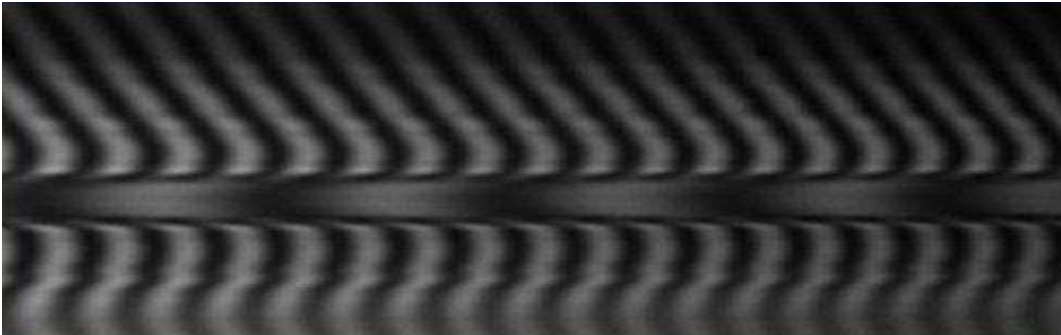


Figure 6.7 Spectral interferogram of the 30  $\mu\text{m}$  step sample

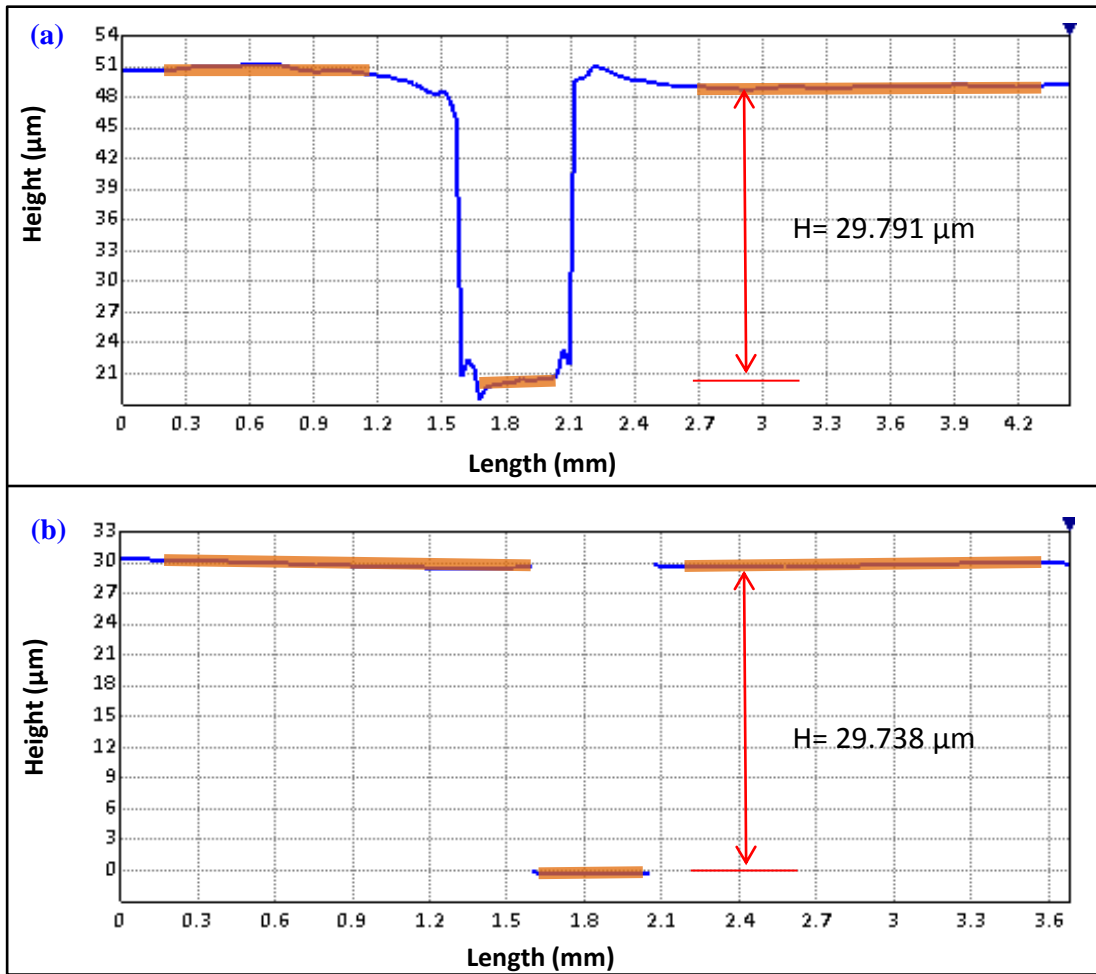


Figure 6.8 Cross-sectional profile results of 30 μm step sample: (a) the LSDI result, (b) the CCI result.

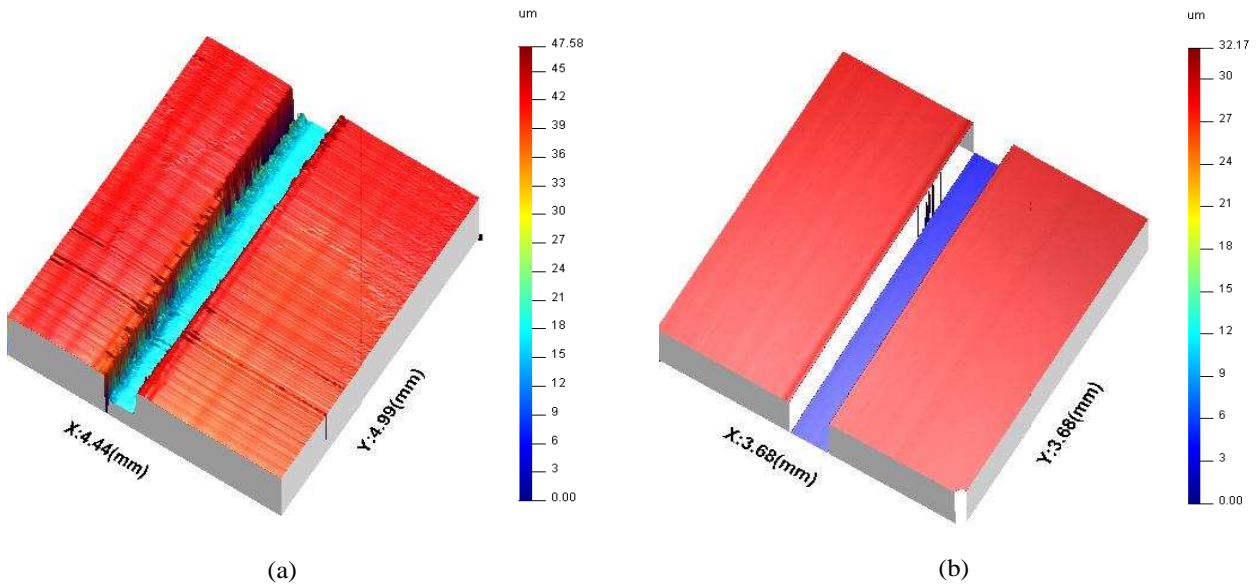


Figure 6.9 Measured surface map of the 30 μm step sample: (a) the LSDI result, (b) the CCI result.

For these two measured step samples, the mean values of the cross-sectional profiles in the interest of region were calculated and listed in Table 6.2.

**Table 6.2 Measurement results of two step heights samples**

Measurement samples	Mean value of one of the cross-sectional profiles ( $\mu\text{m}$ )		Mean value of the surface area-3.6mm x 3.6mm ( $\mu\text{m}$ )	
	LSDI	CCI	LSDI	CCI
9.759 $\mu\text{m}$ step sample	9.741	9.795	9.785	9.792
30 $\mu\text{m}$ step sample	29.791	29.810	29.797	29.738

The relative errors of the measurements can be calculated by

$$e_r = \frac{|h_m - h_t|}{h_t} \times 100\% \quad (6.2)$$

where  $h_t$  represents the reference value,  $h_m$  denotes the measured value and  $e_r$  is the relative error. To approximately evaluate the measurement accuracy, the  $e_r$  values for the above-mentioned measurements were calculated assuming that the height values provided by the Talysurf CCI were the reference values, as shown in the Table 6.3. Different materials and manufacturing processes generate different surface properties and may affect the measurement results, which is one of the reasons why the Rubert electroformed reference sample has a relatively higher relative error than that of the Wyko sample.

**Table 6.3 Relative errors of measurement**

	Wyko sample (9.759 $\mu\text{m}$ )	Rubert sample (30 $\mu\text{m}$ )
$h_t$ ( $\mu\text{m}$ )	9.792	29.738
$h_m$ ( $\mu\text{m}$ )	9.785	29.797
Relative errors $e_r$	0.07%	0.2%

On the whole, the measurement results obtained from the experimental setup closely align with the calibrated specifications given by the manufacturer as well as the measurement results by the commercial instrument CCI 3000, which verifies that cylindrical-LSDI has sufficient

resolution to inspect the surface over a large range. The following section will further demonstrate the experimental system in terms of detecting the defects on a flat mirror surface.

**6.4.3 Inspection of the flat surface**

In this section, inspection of a protected gold mirror surface (PF10-03-M01, Thorlabs) using the bench LSDI is presented. The measured mirror has a flatness less than  $\lambda/10$  (@ 633 nm), which was approximately validated through the peak-valley (PV) value of the surface profile measured by LSDI. As shown in Figure 6.10, the PV value is 35 nm and falls within the scope of the given flatness.

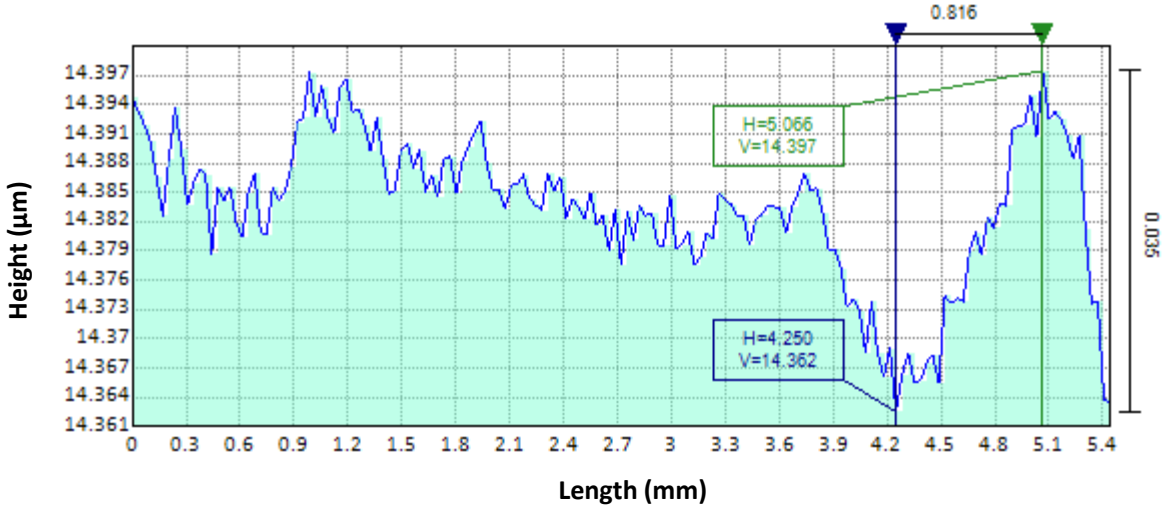


**Figure 6.10 Surface profile measurement of the mirror surface**

When an artificial scratch present on the mirror is within the FOV of the optical probe of LSDI, it can be detected with the deformed fringe pattern across the spectral interferogram, as shown in Figure 6.11.

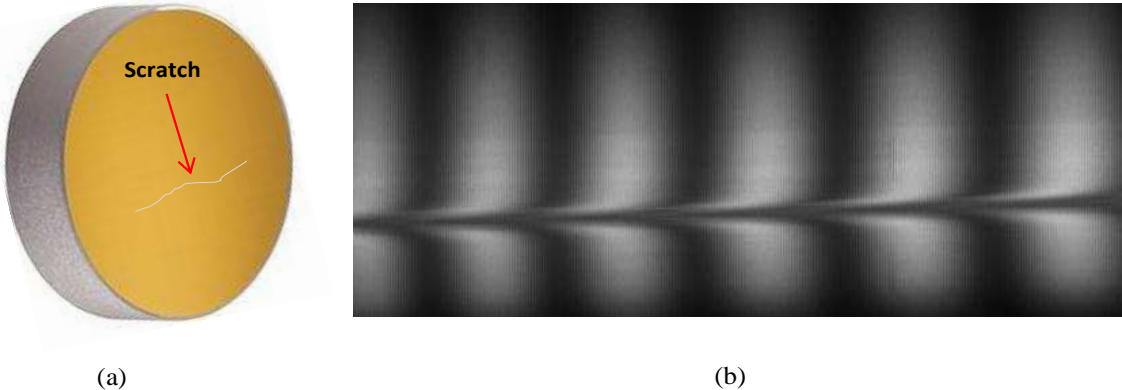
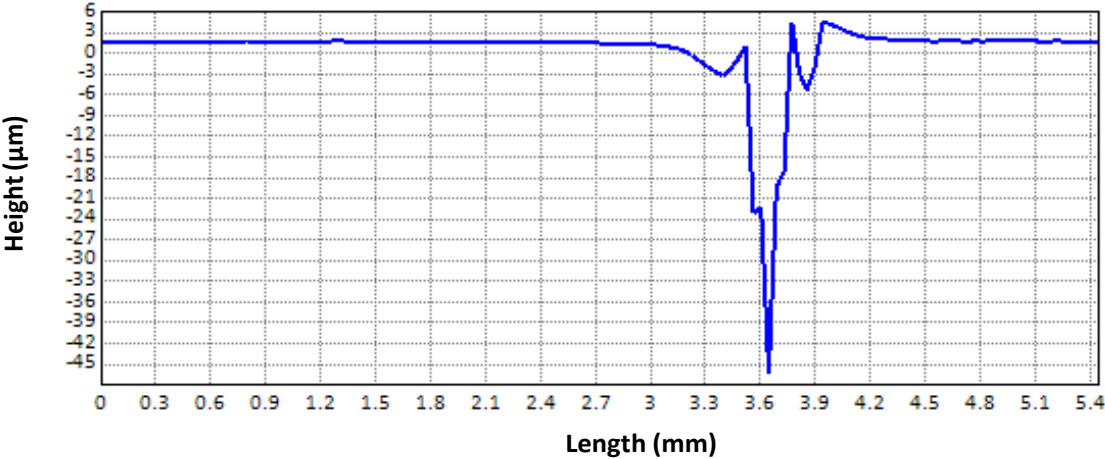
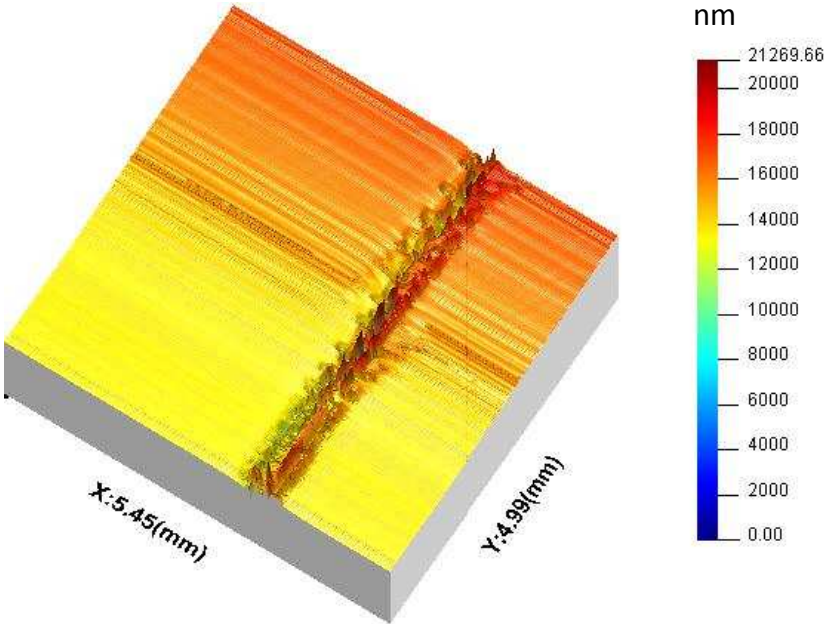


**Figure 6.11 A defective mirror and the corresponding fringe pattern**

Figure 6.12 shows the surface inspection results in terms of the scratch. The dramatic drop in the surface profile indicates the location of the defect on the tested surface. The acquired measurement results of the defective mirror further demonstrated that the LSDI has potential to be applied to surface inspection on production lines where only defects on the workpieces are concerned in terms of process control.



(a)



(b)

Figure 6.12 Surface inspection results of the defective mirror with a scratch: (a) cross-sectional profile, (b) measured surface map.

## 6.5 Prototype implementation

### 6.5.1 Key points of design

The methodology of LSDI has been verified by establishing an experimental setup on the optical table and measuring three typical samples, which offers a good basis for the prototype design. Though a good performance of the bench setup has been achieved, several key points of design still need to be clarified before implementation of the proof-of-concept prototype. First of all, it is important to mention that for the bench setup the illuminated line beam on the measured surface was finally imaged on the camera within 220 pixels (total number: 480), which means a low pixel utilisation as well as a low lateral sampling resolution along the surface profile (24.8  $\mu\text{m}$ ). It may be an issue when the smaller defects or structure features need to be characterised. In order to improve the lateral resolution, the optical system of the interferometer has been optimised such as adjusting the focal lengths of some optics components to acquire a sufficient magnification on the camera. More specifically, a tube lens with a longer focal length (75 mm) has been used and the focal lengths of both doublets in the spectrometer part are set as 60 mm. After the adjustment, the interference beam can cover the full frame of the camera. The calibration of the FOV of the metrology system will be presented in section 6.6.1.

Secondly, attention should be paid to the location of the slit because the structures on the sample may not be well resolved unless the slit is properly placed. The slit is used in the spectrometer to block the light that is redundant for measurement and its ideal position should be the focal plane of the tube lens. However, due to the different magnifications between x axis and y axis of the cylindrical lens, optical aberrations and alignment errors, the interference beam is focused by the tube lens with slightly different magnifications in the tangential plane and sagittal plane of the optical system. The optical software ZEMAX was used to study this issue, as illustrated in Figure 6.13. In simulation, several detectors were set after the tube lens at different positions. The shape of rays density in the spot diagram roughly shows that the best focal plane in x axis and y axis are not at the same position. For a further demonstration, the simulated Root-Mean-Square (RMS) spot size along x and y directions at different defocus positions were recorded (see Appendix A.2) and depicted in Figure 6.14. The simulation results show that the spot sizes in x axis are always bigger than the corresponding sizes in y axis and there is a certain deviation between the focal planes in these two orthogonal directions. Since the LSDI measures the surface

profile along x axis, the slit should be set at the tangential focal plane of the optical system to resolve the features on the sample surface.

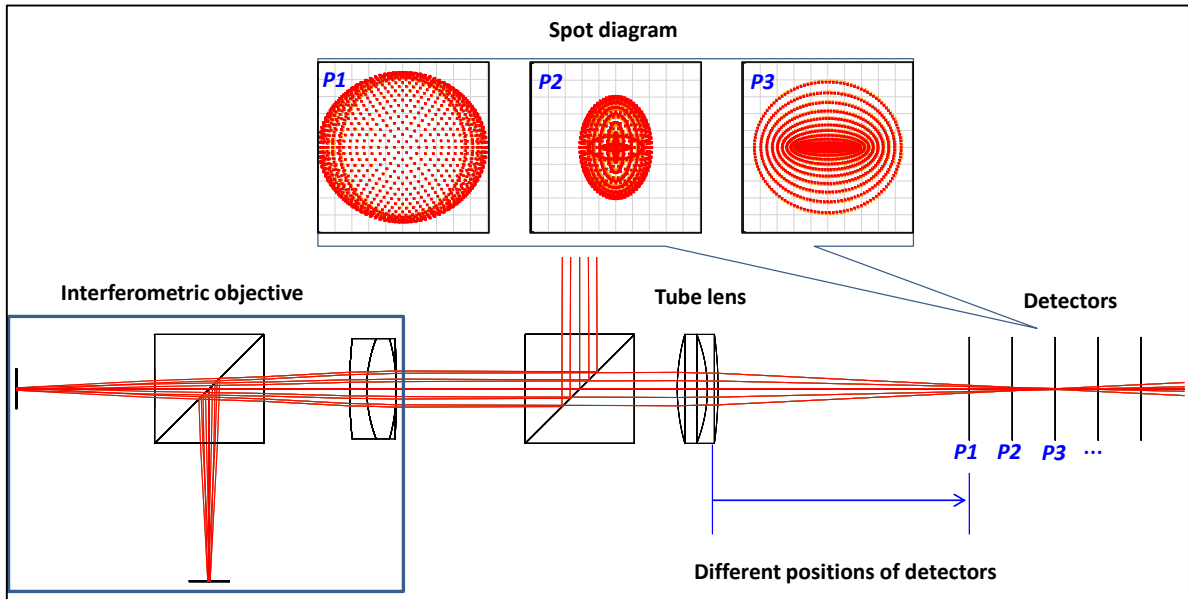


Figure 6.13 Study of spot shape using ZEMAX simulation

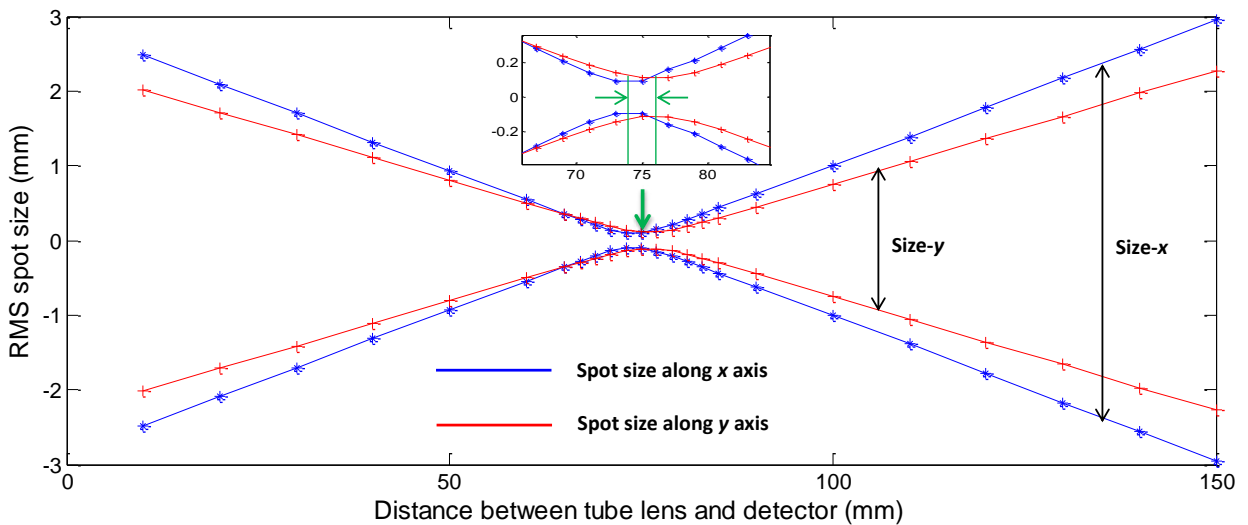


Figure 6.14 Different spot sizes in x and y axis

Thirdly, alignment errors may produce great influence on the overall performance of the system. Excepting that the interferometric objective should be properly aligned as illustrated in chapter 4, alignments of the optical components in spectrometer are also crucial. As the simulation shown in Figure 6.15, the location error of collimator 2 makes the beam unparallel and impinged upon the grating with an angle with respect to the normal axis of the grooves,

which consequently results in the distortions of spectral lines on the camera. The experimental result of three distorted spectral lines captured by the camera (see Figure 6.16) is in accordance with the simulation result in Figure 6.15. Actually, replacing this spherical collimator with a cylindrical lens to collimate the light only in the sagittal plane can also effectively improve the lateral resolution along the profile direction. However, it suffers from the same problem as the misalignment of the collimator (distorted imaging on the camera), which on the whole makes it not a good solution at all.

Additionally, misalignments such as inaccurate tip/tilt of the camera and the relative distance between camera and imaging lens will lead to either low fringe visibility (Figure 6.17(a)) or overlapping of the spectral lines (Figure 6.17(b)). Maximum fringe visibility in the full FOV of the optical probe and sharp image of spectral lines are two criteria for a good alignment of the camera. As shown in Figure 6.17(c), the two spectral lines in Figure 6.17(b) are well separated by properly adjusting the position of the camera.

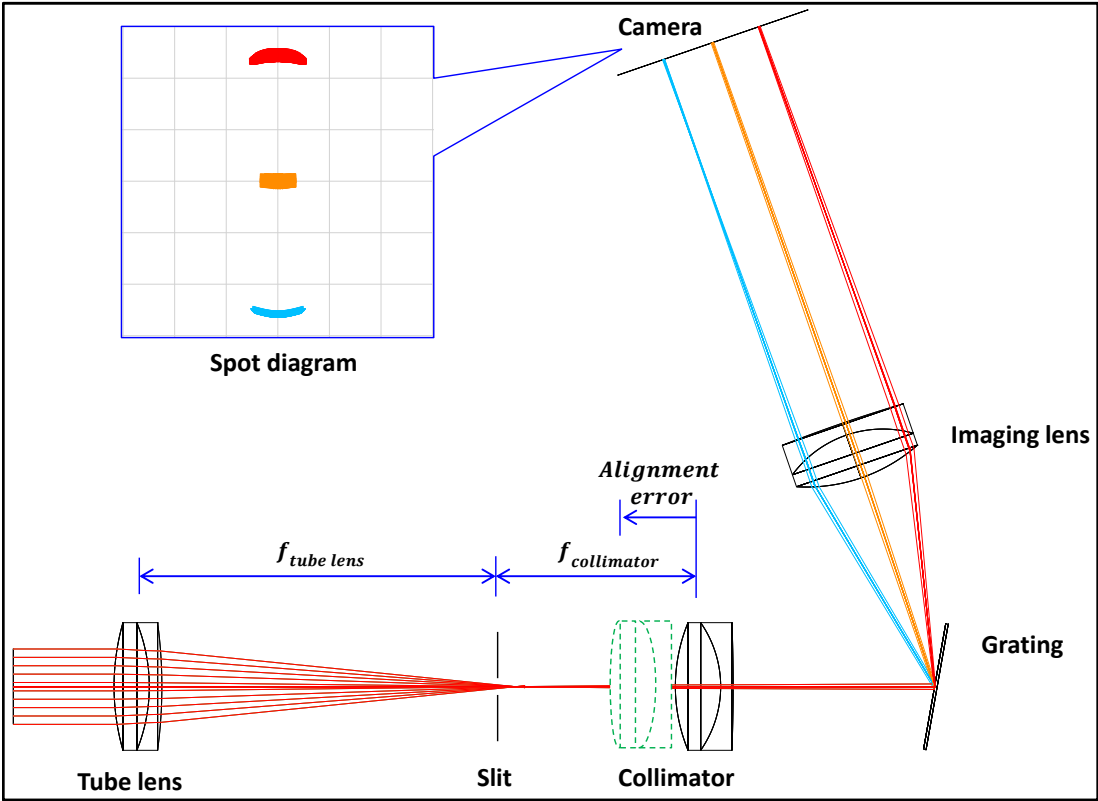


Figure 6.15 Effect resulting from the misalignment of the collimator

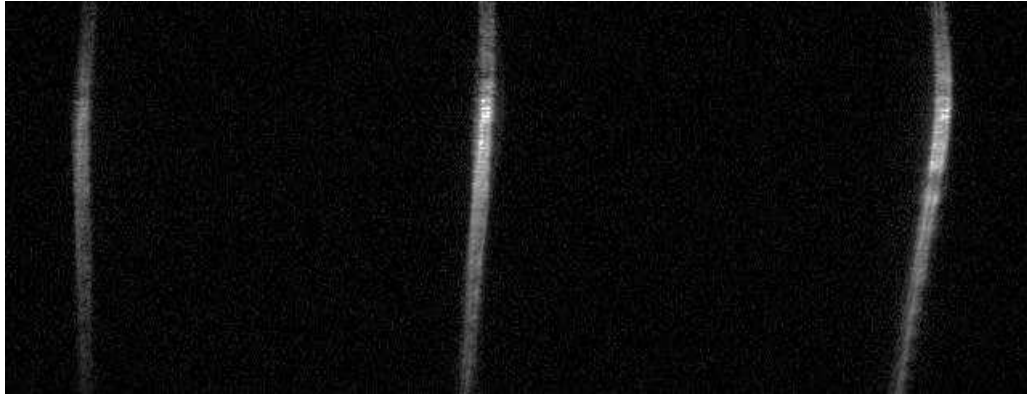
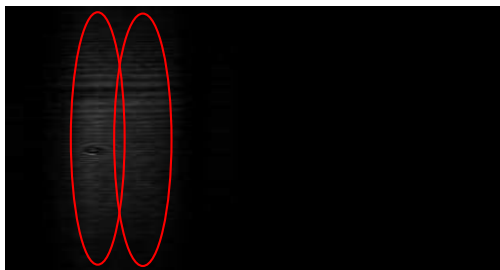


Figure 6.16 Distorted spectral lines observed in experiment due to the misalignment of collimator 2



(a)



(b)



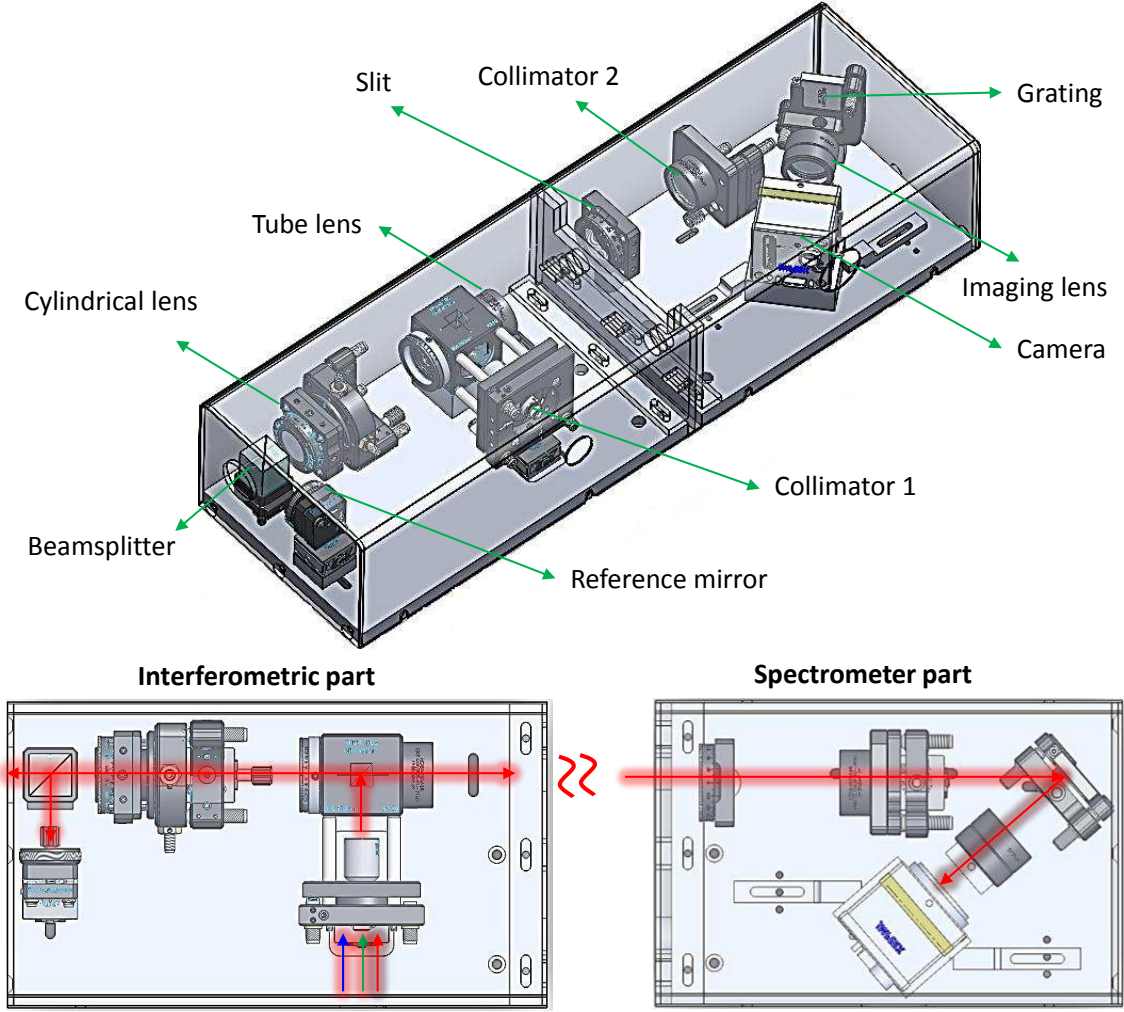
(c)

Figure 6.17 Effect resulting from the misalignment of the camera: (a) low fringe visibility, (b) overlapping of the spectral lines, (c) well-separated spectral lines.

### 6.5.2 Initial prototype

The initial prototype of LSDI was designed and shown in Figure 6.18. A multi-mode fibre with NA of 0.39 is used to transfer the light from the illumination device to the interferometric system. A triplet fibre collimator (NA=0.25), producing beam quality superior to aspheric lens collimators, is selected for beam collimation. The diaphragm iris placed before the cylindrical

lens allows the light beam to pass through with a diameter of 8 mm. As discussed in chapter 4, the optimal angle between the diffraction grating and optical axis is set around  $41^\circ$  to acquire the nearly linear distribution of spectrum on the camera. All the optical components were properly arranged to achieve a compact configuration and finally the prototype has a size of 468 mm x 140 mm x 91 mm (length x width x height). Table 6.4 details the main commercial components used by the prototype.



**Figure 6.18 Initial prototype of cylindrical-LSDI**

There are two main parts which comprise the prototype, namely the interferometric part and the spectrometer part. The interferometric part works as the optical probe head to observe the tested surface and the spectrometer part spatially disperses the interference signals into a series of constituent monochromatic interferograms. Four mounting holes were made on the prototype base, making it is convenient to be embedded into an industrial machine. After wavelength

calibration wavenumber  $k$  spreads along the chromaticity axis in a range of  $1.59\mu\text{m}^{-1}$  to  $1.78\mu\text{m}^{-1}$ , which corresponds to a wavelength span of 562.01 nm to 628.24 nm. The calibration data are given in Appendix A.3. Figure 6.19 depicts the calibration of chromaticity axis of camera using the method illustrated in section 4.4.

**Table 6.4 Off-the-shelf components used for prototype design (cylindrical – LSDI)**

Components	Model	Suppliers	Main parameters
Optical fibre	M75L02	Thorlabs, Inc.	Core diameter $\text{\O}200\ \mu\text{m}$ , 0.39 NA
Collimator 1	TC25FC-633		FC/PC Triplet collimator, $f=24.98$ , mm, NA=0.25, clear aperture $\text{\O}12.5\text{mm}$
Cylindrical lens	ACY254-075-A		$f = 75$ mm, $\text{\O}1''$ Achromatic doublet
Tube lens	AC254-075-A-ML		$f=100$ mm, $\text{\O}1''$ Achromatic Doublet
Collimator 2	AC254-060-A-ML		$f=60$ mm, $\text{\O}1''$ Achromatic Doublet
Diffraction grating	GH25-12V		Visible Reflective Holographic Grating, 1200/mm, 25 mm x 25 mm x 6 mm
Imaging lens	AC254-060-A-ML		$f=60$ mm, $\text{\O}1''$ Achromatic Doublet
Camera	ICL-B0620	Imperx	Resolution 480 x 640, 7.4 $\mu\text{m}$ pixel size, 208 fps

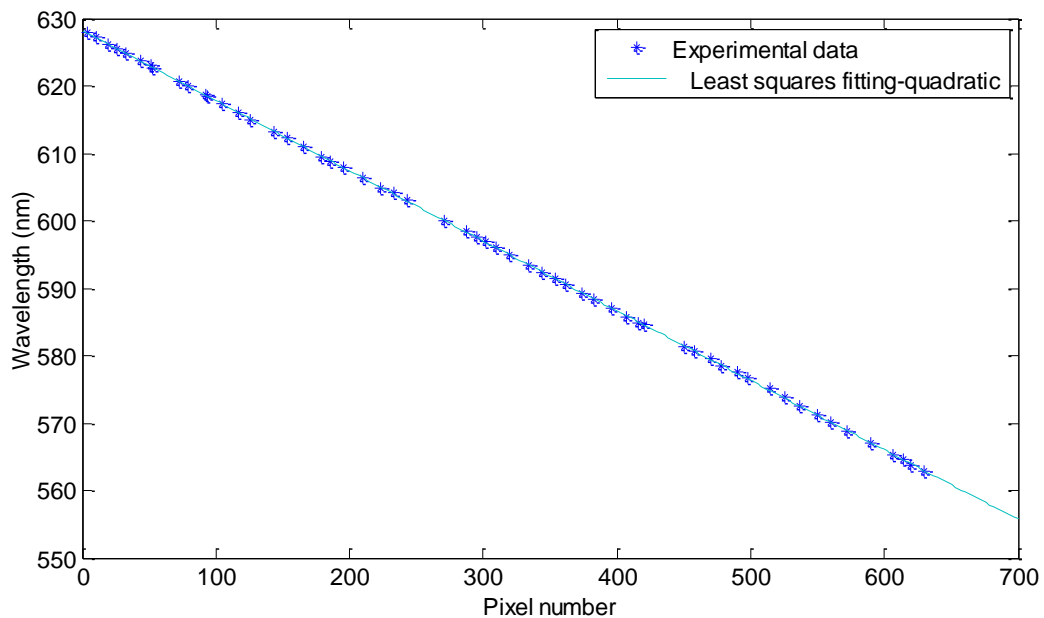


**Figure 6.19 Calibration of chromaticity axis of camera for cylindrical-LSDI prototype**

## **6.6 System performance**

The performance of a metrology device is determined by many factors such as optical arrangement, detector, algorithm and environment condition. All developed metrological instruments need to be carefully calibrated before they are used for surface characterisation, especially for the workpiece that functionally relies on micro/nano scale and ultra-precision structured surfaces. Meanwhile, these calibrated optical specifications provide the reference for selecting the suitable instruments or configurations for various metrological applications.

### **6.6.1 Lateral range and resolution**

The lateral resolution, also known as optical resolution, quantifies the ability of a 3D metrology instrument to resolve two close radiating points on the surface (Yoshizawa, 2009). In the case of the optical probing head using a cylindrical lens, there is no focusing effect in x axis (surface profile direction) due to its imaging property. Therefore, the resolution along x axis is determined by the geometric imaging characteristic of the system, which is equal to the lateral sampling resolution along the surface profile.

The lateral range of the system varies with the objectives used. Unlike the areal measurement instrument, the lateral range (or FOV) of the LSDI is normally given in the direction of the tested surface profile. It is defined as the length of surface profile observed by the objective. As mentioned in previous sections, the effective sampling length on the specimen is dependent on several factors such as the NA of the illumination system, the diameter of the iris diaphragm, the size of sensor for receiving the image and the overall magnification produced by all optics in the optical system. Actually, the developed optical apparatus generates an image on a sensor plane with a size bigger than the sensor size in the vertical direction (3.552 mm), which provides the room for the camera to be adjusted to receive the image section with best fringe quality. The exact lateral range of cylindrical-LSDI can be calibrated by first determining the lateral sampling resolution, also known as CCD pixelation presentation.

One of the methods to determine the CCD pixelation presentation on the sample along the measured profile direction is employing a target with standard scales, such as the USAF target shown in Figure 6.20. This target is comprised of white and black bars which are categorised into different groups on the resolution target according to the precisely defined widths and spacings. The black bars are the reflective surface while the white ones are transparent. By recording the reflected beam from the lithographically imprinted structures on the target and

analysing the obtained intensity modulation, the CCD pixelation presentation can then be determined.



**Figure 6.20 USAF target: (a) the image of the USAF test target, (b) size chart of group 0.**

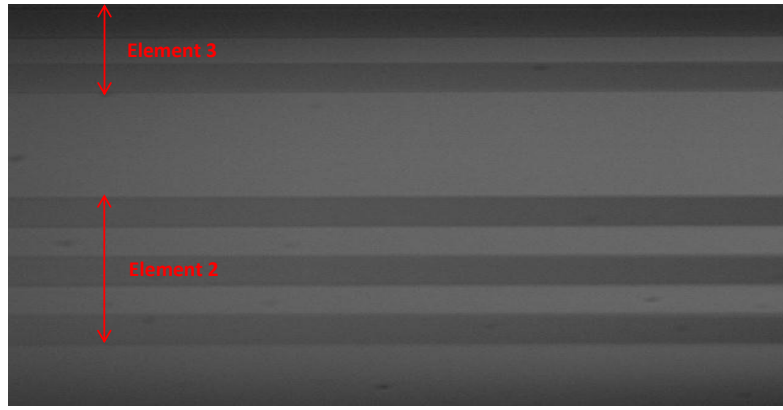
The intensity change was measured along the vertical lines of the group 0. Figure 6.21(a) shows the image of one measured profile. It was found that the line beam generated by the cylindrical lens covered the measurement range on the target from element 2 to element 3. By analysing the intensity modulation in Figure 21(b), it can be obtained that 5 bars in element 2 are covered by 182 pixels, therefore the CCD pixelation presentation ( $P_d$ ) or lateral resolution can be calculated by

$$P_d = 446.4 \mu\text{m} / (182 / 5) = 12.26 \mu\text{m} \quad (6.3)$$

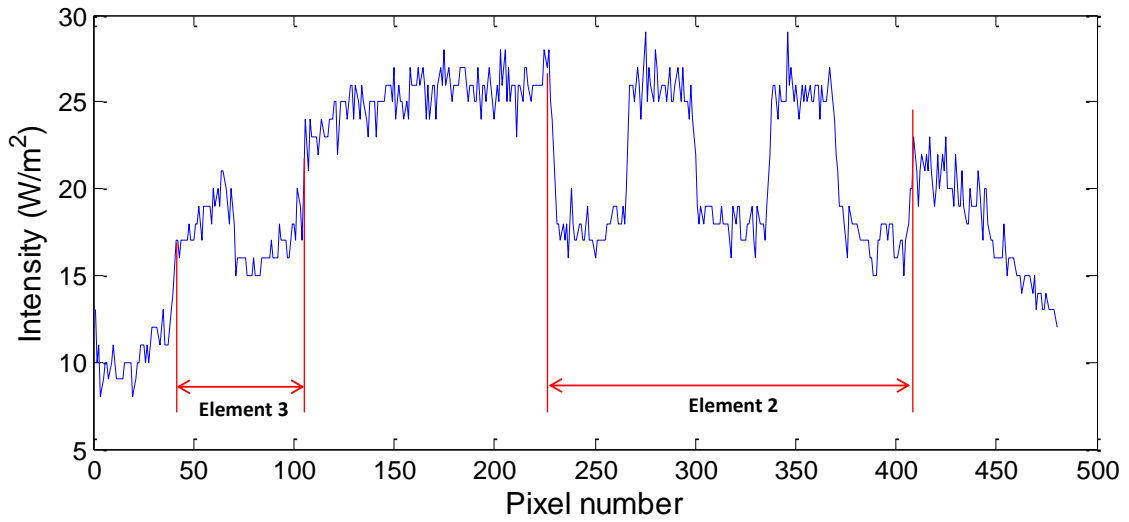
This means each pixel along x axis represents 12.26  $\mu\text{m}$  on the tested surface. Then the lateral range ( $R_{LY}$ ) in x axis can be obtained by

$$R_{LY} = N_p * P_d = 480 * 12.26 \mu\text{m} = 5.885 \text{ mm} \quad (6.4)$$

where  $N_p$  represents the number of CCD pixels along x axis.



(a)



(b)

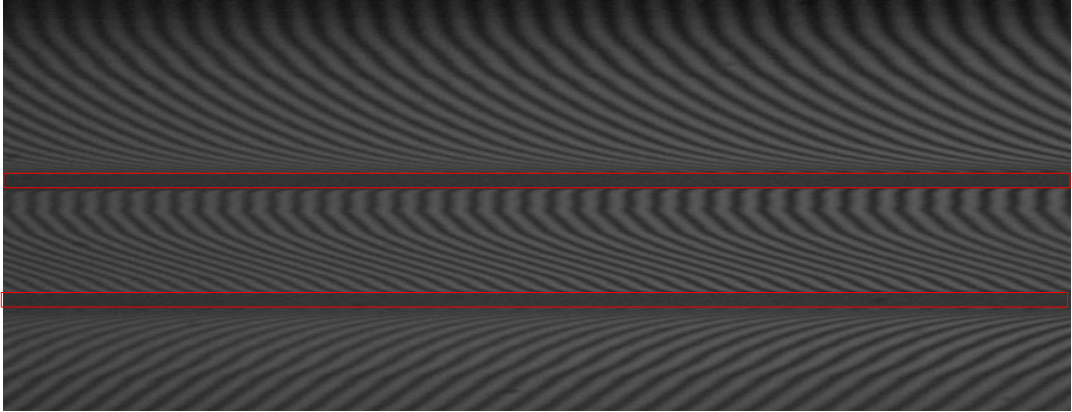
**Figure 6.21 Determination of the CCD pixelation: (a) image of the USAF target captured by camera, (b) corresponding intensity modulation.**

### 6.6.2 Axial measurement range

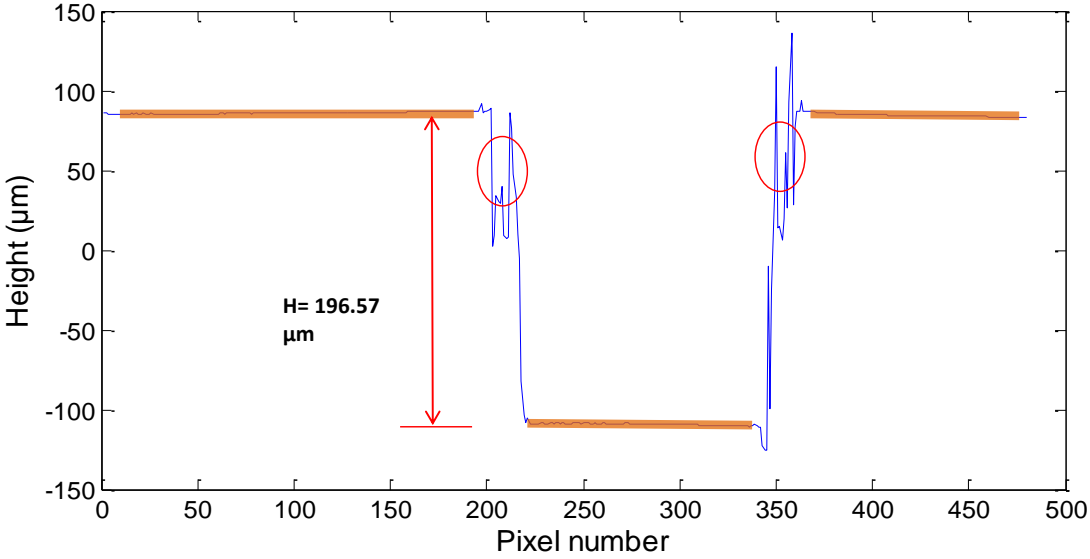
According to the measurement technique used, the axial measurement range is generally determined by factors such as depth of field, coherence length, scanning range and the working distance of the objective. In the case of the dispersive interferometer, the axial measurement range is however determined by the finite spectrometer resolution. The maximum measurement range can be estimated when the fringe period becomes less than 2 pixels wide. The theoretical maximum axial measurable range ( $Z_M$ ) can be given by (Kumar, et al., 2010)

$$Z_M = \lambda_0^2 (4\delta_\lambda)^{-1} \quad (6.5)$$

where  $\lambda_0$  is the centre wavelength and  $\delta_\lambda$  is the spectrometer resolution. For the developed prototype, the received spectrum has a 66.2 nm bandwidth (centred at  $\lambda_0 = 596$  nm) spreading along the 640 horizontal pixels, which then provides a per pixel bandwidth of  $\delta_\lambda = 0.1$  nm. The maximum measurement range  $Z_M$  is therefore calculated as 885  $\mu\text{m}$  using equation (6.5). The calculation shows that the LSDI technique greatly extends the axial measurement range compared to other white light interferometers and is capable of performing profile measurement even when the height variation of the features on tested surface well exceeds DOF.



(a)



(b)

**Figure 6.22 Measurement result of a reference sample with 200  $\mu\text{m}$  step height: (a) spectral interferogram, (b) surface profile result.**

Practically, the theoretical calculation  $Z_M$  may not be achieved due to the influence of many factors such as bandwidth of the spectral lines, residual aberrations from the optical components, system noise and alignment errors. Even so, we still succeeded to measure a sample with a step height of 200  $\mu\text{m}$  (from Rubert & Co. Ltd.). The measured average height is 196.57  $\mu\text{m}$ , as shown in Figure 6.22. From the captured spectral interferogram, it can be observed that the step surfaces are well resolved. The areas marked within red rectangles in the interferogram generate measurement errors due to the irregularity of interference fringes from the surface edge. However, these errors have no influence on the evaluation of LSDI's axial measurement ability. Calibration of the axial measurement range will be further investigated by using a set of artefacts.

### 6.6.3 Angular measurement range

There is a limitation that exists in almost all interferometers, which is measuring surfaces with gradient (Kaplonek & Lukianowicz, 2012). The sloped surface cannot be measured if the light reflected from the slope is not gathered by the objective (Malacara, 2007). The maximum measurable slope ( $\beta$ , also known as maximum acceptable surface gradient) depends on the NA of the objective. If the angle of the measured surface exceeds half of the angular aperture of the objective ( $\alpha$ ), no light beam can be detected (see Figure 6.23).

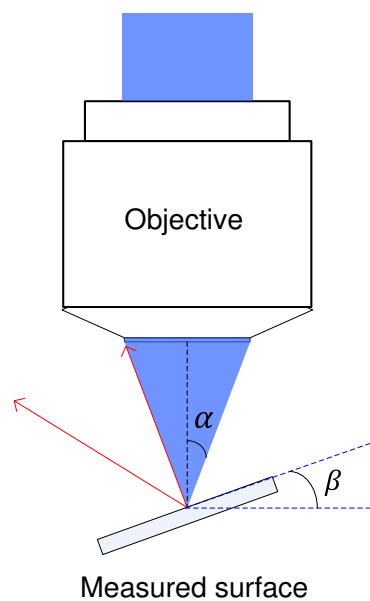


**Figure 6.23 Schema of the maximum measurable slope**

The following formula is therefore used to theoretically evaluate the maximum measurable slope.

$$\beta = \alpha = \arcsin(\text{NA}/n) \quad (6.6)$$

The term  $n$  represents the refractive index, which approximately equals 1.0 because our prototype performs measurement in the air. Suppose the entrance pupil of the beam is 6 mm and the cylindrical lens used has a focal length of 75 mm, then the measurable slope is calculated as  $\pm 2.3^\circ$ . However, it is not a limitation under all circumstances because the surface finish has an influence on the measurable slope as well. For a tested sample with rough surface, the maximum measurable slope can be higher than the theoretical value because the light can travel back to the objective through diffuse reflection (Kumar, et al., 2010; Malacara, 2007).

Four concave mirrors with  $\lambda/4$  (@ 633 nm) surface irregularity were measured to experimentally assess the slope measurement ability of cylindrical-LSDI (Figure 6.24 and Figure 6.25). As shown in Figure 6.24, the concave surface with a radius of curvature (RC) of 610 mm can be accurately measured. However, when the RC is less than a certain value, the effective fringes for measurement are not available in the full field of view due to the focus effect from the spherical sample surface. In this case, there is no longer a planar-wavefront received on the slit plane after the line measured beam is reflected by the concave mirror and passes through the cylindrical lens and the tube lens. Therefore measurement errors in the measured profiles are produced, which means the lateral measurable range of cylindrical-LSDI decreases. Figure 6.25 shows the surface map results obtained by translating the samples along  $y$  axis. The maximum angle  $\beta$  limits the measurable scanning range in  $y$  axis. All the obtained results show that the developed LSDI prototype has certain angular measurement ability dependent on the NA of the objective used. To handle the inevitable limitation in measuring the surface slope, however, a priori information is required for the surface features to be measured before the metrology device is applied to inspection of samples with high slopes such as solder ball grid array and steel ball bearing in terms of quality assurance.

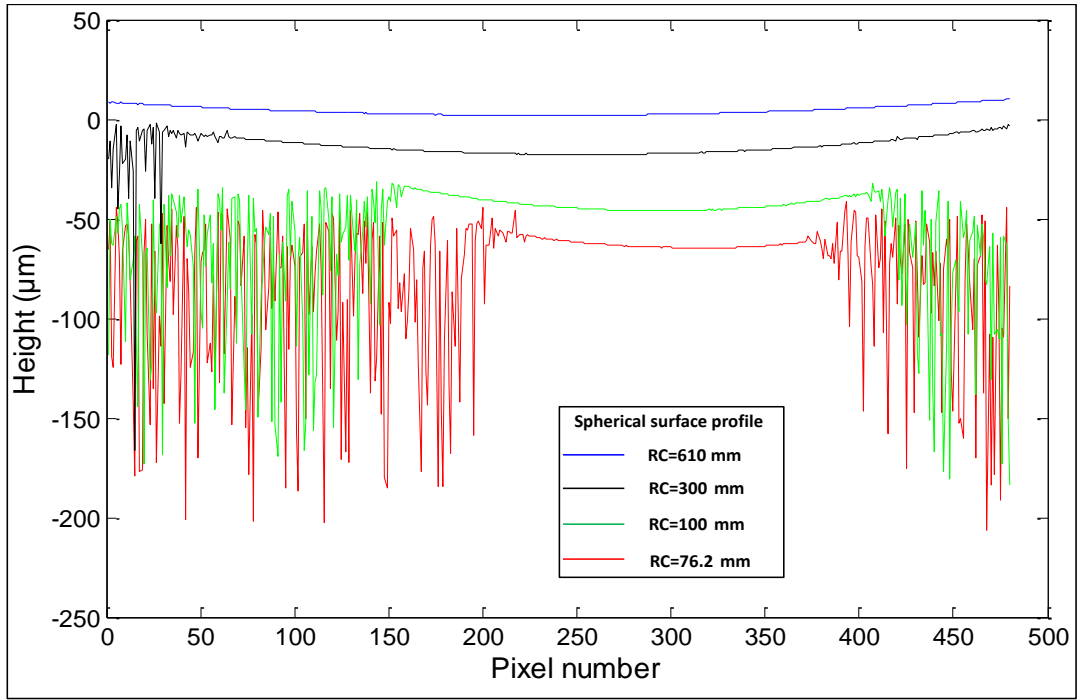


Figure 6.24 Profile results of the concave mirrors using cylindrical-LSDI

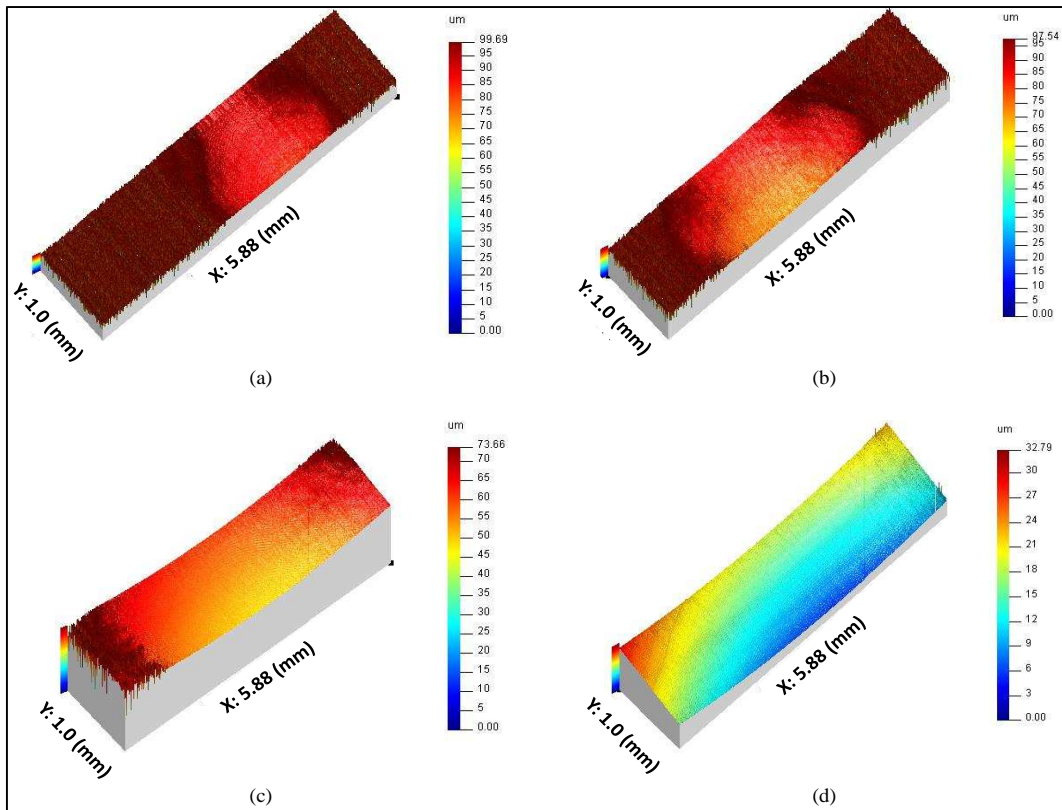


Figure 6.25 Surface map results of the concave mirrors: (a) RC=76.2 mm, (b) RC=100 mm, (c) RC=300 mm, (d) RC=610 mm.

Additionally, there are two solutions for measuring a sample with the higher slope surfaces, namely rotating the instrument and using an objective with a higher NA. There is a trade-off to be made when selecting one of them for measurement. Rotating the instrument is capable to measure the surface with various slopes; however, a complicated and bulky mechanical rotation system needs to be involved. Adopting an objective with higher NA can enhance the angular measurement ability while it suffers from the high cost and small lateral measurement range, which makes it more dependent on data stitching techniques for fully characterising a surface.

Another feasible way, introducing dual-optical wedges into interferometric objective, is proposed for consideration of mitigating the problem of measuring a high slope surface. Figure 6.26 shows the working principle of the rotatable dual wedges. By giving a relative rotation angle between the two wedges, the incident light can acquire a deviation angle ( $\delta$ ), which can be expressed by

$$\delta = 2(n-1)\theta \cos(\varphi/2) \quad (6.7)$$

where  $n$  represents the refractive index of the optical wedge,  $\theta$  is the wedge angle and  $\varphi$  is the relative rotation angle between two wedges. Therefore, the dual-optical wedges can work as a simple rotation system by generating different deviation angles for slope surface measurements. As shown in Figure 6.27, in order to balance the OPD, two pairs of dual-optical wedges are inserted into both measurement arm and reference arm of the interferometer.

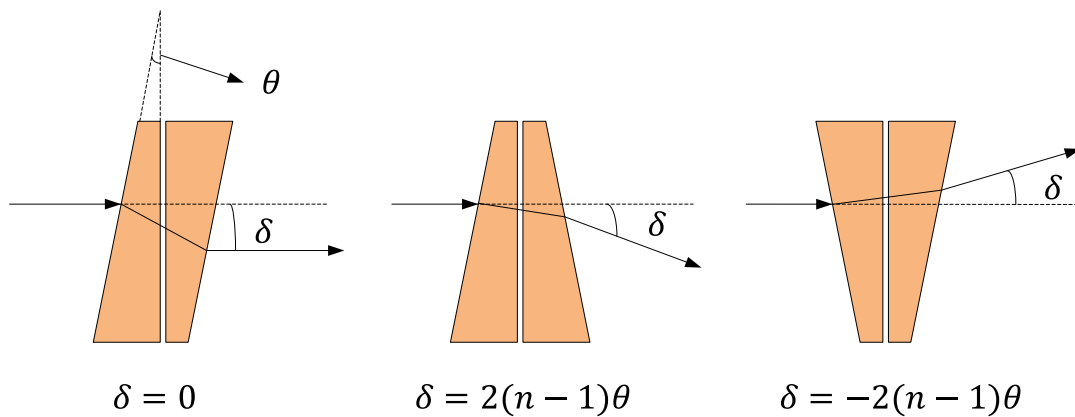


**Figure 6.26** Beam deviations by rotating two optical wedges with different angles

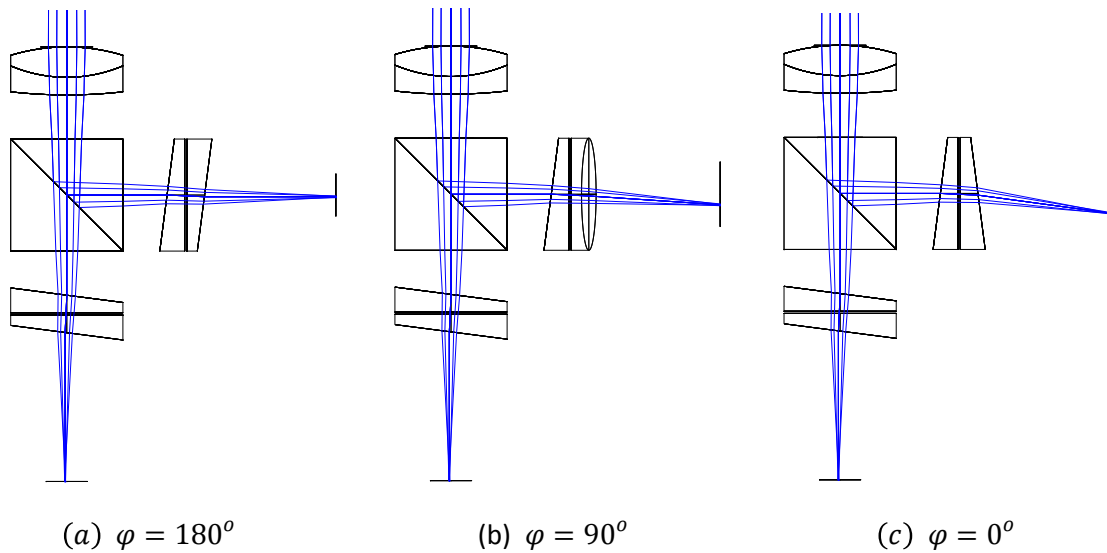


**Figure 6.27** Introducing two pairs of dual-optical wedges into interferometric objective.  $\varphi$  : Relative rotation angle between two optical wedges.

When inspecting the samples with high slopes, the dual wedges in the measurement arm can be rotated with an angle to allow the probing beam to regain the acceptable surface gradient for measurement. The wedges in the reference arm are kept a relative angle of  $180^\circ$  at all times. Suppose the wedge angle  $\theta$  is  $10^\circ$ ,  $n$  is equal to 1.52 and  $\varphi = 0^\circ$ , the deviation angle is calculated as  $10.4^\circ$ . Therefore, it is possible for this system to cover the angular measurement range up to  $\pm (10.4^\circ + 2.3^\circ)$ . The method has the benefit of increasing the measurable angle by simply rotating the wedges. However, it still cannot overcome the limitation in measuring the high slopes. Additionally, except the simulation illustrated above, further investigation is required since the wedges inserted in the optical system bring extra issues such as chromatic aberrations, alignment endeavour and data stitching.

#### 6.6.4 Measurement noise

Measurement noise is defined as a combination of the internal noise of the instrument, environmental noise and the noise resulting from the scanning during the measurement (Giusca & Leach, 2013). In general there are two methods for assessment of measurement noise. The first one is measuring a standard flat artefact with precise surface quality and making a comparison with the certified value. The other method is to isolate the noise from the surface roughness using a subtraction technique or averaging technique (Giusca & Leach, 2013). In this

section, the subtraction technique is adopted for estimating the measurement noise of cylindrical-LSDI.

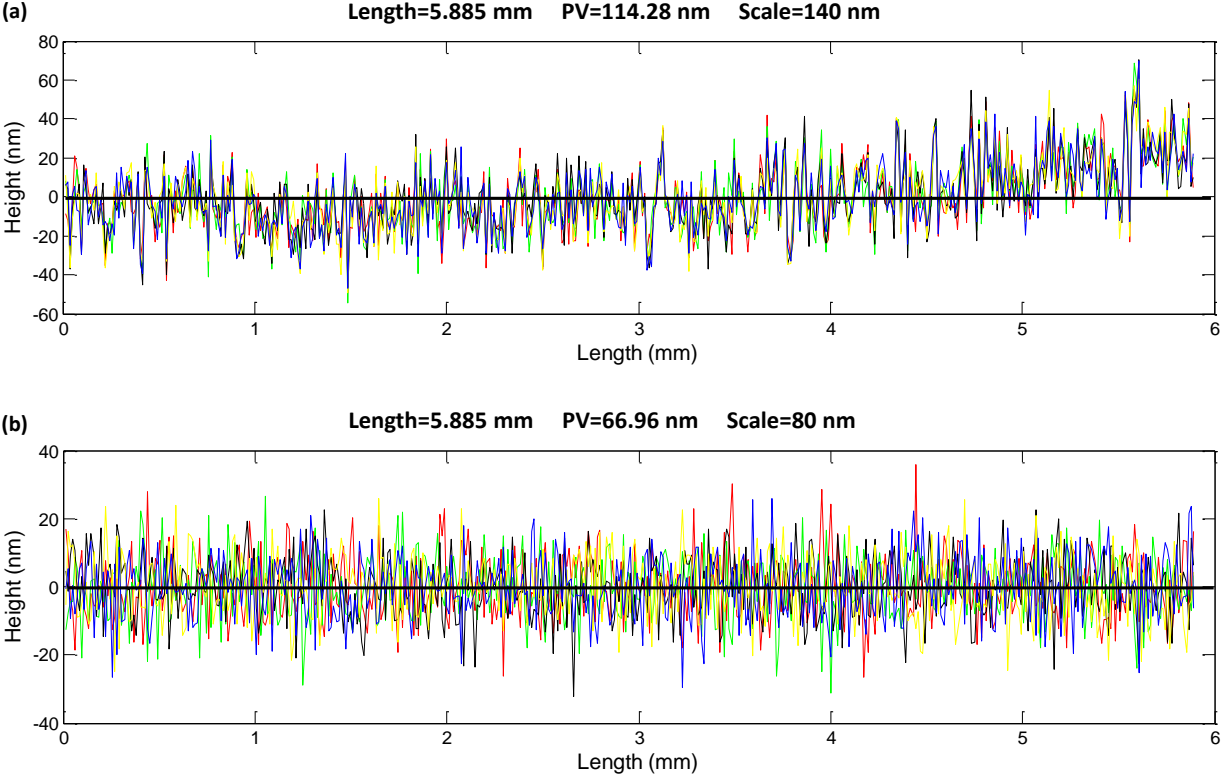


**Figure 6.28** Subtraction technique for estimating the measurement noise of cylindrical-LSDI: (a) five profiles with surface roughness, (b) four new profiles after removing the intrinsic roughness.

A standard flat artefact is employed for this purpose, which has a RMS height of the scale limited surface  $S_q$  equal to 4 nm (see Appendix C.1). This sample was measured using cylindrical-LSDI prototype at the same position for five times and the profile results are shown in Figure 6.28(a). Then the first measurement was subtracted from the second one, and the second from the third and so on until four new measurement noise profiles were obtained (see Figure 6.28(b)). The RMS heights ( $R_q$ ) of the four new profiles were calculated by equation (6.8). Finally the measurement noises can be obtained using equation (6.9) and the standard deviation of these measurements is given in equation (6.10). The calculations show that the developed LSDI prototype has an average measurement noise of 6.287 nm with an associated standard deviation of 0.007 nm, as shown in Table 6.5. Considering the calibration was carried

out in the normal optics laboratory, this estimated measurement noise is acceptable for this initial prototype.

$$R_q = \sqrt{\frac{1}{n} \sum_{i=1}^n r(i)^2} \quad (6.8)$$

$$M_{\text{noise}} = R_q / \sqrt{2} \quad (6.9)$$

$$\sigma = \sqrt{\frac{1}{(N-1)} \sum_{i=1}^n (M_i - \overline{M})^2} \quad (6.10)$$

**Table 6.5 Measurement noise estimation of cylindrical- LSDI**

M <sub>noise</sub> (nm)				Average $\overline{M_{\text{noise}}}$ (nm)	Standard deviation $\sigma$ (nm)
6.278	6.294	6.291	6.288	6.287	0.007

## 6.7 Measurement results

In order to confirm the performance of the cylindrical-LSDI prototype in terms of profile measurement, two step samples with height values of 4.707  $\mu\text{m}$  and 100 nm have been measured, respectively.

### 6.7.1 Case 1: Standard step sample (4.707 $\mu\text{m}$ )

In this case-study, a 4.707  $\mu\text{m}$  standard step sample was measured by both LSDI prototype and CCI 3000. The measurement results by CCI are shown in Appendix C.2. Assuming that the average height is determined by the difference between the mean line values of the upper and lower profiles, and then the step height is calculated with an average value of 4.699  $\mu\text{m}$  by CCI. Both FFT algorithm and Carré algorithm discussed in chapter 5 were used to analyse the interferogram captured by cylindrical-LSDI to evaluate their performance, as shown in Figure 6.29(a). The surface profile results show a good agreement (18 nm difference on average) between the Carré algorithm and the FFT algorithm, which gives the average height as 4.663  $\mu\text{m}$  and 4.645  $\mu\text{m}$ , respectively. The spiky errors, resulting from the irregularity of interference signals at the surface edge, have no influence on the measurement of other pixels because each point is analysed individually and independently. On the whole, the LSDI results align with the

CCI result acceptably. In addition, Figure 6.29(b) shows the surface map result by translating the sample.

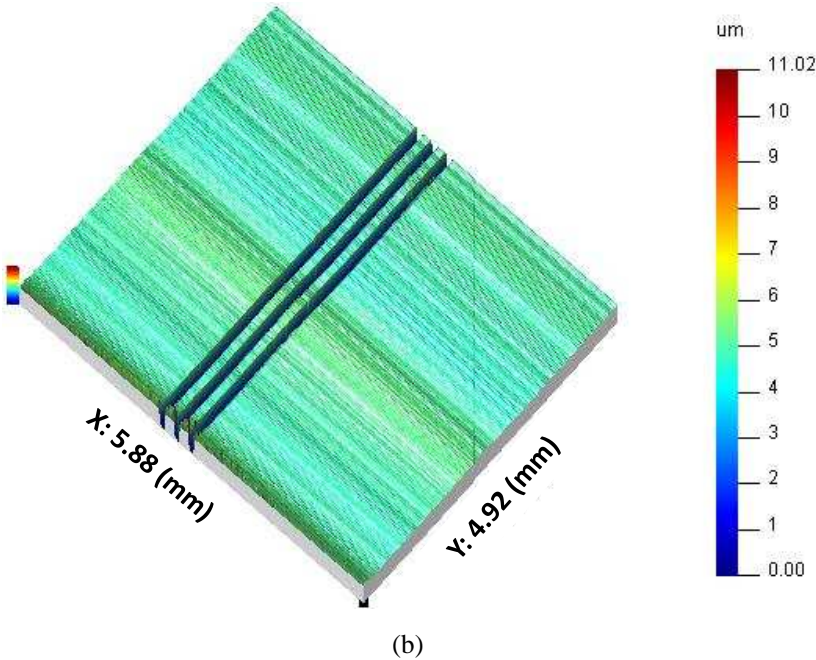
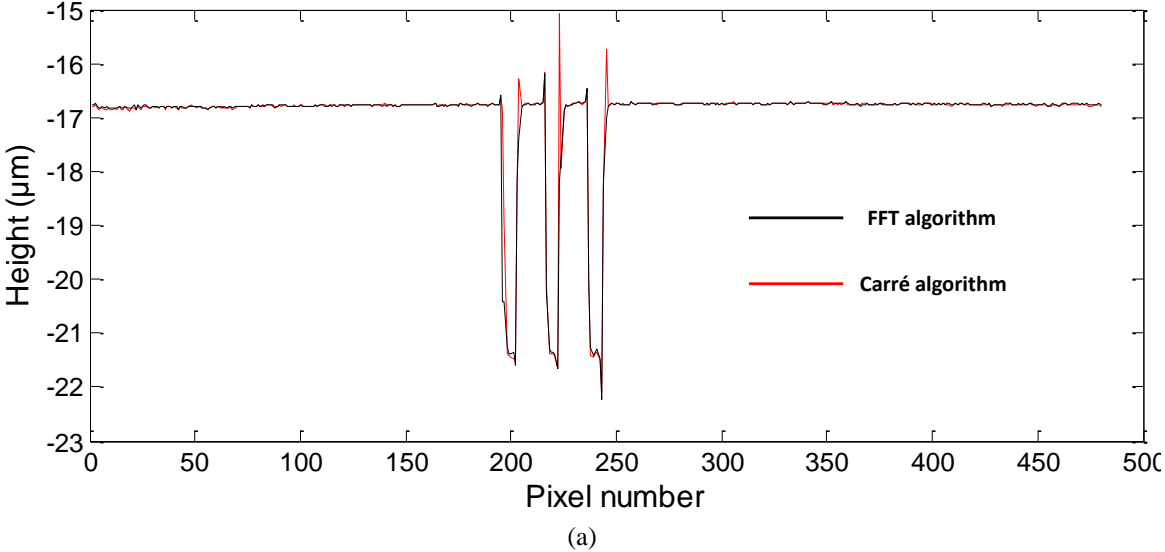
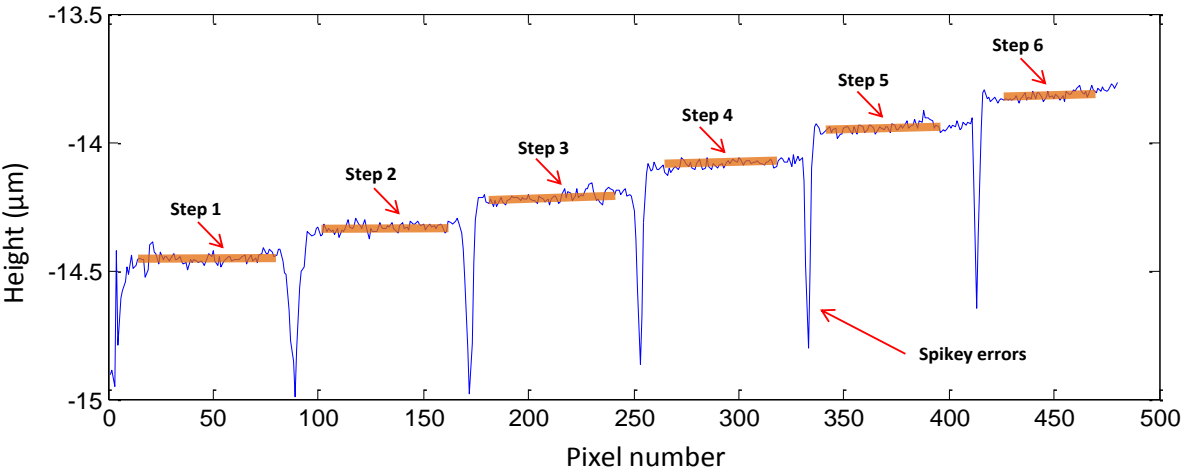


Figure 6.29 Measurement results for 4.707 μm standard step height sample: (a) surface profiles using FFT algorithm and Carré algorithm, respectively, (b) constructed surface map through scanning.

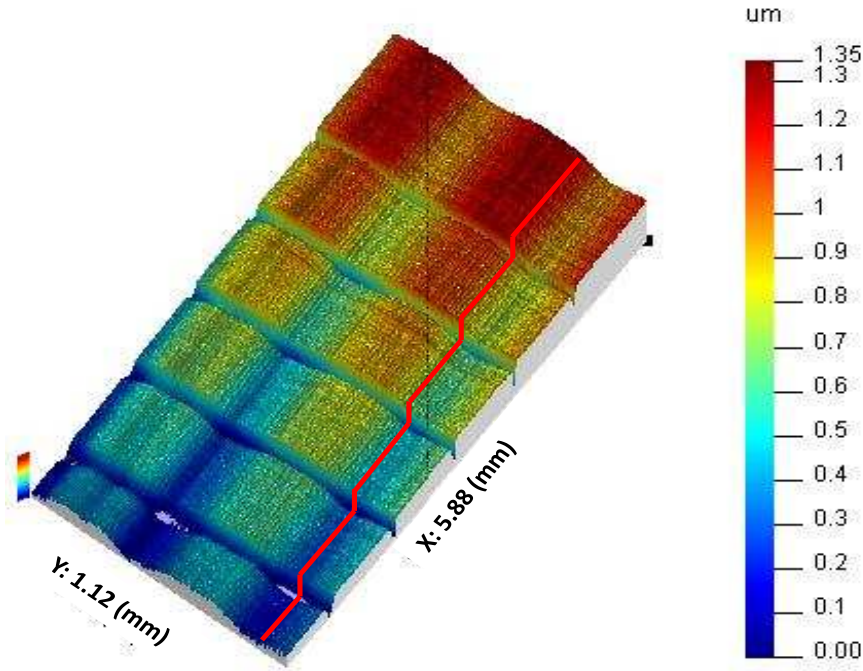
6.7.2 Case 2: Diamond-turned step sample (100 nm)

The same measurement procedure was used to measure the 100 nm diamond-turned step sample and the results are shown in Figure 6.30. The measured average heights are calculated as 84.6 nm, 93.1 nm, 109.1 nm, 92.8 nm and 102.3 nm from left to right in Figure 6.30(a). CCI

3000 measured the step sample using a 5X objective, which provides the measurement area of 3.6 mm x 3.6 mm. Therefore just 5 step surfaces can be covered by the probe of CCI for each measurement. The first four step height values corresponding to LSDI results are 94 nm, 95 nm, 103 nm and 99 nm, as shown in Appendix C.3. For the surface map result in Figure 6.30(b), the surface irregularity in y axis results from the scanning error and does not affect the performance of profile measurement because every profile is measured independently.



(a)



(b)

**Figure 6.30 Measurement results for 100 nm step height sample: (a) surface profile using FFT algorithm, (b) constructed surface map through scanning.**

## 6.8 Summary

This chapter introduces a cylindrical-LSDI which obtains a long surface profile in a single shot by analysing the channelled spectrum without any mechanical scanning. Since there is no focusing effect in x axis, the optical probe using cylindrical lens greatly extends the lateral measurement range when used to observe the tested surface.

A built experimental setup first validated the methodology of LSDI by accurately measuring the step samples and detecting defects present on a flat mirror, which offers the basis for the prototype design. After that, a compact prototype has been developed with improvement of the lateral resolution of the interferometric system. Other alignment issues in terms of the collimator and camera are discussed as well to achieve good fringe visibility and high quality image of spectral lines.

By using a USAF test target the lateral resolution and the measurement range along the surface profile direction were calibrated as 12.26  $\mu\text{m}$  and 5.885 mm, respectively. As for the axial measurement range of LSDI, it is determined by the spectrometer resolution, not limited by DOF as with other instruments such as WSI. With a theoretical axial measurement range of 885  $\mu\text{m}$ , the 200  $\mu\text{m}$  step height can be well resolved in the spectral interferogram and accurately calculated by analysing the fringe pattern.

Like other interferometers, the angular measurement capability is determined by the NA of the objective. In order to measure a sample with higher slope, using an objective with high NA and rotating the instrument to regain the acceptable surface gradient are two applicable solutions. Another method, introducing two pairs of dual-optical wedges into interferometric objective to mitigate the measurement problem of high slope surface, is simulated using ZEMAX and discussed with theoretical calculation. It is a simple method at a low cost. However, further investigation needs to be carried out to validate the applicability.

The performance of the cylindrical-LSDI prototype was verified by measuring two step samples with height values of 4.707  $\mu\text{m}$  and 100 nm, respectively. The spiky errors in the measured profile and the surface irregularity of the surface map (along the scanning direction) have no influence on the system performance because each point and each profile are processed individually. The obtained profile results closely align with the calibrated specifications given by the manufacturer as well as the measurement results by the other commercial instrument, which confirms that cylindrical-LSDI may potentially be applied to in-line surface inspection in terms

of quality control. Implementation of this prototype offers an attractive solution to improve manufacturing processing and reliability for products in ultra-high-precision engineering.

Moreover, benefiting from the long profile measurement, the cylindrical-LSDI sensor can also achieve large area measurement by rotating the cylindrical lens when it is used for in-situ metrology applications.

# 7 Optical apparatus 2: Microscope based LSDI

## 7.1 Introduction

Though the cylindrical-LSDI can achieve long profile measurement, it will be struggling to resolve smaller structure dimensions and features on tested surface in few micro- or submicro-scale. This chapter presents the second optical apparatus of LSDI which employs a microscope objective to inspect the tested sample, as shown in Figure 7.1. Interferometric microscopes with different magnifications are commercially available, enabling the microscope based LSDI (referred to as microscope-LSDI) to be a versatile instrument for characterisation of surface structures with various scales in a wide range. An initial prototype was developed using a 4X interferometric objective with a lateral resolution of approximately 4  $\mu\text{m}$  along the surface profile direction. The performance evaluation through measuring two step samples and an  $\text{Al}_2\text{O}_3$  coated polyethylene naphthalate (PEN) film is presented. Investigation of the effect from environmental disturbances is performed as well. The accurate experimental results provide the basis for in-line metrology for production lines such as R2R surface inspection where only defects on the film surface are concerned in terms of quality assurance.

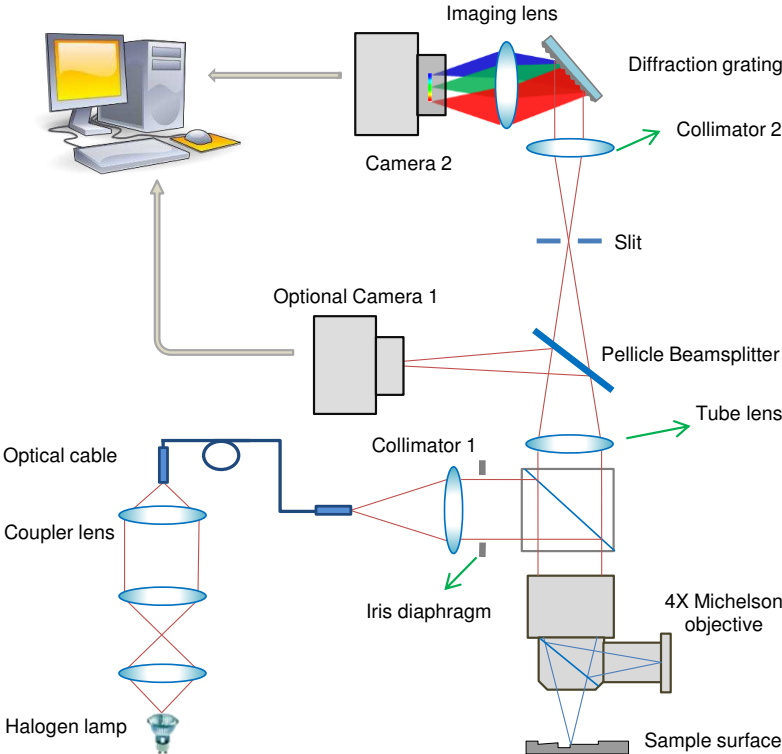


Figure 7.1 Schematic diagram of microscope based LSDI

## 7.2 Surface profile measurement with high lateral resolution

The white light illumination for the system is still provided by the light source device illustrated in chapter 4. The tested surface is observed through a 4X Michelson interferometric objective. The interference beam is focused by a spherical tube lens and split into two parts by a pellicle beamsplitter. The reflected part is received by camera 1 which provides real-time image of the tested surface and then benefits the measurement with additional information. The transmitted part first passes through a slit to block the light redundant for measurement, then a narrow line of light which represents an interference signal of a surface profile is selected and diffracted by the grating before finally being received on camera 2. The direction of the slit is also set to be parallel to the columns of camera pixels in this optical apparatus to provide the dispersion axis along the rows. Likewise, the height information of the profile is registered in a two-dimensional spectral interferogram with lateral information in the vertical direction and the chromaticity axis in the horizontal direction. A surface profile can be measured in a single shot and a surface map, constructed by numbers of individual profiles, can be acquired by laterally translating the sample.

The operation and data capturing for the microscope-LSDI are similar to cylindrical-LSDI.

## 7.3 Prototype design

The off-the-shelf optical components shown in Table 7.1 were used for the prototype design. Excepting the alignment issues discussed in chapter 6, several general concerns especially for utilisation of microscope are presented in this section as well.

**Table 7.1 Off-the-shelf components used for prototype design (microscope- LSDI)**

Components	Model	Suppliers	Main parameters
Collimator 1	TC25FC-633	Thorlabs, Inc.	FC/PC Triplet collimator, f=24.98 mm, NA=0.25
Tube lens	AC254-250-A-ML		f=250 mm, Ø1" Achromatic Doublet
Collimator 2	AC254-075-A-ML		f=75 mm, Ø1" Achromatic Doublet
Diffraction grating	GH25-12V		Visible Reflective Holographic Grating, 1200/mm, 25 mm x 25 mm x 6 mm
Imaging lens	AC254-075-A-ML		f=75 mm, Ø1" Achromatic Doublet

Optical fibre	M76L02		Core diameter $\varnothing 400 \mu\text{m}$ , 0.39 NA
Interferometric objective	A-IOB-004X	Polytec	Michelson type, 30 mm working distance, NA=0.1
Camera 1	CMLN-13S2M-CS	Point Grey	Resolution 960 x 1280, 3.75 $\mu\text{m}$ pixel size, 18 fps.
Camera 2	ICL-B0620	Imperx	Resolution 480 x 640, 7.4 $\mu\text{m}$ pixel size, 208 fps.

### 7.3.1 Microscope objective

There are two types of microscope objectives, namely finite objectives and infinity corrected objectives, as shown in Figure 7.2. For many years, microscope objectives with a fixed tube length were manufactured. The tube length was standardised by the Royal Microscopical Society as 160 mm during the nineteenth century (Heavens, 1989). For a microscope optical system using the finite objective, the mismatching in the tube length will impair the image quality due to introduction of spherical aberrations. Additionally, the insertion of optical accessories such as a prism, a polarizer or a fluorescence illuminator in the convergence optical path will generate ghost images as well as lengthen the tube length. Though compensation can be made using other optical components, it leads to the changes of the system magnification and light transmission.

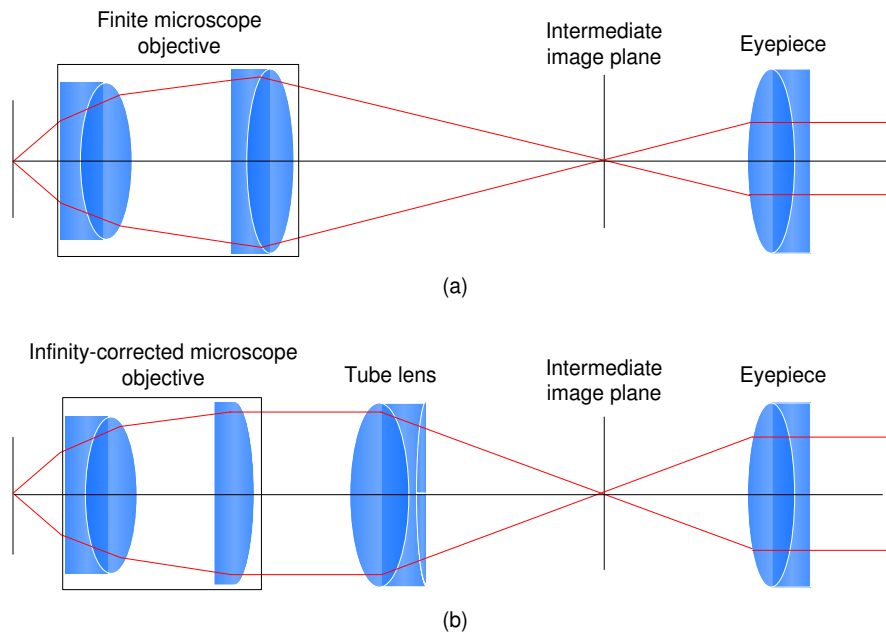


**Figure 7.2 Typical microscope optical systems: (a) using finite microscope objective, (b) using infinity-corrected microscope objective.**

The infinity-corrected objectives are designed to project the image of the specimen to infinity. It allows the optical accessories to be inserted into the parallel optical path between tube lens and objective without producing focus artifacts and optical aberrations (Murphy, 2002). A tube lens is required to bring the image at infinity into focus at the intermediate image plane (Rost & Oldfield, 2000). As the optical apparatus shown in Figure 7.1, a beamsplitter is set between the tube lens and the objective. Therefore, the infinity-corrected type of objective is employed in microscope-LSDI for inserting the beamsplitter with minimal effect to the optical system.

### 7.3.2 Tube lens

For the developed system, a spherical tube lens is used to generate the intermediate image on the slit plane. Subsequently, this image is observed by the spectrometer of LSDI. For the tube lens two aspects should be considered in terms of focal length ( $f_{TL}$ ) and position with respect to objective (D), as shown in Figure 7.3.

The magnification ( $M_{\text{objective}}$ ) produced by an infinity-corrected objective is calculated by dividing  $f_{TL}$  by the focal length of objective ( $f_{MS}$ ). For the 4X interferometric objective used in our system,  $f_{MS}$  equals 50 mm and therefore  $f_{TL}$  can be calculated as 200 mm (minimal value) to match the magnification of the objective. Additionally, it is suggested that the optimal focal length of the tube lens should be set between 200 and 250 millimetres, because a longer  $f_{TL}$  can generate a smaller off-axis angle and thus system artifacts can be reduced (Abramowitz et al., 2015). Moreover, for consideration of a bigger image desired on the sensor plane, the  $f_{TL}$  for the developed microscope-LSDI is finally determined as 250 mm, which makes the actual magnification  $M_{\text{objective}}$  equal to 5.

The space (D) between the objective and the tube lens (see Figure 7.3) is dependent on the dimensions of extra optical components to be inserted, such as the beamsplitter in the optical system of LSDI. The minimum space should allow the beamsplitter to be fitted in. However, there is an upper limit for this space. If the tube lens is set too far from the objective, some the off-axis rays may not be collected by the tube lens as well as the following optics. In this case, the so-called vignetting phenomenon occurs, which makes the image on the camera suffer from

darkened or blurred edges. Actually, the microscope-LSDI developed in this research work is unlikely to suffer from vignetting because of the demand of designing a compact prototype.

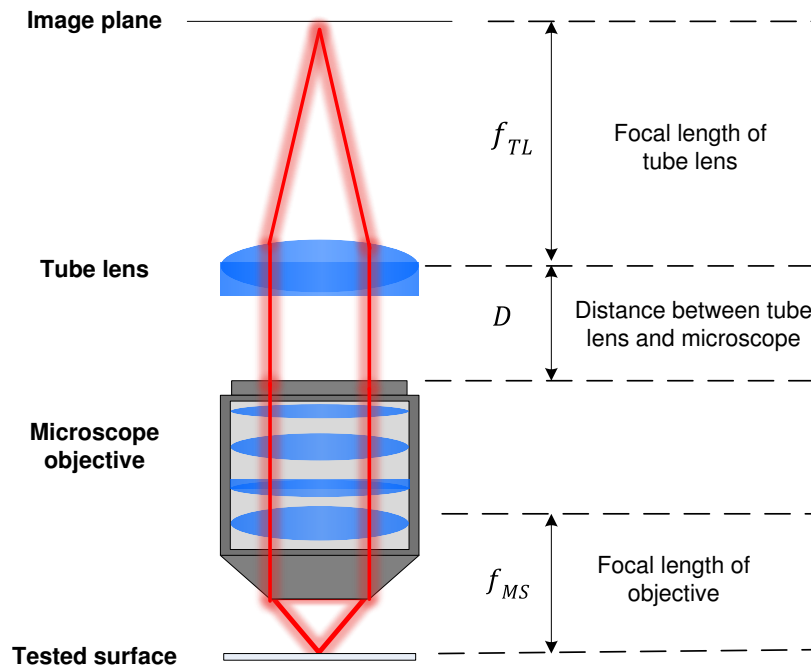


Figure 7.3 Dimension specifications of an infinity microscope system

### 7.3.3 FOV of the interferometric objective

Since the microscope-LSDI has a higher lateral resolution than the cylindrical-LSDI, the FOV of the objective (lateral measurement range) would be much smaller if the same camera is employed. Investigating the spot size in the optical system can acquire the theoretical FOV of LSDI, as shown in Figure 7.4.

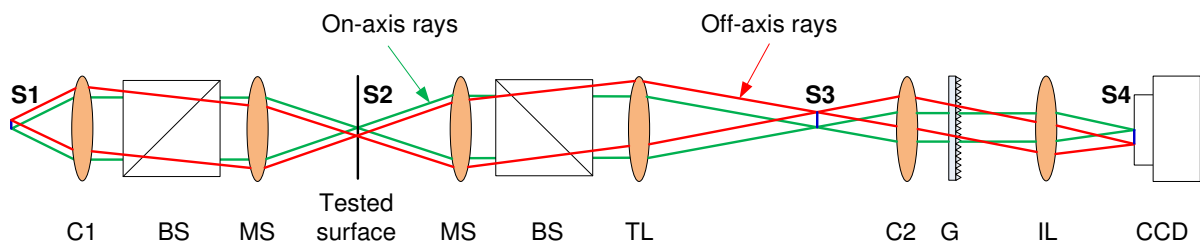


Figure 7.4 Perspective of the optical setup. S1-S4, spot image; C1, collimator 1; BS, beamsplitter; MS, microscope TL, tube lens; C2, collimator 2; G, grating; IL, imaging lens.

According to the geometrical optics theory, the sizes of the spot images shown in Figure 7.4 can be expressed by

$$\left\{ \frac{S2}{S1} = \frac{f_{MS}}{f_{C1}}, \frac{S3}{S2} = \frac{f_{TL}}{f_{MS}}, \frac{S4}{S3} = \frac{f_{IL}}{f_{C2}} \right\} \quad (7.1)$$

where S1, S2, S3 and S4 represent the spot sizes at different focal planes,  $f_{C1}$ ,  $f_{MS}$ ,  $f_{TL}$ ,  $f_{C2}$  and  $f_{IL}$  are the focal lengths corresponding to collimator 1, microscope, tube lens, collimator 2 and imaging lens. The spot image S4 received by camera is one of factors to determine the system's FOV, which can be calculated through multiplying the spot image S1 by the system magnification. Therefore the spot image S4 can be obtained by

$$S4 = \frac{f_{TL}}{f_{C1}} * \frac{f_{IL}}{f_{C2}} * S1 \quad (7.2)$$

The equation (7.2) shows that increasing S1, which is equal to the core diameter of the fibre, can produce a larger image on the image plane. Since the spot size S1 and all focal lengths of optics are given in Table 7.1, the spot size (S4) received on the CCD plane can be calculated as 4.003 mm along the measured profile direction, which is larger than the corresponding sensor size in height ( $S_{camera} = 480 * 7.4 \mu m = 3.552 \text{ mm}$ ). It means that all pixels on the sensor are used for measurement. In this case, the FOV of the objective can be theoretically calculated by

$$FOV = \frac{S_{camera}}{M_{objective}} = \frac{(480 * 7.4)}{5} \mu m = 710 \mu m \quad (7.3)$$

The exact FOV of the developed microscope-LSDI will be experimentally calibrated and presented in section 7.4.

### 7.3.4 Initial prototype

By following a similar design concept to the cylindrical lens prototype, the microscope-LSDI has been developed with an overall dimension of 498 mm x 140 mm x 91 mm (length x width x height), as shown in Figure 7.5. An extra small CCD camera is equipped at one of the branches of the optical system to present real-time image of the tested surface and contribute to search the small surface features within measurement FOV in particular metrology applications. It was shown that the developed system covers a range of  $1.49 \mu m^{-1}$  to  $1.62 \mu m^{-1}$  for

wavenumber  $k$  after performing the calibration of the chromaticity axis (Figure 7.6), which corresponds to a wavelength  $\lambda$  span of 616.56 nm to 670.02 nm. The calibration data are given in Appendix A.4.

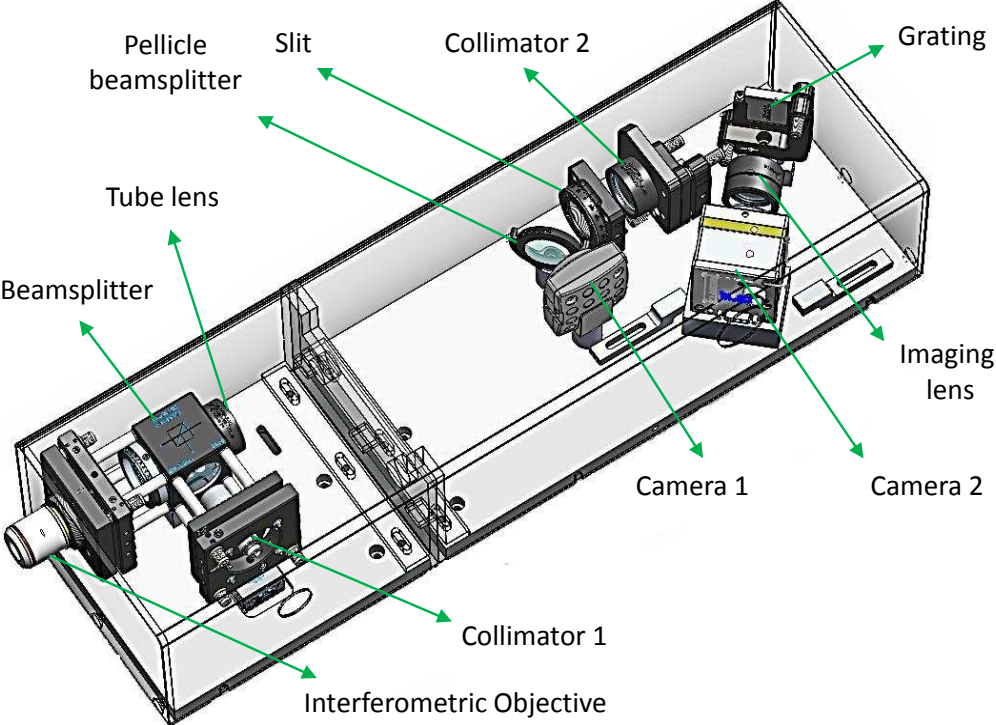


Figure 7.5 Initial prototype of microscope-LSDI

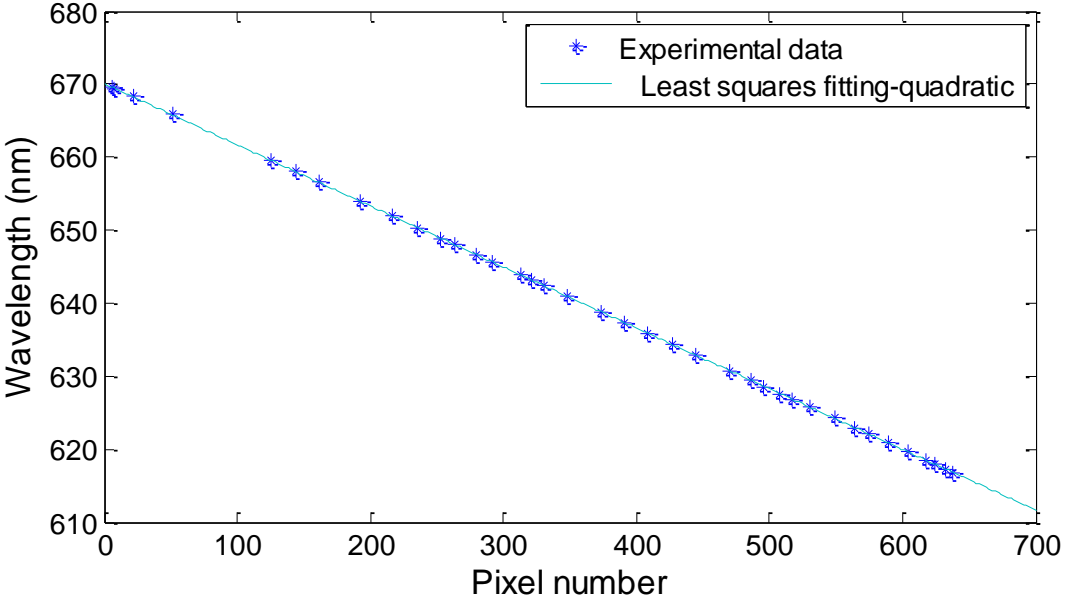


Figure 7.6 Calibration of chromaticity axis of camera for microscope-LSDI prototype

7.4 System features

7.4.1 Lateral range and resolution

A positive target (a microscope slide with 50 μm vacuum sputtered divisions, see Figure 7.7) was used to determine the CCD pixelation presentation  $P_d$  on the sample along the measured profile direction, which can consequently calculate the lateral measurement range/FOV of the system. Figure 7.8 shows the image of the target using a 4X objective and the curve representing relationship between divisions and pixelation (only showing 265 pixels). It was found that a length of 50 μm is covered by every 34 pixels, which means each pixel along the vertical direction represents 1.47 μm on the tested surface. Then the lateral measurement range along x axis can be calculated as 705.6 μm by equation (6.4), which represents the effective length of surface profile tested by the objective for each measurement. The calibrated FOV closely aligns with the theoretical calculation in equation (7.3).

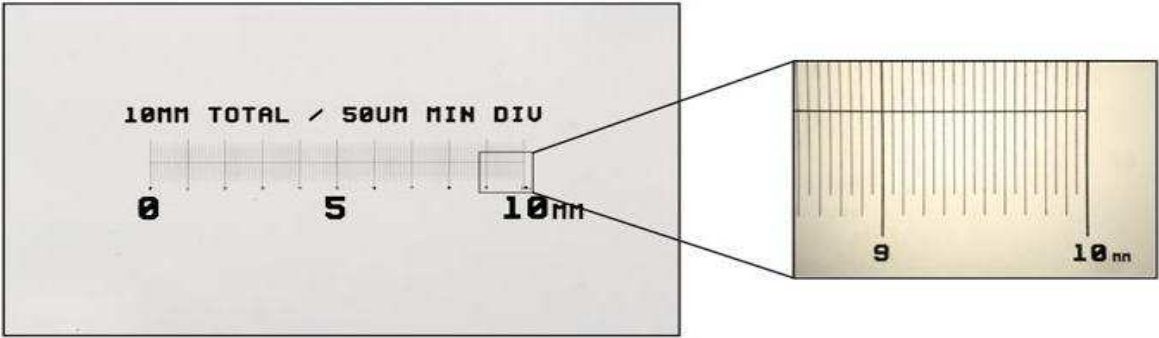


Figure 7.7 Microscope slide R1L3S1P under magnification [adapted from Thorlabs, Inc.]

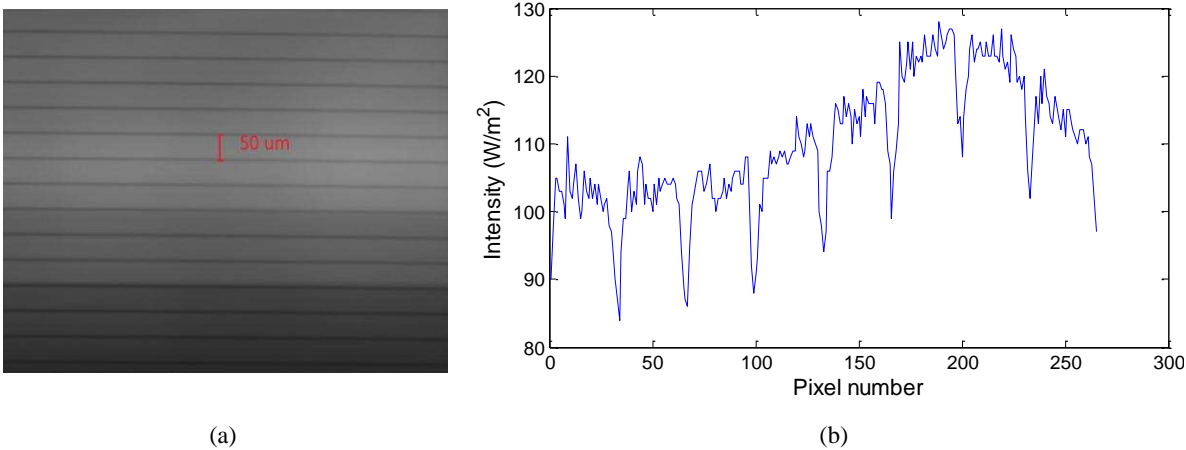


Figure 7.8 Determination of the CCD pixelation: (a) image of the stage micrometre using 4X objective, (b) relationship between divisions and pixelation.

Lateral resolution of the microscope-LSDI is limited by two factors, namely optical resolution and pixel-limited resolution. The optical resolution varies with the NA of the objective. Systems with a low magnification objective may suffer from the camera-limited issue. Practically, determination of the lateral period limit using a sinusoidal artefact can be used to evaluate the lateral resolution for a 3D optical interferometer (Giusca & Leach, 2013). In this thesis Rayleigh criterion expressed in equation (7.4) is applied to theoretically calculate a useful approximation to understand the expected behaviour in terms of lateral resolution.

$$\delta_{\text{Rayleigh}} = 0.61\lambda / \text{NA} \quad (7.4)$$

This resolution is not a constant value because broadband illumination is used for measurement. For the 4X objective with the NA of 0.1, the theoretical optical resolution calculated at the maximum wavelength 670.02 nm is 4.087  $\mu\text{m}$ . Compared to the calculated pixelation result (1.47  $\mu\text{m}$ ), it shows that the lateral resolution of the developed system is restricted by the diffraction limit, not pixel-limited.

#### 7.4.2 Axial measurement range

The wavelength calibration shows that the chromaticity axis covers the spectrum with a bandwidth of 53.5 nm (centred at  $\lambda_0 = 596$  nm), which provides a per pixel bandwidth of  $\delta_\lambda = 0.08$  nm. Therefore, the theoretical maximum axial measurement range of microscope-LSDI is calculated as 1.29 mm by equation (6.5). Experimentally, a micro fluid chip with a step height of 100  $\mu\text{m}$  was measured using the designed prototype. The step can be well resolved and the measured average height is 101.479  $\mu\text{m}$ . The LSDI measurement results are shown in Figure 7.9.

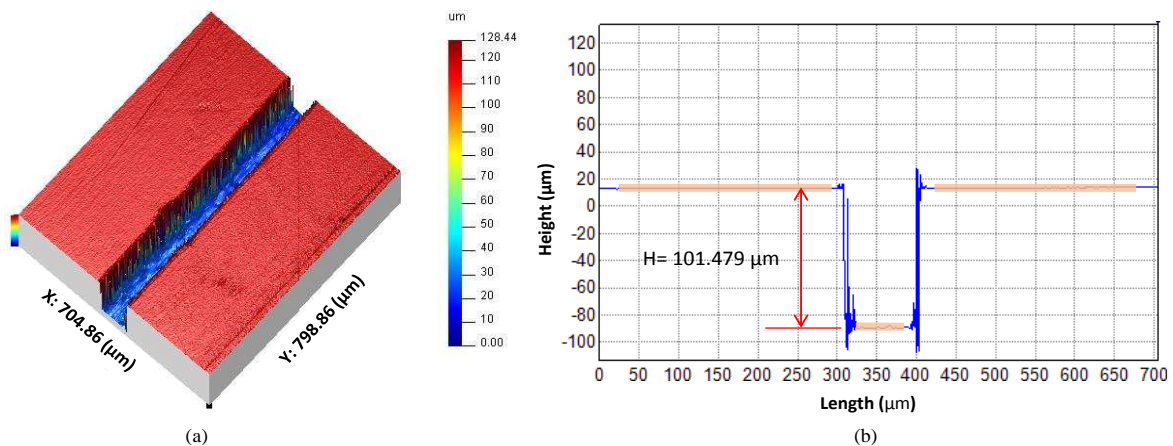


Figure 7.9 Results for micro fluid chip-100  $\mu\text{m}$  step height: (a) measured surface, (b) cross-sectional profile.

### 7.4.3 Angular measurement range

The angular measurement range for microscope-LSDI is assessed by theoretical calculation using equation (6.6). For the interferometric objective with the NA of 0.1, the maximum measurable surface slope can therefore be calculated as  $\pm 5.7^\circ$  for samples with well-polished surfaces. Likewise, a sample with higher slopes ( $> \pm 5.7^\circ$ ) still may be characterised if it is manufactured with a rough surface.

### 7.4.4 Measurement noise

To evaluate the measurement noise of the microscope-LSDI prototype, the same flat sample and technique described in section 6.6.4 were adopted. The measured profiles with roughness components are depicted in Figure 7.10(a), which have a maximum PV value of 55.36 nm over the evaluated length of 705.6  $\mu\text{m}$ . Figure 7.10(b) shows the four new profiles after isolating the roughness and the measurement noise can be obtained by measuring the  $R_q$  values of these scale limited profiles, as listed in Table 7.2. The calculations show that the developed prototype has a average measurement noise of 3.095 nm with an associated standard deviation of 0.03 nm, which is acceptable because the calibration was carried out in the normal optics laboratory.

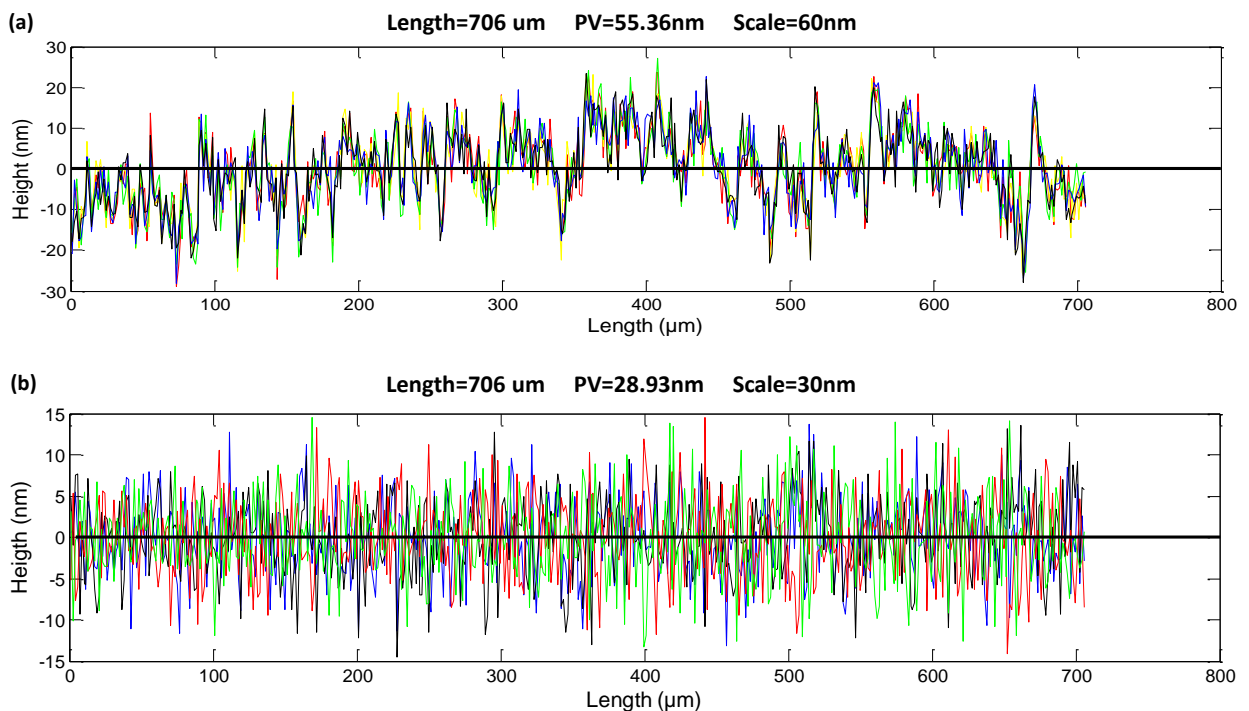


**Figure 7.10** Subtraction technique for estimating the measurement noise of microscope-LSDI: (a) five profiles with surface roughness, (b) four new profiles after removing the intrinsic roughness.

**Table 7.2 Measurement noise evaluation of microscope-LSDI**

$M_{\text{noise}}$ (nm)				Average $\overline{M_{\text{noise}}}$ (nm)	Standard deviation $\sigma$ (nm)
3.061	3.129	3.075	3.116	3.095	0.03

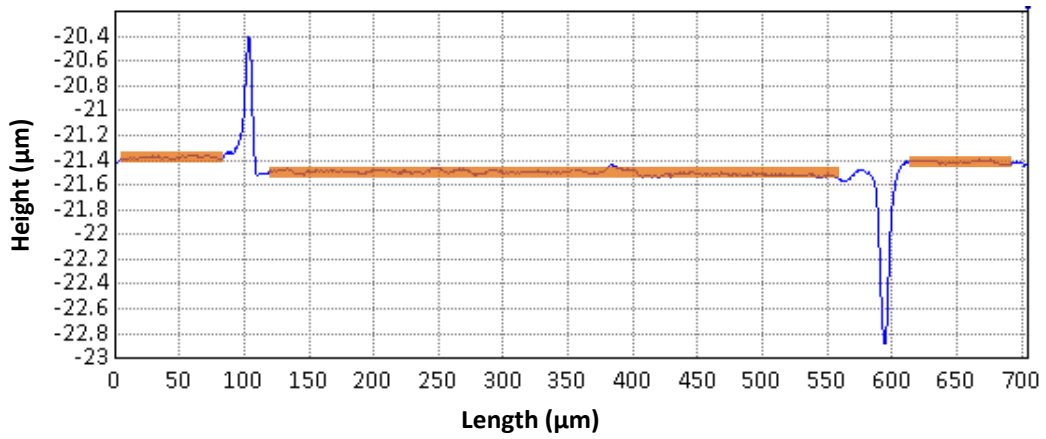
### 7.5 Application 1: Evaluation of step height samples

Evaluation of step height samples is one of the most popular applications for the developed metrology system. Two step height samples with height values of 100 nm and 500 nm were measured to confirm the performance of microscope-LSDI prototype.

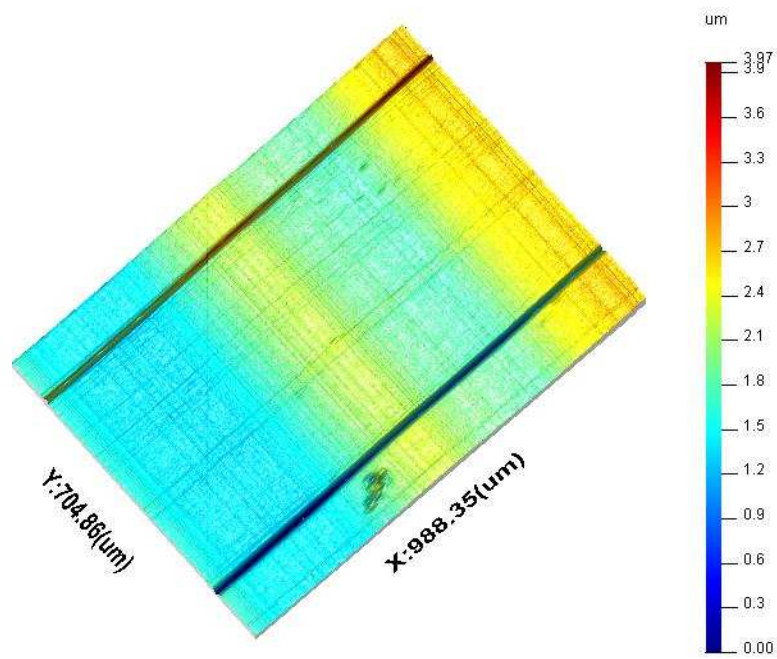
First, to verify a good precision of the metrology system, a standard sample from NPL (National Physical Laboratory) with step heights of 100 nm was measured and the results are shown in Figure 7.11. The corresponding measurement results obtained by CCI 3000 at almost the same area are provided in Appendix C.4 as the traceable reference (measured average height: 103.5 nm). The surface profile acquired by microscope-LSDI has an average height of 104.9 nm, which is in good agreement with the result by CCI. The measurement results demonstrate that the developed prototype has nano-scale resolution enabling precise surface metrology in terms of quality assurance.

By keeping the sample still and measuring the same profile on the sample many times in quick succession, the measurement repeatability can be evaluated using equation (6.10). Other three of metrological characteristics, namely amplification coefficient, linearity error and perpendicularity of the axes, require a series of measurements of a range of artefacts with various heights and will be investigated as the future work for system calibration.

Another sample manufactured by Rubert & Co. Ltd. with step height of 500 nm was measured as well. The measurement results by CCI 3000 and microscope-LSDI were obtained with a consistence between them, which are shown in Appendix C.5 and Figure 7.12. The height values of one measured profile listed in Table 7.3 show that there is around 20 nm difference between the step surfaces of the sample ( $H_1$  versus  $H_2$ ), which may result from the manufacturing errors or damage sustained after a prolonged period of use. However, it has no influence on the assessment of the LSDI's performance.



(a)

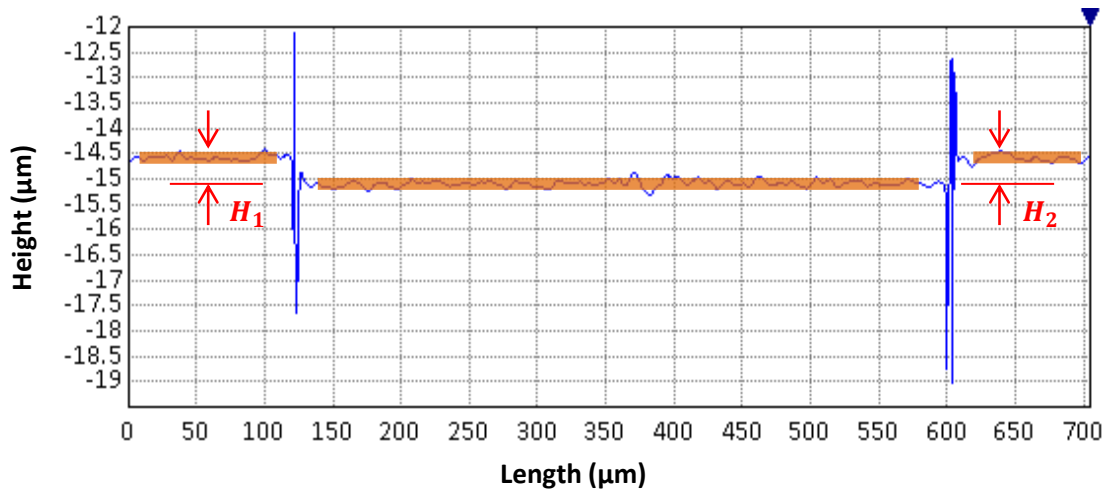


(b)

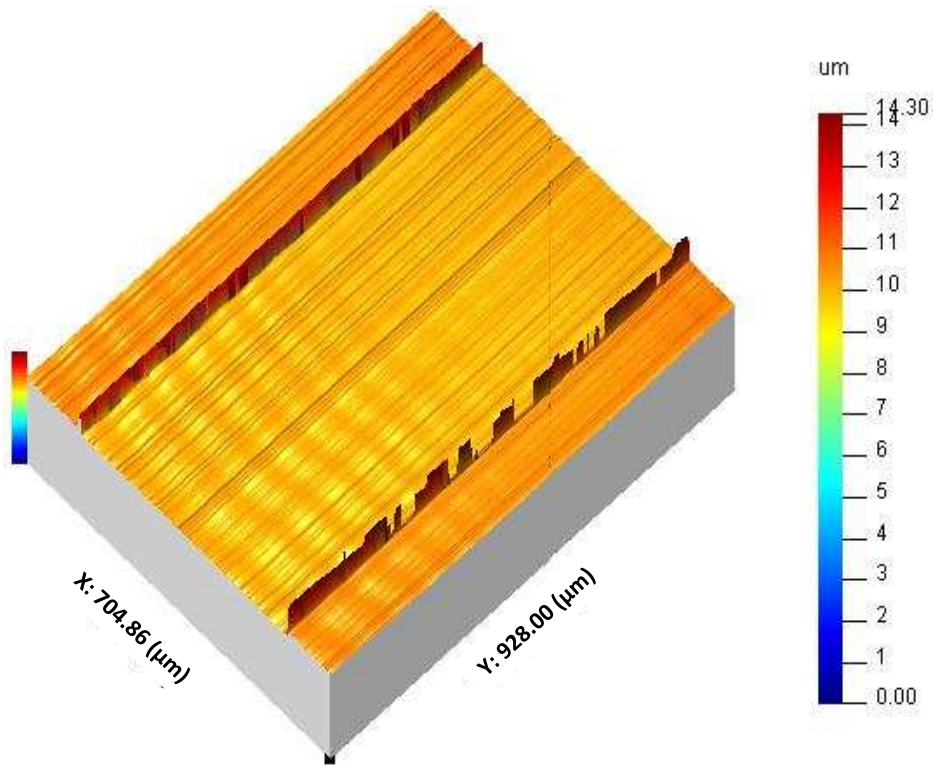
Figure 7.11 Measurement results for 100 nm standard step height sample: (a) surface profile using FFT algorithm, (b) constructed surface map through scanning.

Table 7.3 Measured average heights of 500 nm step height

Average step height values (CCI 3000)		Average step height values (Microscope-LSDI)	
H <sub>1</sub>	H <sub>2</sub>	H <sub>1</sub>	H <sub>2</sub>
449.8 nm	463.11 nm	462.1 nm	486.6 nm



(a)



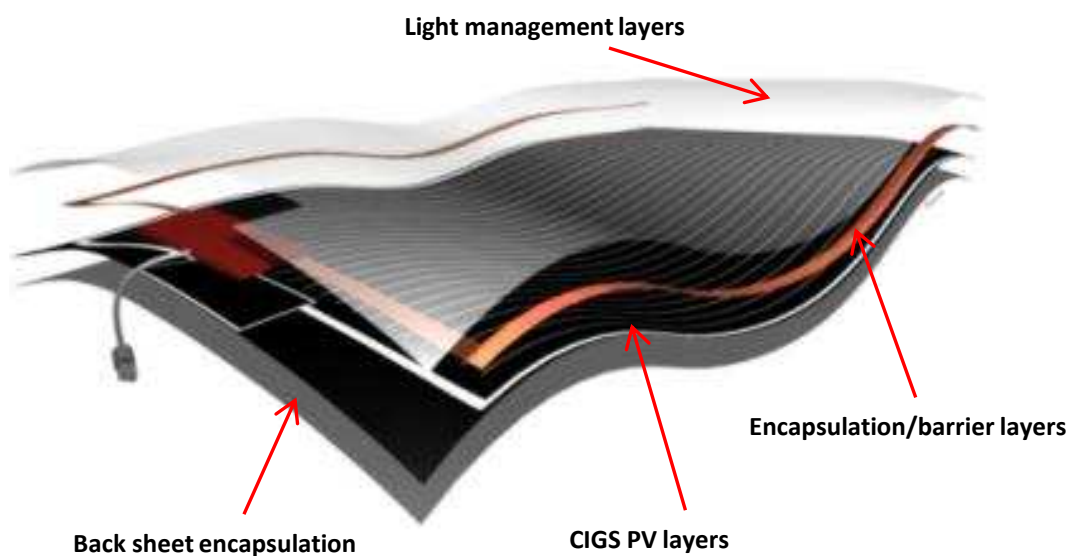
(b)

Figure 7.12 Measurement results for 500 nm reference step height sample: (a) surface profile using FFT algorithm, (b) constructed surface map through scanning.

## 7.6 Application 2: In-line defect detection for PEN film surface

R2R technology has been adopted to fabricate multi-layer flexible devices for achieving a reduction in production costs and throughput time. Such flexible PV films technology is widely

used in integrated field through offering particular design option and extends its applications to Building-Integrated-Photovoltaic products (Elrawemi, et al., 2013; Schwager, 2012). Figure 7.13 shows schematic of the flexible PV Module. In order to maintain high performance and a long lifespan, an effective barrier is required to protect the active elements from environmental degradation due to water and oxygen ingress. It has been proved that a thin coating of Aluminium oxide ( $\text{Al}_2\text{O}_3$ ) by atomic layer deposition (ALD) is an effective transparent barrier film for providing the environmental protection for the PV cells because of its uniformity and pinhole-free morphology (Ali et al., 2015; Carcia, et al., 2006; Cimalla et al., 2014; Hegedus et al., 2010).



**Figure 7.13 Schematic of the flexible PV Module [adapted from Flisom, Switzerland]**

However, some function-affecting defects are inevitably generated during the manufacturing processes of multi-layer film products. Actually, one of the biggest challenges faced by industry when using R2R is characterisation of surface roughness, defects, and other imperfections due to their great influence on functional performance. It has been demonstrated that defects especially present on the barrier film during  $\text{Al}_2\text{O}_3$  ALD process are significant in the deterioration of the PV module efficiency and lifespan. Some work has been carried out on the correlation of water vapour transmission rate (WVTR) and the significant defects (different types and sizes) present on the barrier substrate using areal surface metrology (Blunt et al., 2013). WVTR is a parameter used to represent the passage of water vapour through the films and can be measured using a standard MOCON test. It was found that defects on the  $\text{Al}_2\text{O}_3$  barrier film correlating with high

WVTR can be classified into four main types, namely pit holes, particulate debris, delamination and surface relief (Elrawemi et al., 2014; Rebeggiani, 2013). Figure 7.14 shows some main defects present on the PEN film substrate using AFM.

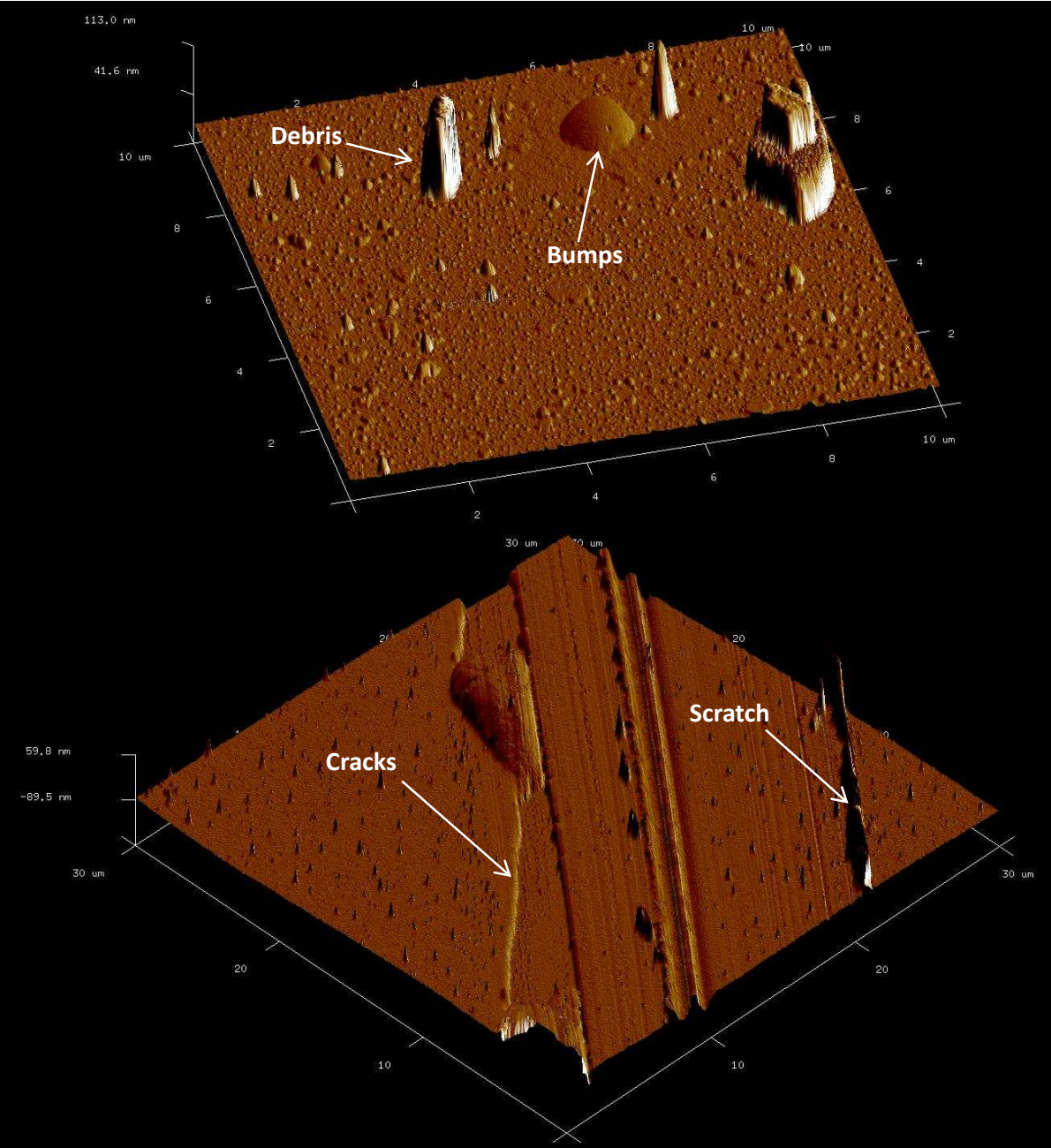


**Figure 7.14 Main defects present on the PEN film substrate by AFM [Adapted from Elrawemi, 2015]**

Therefore, surface inspection needs to be performed during the R2R manufacturing process in order to detect these significant defects and finally guarantee that the barriers are in good condition. As discussed in chapter 1, defect assessment can be performed using many techniques

such as optical microscopy, scanning electron microscopy and optical interferometry. However, the key challenge of in-line metrology requires inspection of the foil surface with a sufficient resolution as well as at a production speed, which makes the microscope-LSDI a good solution for defect assessment due to its advantage of single shot measurement. This section will present detection of the defects on a multi-layer PEN film using the developed microscope-LSDI prototype.

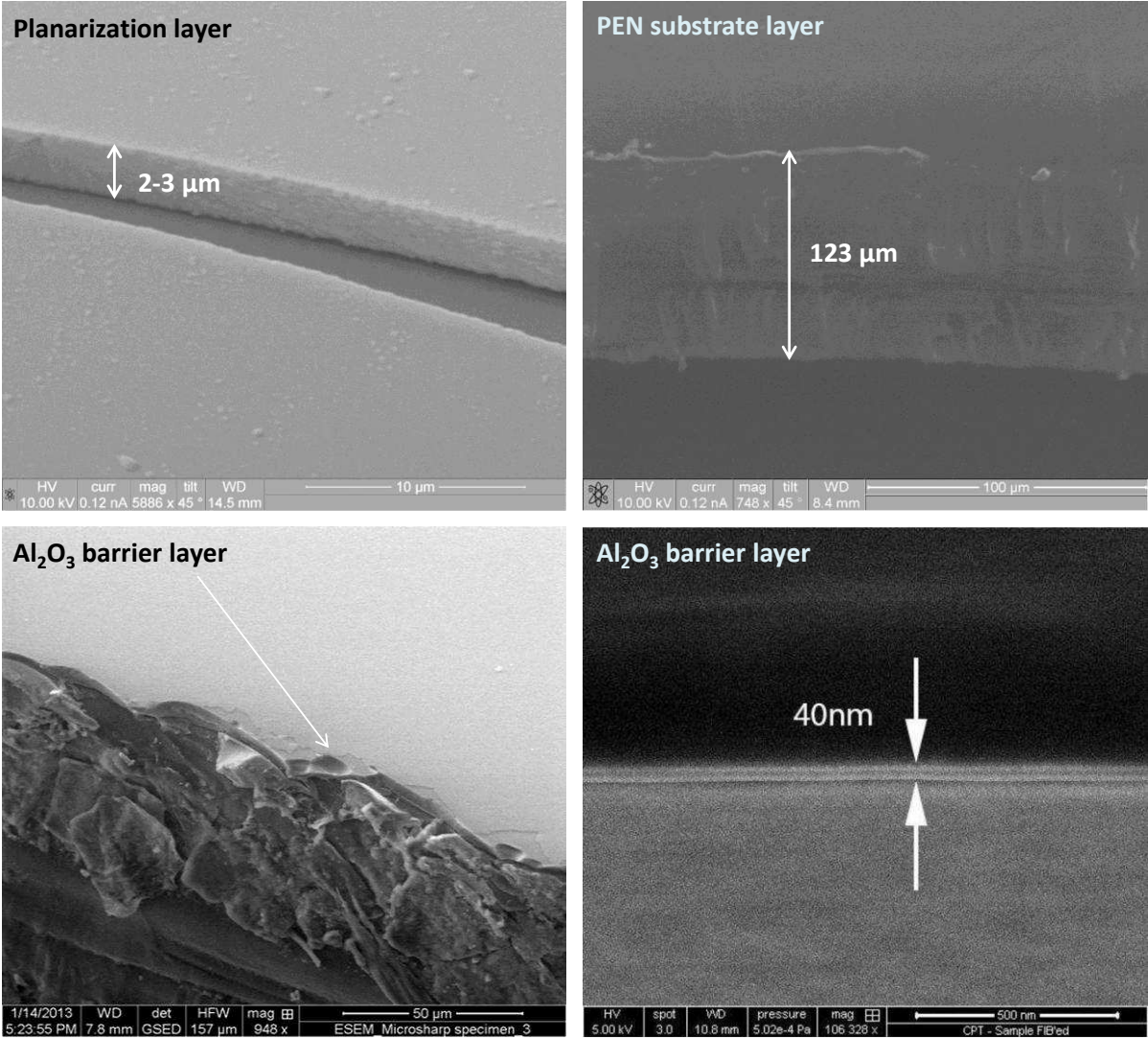


**Figure 7.15 Structure of the PEN film by Environmental Scanning Electron Microscopy (ESEM) [Adapted from Elrawemi, 2015]**

The PEN film sample, manufactured by the Centre for Process Innovation (CPI), is composed of three layers, namely a PEN substrate layer (120-123 μm), a planarization layer (2-3 μm) for planarising the pits and spikes features on the PEN substrate and lastly an ALD barrier

(40 nm) for prevention of moisture and oxygen ingress. Figure 7.15 clearly shows the structure of the PEN film sample by Environmental Scanning Electron Microscopy.

The defects on the PEN film sample can also be observed by camera 1 equipped in the developed metrology system, as shown in Figure 7.16. In order to better understand the performance of the developed LSDI, two areas with some significant defects have been selected for inspection. The raw results acquired by Talysurf CCI 3000 (a) and LSDI (b) are shown in Figure 7.17 and Figure 7.18 without any data post-processing such as surface levelling and filtering. The measured surface map shown in Figure 7.17(b) and Figure 7.18(b) are generated by numbers of profiles which represents a scanning length of 2.31 mm. The surface topography results shown in Figure 7.17 and Figure 7.18 have different forms which mainly result from the different surface tensions generated when fixing the film sample in the two separate measurements. The acquired results demonstrate that LSDI is capable of detecting most of the defects detectable by CCI and that the relative positions between the detected defects are well matched. To further validate the performance of microscope-LSDI, surface levelling and form removing were performed on the raw data in Figure 7.17. Seven film function-affecting defects were selected and labelled for investigation in terms of the size and the location, as shown in Figure 7.19.

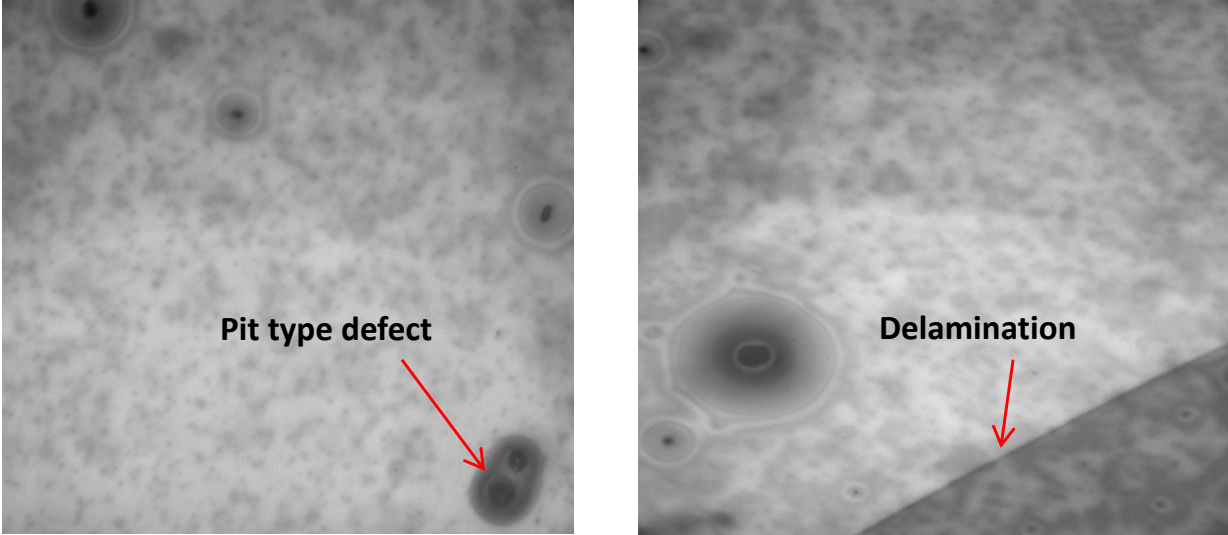


**Figure 7.16 Images of defects observed by camera 1 in microscope-LSDI prototype**

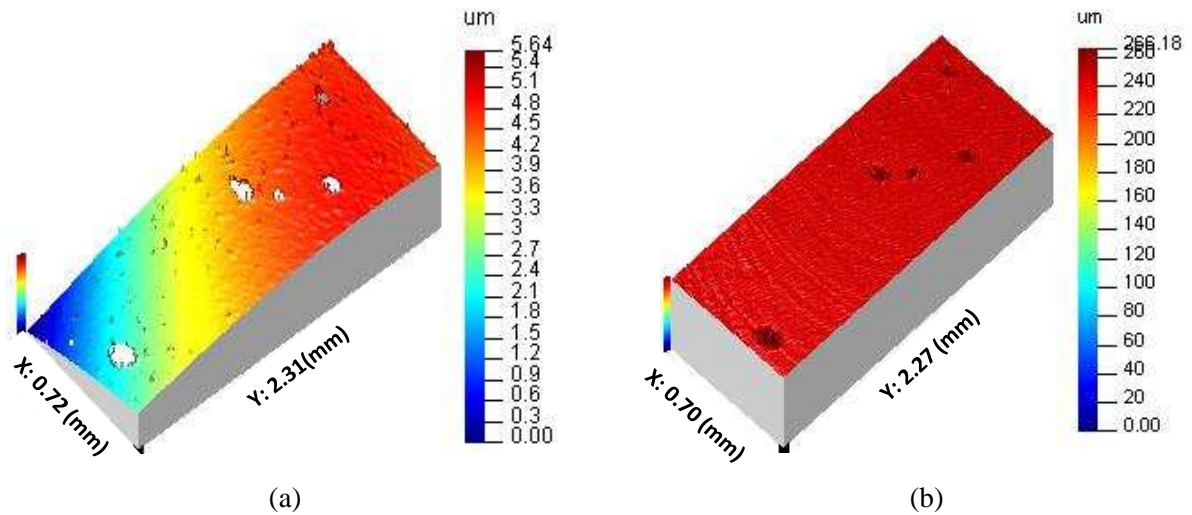


Figure 7.17 Surface map of defects on the area 1 of the barrier film surface (raw results without data post-processing): (a) CCI result, (b) LSDI result.

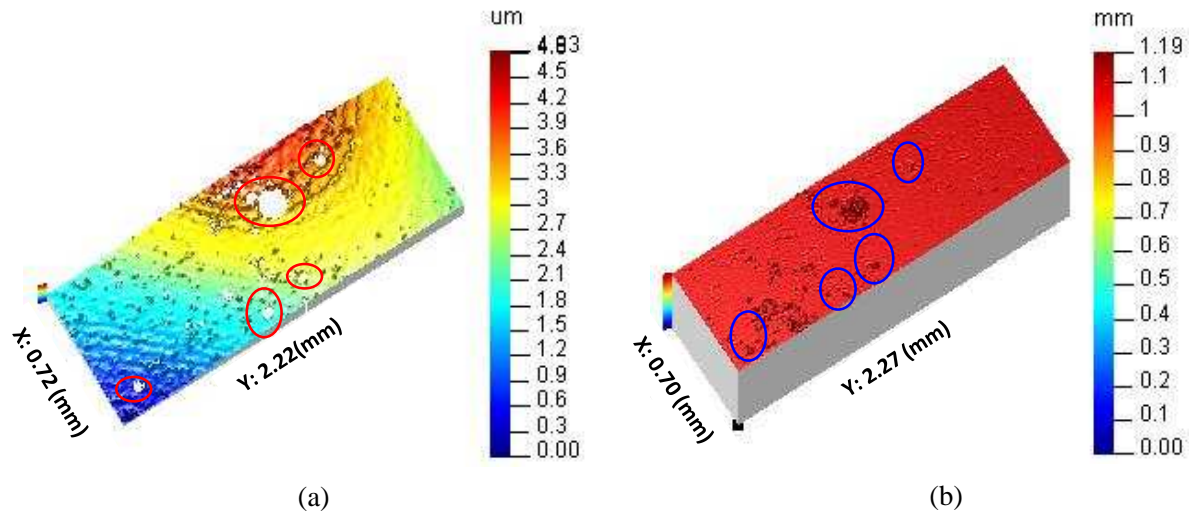


Figure 7.18 Surface map of defects on the area 2 of the barrier film surface (raw results without data post-processing): (a) CCI result, (b) LSDI result.

The sizes of the defects were determined by measuring length and width along the vertical axis, x, and the horizontal axis, y, respectively. The position of defect 1 was set as a reference point (see Figure 7.19(b)) to acquire the relative positions of other 6 defects. Then the defect specifications for both LSDI and CCI are obtained and listed in Table 7.4. The sizes and positions of the defects correlate well between the CCI measurement of the sample and the measurement performed using LSDI. Considering the effect from experimental conditions such as different fixed modes of the sample, different measuring principles (profile measurement

versus areal measurement) and scanning errors from the linear translation stage, the measurement differences of the sizes and the relative positions are tolerated and do not affect the assessment of LSDI's performance because only successful defect detection is concerned for this measurement.

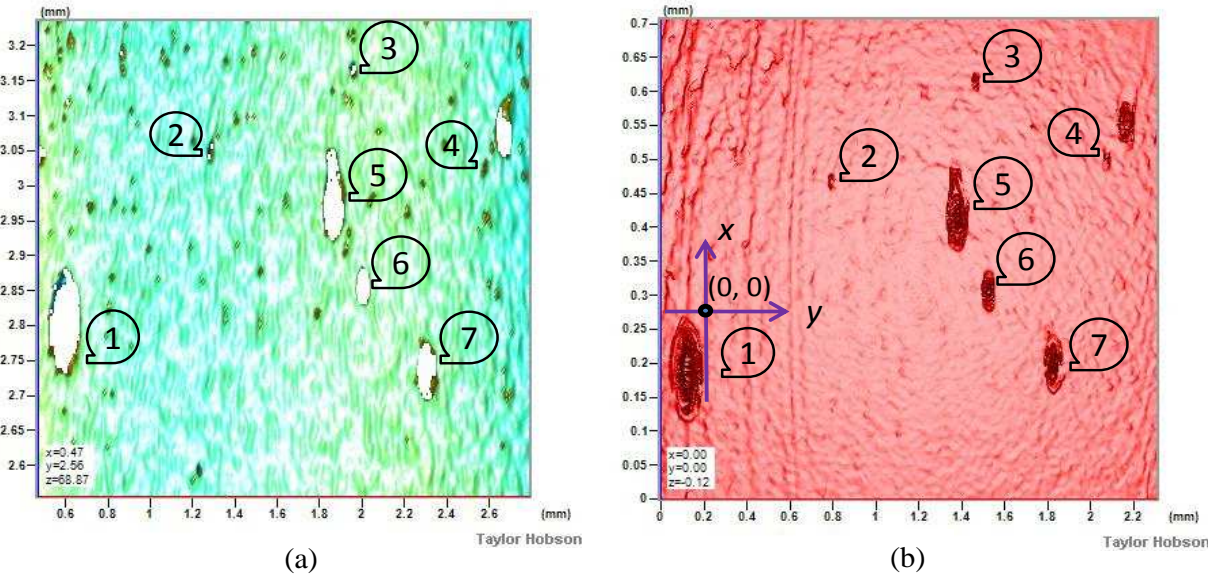


Figure 7.19 2D view of defects on the Al<sub>2</sub>O<sub>3</sub> ALD barrier film surface (performed data processes such as form removing and levelling): (a) CCI result, (b) LSDI result.

Table 7.4 Defects specifications (size, location)

	Size width×length (mm)		Position (x, y) (mm)	
	CCI	LSDI	CCI	LSDI
<b>Defect 1</b>	0.17×0.17	0.17×0.16	Reference point (0, 0)	
<b>Defect 2</b>	0.03×0.04	0.03×0.04	(0.20, 0.62)	(0.21, 0.61)
<b>Defect 3</b>	0.05×0.03	0.05×0.03	(0.34, 1.30)	(0.36, 1.29)
<b>Defect 4</b>	0.04×0.03	0.04×0.03	(0.19, 1.91)	(0.24, 1.90)
<b>Defect 5</b>	0.12×0.14	0.12×0.14	(0.20, 1.25)	(0.23, 1.24)
<b>Defect 6</b>	0.08×0.05	0.08×0.06	(0.04, 1.37)	(0.07, 1.36)
<b>Defect 7</b>	0.10×0.09	0.10×0.09	(-0.10, 1.68)	(-0.05, 1.68)

The results above verified that the proposed LSDI has a good performance for defect assessment. Requiring only one shot for a surface profile makes it an environmentally robust metrology sensor with instantaneous measurement. The limitation of this system, when

considering the challenge of in-line metrology in high speed production lines, has been determined to be the camera speed and computing speed. In theory, the microscope-LSDI can inspect moving samples with a speed of 1.2 m/min by using a camera capable of capturing 2000 frames per second to detect the defects with size large than 10  $\mu\text{m}$ . Furthermore, utilisation of updated GPUs will achieve data parallelism and then surface profiles can be presented in real-time. Overall, the developed prototype may potentially be suitable for rapid in-line metrology for defects detection on flexible PV film surfaces.

### 7.7 Investigation of the effect from environmental disturbances

In general, environmental disturbances such as vibration and air turbulence can cause variations of the OPD between the two arms of the interferometer, and subsequently produce measurement errors if they exceed the measurement resolution (Muhamedsalih, 2013). In this section, the effect of environmental disturbances to the LSDI's performance is approximately evaluated by artificially introducing vibration and air turbulence. Figure 7.20 shows the interference patterns of the same row captured at certain time interval. Due to the environmental disturbances the numbers of fringe cycles of the signals have changed. However, it does not mean that the measured profile will be greatly affected. Because close variations of fringe cycles will be applied to all row signals within the whole frame if a fast camera is used, an offset of approximately the same magnitude is generated in the absolute distances for every point along the surface profile with respect to the reference plane.

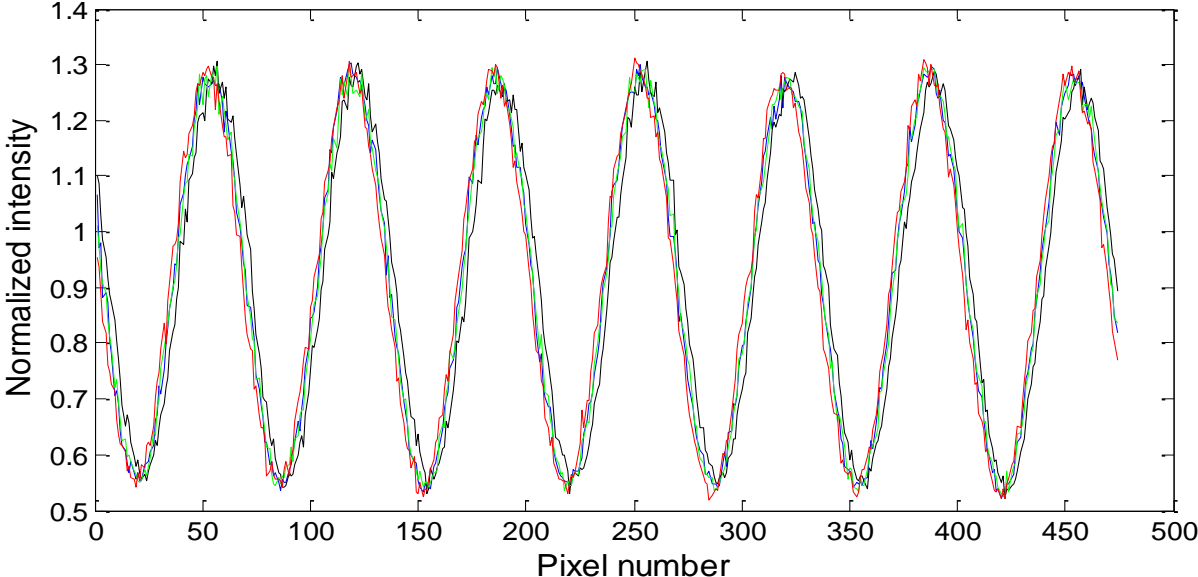
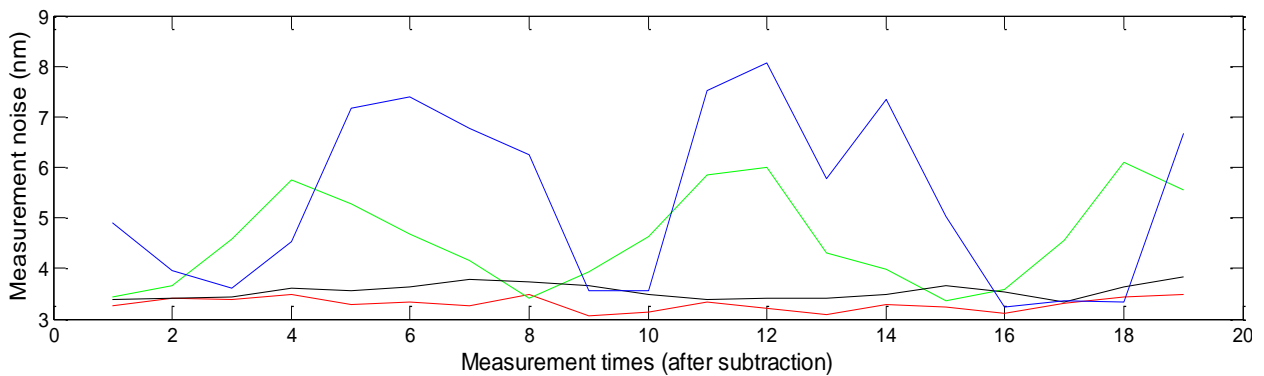


Figure 7.20 Interference signals affected by the environmental disturbances

The same surface profile on the standard flat artefact ( $S_q = 4 \text{ nm}$ ) was measured 20 times under each different environmental condition such as no additional environmental noise, air turbulence applied, vibration applied and the combination of vibration and air turbulence. The vibrations generated by all these environment disturbances have a frequency within the range of 20-200 Hz.

The measurement noises were calculated using a subtraction technique to investigate the environmental effect to the measurements, as shown in Figure 7.21 and Table 7.5. The Mean values of measurement noises corresponding to the environmental conditions mentioned above are 3.294 nm, 3.549 nm, 4.569 nm, 5.4370 nm, respectively. The nanoscale variations of measurement noises are acceptable for defects inspection in terms of quality assurance.

Actually, since the CCD camera used in the developed sensor has a frame rate of 208 fps, it can achieve minimised effects resulting from the external perturbations and environmental noises provided that the disturbance frequency in the manufacturing shop is less than 200 Hz. The obtained results in this investigation will vary with the frequencies of the environmental noise and the camera capturing speed. Enhancement of the camera speed will shorten the capturing time of each interferogram and can further reduce the environmental effect to the system. It also means that the developed LSDI sensor is capable of enduring a higher level of environmental disturbance as well as keeping high measurement accuracy. On the whole, the developed instantaneous LSDI system is environmentally robust to carry out real time measurement on most of the shop floor.



**Figure 7.21 Measurement noise curves under different environmental conditions. Red line, almost no environmental noise; Black line, air turbulence applied; Green line, vibration applied; Blue line, vibration & air turbulence applied.**

**Table 7.5 Measurement noises under different environmental conditions**

	Average $\overline{M}_{\text{noise}}$ (nm)	Standard deviation $\sigma$ (nm)
<b>No environmental disturbances</b>	3.294	0.1331
<b>Air turbulence applied</b>	3.549	0.1485
<b>Vibration applied</b>	4.569	0.9360
<b>Vibration &amp; Air turbulence applied</b>	5.370	1.7184

By combining the 20 measured profiles obtained under different experimental conditions into surface maps, the results in Figure 7.22 can be acquired. It can be observed that surface irregularities with waviness of different frequencies are generated due to changes of OPDs in the construction direction. These waviness frequencies are also dependent on the frequencies of the applied disturbances and the capturing speed of camera. For the developed LSDI, surface irregularities do not affect the surface profile measurement because each profile is processed individually using a single frame.

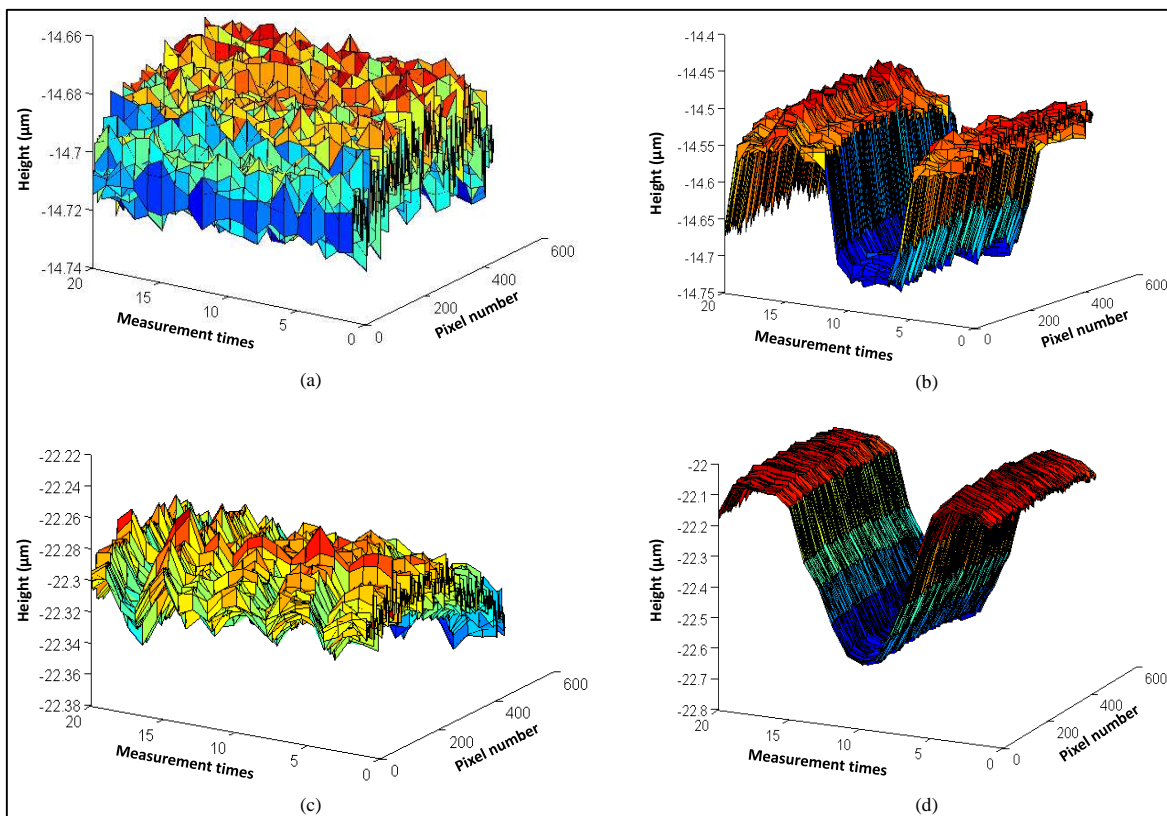


**Figure 7.22 Surface maps constructed by 20 surface profiles: (a) almost no environmental noise, (b) vibration applied, (c) air turbulence applied, (d) vibration & air turbulence applied.**

## 7.8 Summary

This chapter presents a microscope-LSDI which aims at characterisation of surface features and defects in micro-scale (diffraction-limited resolution: 4  $\mu\text{m}$ ). The initial developed prototype has a theoretical axial measurement range of 1.29 mm and angular measurable range of  $\pm 5.7^\circ$  for polished surface. A measurement noise of 3.095 nm for the developed microscope-LSDI is acceptable since the calibration was conducted in normal optics laboratory. The lateral measurable range was calibrated as 705.6  $\mu\text{m}$  for the 4X interferometric objective using a microscope slide with 50  $\mu\text{m}$  vacuum sputtered divisions, which is in good agreement with the theoretical calculation.

Two step height samples were inspected using the developed prototype to evaluate the system's performance. The measurement results acquired using both LSDI and commercial instrument CCI align with each other acceptably. The measurement of 100 nm step sample demonstrated that the developed LSDI has nano-scale measurement repeatability enabling precise surface metrology for quality assurance.

Defects produced during R2R manufacturing processes are significant in the deterioration of the performance and lifespan of such film products. Therefore, implementation of the LSDI to detect the defects present on the PEN film is presented in detail. The measurement results verified that LSDI is capable of detecting most of the defects detectable by CCI, and the sizes and locations between the detected defects are well matched. By combining a high speed camera with GPUs and multi-core processor computing technology, the required time for frame grabbing and data processing can be further reduced, enabling this system to be qualified for real-time surface inspection. On the whole, the proposed system offers an attractive solution for quality assurance in R2R manufacturing processes and will consequently enhance the performance as well as the yield of the PV film products.

Lastly the effect from the environmental disturbances is investigated as well. The analysis results shows the developed LSDI is capable of minimising the effect of external perturbations and environmental noise and is environmentally robust for use on the shop floor by performing instantaneous measurement in a single shot.

## 8 Conclusion and Future Work

### 8.1 Discussion

With the development of advanced manufacturing technologies such as R2R and AM techniques, ultra-precision surfaces are enabled to be fabricated with increasingly large areas and complicated structures. Process control is a necessity during manufacturing processes for ensuring great performance of a work piece. For this purpose, applicable metrological techniques which meet the demands of modern manufacturing need to be developed to characterise the functional surface of workpiece. The costly trial-and-error approach is not capable of matching the ongoing evolution in advanced manufacturing in terms of cost-effectiveness as well as high product yield. This is a driving factor for the development of in-line metrology which can be utilised on production lines to guarantee the high performance of the products. Metrology performed in manufacturing environment requires the measurement systems to be environmentally robust, fast, reliable and easily integrated into machine. The line-scan dispersive interferometry investigated in this thesis offers a promising solution for in-line metrology. This technique can obtain a surface profile in a single shot without any mechanical scanning in depth direction, enabling instantaneous measurement on the shop floor with minimal effects from the environmental disturbances.

In principle, the developed metrology device is comprised of four main parts, namely light source, interferometric objective, spectrometer and data processing unit. The light device is a separate entity, which provides the broadband low-coherence white light for the interferometer. The interferometric objective works as the optical probe to observe the tested surface with a specific FOV. There is a trade-off to be made between the measurement range and lateral resolution according to the requirements of the metrological application. The Michelson type of interferometric objective has a good balance of the optical aberrations between the two arms of the interferometer and is simple to align. The spectrometer is used to spatially disperse the interference beam along the chromaticity axis of the CCD camera, in which way an extended axial measurement range is achieved without the  $2\pi$  phase ambiguity problem. The axial measurable range of LSDI technique has an overwhelming advantage over conventional interferometry. The higher spectral resolution is achieved by the spectrometer, the larger a measurable range can be acquired in depth. The optimal angle of the diffraction grating with

respect to the optical axis can be determined when a nearly linear distribution of spectrum on the camera is acquired. The data processing unit interprets each spectral interferogram using algorithms with nano-scale resolution to acquire the height information of a surface profile. Additionally, the measurement speed can be further accelerated through using a high speed camera for data capturing and GPUs for data parallelism.

In practice, alignment of the optical components has significant influence on the system's performance. For instance, improper position of the camera may result in low fringe visibility and the overlap of two adjacent spectral lines. The optical software ZEMAX is employed to simulate the LSDI system in terms of various alignment errors, which provides a good basis for assembly of the optical apparatuses. The simulations show that the tip/tilt of beamsplitter in the interferometric objective changes the OPD of the interferometer due to the optical axis deviation, and large offset of the collimator along the optical axis affects the collimation quality which consequently causes distortion of spectral lines on the camera.

Two developed optical apparatuses, different in the interferometric objectives used, can be used for different applications. The cylindrical-LSDI has an advantage of long profile measurement, which is effective for large range metrology of the functional surface on a production line and is suitable for surface inspection in terms of surface textures, forms and blemishes with sizes of tens of micrometres. However, the lateral resolution of cylindrical-LSDI becomes an issue for consideration of the enhancement for applications where the smaller structure dimensions and features on the tested surface need to be resolved. Then the second prototype, microscope-LSDI, has a higher lateral resolution using a 4X objective as the optical probe and aims at characterisation of surface roughness, defects with size of few micrometres and other imperfections of ultra-precision surfaces. One of the most promising applications for the microscope-LSDI is to detect the defects present on the R2R film surface for quality control. By properly arranging the optics, both of the optical apparatuses can achieve the axial measurable range up to a few millimetres, which is a difficult task for other interferometric techniques such as PSI and WSI.

## **8.2 Conclusion**

The aim of this project is to investigate the potential for using line-scan dispersive interferometry for in-line metrology in manufacturing environments in terms of quality assurance. Two proof-of-concept prototypes, having different performances in lateral

measurement range and resolution and being used in different metrological tasks, have been developed for this purpose. Both of them perform surface profile measurement without mechanical scanning.

One of the achievements in this thesis is development and demonstration of a single shot cylindrical-LSDI with long profile measurement capability. Due to the geometrical imaging characteristics of the cylinder, the tested surface is observed by a focused line beam. Therefore, implementation of the cylindrical-LSDI offers one possible solution to achieve large-scale measurement of the additively manufactured products. Through a series of measurements of a range of reference samples, the system's performance has been experimentally evaluated. For instance, the lateral measurable range of the cylindrical prototype was calibrated as 5.885 mm using a USAF target. A 200  $\mu\text{m}$  step height and four spherical mirrors were used to evaluate the axial and angular measurable range, respectively. On the whole, the cylindrical-LSDI was demonstrated with good measurement accuracy by successfully measuring step samples ranging 100 nm to 200  $\mu\text{m}$  with measurement results closely aligning with the commercial instrument CCI 3000.

The second contribution is development and demonstration of an instantaneous microscope-LSDI (using a 4X interferometric objective of Michelson type) to provide micro-scale lateral resolution for precise surface characterisation and defect detection. For this optical apparatus, real-time image of tested surface can be displayed as well using an extra camera in one of the branches of the optical arrangement. Likewise, experimental investigations were performed to evaluate the actual capability of the microscope-LSDI using different samples for surface profile measurements. In addition to the popular application of measuring step samples, implementation of the microscope-LSDI to detect the defects present on the  $\text{Al}_2\text{O}_3$  barrier film surface was investigated in particular. By detecting most of the defects detectable by CCI as well as good agreements between measurement results in terms of sizes and relative positions, the metrology device offers an attractive solution for quality assurance in R2R manufacturing process.

The third contribution in this thesis is development of the efficient and accurate algorithms to analyse the spectral interferogram. The measurement results obtained by the two algorithms (FFT algorithm and the Carré algorithm) are in good agreement with each other. Since the FFT algorithm has a faster computing speed, it is an optimal option for the in-line metrology applications where instantaneous measurement is required in terms of processing speed to

achieve presentation of the surface profile in real-time. Additionally, further acceleration of computing process through data parallelism using GPU technology (based on FFT technique) was demonstrated in this research project.

On the whole, the developed metrology sensors were demonstrated with good performances in the measurement accuracy and speed. The process time is only 125 ms for a single interferogram and can be improved further by updating the algorithm and hardwares of the computer. The measurement noises of cylindrical-LSDI and microscope-LSDI are given as 6.287 nm over the evaluated length of 5.885 mm and 3.095 nm over 705.6  $\mu\text{m}$ , respectively. Considering the calibrations were performed in the normal optics laboratory, the obtained results are acceptable for these two initial prototypes at this research stage. Additionally, the environmentally robust feature of the LSDI technique was investigated experimentally as well. Performing profile measurement in a single shot without any mechanical scanning allows the LSDI technique to minimise the effect from the external vibration and air turbulence.

The outcome of the research work illustrated in this thesis is to validate the feasibility of using LSDI technique for in-line metrology of functional surface for quality control. Improvements however can be made in several aspects to enhance the LSDI's performance such as measurement speed, accuracy and device size, which will be presented in the following section as future work.

### **8.3 Future work**

Future work can be carried out for further improvement that will enable enhanced metrology systems in terms of compactness, accuracy and data acquisition and analysis speed. The main aim is to implement the LSDI device for nano-scale in-line surface metrology on the shop floor.

- The LSDI device is to be optimised in terms of both axial resolution and lateral resolution to allow for in-line metrology of surface roughness and additive manufacturing products. The prototypes currently have been developed using the objectives with magnification of 4X and fixed focal length of 75 mm, respectively. To make the metrology system versatile across various applications, implementation of prototypes equipped with various magnifications of interferometric objectives is to be investigated to enable surface profile measurements with different FOVs, resolutions and angular measurable ranges. By choosing an objective with high magnification, the lateral resolution can be improved directly. For improvement of axial resolution, optimisation of the metrology device in

terms of accurate algorithms, precise alignments and minimal measurement noise needs to be investigated. More specifically, by using a 20X Mirau type objective in microscope-LSDI the lateral resolution can be raised to  $0.9\ \mu\text{m}$  in sub-micrometre level and the angular measurement ability theoretically allows the surface slope with angle up to  $23.6^\circ$  to be tested. The enhanced system may potentially to be used for characterisation of the precise surface after post-process. Likewise, by using cylindrical lenses with short focal lengths in Linnik configuration, the angular measurable range can increase as well. Combined with the advantage of long profile measurement, it may generate a great deal of interest in applying the technique for large-scale metrology of freeform surface or AM products with high slopes.

- Improve the measurement speed by accelerating capturing time and computing time, in both hardware and software aspects. A fast CMOS camera can be a solution for reducing the capturing time for each interferogram, which also makes the metrology device even more environmentally robust. At the same time, an essential issue needs to be considered to match the high speed camera. Achieving high frame rate will however shorten the exposure time, which may lead to a high measurement noise or low fringes visibility. Therefore, the efficiency of the optical apparatus is required to be enhanced to provide a high power output on the sensor. Moreover, use of a high power light source is also a good alternative enabling the camera to receive the sufficient light. As for the computing time, updating the hardware (GPUs and computer processor), developing efficient algorithms and optimally organising the blocks and threads in GPUs are to be investigated for acceleration of analysis time.
- Miniaturisation of this fast line-sensor to be embedded in processing machines free of large space occupation. Building the optical device using folding mirrors, developing a spectrometer on a single chip and completely separating the current bulky spectrometer from the optical probe are three techniques to be investigated to make the whole sensor more compact.
- A set of artefacts and calibration schemes to be manufactured and/or designed to test the key aspects of the proof-of-concept prototypes in terms of vertical range/resolution, lateral range/resolution, angular measurable range, uncertainty, repeatability, sensitivity etc. A series of measurements need to be performed using these artefacts to validate the

potential of finalised prototypes for various metrology applications in manufacturing environments.

- Investigate the automation of the metrology system to implement the prototype on a real production line. Currently all measurements are carried out off-line in the optics laboratory. The frame acquisition and data analysis were conducted separately by clicking the corresponding buttons in camera software and mathematical software such as Matlab and Microsoft Visual studio. A user friendly piece of software needs to be developed by combining the capturing and analysis processes together to complete each measurement with only one click. Additionally, presentation of the tested surface profile in friendly graphical user interface will be investigated as well.
- Furthermore, considering further enhancement of measurement efficiency, the methods to allow the spectrometer to realise surface topography in a single shot or the objective (such as the lens array) to observe multiple profiles on the tested surface at the same time will be investigated as well.

## Publications and Awards

### Refereed Journal Papers

Tang, D., Gao, F. and Jiang, X. (2014) On-line surface inspection using cylindrical lens-based spectral domain low-coherence interferometry. *Applied optics*, 53(24), pp.5510-5516.

### Refereed Conference Papers

Gao, F., Tang, D., and Jiang, X. (2013) White Light Spectral Interferometry for Real Time Surface Profile Measurement. In: ASPEN 2013, 12-15, November 2013, Taipei, Taiwan.

Tang, D., Gao, F. and Jiang, X. (2014) Cylindrical Lenses Based Spectral Domain Low-Coherence Interferometry for On-line Surface Inspection. In: Euspen 14th International Conference & Exhibition, 2nd - 6th June 2014, Dubrovnik, Croatia.

Jiang, X., Tang, D. and Gao, F. (2015) In-Situ Surface Inspection Using White Light Channelled Spectrum Interferometer. In: 15th International Conference on Metrology and Properties of Engineering Surfaces, 2-5 March 2015, Charlotte, North Carolina, USA.

Gao, F., Muhamedsalih, H., Tang, D., Elrawemi, M., Blunt, L., Jiang, X., Edge, S., Bird, D. and Hollis, P. (2015) In-situ defect detection systems for R2R flexible PV films. In: ASPE 2015 Summer Topical Meeting. American Society for Precision Engineering, Colorado, USA, pp. 44-49. ISBN 978-1-887706-68-1

Tang, D., Gao, F. and Jiang, X. (2016) Implementation of line-scan dispersive interferometry for defect detection. In: Euspen 16th International Conference & Exhibition, May 2016, Nottingham, UK. (Accepted)

### Non-refereed Conference Papers

Tang, D., Gao, F. and Jiang, X. (2013) Spectral Domain Low- Coherence Interferometry for On-line Surface Inspection. In: Proceedings of Computing and Engineering Annual Researchers' Conference 2013 : CEARC'13. University of Huddersfield, Huddersfield, pp. 194-199. ISBN 9781862181212

### Awards

Tang, D., **HEIDENHAIN GmbH scholarship**, euspen's 14th International Conference, Dubrovnik 2014.

Tang, D., **Best Poster** from one of the 4 EPSRC Manufacturing themes: Manufacturing Informatics, The 3rd EPSRC Manufacturing the Future: Glasgow on 23rd & 24th September 2014.

## References

- Abramowitz, M., Spring, K. R., Long, J. C., & Davidson, M. W. (2015). Infinity-Corrected Optical Systems. Retrieved from <http://micro.magnet.fsu.edu/primer/anatomy/infinityhome.html>
- Adhikari, R. (2004). Sensitivity and noise analysis of 4 km laser interferometric gravitational wave antennae. Massachusetts Institute of Technology.
- Adi, S., Adi, H., Chan, H.-K., Young, P. M., Traini, D., Yang, R., & Yu, A. (2008). Scanning white-light interferometry as a novel technique to quantify the surface roughness of micron-sized particles for inhalation. *Langmuir*, 24(19), 11307-11312.
- Ali, R., Saleem, M. R., Pääkkönen, P., & Honkanen, S. (2015). Thermo-Optical Properties of Thin-Film TiO<sub>2</sub>-Al<sub>2</sub>O<sub>3</sub> Bilayers Fabricated by Atomic Layer Deposition. *Nanomaterials*, 5(2), 792-803.
- Ali, S. H. (2012). Advanced nanomeasuring techniques for surface characterization. *ISRN Optics*, 2012.
- Alvarez, L., & Siqueiros, J. (2010). Scanning probe microscopy. *Microscopy: Science, Technology, Applications and Education*.
- Balasubramanian, N. (1982). Optical system for surface topography measurement: Google Patents.
- Bennett, J., & Dancy, J. (1981). Stylus profiling instrument for measuring statistical properties of smooth optical surfaces. *Applied optics*, 20(10), 1785-1802.
- Bennett, J., & Mattsson, L. (1989). Introduction to surface roughness and scattering. Introduction to Surface Roughness and Scattering by Jean Bennett, Lars Mattsson Washington DC: Optical Society of America, 1989, 1.
- Bhushan, B. (2000). *Modern Tribology Handbook, Two Volume Set*: Crc Press.
- Binnig, G., Quate, C. F., & Gerber, C. (1986). Atomic force microscope. *Physical review letters*, 56(9), 930.
- Binnig, G., & Rohrer, H. (1983). Scanning tunneling microscopy. *Surface science*, 126(1), 236-244.
- Blasco, J., Aleixos, N., & Moltó, E. (2003). Machine vision system for automatic quality grading of fruit. *Biosystems Engineering*, 85(4), 415-423.
- Blunt, L., Fleming, L., Elrawemi, M., Robbins, D., & Muhamedsalih, H. (2013). In-line metrology of functional surfaces with a focus on defect assessment on large area Roll to Roll substrates.
- Blunt, L., & Jiang, X. (2003). Advanced techniques for assessment surface topography: development of a basis for 3D surface texture standards" surfstand": Elsevier.
- Blunt, L., Robbins, D., Fleming, L., & Elrawemi, M. (2014). The use of feature parameters to asses barrier properties of ALD coatings for flexible PV substrates. Paper presented at the *Journal of Physics: Conference Series*.
- Boppart, S. A. (2003). Optical coherence tomography: technology and applications for neuroimaging. *Psychophysiology*, 40(4), 529-541.
- Bowe, B., & Toal, V. (1998). White light interferometric surface profiler. *Optical Engineering*, 37(6), 1796-1799.
- Braga, P. C., & Ricci, D. (2004). *Atomic force microscopy: biomedical methods and applications (Vol. 242)*: Springer Science & Business Media.

- Bremen, S., Meiners, W., & Diatlov, A. (2012). Selective Laser Melting. *Laser Technik Journal*, 9(2), 33-38.
- Brezinski, M. E. (2006). *Optical coherence tomography: principles and applications*: Academic press.
- Calatroni, J., Guerrero, A. L., Sainz, C., & Escalona, R. (1996). Spectrally-resolved white-light interferometry as a profilometry tool. *Optics & Laser Technology*, 28(7), 485-489.
- Carcia, P., McLean, R., Reilly, M., Groner, M., & George, S. (2006). Ca test of Al~ 2O~ 3 gas diffusion barriers grown by atomic layer deposition on polymers. *Applied physics letters*, 89(3), 031915.
- Carré, P. (1966). Installation et utilisation du comparateur photoélectrique et interférentiel du Bureau International des Poids et Mesures. *Metrologia*, 2(1), 13.
- Charette, P. G., & Hunter, I. W. (1996). Robust phase-unwrapping method for phase images with high noise content. *Applied optics*, 35(19), 3506-3513.
- Cheng, Y.-Y., & Wyant, J. C. (1984). Two-wavelength phase shifting interferometry. *Applied optics*, 23(24), 4539-4543.
- Chin, R. T., & Harlow, C. A. (1982). Automated visual inspection: A survey. *Pattern Analysis and Machine Intelligence, IEEE Transactions on*(6), 557-573.
- Choma, M., Sarunic, M., Yang, C., & Izatt, J. (2003). Sensitivity advantage of swept source and Fourier domain optical coherence tomography. *Optics express*, 11(18), 2183-2189.
- Cimalla, V., Baeumler, M., Kirste, L., Prescher, M., Christian, B., Passow, T., . . . Himmerlich, M. (2014). *Densification of thin aluminum oxide films by thermal treatments. Materials Sciences and Applications*, 2014.
- Conchello, J.-A., Kim, J. J., & Hansen, E. W. (1994). Enhanced three-dimensional reconstruction from confocal scanning microscope images. II. Depth discrimination versus signal-to-noise ratio in partially confocal images. *Applied optics*, 33(17), 3740-3750.
- Conroy, M., & Armstrong, J. (2005). A comparison of surface metrology techniques. Paper presented at the *Journal of Physics: Conference Series*.
- Cotel, A., Liard, A., Desserouer, F., & Pichon, P. (2014). Overview of diffraction gratings technologies for space-flight satellites and ground-based telescopes. Paper presented at the *International Conference on Space Optics*.
- Creath, K. (1988). Phase-measurement interferometry techniques. *Progress in optics*, 26(26), 349-393.
- Danzl, R., Helml, F., & Scherer, S. (2009). Focus variation—a new technology for high resolution optical 3D surface metrology. Paper presented at the *Proceedings of the 10th international conference of the Slovenian society for non-destructive testing*.
- Danzl, R., Helml, F., & Scherer, S. (2011). Focus variation—a robust technology for high resolution optical 3D surface metrology. *Strojniški vestnik-Journal of mechanical engineering*, 57(3), 245-256.
- Davidson, M., Kaufman, K., & Mazar, I. (1987). The coherence probe microscope. *Solid State Technology*, 30(9), 57-59.
- Davim, J. P. (2010). *Surface integrity in machining (Vol. 1848828742)*: Springer.
- De Chiffre, L., Kunzmann, H., Peggs, G., & Lucca, D. (2003). Surfaces in precision engineering, microengineering and nanotechnology. *CIRP Annals-Manufacturing Technology*, 52(2), 561-577.

- De Donno, D., Esposito, A., Tarricone, L., & Catarinucci, L. (2010). Introduction to GPU computing and CUDA programming: A case study on FDTD [EM programmer's notebook]. *Antennas and Propagation Magazine, IEEE*, 52(3), 116-122.
- De Groot, P. J. (1995). Vibration in phase-shifting interferometry. *JOSA A*, 12(2), 354-365.
- Debnath, S. K., & Kothiyal, M. P. (2005). Optical profiler based on spectrally resolved white light interferometry. *Optical Engineering*, 44(1), 013606-013606-013605.
- Debnath, S. K., & Kothiyal, M. P. (2006). Analysis of spectrally resolved white light interferometry by Hilbert transform method. Paper presented at the SPIE Optics+ Photonics.
- Debnath, S. K., & Kothiyal, M. P. (2006). Improved optical profiling using the spectral phase in spectrally resolved white-light interferometry. *Applied optics*, 45(27), 6965-6972.
- Debnath, S. K., Kothiyal, M. P., Schmit, J., & Hariharan, P. (2006). Spectrally resolved white-light phase-shifting interference microscopy for thickness-profile measurements of transparent thin film layers on patterned substrates. *Optics express*, 14(11), 4662-4667.
- Deck, L. (1996). Vibration-resistant phase-shifting interferometry. *Applied optics*, 35(34), 6655-6662.
- Deck, L., & Demarest, F. (1993). Two-color light-emitting-diode source for high-precision phase-shifting interferometry. *Optics letters*, 18(22), 1899-1901.
- Deck, L. L. (2001). Multiple-surface phase-shifting interferometry. Paper presented at the International Symposium on Optical Science and Technology.
- Deck, L. L., & Evans, C. (2005). High performance Fizeau and scanning white-light interferometers for mid-spatial frequency optical testing of free-form optics. Paper presented at the Optics & Photonics 2005.
- Decker, J. E., Miles, J. R., Madej, A. A., Siemsen, R. F., Siemsen, K. J., de Bonth, S., . . . Pekelsky, J. R. (2003). Increasing the range of unambiguity in step-height measurement with multiple-wavelength interferometry—application to absolute long gauge block measurement. *Applied optics*, 42(28), 5670-5678.
- Dorrer, C., Belabas, N., Likforman, J.-P., & Joffre, M. (2000). Spectral resolution and sampling issues in Fourier-transform spectral interferometry. *JOSA B*, 17(10), 1795-1802.
- Drexler, W., & Fujimoto, J. G. (2008). *Optical coherence tomography: technology and applications*: Springer Science & Business Media.
- Ducros, M., Laubscher, M., Karamata, B., Bourquin, S., Lasser, T., & Salathe, R. (2002). Parallel optical coherence tomography in scattering samples using a two-dimensional smart-pixel detector array. *Optics Communications*, 202(1), 29-35.
- El Gawhary, O., Kumar, N., Pereira, S., Coene, W., & Urbach, H. (2011). Performance analysis of coherent optical scatterometry. *Applied Physics B*, 105(4), 775-781.
- Elrawemi, M., Blunt, L., & Fleming, L. (2014). Metrology and Characterisation of Defects on Barrier Layers for Thin Film Flexible Photovoltaics. Paper presented at the EUSPEN 14th International Conference 2014, Dubrovnik, Croatia.
- Elrawemi, M., Blunt, L., Fleming, L., & Sweeney, F. (2013). Further development of surface metrology methods for predicting the functional performance of flexible photovoltaic barrier films. *Surface Topography: Metrology and Properties*, 1(1), 015006.
- Gaigalas, A., Wang, L., He, H.-J., & DeRose, P. (2009). Procedures for wavelength calibration and spectral response correction of CCD array spectrometers. *Journal of Research of the National Institute of Standards and Technology*, 114(4), 215-228.

- Gao, F., Leach, R. K., Petzing, J., & Coupland, J. M. (2008). Surface measurement errors using commercial scanning white light interferometers. *Measurement Science and Technology*, 19(1), 015303.
- Gao, F., Muhamedsalih, H., & Jiang, X. (2012). Surface and thickness measurement of a transparent film using wavelength scanning interferometry. *Optics express*, 20(19), 21450-21456.
- Gauler, A. L. (1982). Comparison of two common methods of surface topography evaluation. *Optical Engineering*, 21(6), 216991-216997.
- George, M. (2014). Design and Development of a State of the Art R2R Production Platform For Flexible Transparent Barrier Films. Paper presented at the Web Coating & Handling Conference, South Carolina.
- Gèuntherodt, H.-J., & Wiesendanger, R. (1994). *Scanning tunneling microscopy I: general principles and applications to clean and adsorbate-covered surfaces*: Springer-Verlag.
- Ghim, Y.-S., & Kim, S.-W. (2009). Spectrally resolved white-light interferometry for 3D inspection of a thin-film layer structure. *Applied optics*, 48(4), 799-803.
- Giusca, C., & Leach, R. K. (2013). Measurement Good Practice Guide No. 127- Calibration of the metrological characteristics of coherence scanning interferometers (CSI) and phase shifting interferometers (PSI). National Physical Laboratory.
- Giusca, C. L., & Leach, R. K. (2013). Calibration of the scales of areal surface topography measuring instruments: part 3. Resolution. *Measurement Science and Technology*, 24(10), 105010.
- Grajciar, B., Pircher, M., Fercher, A., & Leitgeb, R. (2005). Parallel Fourier domain optical coherence tomography for in vivo measurement of the human eye. *Optics express*, 13(4), 1131-1137.
- Gregg, A., York, L., & Strnad, M. (2005). Roll-to-roll manufacturing of flexible displays. *Flexible Flat Panel Displays*, 3, 409.
- Grimm, T., Wiora, G., & Witt, G. (2015). Characterization of typical surface effects in additive manufacturing with confocal microscopy. *Surface Topography: Metrology and Properties*, 3(1), 014001.
- Grous, A. (2013). *Applied Metrology for Manufacturing Engineering*: John Wiley & Sons.
- Harasaki, A., & Wyant, J. C. (2000). Fringe modulation skewing effect in white-light vertical scanning interferometry. *Applied optics*, 39(13), 2101-2106.
- Harding, K. (2013). *Handbook of Optical Dimensional Metrology*: CRC Press.
- Hariharan, P. (2010). *Basics of interferometry*: Academic Press.
- Hariharan, P., Oreb, B., & Eiju, T. (1987). Digital phase-shifting interferometry: a simple error-compensating phase calculation algorithm. *Applied optics*, 26(13), 2504-2506.
- Harris, F. J. (1978). On the use of windows for harmonic analysis with the discrete Fourier transform. *Proceedings of the IEEE*, 66(1), 51-83.
- Hart, M., Vass, D. G., & Begbie, M. L. (1998). Fast surface profiling by spectral analysis of white-light interferograms with Fourier transform spectroscopy. *Applied optics*, 37(10), 1764-1769.
- Hassan, M. A., Martin, H., & Jiang, X. (2014). Surface profile measurement using spatially dispersed short coherence interferometry. *Surface Topography: Metrology and Properties*, 2(2), 024001.
- Heavens, O. (1989). *Geometrical and Instrumental Optics*.
- Heeren, H., & El-Fataty, A. (2008). Metrology and characterization for micro and nano technology Design for Purpose Metrology Expert Workshop. Loughborough, UK.

- Hegedus, S., Carcia, P., McLean, R., & Culver, B. (2010). Encapsulation of Cu (InGa) Se 2 solar cells with ALD Al<sub>2</sub>O<sub>3</sub> flexible thin-film moisture barrier: stability under 1000 hour damp heat and UV exposure. Paper presented at the Photovoltaic Specialists Conference (PVSC), 2010 35th IEEE.
- Helmlí, F. (2011). Focus variation instruments Optical Measurement of Surface Topography (pp. 131-166): Springer.
- Hiersemenzel, F., Petzing, J. N., Leach, R. K., Helmlí, F., & Singh, J. (2012). Areal texture and angle measurements of tilted surfaces using focus variation methods.
- Hlubina, P. (2002). Dispersive white-light spectral interferometry to measure distances and displacements. *Optics Communications*, 212(1), 65-70.
- Hocken, R., Chakraborty, N., & Brown, C. (2005). Optical metrology of surfaces. *CIRP Annals-Manufacturing Technology*, 54(2), 169-183.
- Huntley, J. (1989). Noise-immune phase unwrapping algorithm. *Applied optics*, 28(16), 3268-3270.
- Huntley, J. M., Widjanarko, T., & Ruiz, P. D. (2010). Hyperspectral interferometry for single-shot absolute measurement of two-dimensional optical path distributions. *Measurement Science and Technology*, 21(7), 075304.
- Iftimia, N. V., Hammer, D. X., Bigelow, C. E., Ustun, T., de Boer, J. F., & Ferguson, R. D. (2006). Hybrid retinal imager using line-scanning laser ophthalmoscopy and spectral domain optical coherence tomography. *Optics express*, 14(26), 12909-12914.
- ISO. (1997). Geometrical Product Specifications (GPS)--Surface Texture: Profile Method--Terms, Definitions and Surface Texture Parameters: International Organization for Standardization.
- ISO. (2012). Geometrical Product Specifications (GPS)--Surface Texture: Areal--Part 2: Terms, Definitions and Surface Texture Parameters: International Organization for Standardization.
- ISRA-Vison. (2015). Camera Based Inspection of Substrate Surfaces R2R Summer School Programme. Huddersfield: The Centre for Precision Technologies, University of Huddersfield.
- Jackson, P., Hariskos, D., Lotter, E., Paetel, S., Wuerz, R., Menner, R., . . . Powalla, M. (2011). New world record efficiency for Cu (In, Ga) Se<sub>2</sub> thin-film solar cells beyond 20%. *Progress in Photovoltaics: Research and Applications*, 19(7), 894-897.
- Jiang, X., Scott, P. J., Whitehouse, D. J., & Blunt, L. (2007). Paradigm shifts in surface metrology. Part I. Historical philosophy. Paper presented at the Proceedings of the Royal Society of London A: Mathematical, Physical and Engineering Sciences.
- Jiang, X., Wang, K., Gao, F., & Muhamedsalih, H. (2010). Fast surface measurement using wavelength scanning interferometry with compensation of environmental noise. *Applied optics*, 49(15), 2903-2909.
- Jiang, X., & Whitehouse, D. J. (2012). Technological shifts in surface metrology. *CIRP Annals-Manufacturing Technology*, 61(2), 815-836.
- Joo, K.-N., & Kim, S.-W. (2006). Absolute distance measurement by dispersive interferometry using a femtosecond pulse laser. *Optics express*, 14(13), 5954-5960.
- Kafri, O. (1989). Fundamental limit on accuracy in interferometry. *Optics letters*, 14(13), 657-658.
- Kang, M.-G., Lee, S.-Y., & Kim, S.-W. (1999). Self-compensation of PZT errors in white light scanning interferometry. *Journal of the optical society of Korea*, 3(2), 35-40.

- Kaplonek, W., & Lukianowicz, C. (2012). Coherence correlation interferometry in surface topography measurements: INTECH Open Access Publisher.
- Ke, C., Shih, V., Huang, J., Chen, L., Wang, W., Huang, G., . . . Liu, H. (2010). A paradigm shift in scatterometry-based metrology solution addressing the most stringent needs of today as well as future lithography. Paper presented at the SPIE Advanced Lithography.
- Kemao, Q., Fangjun, S., & Xiaoping, W. (2000). Determination of the best phase step of the Carré algorithm in phase shifting interferometry. *Measurement Science and Technology*, 11(8), 1220.
- Keranen, K., Jaakola, T., Korhonen, P., Antonipieri, M., Salomon, J., Visentin, L., . . . Pira, N. L. (2012). Demonstrators for autonomous automotive and signage applications by bonding flexible solar cells, batteries and LED elements on large area polycarbonate backplanes. Paper presented at the Electronic System-Integration Technology Conference (ESTC), 2012 4th.
- Kimbrough, B. (2015). In-line roll-to-roll metrology for flexible electronics. Paper presented at the SPIE Optical Engineering+ Applications.
- Kimbrough, B., Frey, E., & Millerd, J. (2008). Instantaneous phase-shift Fizeau interferometer utilizing a synchronous frequency shift mechanism. Paper presented at the Optical Engineering+ Applications.
- Kirk, D. B., & Wen-mei, W. H. (2012). Programming massively parallel processors: a hands-on approach: Newnes.
- Krebs, F. C., Fyenbo, J., & Jørgensen, M. (2010). Product integration of compact roll-to-roll processed polymer solar cell modules: methods and manufacture using flexographic printing, slot-die coating and rotary screen printing. *Journal of Materials Chemistry*, 20(41), 8994-9001.
- Kühnhold, P., Xie, W., & Lehmann, P. (2013). Comparison of Michelson and Linnik interference microscopes with respect to measurement capabilities and adjustment efforts. Paper presented at the SPIE Optical Metrology 2013.
- Kumar, M., Islam, M. N., Terry, F. L., Aleksoff, C. C., & Davidson, D. (2010). High resolution line scan interferometer for solder ball inspection using a visible supercontinuum source. *Optics express*, 18(21), 22471-22484.
- Kumar, N., Petrik, P., Ramanandan, G. K., El Gawhary, O., Roy, S., Pereira, S. F., . . . Urbach, H. P. (2014). Reconstruction of sub-wavelength features and nano-positioning of gratings using coherent Fourier scatterometry. *Optics express*, 22(20), 24678-24688.
- Kumar, U. P., Mohan, N. K., & Kothiyal, M. (2008). Multiple wavelength interferometry for surface profiling. Paper presented at the Optical Engineering+ Applications.
- Kurada, S., & Bradley, C. (1997). A review of machine vision sensors for tool condition monitoring. *Computers in Industry*, 34(1), 55-72.
- Kuwamura, S., & Yamaguchi, I. (1997). Wavelength scanning profilometry for real-time surface shape measurement. *Applied optics*, 36(19), 4473-4482.
- Leach, R. (2011). *Optical measurement of surface topography*: Springer.
- Leach, R. (2014). *Fundamental principles of engineering nanometrology*: Elsevier.
- Leach, R., Evans, C., He, L., Davies, A., Duparré, A., Henning, A., . . . O'Connor, D. (2015). Open questions in surface topography measurement: a roadmap. *Surface Topography: Metrology and Properties*, 3(1), 013001.
- Leach, R., & Sherlock, B. (2014). Applications of super-resolution imaging in the field of surface topography measurement. *Surface Topography: Metrology and Properties*, 2(2), 023001.

- Lee, C., Kang, H., Kim, H., Nguyen, H. A. D., & Shin, K. (2010). Quality control with matching technology in roll to roll printed electronics. *Journal of mechanical science and technology*, 24(1), 315-318.
- Lerner, J., & Thevenon, A. (1988). *The optics of spectroscopy*. Tutorial Jobin-Yvon.
- Lerner, J. M. (2006). Imaging spectrometer fundamentals for researchers in the biosciences—a tutorial. *Cytometry Part A*, 69(8), 712-734.
- Lewis, I. R., & Edwards, H. (2001). *Handbook of Raman spectroscopy: from the research laboratory to the process line*: CRC Press.
- Logofătu, P., Apostol, D., Damian, V., Nascov, V., Garoi, F., Timcu, A., & Iordache, I. (2004). Scatterometry, an optical metrology technique for lithography. Paper presented at the Semiconductor Conference, 2004. CAS 2004 Proceedings. 2004 International.
- Lonardo, P., Lucca, D., & De Chiffre, L. (2002). Emerging trends in surface metrology. *CIRP Annals-Manufacturing Technology*, 51(2), 701-723.
- Luo, X., Jayas, D., & Symons, S. (1999). Identification of damaged kernels in wheat using a colour machine vision system. *Journal of cereal science*, 30(1), 49-59.
- Mainsah, E., & Chetwynd, D. (2013). *Metrology and properties of engineering surfaces*: Springer Science & Business Media.
- Malacara, D. (2007). *Optical shop testing* (Vol. 59): John Wiley & Sons.
- Malacara, Z., & Servin, M. (2005). *Interferogram analysis for optical testing* (Vol. 84): CRC press.
- Martin, H. P. (2010). Investigations into a multiplexed fibre interferometer for on-line, nanoscale, surface metrology. Doctoral degree, The University of Huddersfield.
- Michelson, A. A., & Morley, E. W. (1887). On the Relative Motion of the Earth and of the Luminiferous Ether. *Sidereal Messenger*, vol. 6, pp. 306-310, 6, 306-310.
- Mohammadi, H., & Eslami, E. (2010). Investigation of spectral resolution in a Czerny Turner spectrograph. *Instruments and Experimental Techniques*, 53(4), 549-552.
- Morse, J. (2012). *Nanofabrication technologies for Roll-to-roll processing*.
- Muhamedsalih, H. (2013). Investigation of Wavelength Scanning Interferometry for Embedded Metrology. Doctoral thesis, University of Huddersfield.
- Muhamedsalih, H., Blunt, L., Martin, H., Hamersma, I., Elrawemi, M., & Feng, G. (2015). An integrated opto-mechanical measurement system for in-process defect measurement on a roll-to-roll process.
- Muhamedsalih, H., Blunt, L., Martin, H., Jiang, X., & Elrawemi, M. (2014). An interferometric auto-focusing method for on-line defect assessment on a roll-to-roll process using wavelength scanning interferometry.
- Muhamedsalih, H., Gao, F., & Jiang, X. (2012). Comparison study of algorithms and accuracy in the wavelength scanning interferometry. *Applied optics*, 51(36), 8854-8862.
- Muhamedsalih, H., Jiang, X., & Gao, F. (2013). Accelerated surface measurement using wavelength scanning interferometer with compensation of environmental noise. *Procedia CIRP*, 10, 70-76.
- Murphy, D. B. (2002). *Fundamentals of light microscopy and electronic imaging*: John Wiley & Sons.
- Nakamura, Y., Makita, S., Yamanari, M., Itoh, M., Yatagai, T., & Yasuno, Y. (2007). High-speed three-dimensional human retinal imaging by line-field spectral domain optical coherence tomography. *Optics express*, 15(12), 7103-7116.
- Niehues, J., Lehmann, P., & Xie, W. (2012). Low coherent Linnik interferometer optimized for use in nano-measuring machines. *Measurement Science and Technology*, 23(12), 125002.

- NVIDIA. (2015). NVIDIA CUDA C: Programming Guide. Retrieved from <http://eprints.hud.ac.uk/19194/1/483971Revised29Oct13.pdf>
- Ohta, T., Nishizawa, N., Ozawa, T., & Itoh, K. (2008). Highly-sensitive and high-resolution all-fiber three-dimensional measurement system. *Applied optics*, 47(13), 2503-2509.
- Onodera, R., & Ishii, Y. (1997). Fourier description of the phase-measuring process in two-wavelength phase-shifting interferometry. *Optics Communications*, 137(1), 27-30.
- Padula, S. (2009). Measurement Variability of Vertical Scanning Interferometry Tool Used for Orbiter Window Defect Assessment.
- Pavlíček, P., & Häusler, G. (2005). White-light interferometer with dispersion: an accurate fiber-optic sensor for the measurement of distance. *Appl. Opt.*, 44(25), 2978-2983.
- Pereira, S. F. (2015). Optical scatterometry for metrology and surface inspection R2R Summer School Programme in Huddersfield Jun. 2015. Huddersfield: The Centre for Precision Technologies, University of Huddersfield.
- Persson, U. (1998). In-process measurement of surface roughness using light scattering. *Wear*, 215(1), 54-58.
- Petroll, W., Cavanagh, H., & Jester, J. (1993). Three-dimensional imaging of corneal cells using in vivo confocal microscopy. *Journal of microscopy*, 170(3), 213-219.
- Pförtner, A., & Schwider, J. (2001). Dispersion error in white-light Linnik interferometers and its implications for evaluation procedures. *Applied optics*, 40(34), 6223-6228.
- Platform, A. (2014). Additive manufacturing: Strategic research agenda. UK: AM Sub-Platform. Retrieved July, 30, 2014.
- Polhemus, C. (1973). Two-wavelength interferometry. *Applied optics*, 12(9), 2071-2074.
- Popov, E. (2012). Introduction to diffraction gratings: summary of applications. *Gratings: Theory and Numeric Applications*, 1.1-1.23.
- Qian, K. (2001). Comparison of some phase-shifting algorithms with a phase step of  $\pi/2$ . Paper presented at the International Symposium on Photonics and Applications.
- Raja, J., Muralikrishnan, B., & Fu, S. (2002). Recent advances in separation of roughness, waviness and form. *Precision Engineering*, 26(2), 222-235.
- Rebeggiani, S. (2013). On Polishability of Tool Steels. Doctoral thesis, Chalmers University of Technology.
- Reolon, D., Jacquot, M., Verrier, I., Brun, G., & Veillas, C. (2006). Broadband supercontinuum interferometer for high-resolution profilometry. *Optics express*, 14(1), 128-137.
- Rossi, G., & Nulman, M. (1993). Effect of local flaws in polymeric permeation reducing barriers. *Journal of applied physics*, 74(9), 5471-5475.
- Rost, F., & Oldfield, R. (2000). *Photography with a Microscope*: Cambridge University Press.
- Roy, S., Assafrao, A., Pereira, S., & Urbach, H. (2014). Coherent Fourier scatterometry for detection of nanometer-sized particles on a planar substrate surface. *Optics express*, 22(11), 13250-13262.
- Ruprecht, A. K., Koerner, K., Wiesendanger, T. F., Tiziani, H. J., & Osten, W. (2004). Chromatic confocal detection for high-speed microtopography measurements. Paper presented at the Electronic Imaging 2004.
- Ryoo, S., Rodrigues, C. I., Bagsorkhi, S. S., Stone, S. S., Kirk, D. B., & Hwu, W.-m. W. (2008). Optimization principles and application performance evaluation of a multithreaded GPU using CUDA. Paper presented at the Proceedings of the 13th ACM SIGPLAN Symposium on Principles and practice of parallel programming.
- Sainz, C., Calatroni, J., & Tribillon, G. (1990). Refractometry of liquid samples with spectrally resolved white light interferometry. *Measurement Science and Technology*, 1(4), 356.

- Schneir, J., Dagata, J. A., Harary, H. H., Evans, C. J., Melmed, A., Elswijk, H., & Sauvageau, J. (1989). Scanning tunneling microscopy of optical surfaces. Paper presented at the 33rd Annual Technical Symposium.
- Schnell, U., Gray, S., & Dändliker, R. (1996). Dispersive white-light interferometry for absolute distance measurement with dielectric multilayer systems on the target. *Optics letters*, 21(7), 528-530.
- Schreiber, H., & Bruning, J. H. (2006). Phase shifting interferometry. *Optical Shop Testing*, Third Edition, 547-666.
- Schulz-Ruhtenberg, M., Kolbusch, T., Abreu Fernandes, S., Wiesner, M., Melle, T., Bergfeld, S., . . . Ostendorf, A. (2014). Seminal Tools for Roll-to-Roll Manufacturing. *Laser Technik Journal*, 11(1), 21-25.
- Schwager, F. (2012). Encapsulation of Flexible Thin-Film Photovoltaic Cells. 20th World Petroleum Congress Proceedings, (978 0 85293 615 3 F17).
- Schwider, J., Burow, R., Elssner, K.-E., Grzanna, J., Spolaczyk, R., & Merkel, K. (1983). Digital wave-front measuring interferometry: some systematic error sources. *Applied optics*, 22(21), 3421-3432.
- Schwider, J., & Zhou, L. (1994). Dispersive interferometric profilometer. *Optics letters*, 19(13), 995-997.
- Scott, C. C., Luttge, A., & Athanasiou, K. A. (2005). Development and validation of vertical scanning interferometry as a novel method for acquiring chondrocyte geometry. *Journal of Biomedical Materials Research Part A*, 72(1), 83-90.
- Serry, F., & Schmit, J. (2006). Characterization and Measurement of Microcomponents with Atomic Force Microscope. *Optical Inspection of Microsystems*, 121-143.
- Shankar, N., & Zhong, Z. (2005). Defect detection on semiconductor wafer surfaces. *Microelectronic Engineering*, 77(3), 337-346.
- Sherrington, I., & Smith, E. (1988). Modern measurement techniques in surface metrology: part I; stylus instruments, electron microscopy and non-optical comparators. *Wear*, 125(3), 271-288.
- Shi, K., Li, P., Yin, S., & Liu, Z. (2004). Chromatic confocal microscopy using supercontinuum light. *Optics express*, 12(10), 2096-2101.
- Shulman, A. R. (1970). *Principles of optical data processing for engineers*: National Aeronautics and Space Administration.
- Søndergaard, R. R., Hösel, M., & Krebs, F. C. (2013). Roll-to-Roll fabrication of large area functional organic materials. *Journal of Polymer Science Part B: Polymer Physics*, 51(1), 16-34.
- Standard, A. (2012). F2792. 2012 Standard terminology for additive manufacturing technologies. West Conshohocken, PA: ASTM International. See [www.astm.org](http://www.astm.org).(doi: 10.1520/F2792-12).
- Stout, K., & Blunt, L. (2001). A contribution to the debate on surface classifications—random, systematic, unstructured, structured and engineered. *International Journal of Machine Tools and Manufacture*, 41(13), 2039-2044.
- Stover, J. C. (1995). *Optical scattering: measurement and analysis (Vol. 2)*: SPIE optical engineering press Bellingham, WA.
- Sykora, D. M., & de Groot, P. (2011). Instantaneous measurement Fizeau interferometer with high spatial resolution. Paper presented at the SPIE Optical Engineering+ Applications.
- Takeda, M., Ina, H., & Kobayashi, S. (1982). Fourier-transform method of fringe-pattern analysis for computer-based topography and interferometry. *JosA*, 72(1), 156-160.

- Takeda, M., & Yamamoto, H. (1994). Fourier-transform speckle profilometry: three-dimensional shape measurements of diffuse objects with large height steps and/or spatially isolated surfaces. *Applied optics*, 33(34), 7829-7837.
- Tang, D., Gao, F., & Jiang, X. (2014). On-line surface inspection using cylindrical lens-based spectral domain low-coherence interferometry. *Applied optics*, 53(24), 5510-5516.
- Taylor-Hobson. (2005). Talysurf CCI 6000. Retrieved from [http://blogs.univ-poitiers.fr/surfacestopo/files/2014/01/Talysurf\\_CCI6000.pdf](http://blogs.univ-poitiers.fr/surfacestopo/files/2014/01/Talysurf_CCI6000.pdf)
- Texture, S. (1995). Surface roughness, waviness and lay. American Society of Mechanical Engineers Standard B, 46, 1.
- Thiel, J., Pfeifer, T., & Hartmann, M. (1995). Interferometric measurement of absolute distances of up to 40 m. *Measurement*, 16(1), 1-6.
- Thomas, T. R. (1998). *Rough surfaces*: World Scientific.
- Thonya, P., Herissonb, D., Henryb, D., Severgnini, E., & Vasconic, M. (2003). Review of CD measurement and Scatterometry. Paper presented at the 2003 International Conference on Characterization and Metrology for ULSI Technology AIP Conference Proceedings.
- Tiziani, H. J., & Uhde, H.-M. (1994). Three-dimensional image sensing by chromatic confocal microscopy. *Applied optics*, 33(10), 1838-1843.
- Triantaphyllou, A., Giusca, C. L., Macaulay, G. D., Roerig, F., Hoebel, M., Leach, R. K., . . . Milne, K. A. (2015). Surface texture measurement for additive manufacturing. *Surface Topography: Metrology and Properties*, 3(2), 024002.
- Vacharanukul, K., & Mekid, S. (2005). In-process dimensional inspection sensors. *Measurement*, 38(3), 204-218.
- Van Loenen, E., Dijkkamp, D., Hoeven, A., Lenssinck, J., & Dieleman, J. (1990). Evidence for tip imaging in scanning tunneling microscopy. *Applied physics letters*, 56(18), 1755-1757.
- Van Wingerden, J., Frankena, H. J., & Smorenburg, C. (1991). Linear approximation for measurement errors in phase shifting interferometry. *Applied optics*, 30(19), 2718-2729.
- Vorburger, T. V., Marx, E., & Lettieri, T. R. (1993). Regimes of surface roughness measurable with light scattering. *Applied optics*, 32(19), 3401-3408.
- Vorburger, T. V., Rhee, H.-G., Renegar, T. B., Song, J.-F., & Zheng, A. (2007). Comparison of optical and stylus methods for measurement of surface texture. *The International Journal of Advanced Manufacturing Technology*, 33(1-2), 110-118.
- Whitehouse, D. J. (1997). Surface metrology. *Measurement Science and Technology*, 8(9), 955.
- Whitehouse, D. J. (2004). *Surfaces and their Measurement*: Elsevier.
- Widjanarko, T., Huntley, J. M., & Ruiz, P. D. (2012). Single-shot profilometry of rough surfaces using hyperspectral interferometry. *Optics letters*, 37(3), 350-352.
- Willmann, J., Stocker, D., & Dörsam, E. (2014). Characteristics and evaluation criteria of substrate-based manufacturing. Is roll-to-roll the best solution for printed electronics? *Organic Electronics*, 15(7), 1631-1640.
- Wojtkowski, M., Kowalczyk, A., Leitgeb, R., & Fercher, A. (2002). Full range complex spectral optical coherence tomography technique in eye imaging. *Optics letters*, 27(16), 1415-1417.
- Wyant, J. C., Koliopoulos, C. L., Bhushan, B., & George, O. E. (1984). An optical profilometer for surface characterization of magnetic media. *ASLE transactions*, 27(2), 101-113.
- Yamamoto, A., Kuo, C.-C., Sunouchi, K., Wada, S., Yamaguchi, I., & Tashiro, H. (2001). Surface shape measurement by wavelength scanning interferometry using an electronically tuned Ti: sapphire laser. *Optical review*, 8(1), 59-63.

- Yaqoob, Z., Choi, W., Oh, S., Lue, N., Park, Y., Fang-Yen, C., . . . Feld, M. S. (2009). Improved phase sensitivity in spectral domain phase microscopy using line-field illumination and self phase-referencing. *Optics express*, 17(13), 10681-10687.
- Yasuno, Y., Endo, T., Makita, S., Aoki, G., Itoh, M., & Yatagai, T. (2006). Three-dimensional line-field Fourier domain optical coherence tomography for in vivo dermatological investigation. *Journal of biomedical optics*, 11(1), 014014-014014-014017.
- Yatagai, T. (1994). Recent progress in white-light interferometry. Paper presented at the International Conference on Interferometry'94.
- Yoshizawa, T. (2009). *Handbook of optical metrology: Principles and Applications*: CRC Press.
- Young, R. D., Vorburger, T. V., & Teague, E. C. (1980). In-process and on-line measurement of surface finish. *CIRP Annals-Manufacturing Technology*, 29(1), 435-440.
- Zhu, P., & Wang, K. (2012). Single-shot two-dimensional surface measurement based on spectrally resolved white-light interferometry. *Applied optics*, 51(21), 4971-4975.
- Zuluaga, A. F., & Richards-Kortum, R. (1999). Spatially resolved spectral interferometry for determination of subsurface structure. *Optics letters*, 24(8), 519-521.
- ZYGO-Corporation. (2014). *NewView™7300*. Retrieved from [http://www.zygo.com/met/profilers/newview7000/NewView\\_7300\\_Specs.pdf](http://www.zygo.com/met/profilers/newview7000/NewView_7300_Specs.pdf)

# Appendix A (Experimental data)

## A.1 Simulation of cylindrical-LSDI system

The cylindrical-LSDI was modelled using ZEMAX with two configurations and the simulations in terms of alignment errors have been carried out.

OBJ	Surf.Type	Comment	Radius	Thickness	Glass	Semi-Diameter	Conic	Par 0 (unused)	Par 1 (unused)	Par 2 (unused)
	Standard		Infinity	27.264		0.200	0.000			
1*	Standard	Collimator 1	20.890	12.000	N-BAP10	12.700 U	0.000			
2*	Standard		-16.730	2.000	N-SF6H	12.700 U	0.000			
3*	Standard		-79.800	40.000		12.700 U	0.000			
4*	Standard	Diaphragm	Infinity	20.000		12.700 U	0.000			
*	Standard	Beamsplitter	Infinity	12.700	BK7	12.700 P	0.000			
6*	Tilted			0.000	MIRROR	12.700 P	0.000	0.000	0.000	-1.000
7	Coordinat..			0.000		0.000		0.000	0.000	0.000
8*	Tilted			-12.700	BK7	12.700 P				
9*	Standard		Infinity	-30.000		12.700 P	0.000			1.000
10*	Toroidal	Cylindrical-lens	-43.480	-6.880	N-BK7	5.000 U	0.000	0	0.000	0.000
11*	Toroidal		32.430	-4.000	N-SF2	11.685 U	0.000	0	0.000	0.000
12*	Toroidal		113.960	-20.000		11.685 U	0.000	0	0.000	0.000
13	Coordinat..	Tilt of BS		0.000		0.000				
14*	Standard	Beamsplitter	Infinity	-12.700 P	BK7	12.700 P	0.000			
15*	Tilted			0.000	MIRROR	12.700 P			0.000	1.000
16	Coordinat..			0.000		0.000			0.000	0.000
17*	Tilted			12.700	BK7	12.700 P			0.000	-1.000
18*	Standard		Infinity	32.084		12.700 P	0.000			
19	Coordinat..	Tilt of BS		-32.084 P		0.000			0.000	0.000
20	Standard	BS dummy	Infinity	32.084	P	4.853	0.000			
21	Tilted	Sample/Reference		-32.084 P	MIRROR	4.650			0.000	0.000
22	Standard	BS dummy	Infinity	-12.700		4.449	0.000			
23	Coordinat..	Tilt of BS		12.700 I		0.000			0.000	0.000
24*	Standard	Beamsplitter	Infinity	-12.700 P	BK7	12.700 P	0.000			
25*	Tilted			0.000	MIRROR	12.700 P			0.000	-1.000
26	Coordinat..			0.000		0.000			0.000	0.000
27*	Tilted			12.700 P	BK7	12.700 P			0.000	1.000
28*	Standard		Infinity	-12.700 I		12.700 P	0.000			

Lens Data Editor: Config 1/2

Edit Solve View Help

Surf>Type	Comment	Radius	Thickness	Glass	Semi-Diameter	Conic	Par 0 (unused)	Par 1 (unused)	Par 2 (unused)	Par
28*	Standard	Infinity	-12.700 I		12.700 P	0.000				
29	Coordinat..	Tilt of BS	12.700 P	-	0.000			0.000 P	0.000 P	
30	Standard	BS dummy	20.000	P	4.876	0.000				
31*	Toroidal	Cylindrical-lens	4.000	N-SF2	11.685 U	0.000	0	0.000	0.000	
32*	Toroidal		6.880	N-BK7	11.685 U	0.000	0	0.000	0.000	
33*	Toroidal		30.000		11.685 U	0.000	0	0.000	0.000	
34*	Standard	Beamsplitter	12.700 P	BK7	12.700 P	0.000				
35*	Tilted		0.000	BK7	12.700 P			0.000	1.000	
36	Coordinat..		0.000	-	0.000			0.000	0.000	
37*	Tilted		12.700 P	BK7	12.700 P			0.000	1.000	
38*	Standard		10.000		12.700 P	0.000				
39*	Standard	Tube lens	7.000	N-BK7	12.700 U	0.000				
40*	Standard		2.500	SF5	12.700 U	0.000				
41*	Standard		83.500		12.700 U	0.000				
42*	Standard	Slit	38.220		10.000 U	0.000				
43*	Standard	Collimator 2	2.500	SF10	12.700 U	0.000				
44*	Standard		9.000	N-BAF10	12.700 U	0.000				
45*	Standard		40.000		12.700 U	0.000				
46	Coordinat..		0.000	-	0.000			0.000	0.000	
47*	Diffracti..	Grating	0.000	MIRROR	10.000 U	0.000		1.200	1.000	
48	Coordinat..		-39.912	-	0.000			0.000	0.000	
49*	Standard	Imaging lens	-2.000	N-SF6HT	12.700 U	0.000				
50*	Standard		-7.000	N-BAF10	12.700 U	0.000				
51*	Standard		-45.100 V		12.700 U	0.000				
IMA	Standard	Detector plane	-		6.959	0.000				

## A.2 Investigation of spot sizes in both x and y direction

The RMS spot sizes in both tangential plane and sagittal plane were investigated using ZEMAX simulation. By setting a series of detectors after the tube lens along the optical axis, the recorded spot sizes are listed in the table below.

<b>Distance between tube lens and detector (mm)</b>	<b>RMS Spot size - x axis (mm)</b>	<b>RMS Spot size - y axis (mm)</b>
10	2.48	2.02
20	2.09	1.71
30	1.70	1.41
40	1.31	1.11
50	0.932	0.803
60	0.548	0.501
65	0.358	0.352
67	0.283	0.295
69	0.211	0.239
71	0.143	0.186
73	0.094	0.142
75	0.095	0.112
77	0.16	0.113
79	0.213	0.143
81	0.286	0.189
83	0.360	0.242
85	0.436	0.298
90	0.627	0.445
100	1.01	0.746
110	1.39	1.05
120	1.78	1.36
130	2.17	1.66
140	2.56	1.97
150	2.95	2.27

### A.3 Wavelength calibration data for cylindrical-LSDI

By using the built light source device (see Figure 4.16) and the commercial spectrometer CCS100, the relationships between the spectral lines and pixel numbers are listed in the table below. After the quadratic least squares fitting, the coefficients for equation (4.5) can be obtained as

$$A = 1.3743e-006;$$

$$B = -0.10453;$$

$$C = 628.23;$$

Pixel number	Wavelength (nm)		Pixel number	Wavelength (nm)
631	562.8862		303	596.8806
621	563.8248		296	597.5880
615	564.6463		288	598.4134
607	565.2331		272	599.9464
591	566.9939		244	603.0132
573	568.8727		234	604.0750
561	570.1647		224	604.9009
551	571.1045		211	606.4349
538	572.5144		197	607.8512
526	573.9247		186	608.7954
515	575.1002		180	609.5037
499	576.6346		167	610.9203
491	577.5693		154	612.2191
479	578.5101		144	613.2818
471	579.4511		127	615.0532
459	580.7451		118	615.9981
451	581.2158		106	617.2974
421	584.5110		95	618.3605
417	584.8641		93	618.7149
408	585.8060		80	619.8964
397	586.9834		73	620.7234
384	588.3965		54	622.6140
375	589.3388		52	622.9686
363	590.5167		45	623.7958
355	591.4592		34	624.8595
345	592.4018		27	625.4504
335	593.3115		20	626.1596
320	594.9945		11	627.2234
311	595.9375		5	627.8145

#### A.4 Wavelength calibration data for microscope-LSDI

Likewise, for the microscope-LSDI the relationships between the spectral lines and pixel numbers are listed in the table below. The coefficients for equation (4.5) after the quadratic least squares fitting are shown as follows.

$$A = 9.9998e-007;$$

$$B = -0.08417;$$

$$C = 670.1;$$

Pixel number	Wavelength (nm)		Pixel number	Wavelength (nm)
6	669.5758		391	637.3921
22	668.2741		409	635.8546
7	669.3391		427	634.3173
51	665.9072		445	632.8983
126	659.5168		470	630.6518
144	658.0967		486	629.3513
161	656.5583		496	628.5238
193	653.9549		508	627.5780
216	651.9433		517	626.7506
236	650.2868		531	625.6868
253	648.8669		549	624.2685
331	642.3600		564	622.9686
263	648.0387		574	622.1414
280	646.6189		589	620.8416
292	645.5542		632	617.2974
313	643.8979		604	619.6601
321	643.1881		618	618.4787
348	640.9405		624	618.0061
374	638.6931		638	616.8249

## Appendix B (MATLAB scripts)

### B.1 FFT based algorithm

```
clc
clear;

pxs=1;
pxe=480;           % px represents the surface profile direction
pys=1;
pye=640;           % py represents the chromaticity axis
pxl=pxe-pxs+1;
pyl=pye-pys+1;
% wavelength distribution
% A=1.8204E-007;    % Coefficients for 4x microscope-LSDI
% B=0.04153;
% C=616.56;
A = 1.3743e-006;
B = -0.10453;
C = 628.34;        % Coefficients for cylindrical-LSDI

index=1;
for py=(1:pyl)
    lamda(1,index)=A*py^2+B*py+C;
    index=index+1;
end
% Interpolation step in chromaticity axis
sampleX(1:pye)=double(lamda(1:pye));
sample1_X(1:pye)= 1./sampleX;
step = (sample1_X(2)-sample1_X(1));
interSampleX = sample1_X(1):step:sample1_X(end);
% Open background data matrix
fileID = fopen('BackGround.bin');
BG=fread(fileID,[480 640],'double');
fclose(fileID);
% Read the captured interferogram
aoriginal=imread('D:\measurement\Framelink\30stepheight.bmp');
bdouble(1:pxl,1:pyl)=aoriginal(pxs:pxe,pys:pye);

for px=1:pxl
% Background removing
Background_f=double(BG(px,1:pye));
Signal_f=double(bdouble(px,1:pye));
sampleYt1=Signal_f./Background_f;
% Interpolation/Coordinate transform
interSampleYt1 = interp1(sample1_X,sampleYt1,interSampleX, 'spline');
% Performing FFT to the interference signal
FFTlength=size(interSampleX,2);
fftResult=(1/FFTlength)*fft(interSampleYt1);
R=abs(fftResult);
fftFilter(1:length(fftResult))=0;           % Filtering out the unwanted DC
and phase conjugate
R(1:2)=0;
R(round(length(R)/2):length(R))=0;
[MaxPeak LocPeak]=max(R);
```

```

    if (LocPeak > 6)
        LowCutFreq=5;
        HighCutFreq=10;
    else
        LowCutFreq=2;
        HighCutFreq=4;
    end
fftFilter=fftResult;
fftFilter(1:(LocPeak-LowCutFreq))=0;
fftFilter((LocPeak+HighCutFreq):length(fftResult))=0;
ifftFilter=ifft(fftFilter); % Performing inverse FFT
phase=imag(log(ifftFilter)); % Extracting the phase from the imaginary

    phase_set(1)=0;
for j=1:length(phase)-1 % Constructing the Phase_set function
    if abs(phase(j+1)-phase(j)) >(2*pi*0.9)
        phase_set(j+1)=phase_set(j)+ 2*pi;
    else
        phase_set(j+1)=phase_set(j);
    end
end
phase_final=phase + phase_set; % Adding the Phase_set to the determined phase

% Linear Fitting using least square approach
C=0;
D=0;
E=0;
F=0;
FrameNumber=FFTlength;
CutPhaseStart=60;
CutPhaseEnd=FrameNumber-(CutPhaseStart-1);
N=length(phase_final(CutPhaseStart:CutPhaseEnd)); % Cropping the data at both
ends
for(i=CutPhaseStart:CutPhaseEnd)
    C=C+i;
    D=D+phase_final(i);
    E=E+(i*i);
    F=F+(phase_final(i)*i);
end
slop=(F-(1/N)*D*C)/(E-(1/N)*(C^2));
DC=((1/N)*D)-((slop/N)*C);

for i=1:FrameNumber
    PhaseFit(i)=DC+(slop*i); % Continuous phase after Linear fitting
end
PhaseShift=PhaseFit(length(PhaseFit))-PhaseFit(1); % Calculating the phase
variation
% Calculating the height
Height(px)=(PhaseShift)*(1/(4*pi*(interSampleX(1)-interSampleX(FFTlength))));

data=Height/1000; % Transferring the data to um scale

```

## B.2 Carré algorithm

```
clc
clear;

pxs=1;
pxe=480;           % px represents the surface profile direction
pys=1;
pye=640;           % py represents the chromaticity axis
pxl=pxe-pxs+1;
pyl=pye-pys+1;
% wavelength distribution
% A=1.8204E-007;    % Coefficients for 4x microscope-LSDI
% B=0.04153;
% C=616.56;
A = 1.3743e-006;
B = -0.10453;
C = 628.34;        % Coefficients for cylindrical-LSDI
index=1;
for py=(1:pyl)
    lamda(1,index)=A*py^2+B*py+C;
    index=index+1;
end
% Interpolation step in chromaticity axis
sampleX(1:pye)=double(lamda(1:pye));
sample1_X(1:pye)= 1./sampleX;
step = (sample1_X(2)-sample1_X(1));
interSampleX = sample1_X(1):step:sample1_X(end);
% Open background data matrix
fileID = fopen('BackGround.bin');
BG=fread(fileID,[480 640],'double');
fclose(fileID);
% Read the captured interferogram
aoriginal=imread('D:\measurement\Framelink\30stepheight.bmp');
bdouble(1:pxl,1:pyl)=aoriginal(pxs:pxe,pys:pye);
for px=1:pxl
    % Background removing
    Background_f=double(BG(px,1:pye));
    Signal_f=double(bdouble(px,1:pye));
    sampleYt1=Signal_f./Background_f;
    % Interpolation/Coordinate transformation
    interSampleYt1 = interp1(sample1_X,sampleYt1,interSampleX, 'spline');
    % Removing the DC
    v=mean(interSampleYt1);
    interSampleYt1=interSampleYt1-v;
    % Performing FFT to the interference signal
    FFTlength=size(interSampleX,2);
    fftResult=(1/FFTlength)*fft(interSampleYt1);
    R=abs(fftResult);
    R(1:2)=0;
    R(round(length(R)/2):length(R))=0;
    [MaxPeak LocPeak]=max(R);
    shift=round((FFTlength/LocPeak)/6); % Calculating the shift value
    if mod(shift,2)~=0
        shift=shift+1;
    end
    QuadIndexS=1+shift+(shift/2);
```

```

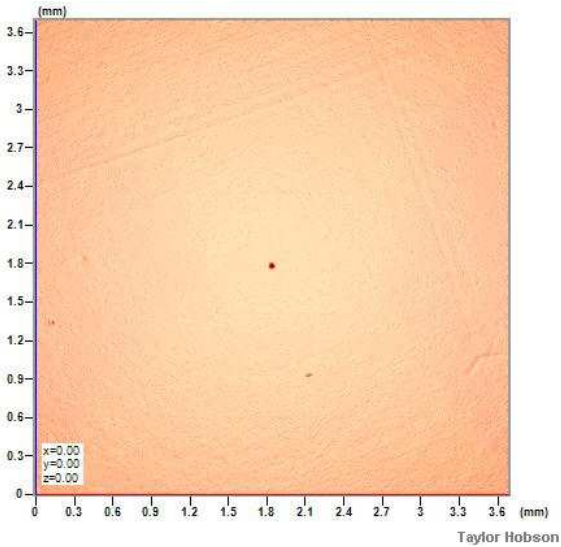
QuadIndexE=FFTlength-(2*shift)+(shift/2);
counter=0;
PhaseAll=0;
for i=QuadIndexS:QuadIndexE
I1=interSampleYt1(1+counter);
I2=interSampleYt1(1+shift+counter);
I3=interSampleYt1(1+2*shift+counter);
I4=interSampleYt1(1+3*shift+counter);
%-- Carre algorithm-----
a=(3*(I2-I3))-(I1-I4);
b=(I2-I3)+(I1-I4);
c=(I2+I3)-(I1+I4);
num1=(a*b);
den=c;
phase=atan((sqrt(abs(num1)/den^2)));
num=(I2-I3);
phase=PhaseUnwrapping(num,den,phase);
%-- End of Carre algorithm -----
counter=counter+1;
PhaseAll(counter)=phase;
end
phase_set(1)=0;
for i=1:length(PhaseAll)-1 % Constructing the Phase_set
function set function
if (PhaseAll(i+1)-PhaseAll(i)) <(-2*pi*0.9)
phase_set(i+1)=phase_set(i)+(2*pi);
elseif (PhaseAll(i+1)-PhaseAll(i)) >(2*pi*0.9)
phase_set(i+1)=phase_set(i)-(2*pi);
else
phase_set(i+1)=phase_set(i);
end
end
phase_final=PhaseAll + phase_set; % Adding the Phase_set to the phase
% Linear Fitting using least square approach
C=0;
D=0;
E=0;
F=0;
FFTlength2=length(phase_final);
for k=1:FFTlength2
C=C+k;
D=D+phase_final(k);
E=E+(k*k);
F=F+(phase_final(k)*k);
end
slop=(F-(1/FFTlength2)*D*C)/(E-(1/FFTlength2)*(C^2));
DC=((1/FFTlength2)*D)-((slop/FFTlength2)*C);
for n=1:FFTlength2
PhaseFit(n)=DC+(slop*n); % Continuous phase after Linear fitting
end
Phasediff=PhaseFit(FFTlength2)-PhaseFit(1); % Calculating the phase variation
% Calculating the height
Height(px)=(Phasediff)*(1/(4*pi*(interSampleX(1)-interSampleX(FFTlength2))));
end
data=Height/1000; % Transferring the data to um scale

```

# Appendix C (Measurement results)

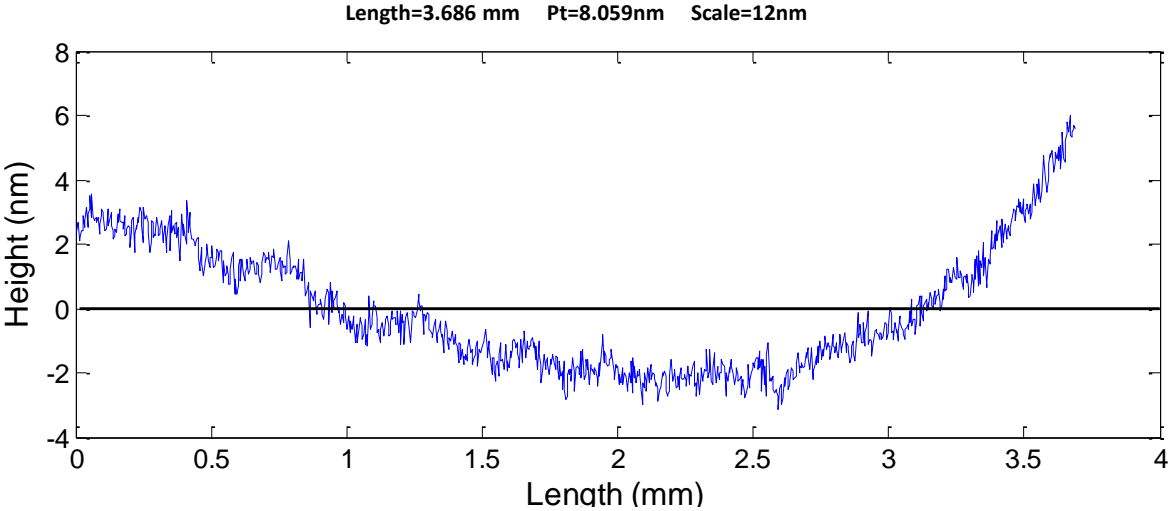
## C.1 Measurement results of the standard flat artefact

The standard flat artefact was measured using Talysurf CCI 3000 which is an advanced 3D optical metrology tool achieving 0.01 nm vertical resolution over a full 100 μm scan range. The objective lens used for this measurement task is 5X magnification with 0.13 NA and 3.6 mm x 3.6 mm measurement range. The measurement results including the areal surface texture parameters and one cross-sectional profile are shown as follows.



	Original results
<b>AMPLITUDE PARAMETERS</b>	
Sa(um)	0.002
Sq(um)	0.004
Ssk	-199.939
Sku	6.553E+04
Sp(um)	0.335
Sv(um)	1.794
Sz(um)	2.130
<b>HYBRID PARAMETERS</b>	
Sdq	0.001
Ssc(1/um)	8.433E-05

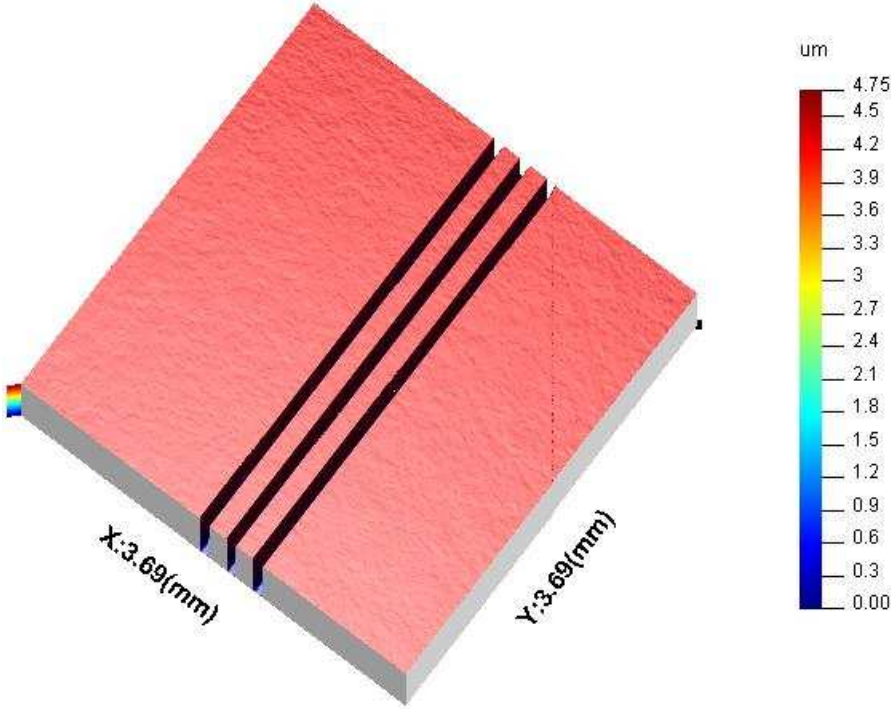
2D view of the measured surface/ Areal surface texture parameters



Cross-sectional profile result

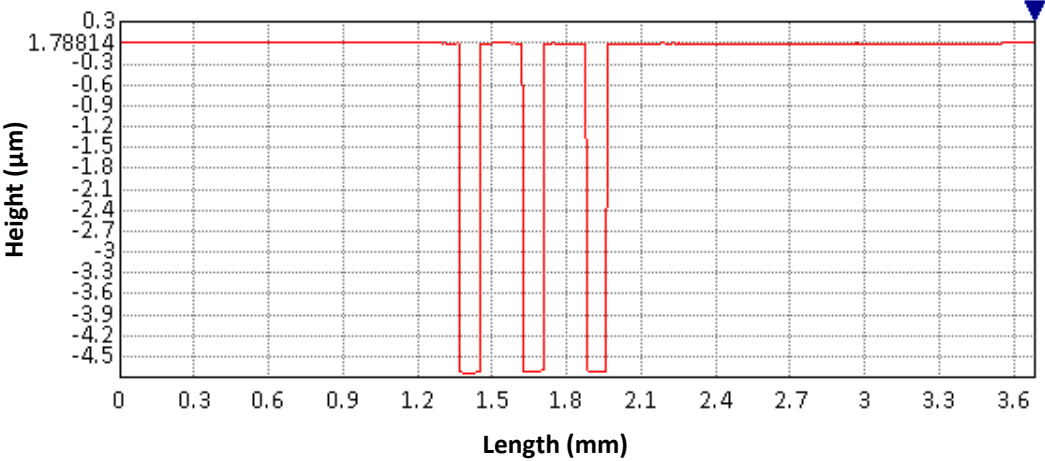
**C.2 Measurement results of the 4.707 μm standard step heights**

The measurement results of the 4.707 μm standard step height using CCI 3000 are shown as follows. The average height value is calculated as 4.699 μm (5X objective).



(a)

**X Profile**

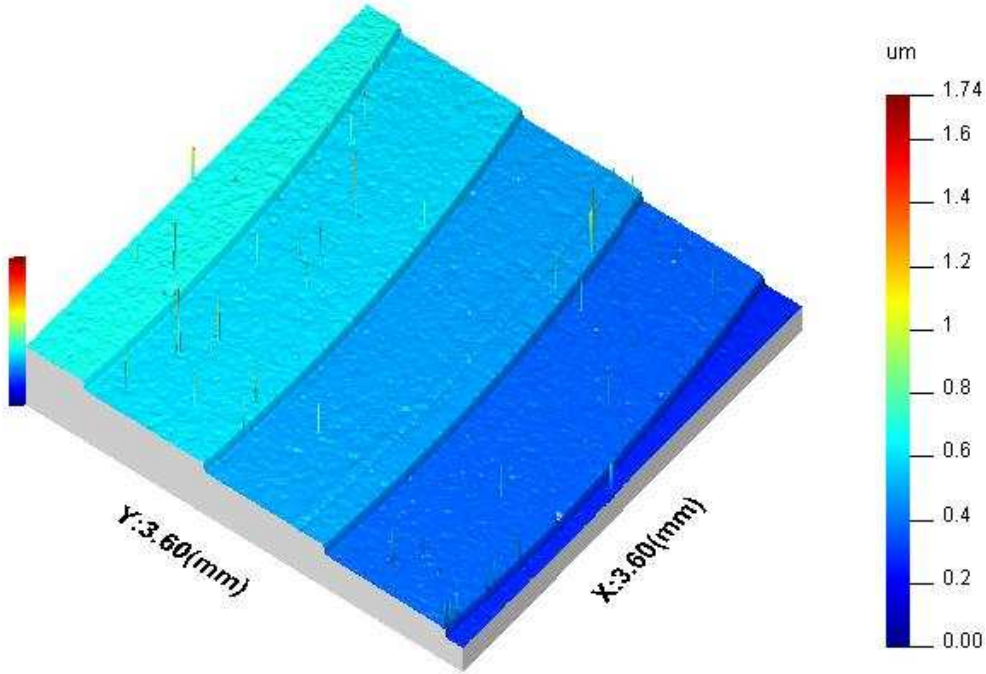


(b)

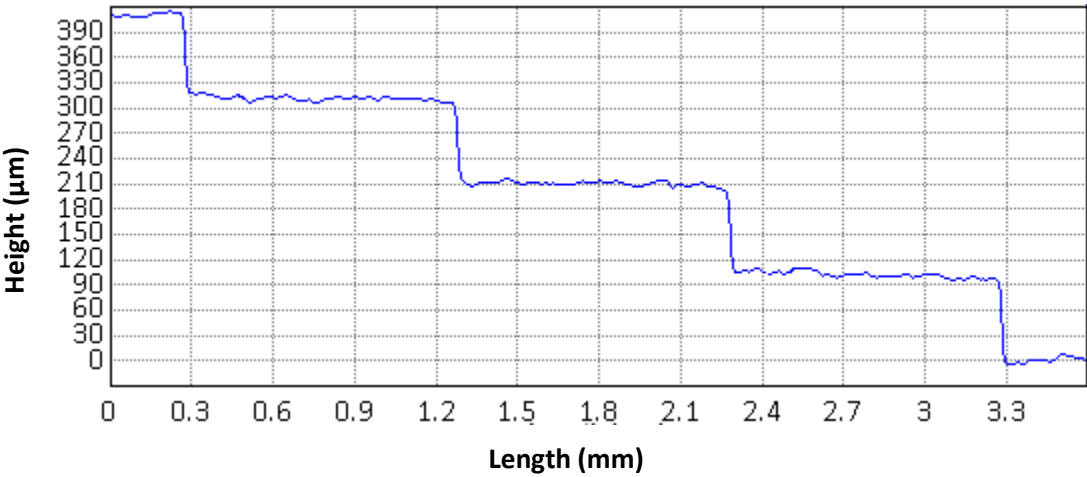
**4.707 μm step sample: (a) measured surface map, (b) cross-sectional profile result.**

**C.3 Measurement results of the 100 nm diamond-turned step sample**

The measurement results of the 100 nm diamond-turned step sample using CCI 3000 are shown as follows. The measured average heights are calculated as 99 nm, 103 nm, 95 nm and 94 nm from the left to right (5X objective).



(a)

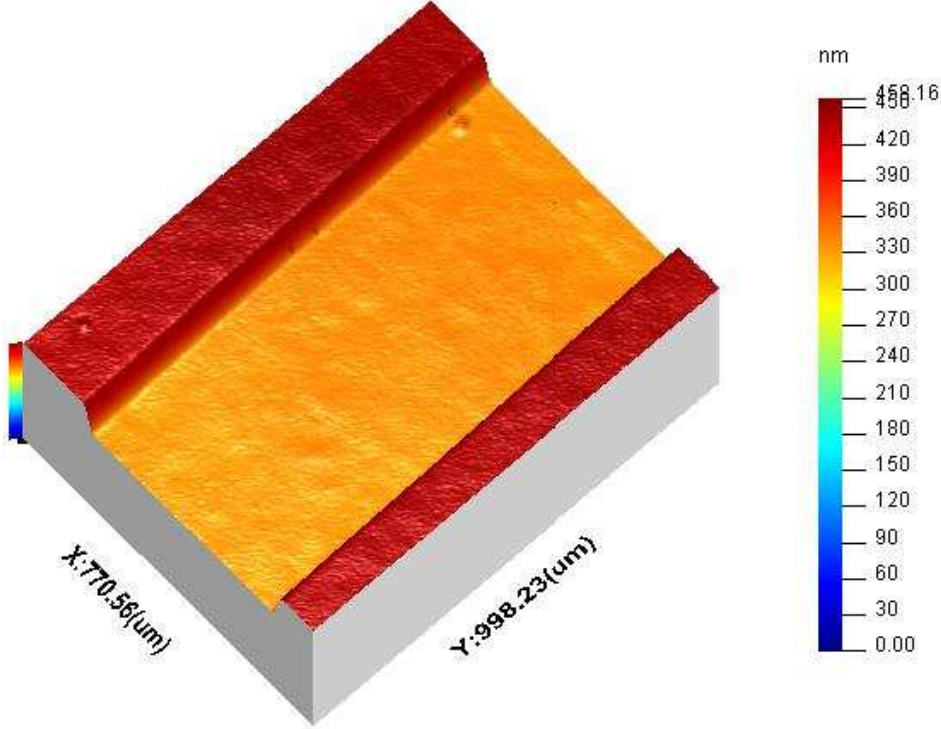


(b)

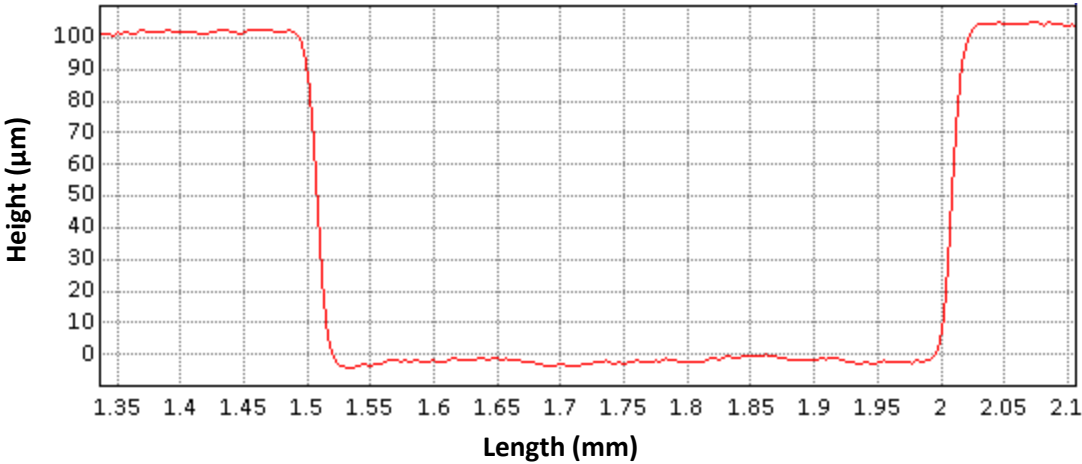
**100 nm diamond-turned step sample: (a) measured surface map, (b) cross-sectional profile result.**

**C.4 Measurement results of the 100 nm standard step height**

The measurement results of the 100 nm standard step sample using CCI 3000 are shown as follows. The measured average height is calculated as 103.5 nm (5X objective).



(a)

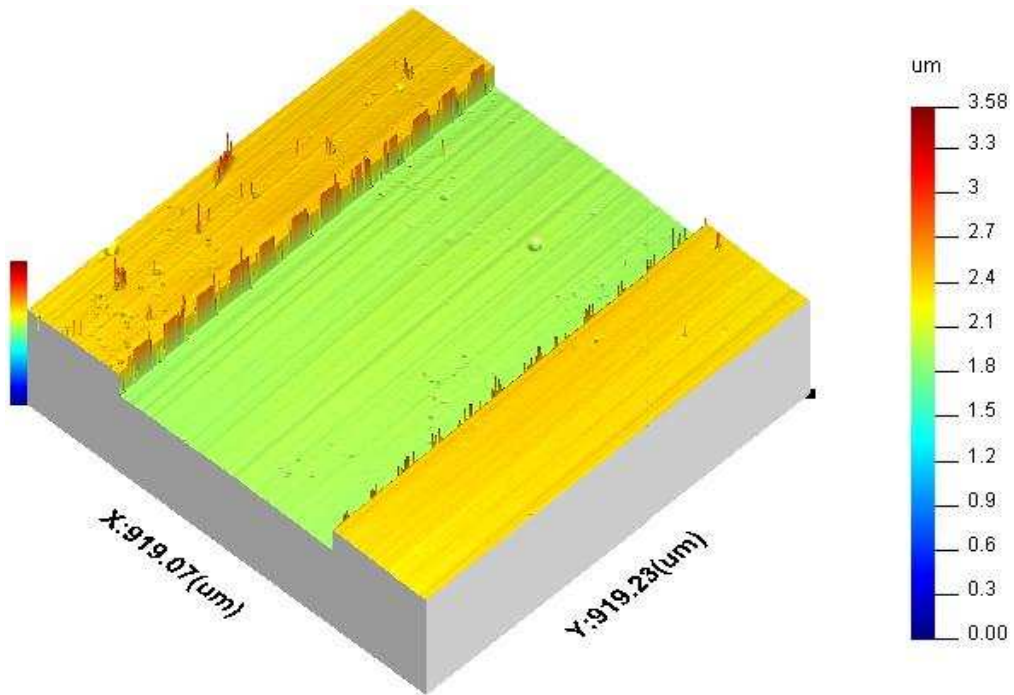


(b)

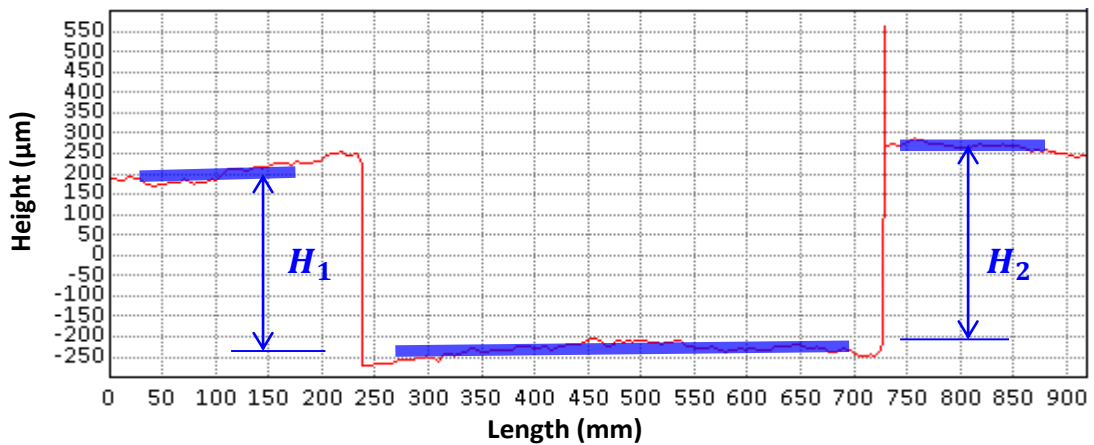
**100 nm standard step sample: (a) measured surface map, (b) cross-sectional profile result.**

### C.5 Measurement results of the 500 nm reference step sample

The measurement results of the 500 nm reference step sample using CCI 3000 are shown as follows (20X objective). The measured average heights are calculated as 449.8 nm ( $H_1$ ) and 463.11 nm ( $H_2$ ), respectively.



(a)



(b)

500 nm step sample: (a) measured surface map, (b) cross-sectional profile result.